Manuel Patrice Geisler

# Improving Searches for Dark Matter Using Missing Transverse Momentum and Jets

An Analysis with the ATLAS Detector at $\sqrt{s} = 13$ TeV

Dissertation

Dissertation

submitted to the

Combined Faculties of the Natural Sciences and Mathematics

of the Ruperto-Carola-University of Heidelberg, Germany

for the degree of

Doctor of Natural Sciences

Put forward by

Manuel Patrice Geisler

born in Bielefeld

Oral examination on February 7th 2018

# Improving Searches for Dark Matter Using Missing Transverse Momentum and Jets

**An Analysis with the ATLAS Detector at $\sqrt{s} = 13$ TeV**

Referees: Prof. Dr. Hans-Christian Schultz-Coulon
Prof. Dr. André Schöning

## Abstract

This thesis presents a novel strategy for searches for Dark Matter at particle colliders using variables that are corrected for detector effects. Dark Matter is experimentally motivated by cosmological evidence and is one of the great contemporary puzzles of physics. This thesis describes the conventional approach of searches for Dark Matter using final states with missing transverse momentum, $p_{\mathrm{T}}^{\mathrm{miss}}$, and hadronic jets and discusses its shortcomings. Several techniques for improvements are put forward. An analysis is presented that implements these improvements. It is performed on $3.2\,\mathrm{fb}^{-1}$ of data collected by the ATLAS experiment in 2015 at $\sqrt{s} = 13\,\mathrm{TeV}$ and measures an unfolded fiducial cross-section ratio in two kinematic regions and in total four differential distributions. The numerator of the ratio is defined as $\sigma(p_{\mathrm{T}}^{\mathrm{miss}} + \mathrm{jets})$ and the denominator as $\sigma(\mathrm{Z}\rightarrow l^{+}l^{-} + \mathrm{jets})$. The ratio leads to the cancellation of many systematic uncertainties and detector-induced effects. Limits on three Dark Matter scenarios are set using the distributions. An improved performance with respect to the conventional $p_{\mathrm{T}}^{\mathrm{miss}}$ + jets Dark Matter search is observed. These distributions can be used to set limits on models containing new physics without using an ATLAS detector simulation. Additional studies are presented investigating further performance enhancements for a future iteration of this analysis.



## Zusammenfassung

In dieser Doktorarbeit wird eine neue Strategie zur Suche nach Dunkler Materie an Teilchenbeschleunigern präsentiert, die Variablen verwendet, die von Detektoreffekten bereinigt sind. Dunkle Materie ist durch kosmologische Beobachtungen experimentell motiviert und eines der großen Rätsel der modernen Physik. Diese Doktorarbeit erklärt den konventionellen Ansatz zur Suche nach Dunkler Materie an Beschleunigerexperimenten in Endzuständen mit fehlendem transversalem Impuls und hadronischen Jets und zeigt dessen Mängel auf. Verschiedene Verbesserungsansätze werden vorgestellt und eine Analyse wird präsentiert, in der diese Ansätze umgesetzt sind. Die Analyse wurde auf dem Datensatz mit $3.2\,\mathrm{fb}^{-1}$ durchgeführt, der von dem ATLAS Experiment 2015 bei einer Schwerpunktsenergie von $\sqrt{s} = 13\,\mathrm{TeV}$ aufgenommen wurde. Sie umfasst ein entfaltetes Wirkungsquerschnittsverhältnis gemessen in zwei kinematischen Regionen und insgesamt vier Differentialverteilungen. Der Zähler des Verhältnisses ist definiert als $\sigma(p_{\mathrm{T}}^{\mathrm{miss}} + \mathrm{jets})$ und der Nenner als $\sigma(\mathrm{Z}\rightarrow l^{+}l^{-} + \mathrm{jets})$. Das Bilden des Quotienten führt zur Aufhebung vieler systematischer Unsicherheiten und Detektor-induzierter Effekte. Ausschlussgrenzen für drei Szenarien Dunkler Materie werden mithilfe der Verteilungen bestimmt. Die Analyse bietet eine verbesserte Leistung verglichen mit den Ausschlussgrenzen der konventionellen $p_{\mathrm{T}}^{\mathrm{miss}}$ + Jets Suche nach Dunkler Materie. Die Ergebnisse in Form der differenziellen Verteilungen können verwendet werden, um neue physikalische Theorien jenseits des Standardmodells der Elementarteilchenphysik zu untersuchen, ohne eine ATLAS-Detektorsimulation zu verwenden. Zusätzliche Studien werden vorgestellt, um weitere Leistungsverbesserungen für eine zukünftige Iteration dieser Analyse zu untersuchen.

# Contents

# Author's Contribution

My work during the PhD falls into three categories:

- I worked on several different aspects of the Level-1 calorimeter trigger of the ATLAS experiment (L1Calo). This includes but is not limited to its operation.
- I contributed to the analysis of the 2015 dataset of proton-proton collisions collected by the ATLAS experiment that culminated in the publication of the unfolded search for Dark Matter [1], which is is described in one of the main chapters of this thesis.
- I studied potential optimisations for the next iteration of this analysis that will likely be performed on the combined 2016 and 2017 datasets collected by the ATLAS experiment.

For the sake of writing a focussed dissertation, my contributions to L1Calo are not further detailed the thesis. Instead, I will summarise the main parts here. My work on L1Calo was performed mostly in the context of the recommissioning of the system for the beginning of Run2 of the LHC and ATLAS in 2015. New hardware, in particular the New Multichip Modules (nMCMs), had been produced and needed to be tested, integrated and commissioned. I developed two graphical user interfaces (GUIs) to assist the firmware loading and testing procedures. The nMCMs showed a better performance than the old hardware (MCMs). I studied this with respect to the levels of electronic noise in general and correlated noise across multiple channels in particular by writing and performing an analysis thereof. The improved performance also required re-optimising the calibration runs, because the old calibrations and thresholds became obsolete. In general the software that dealt with operating L1Calo needed several adaptations to the new system and I contributed to that as well. This includes, but is not limited to, rewriting the bytestream decoder, which translates the binary data stream of the system into human-readable output. Shortly before the proton beams circulated in the LHC for the first time in 2015 after the long shutdown, several splash events were provided by the machine. Collaborators and I used the data from these events to derive a first timing for the new L1Calo system. L1Calo was not the only system to receive an upgrade. Among many others, the Liquid Argon Calorimeter (LAr) had new hardware installed. A demonstrator board was developed and tested that will be produced in large scale for the next long shutdown of the LHC. Since L1Calo and LAr are tightly connected on a hardware level, I was also involved in testing some performance aspects of this board.

The main part of my PhD however was a data analysis, a search for Dark Matter. I contributed to two iterations of this analysis. The first iteration's goal was a proof-of-priciple paper using the 2015 dataset collected by the ATLAS experiment [1]. The second iteration of the analysis is as of now (November 2017) still in preparation and a dataset will be used that exceeds the size of the previous one by more than an order of magnitude.

For the published analysis my contributions are fourfold: I was my institute's main author of the software framework that implements the analysis chain, I worked on general signal region optimisations, on the dominant background contribution, i.e. events containing hadronically

decaying $\tau$ leptons, and the multijet background. For hadronically decaying $\tau$ leptons I defined and optimised the event veto. For the multijet background I developed and implemented the data-driven estimate. The signal region optimisations included a study on varying several selection criteria of the basic event selection, most importantly the $p_{\mathrm{T}}^{\mathrm{miss}}$ and jet cuts, and investigating their impact on signal significances and signal region compositions. Re-optimisations were performed after concluding the studies on the $\tau$ and multijet backgrounds.

For the next iteration of the analysis I conducted several studies that had performance enhancement as the common goal. I re-optimised the multijet background rejection cuts to achieve a higher signal efficiency. I also investigated the possibility of using a cut on $H_{\mathrm{T}}^{\mathrm{miss}}$ instead of the $p_{\mathrm{T}}^{\mathrm{miss}}$ for our signal region definition for an easier treatment of systematic uncertainties on a technical level and a reduction of dataset size. Lastly, I looked into various ways to discriminate between processes involving vector boson fusion and those which do not. Among other things, I studied the potential of quark-gluon discrimination (*"tagging"*) in jets and additional hadronic activity in candidate events. I used this information as inputs for multivariate analyses, mostly Boosted Decision Trees, and studied their performances.

# 1. Introduction

The cosmological evidence for Dark Matter (DM) is long-standing and plentiful. From measurements by the Planck satellite [2] DM accounts for 26.8% of the energy density of the Universe. However, first evidence comes from the 1930s and 1940s, when it was observed by J.H. Oort, F. Zwicky, and others that rotational curves of galaxies behave anomalously [3, 4]. The contemporary interpretation is the postulation of a halo of DM, i.e. matter that does not interact electromagnetically, around the galaxies. Over the course of time more and more evidence pointing towards the existance of this exotic kind of matter was found [5]. While in cosmology DM is well established, its nature has yet to be unravelled. DM can be detected via its production and measurement at collider experiments, such as the ATLAS experiment at the LHC at CERN. Further, complementary, evidence can be gathered via direct and indirect detection measurements.

For all of these detection approaches, DM must not only interact gravitationally with Standard Model (SM) particles. An additional interaction via a weak force, for instance the electro-weak force of the SM, is assumed. These hypothetical DM particles are called weakly interacting massive particles (WIMPs) and are predicted by a multitude of New Physics models, e.g. SUSY, or some extended Higgs models.

In a collider experiment, DM particles do not leave a trace in the detector, because of the absence of electromagnetic and strong interactions. This signature is similar to neutrinos in the SM. As a result DM searches at a collider require the production of an *associated* particle, e.g. hadronic jets or photons. Consequently, the signature at a collider search is a SM particle and missing transverse momentum, $p_{\mathrm{T}}^{\mathrm{miss}}$, a result of the momentum imbalance caused the DM particles escaping the detector. For a SM particle $X$ these searches are called $p_{\mathrm{T}}^{\mathrm{miss}} + X$ searches. The focus of this thesis are $p_{\mathrm{T}}^{\mathrm{miss}}$ + jets searches, where the jet originates in a quark or a gluon.

The conventional approach [6, 7] to searches for the anomalous production of events with $p_{\mathrm{T}}^{\mathrm{miss}}$ + jets is to measure an event yield an to compare it so SM predictions. Based on this and on the statistical and systematic uncertainties of the measurement, limits on Beyond the Standard Model (BSM) models can be set or discovery can be claimed. However, a shortcoming is that once published the results are difficult to reinterpret, because extensive knowledge of the detection apparatus is required to make predictions for the number of observed events.

The analysis presented in the main chapters of this thesis uses a novel approach to $p_{\mathrm{T}}^{\mathrm{miss}}$ + jets searches. One of the novelties is that it presents an *unfolded* measurement designed to be sensitive to DM. This means that the results are corrected for detector effects making them comparable to BSM predictions without subjecting the latter to detector simulations. This is a benefit to researchers who do not have access to detailed software implementations of the experiments of large collaborations, such as ATLAS or CMS. Results are also provided in terms of *differential distributions*, which allows for setting stronger constraints on various BSM theories.

In this analysis the measurement of an unfolded *cross-section ratio* of the form

$$R_{\text{miss}} = \frac{\sigma(p_{\text{T}}^{\text{miss}}+\text{jets})}{\sigma(Z\to l^+l^-+\text{jets})}$$

is performed. The ratio compensates for various systematic uncertainties and detector effects. The definition of numerator and denominator is made such that these uncertainties cancel to large extents, which improves sensitivity. An additional kinematic region is introduced with special sensitivity to the production of DM via vector boson fusion (VBF). This kinematic region and the measurement of variables especially sensitive to VBF allows for investigating classes of DM models that only had loose constraints before and that are interesting from a theoretical perspective. Examples are some effective field theories [8] and invisible decays of the Higgs boson [9].

For future analyses, this thesis also presents studies that can potentially further improve the approach.

This thesis is structured as follows: Chapter 2 introduces the Dark Matter puzzle. Evidence for the existence of Dark Matter is summarised at it is shown that the SM does not explain it. Three models for DM are introduced on which the analysis described later sets limits. Lastly, former detection attempts are discussed. In Chapter 3 the experimental setup is presented and experimental techniques are explained. This includes a brief description of the LHC as well as an overview of the ATLAS detector including its various subdetectors and systems. Furthermore, physics at hadron colliders, the reconstruction of different physics objects with the ATLAS experiment, and Monte Carlo simulations are discussed. In Chapter 4 the conventional ATLAS $p_{\text{T}}^{\text{miss}}$ + jets search for DM is described and its shortcomings are discussed. Several techniques are put forward that can improve the performance and mitigate its shortcomings. These are unfolding, cross-section ratio measurements, sensitivity for vector boson fusion, and boosted decision trees. Chapter 5 presents the central piece of the thesis: a detailed description of the unfolded cross-section ratio measurement that is a search for DM with the 2015 dataset collected by the ATLAS experiment. All central aspects of the are analysis discussed such as event selection, unfolding, and results, but a focus is put on the contributions of the author of this thesis. Chapter 6 presents optimisation studies with the goal of performance enhancement for the next iteration of this analysis on a larger dataset. This encompasses the potential of multivariate analyses, optimisations of the cuts with respect to the multijet background and studies on using a cut on the missing $\text{H}_T$ instead of $p_{\text{T}}^{\text{miss}}$. Lastly, a summary and conclusions are provided in Chapter 7.

# 2. The Dark Matter Puzzle

Over the last decades more and more evidence for Dark Matter has been gathered. This kind of matter interacts gravitationally and contributes to the energy-density of the Universe [2], but has not yet been directly observed. The lack of direct observation implies that it does not interact electromagnetically. In contrast to many other contemporary problems in physics this Dark Matter (DM) puzzle is experimentally motivated. In this chapter a brief overview of the evidence for DM is presented. It is also shown that the well-established Standard Model of particle physics does not provide a fitting candidate for DM. However, there are plenty of theoretical frameworks which could explain it and several models and parametrisations will be introduced that could make the pieces of the puzzle fit together. Lastly, different detection methods and detection efforts for DM are discussed including current exclusion limits.

## 2.1. Evidence of Dark Matter

The cosmological evidence for DM is plentiful. Numerous independent measurements point to the existence of matter that interacts gravitationally but not electromagnetically. The earliest observed anomalies that were later interpreted as evidence of DM go back to the 1930s [3, 4] and are related to irregular dynamics of nebulae and stars. It was later found via red-shift analyses that stars in observed galaxies do not follow the expected velocity distribution with respect to the distance from the galactic centre, $r$. Instead of following the distribution predicted by Newtonian Physics, $\sqrt{1/r}$, the velocities are almost constant outside of the central region. A halo of DM around the galaxies is hypothesized to explain this observation. Figure 2.1 shows as an example the rotation curve of NGC 3198 [10]. The x-axis indicates the distance to the galactic centre in kpc and the y-axis the circular velocity. It can be seen that the observed curve cannot be explained by the galaxy disk and interstellar gas alone. Adding a dark halo however describes the data well. A competing explanation is a different behaviour of Newtonian gravity on large scales, so called modified Newtonian dynamics (MOND) theories [11, 12]. Although MOND theories fit the velocity spectra with high precision, they are effective theories lacking in describing an underlying physical source for the change in dynamics. Nor do they explain other observations [13], such as presented below.

Additional pieces of evidence can be found in some observed occurrences of gravitational lensing [11, 14]. Here, the mass of observed baryonic matter is not sufficient to cause these effects making DM a viable explanation [15]. One prominent example is the galaxy cluster 1E 0657-558, commonly referred to as the *bullet cluster*. It is composed of two separate clusters, which have passed through each other in the past. In addition to showing gravitational lensing in accordance with DM observations it also contradicts MOND theories [16].

More evidence comes from detailed measurements of the cosmic microwave background radiation (CMB). The CMB is a remnant of the cosmological era of recombination that occurred approximately 300000 years after the Big Bang. Today this thermal radiation has a temperature of

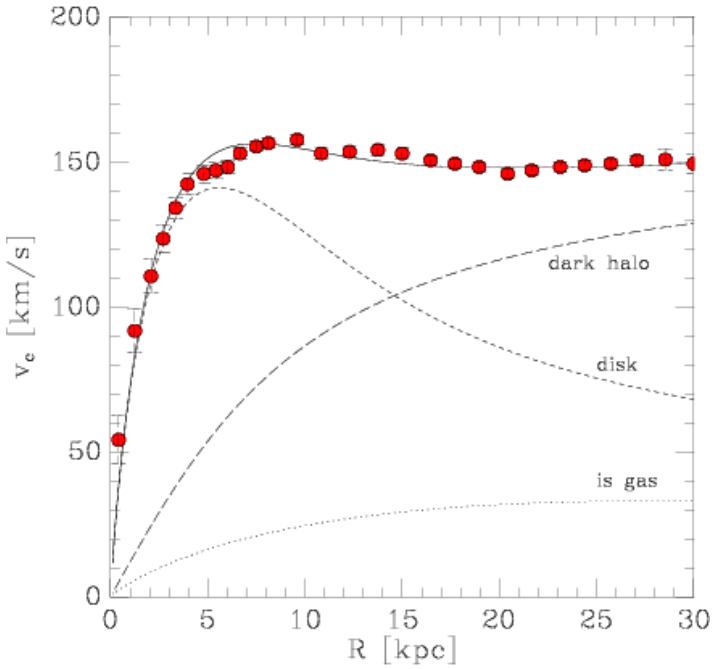


Figure 2.1.: The rotation curve of NGC 3198 is depicted. A dark halo is hypothesised to explain the data points. Data points are shown in red and the lines correspond to the various contributions to the overall rotation curve. *Disk* refers to baryonic matter in the galactic disk, *is gas* is interstellar gas and *dark halo* is the postulated DM. Image taken from [10].

2.7 K and is almost perfectly anisotropic. However, it shows small scale temperature differences, first observed by the Cosmic Background Explorer (CoBE) satellite [17] launched in 1989. These fluctuations can be expanded into a power series with respect to the angular scale. The anisotropies yield characteristic peaks that help to constrain cosmological models of the Universe. Today's *standard model* of cosmology is the ΛCDM model [11]. In the acronym, Λ stands for the cosmological constant in Einstein's theory of general relativity[1] and CDM for cold, i.e. non-relativistic, Dark Matter. It describes the power spectrum with high precision if parameters are chosen accordingly. The fit to the data implies an energy density distribution of the universe as follows: 4.9% baryonic matter, 68.3% Dark Energy from Λ, and 26.8% Dark Matter [2].

Cold DM also yields an explanation for large scale structure formation in the early universe. Small density fluctuations in the DM distribution led to potential wells acting as seeds around which baryonic matter eventually accumulated. This set the foundation for galaxy cluster formation [18] as we observe today.

The evidence presented above is compelling and established in the scientific community. However, the particle nature of DM remains unknown. As is discussed in Section 2.2, DM is beyond the scope of the well established *standard model of particle physics* as the latter does not provide a good candidate to explain the observations.

[1] Λ corresponds to *Dark Energy*, which causes the accelerated expansion of the Universe. In the ΛCDM model it is a free parameter.

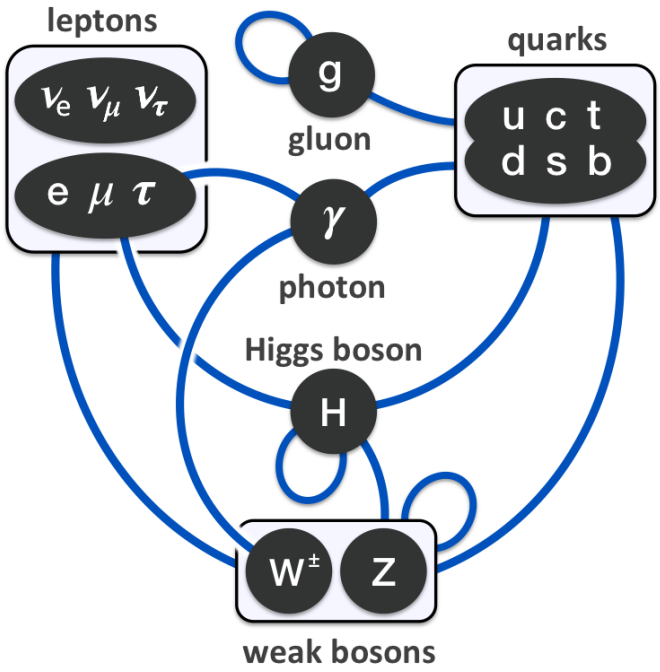


Figure 2.2.: A sketch of the fundamental particles of the standard model and the interactions between them [20].

## 2.2. The Standard Model of Particle Physics

The Standard Model (SM) of particle physics is a theoretical framework that describes all known elementary particles and three of the four known forces of nature: electromagnetism, the weak nuclear force, and the strong nuclear force. Gravity has not yet been successfully incorporated into this framework. In the SM, the interactions between particles are themselves mediated by particles [19].

The particles of the SM are grouped into *fermions* and *bosons*. They differ in spin and carry a variety of quantum numbers. Fermions have half-integer spin and bosons integer spin. Fermions can be further divided into leptons and quarks and each fermion has an antiparticle of opposite physical charges. There are three charged leptons: electrons (e), muons ($\mu$), and tau leptons ($\tau$), which differ in mass and lepton flavour. They are accompanied by charge-neutral neutrinos: $\nu_e, \nu_\mu$, and $\nu_\tau$, which carry the lepton flavours of their charged counterparts, and are treated as massless in the SM[1]. All leptons interact via the weak force and the charged leptons also via electromagnetism. The six quarks are in order of ascending mass: down (d), up (s), strange (s), charm (c), bottom (b), and top (p), covering a mass spectrum of 0.003 GeV (d) to 174 GeV (t). d-, s-, and b-quarks, also called *down-like*, have an electric charge of Q = -1/3. u-, c-, and t-quarks, *up-like*, have charge Q = 2/3. Quarks interact via all three forces of the SM. The d- and u-quarks together with the electron form the first generation of fermions. s, c, and $\mu$ form the second generation and b, t, and $\tau$ the third generation. Particles interact via the exchange of bosons. The massless photon ($\gamma$) is the mediator of the electromagnetic force. The massive

[1] Although observations show neutrino oscillation [21–23] indicating that they in fact have masses.

| Leptons | | | Quarks | | |
|---|---|---|---|---|---|
| Particle | Q | Mass [GeV] | Particle | Q | Mass [GeV] |
| electron ($e^-$) | -1 | 0.0005 | down (d) | -1/3 | 0.003 |
| neutrino ($\nu_e$) | 0 | $< 10^-9$ | up (u) | +2/3 | 0.005 |
| muon ($\mu^-$) | -1 | 0.106 | strange (s) | -1/3 | 0.1 |
| neutrino ($\nu_\mu$) | 0 | $< 10^-9$ | charm (c) | +2/3 | 1.3 |
| tau ($\tau^-$) | -1 | 1.78 | bottom (b) | -1/3 | 4.5 |
| neutrino ($\nu_\tau$) | 0 | $< 10^-9$ | top (t) | +2/3 | 174 |

Table 2.1.: The twelve fundamental particles of the SM and their charges and masses. They are grouped according to their generation. Taken from [19] and modified. Q is the electric charge.

$W^\pm$ and Z bosons mediate the weak force and there are eight massless gluons which are the mediators of the strong force. The latest addition to the SM is the Higgs boson, the discovery of which in 2012 [24, 25] completes the SM. It provides a mechanism by which the massive particles, to which it couples, get their rest-masses. Figure 2.2 shows a sketch of all fundamental particles of the SM and the possible interactions between them. Table 2.1 and 2.2 summarise the particles and list selected features.

As a quantum field theory the SM follows gauge symmetries and is described by the gauge group $SU(3)_C \times SU(2)_L \times U(1)_Y$ [19, 26]. $SU(3)_C$ corresponds to the strong sector and $SU(2)_L \times U(1)_Y$ to the electroweak sector of the SM. The fields in this formulation are the electroweak boson fields $B$, $W^1, W^2$, and $W^3$, the eight gluon fields $G_a$, the fermion fields $\psi$, and the Higgs doublet $H$. The Higgs is a doublet under $SU(2)_L$ and can be expressed as

$$H = \frac{1}{\sqrt{2}} \begin{pmatrix} 0 \\ h + v_0 \end{pmatrix}.$$

Here, $h$ is the real Higgs singlet and $v_0$ is the vacuum expectation value. The generators of the gauge groups and the bosons of the standard model are connected: for *quantum chromo dynamics* (QCD), the eight gluon fields are a consequence of the structure of the $SU(3)_C$ gauge group with its eight degrees of freedom. The $W^i$ and $B$ fields follow similarly from the gauge group $SU(2)_L \times U(1)_L$. Via the Englert–Brout–Higgs–Guralnik–Hagen–Kibble mechanism [27–29] gauge symmetry is spontaneously broken in the electroweak sector leading to a mixing of the massless fields into the well-known observable bosons and the weak bosons gain mass:

| Boson | Mediated Force | Q | Spin | Mass [GeV] |
|---|---|---|---|---|
| Gluon (g) | Strong | 0 | 1 | 0 |
| Photon ($\gamma$) | Electromagnetism | 0 | 1 | 0 |
| W Bosons ($W^\pm$) | Weak | $\pm1$ | 1 | 80.4 |
| Z Boson (Z) | | 0 | 1 | 91.2 |

Table 2.2.: The four force-carrying bosons of the SM. Gravity has not yet been successfully incorporated. Taken from [19] and modified.

$$W^{\pm} = \frac{1}{\sqrt{2}}(W_1 \mp iW_2),$$

$$Z = \cos\Theta_W W_3 - \sin\Theta_W B.$$

Here, $\Theta_W$ is the Weinberg angle. The photon $\gamma$ remains massless and is described by the neutral boson field A:

$$A = \sin\Theta_W W_3 + \cos\Theta_W B.$$

Electroweak gauge bosons can undergo *vector boson fusion*, an aspect that is further discussed in Section 4.2.3. Under $\mathrm{SU}(2)_L$ left-handed fermions exists as doublets and right-handed fermions as singlets. Right-handed neutrinos are not considered part of the SM. Being singlets under $\mathrm{SU}(2)_L$ they would not engage in weak interactions making detection difficult. Quarks can be expressed in terms of their weak eigenstates and their mass eigenstates. They are related via the Cabbibo-Kobayashi-Maskawa (CKM) matrix [19].

For electroweak theory the couplings involved are small allowing for a description of interactions using perturbation theory. The same is true for interactions at high energies for the strong force because of the *asymptotic freedom* of QCD. At low energies however the strong coupling $\alpha_S$ becomes large and perturbation theory no longer applies. This phenomenon is known as *color confinement*, which leads to *hadronisation*, the formation of hadrons. Hadrons are bound states of quarks. A bound state of two quarks is called a meson. Three quarks form baryons, such as neutrons and protons. In 2015 the LHCb experiment at CERN reported the observation of a pentaquark state involving five quarks [30]. Hadronisation has important ramifications for the measurement of quarks and gluons which form so-called *jets*. This is further detailed in Section 3.4.1. Jets can also originate in hadronic initial state radiation (ISR) or final state radiation (FSR), which occurs when a gluon radiates from another coloured object. If perturbation theory applies, cross-sections and transition rates can in principle be calculated to arbitrary orders. The precision of these calculation, cf. Section 3.5, is limited by finite processing power. For non-relativistic fields transition rates $\Gamma_{fi}$ from an initial state $i$ to a final state $f$ are described by Fermi's golden rule:

$$\Gamma_{fi} = 2\pi|T_{fi}|^2\rho(E_i)\,.$$

Here, $\rho(E_i)$ is the density of states and $\mathrm{T}_{fi}$ is the transition matrix element, which incorporates the perturbation, i.e. the interaction that mediates the transition. Fermi's golden rule can be generalised to the relativistic limit by making every constituent Lorentz-invariant. The form of the matrix element depends on the interaction that is considered. For the relatively simple case of the exchange of a scalar particle, the Lorentz-invariant matrix element is

$$\mathcal{M}_{fi} = \frac{g_a g_b}{q_X^2 - m_X^2}\,,$$

where $\mathrm{g}_a$ and $\mathrm{g}_b$ are the couplings of the scalar to the particles undergoing the interaction, and $q_X^2$ and $m_X$ are its four-momentum and mass, respectively. Feynman diagrams form an intuitive

description of particle interactions and Feynman rules allow for an algorithmic translation into probability amplitudes [31].

With massless neutrinos the SM has 19 free parameters[1], which cannot be derived from first principles. Nine of these are the fermion masses: $m_u$, $m_d$, $m_s$, $m_c$, $m_t$, $m_b$, $m_e$, $m_\mu$, and $m_\tau$. Two are connected to the Higgs-mechanism: the vacuum expectation value $v_0$ and the mass of the Higgs boson $m_H$. Three parameters correspond to the couplings of the three gauge interactions: $\alpha$, $G_F$, and $\alpha_S$. And lastly, there are three mixing angles and a CP violating phase in the CKM matrix: $\Theta_{12}$, $\Theta_{23}$, $\Theta_{13}$, $\delta$. The values of these parameters are determined experimentally.

Considering all established elementary particles of the SM, the only candidates for DM are neutrinos. As stated above, experimental evidence shows neutrino oscillation, which implies massive neutrinos. However, the masses of the SM neutrinos must be very low, leading to relativistic particles, which corresponds to hot Dark Matter. But evidence points to the existence of cold DM as explained above. As a consequence, SM neutrinos, although contributing to the DM energy density of the universe through their masses, cannot be the full picture of DM. Further puzzle pieces beyond the SM must exist.

## 2.3. Dark Matter Models

This section introduces three models for Dark Matter that can provide the missing pieces to the DM puzzle and that are relevant to the analysis presented in Chapter 5. There, limits are set on the following DM scenarios: a simplified model, an effective field theory (EFT), and the coupling of the Higgs boson to invisible particles. In these scenarios no or only few assumptions are made beyond the postulation of DM as particles and a coupling to the SM. They are considered because of this generality. The three models are motivated and explained below. However, many more DM models exist. A few examples are supersymmetry, axions and MACHOs: in the UV-complete supersymmetry the lightest neutral supersymmetric particle is a candidate for DM [11, 32, 33]. Axions can be introduced to solve the strong CP problem but are also a candidate for DM because of their assumed low mass and lack of electromagnetic interaction [11]. Dark Matter models do not necessarily need to postulate new particles. Massive Compact Halo Objects (MACHOs) would be cosmological objects, for instance black holes [34], that are another hypothesis for cold DM.

A common Dark Matter forum by ATLAS and CMS [35, 36] investigates various models of weakly interacting massive particles (WIMPs) as candidates for DM and makes recommendations for their collider searches. The first discussed model is such a recommendation.

### Simplified Model via S-Channel Exchange of a Mediator

Simplified models are a class of models that makes few assumptions on physics beyond the SM and that can typically be described by a small number of parameters. More complex models can be transferred into a simplified model by integrating out degrees of freedom.

[1] 25 including massive neutrinos: +3 from the neutrino masses and +3 from new mixing angles.

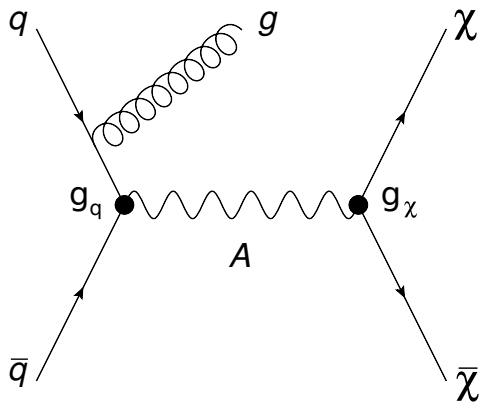


Figure 2.3.: Shown is a Feynman diagram for the production of DM particles $\chi$ in association with a gluon from initial state radiation according to a simplified model via the s-channel exchange of a mediator $A$.

For the model considered here a simple extension to the SM is performed [35]. An additional U(1) gauge symmetry is postulated under which DM and quarks carry charge. A new mediator particle can then be exchanged between them. In this simplified model the DM particle $\chi$ is a Dirac fermion with mass $m_\chi$ and the mediator has spin 1 and mass $M_A$. Figure 2.3 shows an example Feynman diagram for the production of DM via an s-channel exchange of the mediator $A$. Different kinds of coupling can be postulated, e.g. vector or axial-vector, but it is shown that the results in terms of cross-sections and $p_{\mathrm{T}}^{\mathrm{miss}}$ distributions do not show a strong dependence on them [35]. As a consequence, only the axial-vector case is exemplified here, which has also become a benchmark model for ATLAS searches for DM, cf. Section 2.4. For this model the Lagrangian takes the form

$$\mathcal{L}_{\text{axial-vector}} = g_q \sum_{q=u,d,s,c,t,b} A_\mu \bar{q}\gamma^\mu\gamma^5 q + g_\chi A_\mu \bar{\chi}\gamma^\mu\gamma^5\chi \,,$$

where $g_q$ and $g_\chi$ are the couplings of the mediator to quarks and to the DM particles, respectively. Assuming other no other decays contribute, the minimum width of the mediator follows with $\Theta(x)$ as the Heaviside step function as

$$\begin{aligned}\Gamma^A_{\text{min}} = &\frac{g_\chi^2 M_A}{12\pi}\left(1-\frac{4m_\chi^2}{M_A^2}\right)^{\frac{3}{2}}\Theta(M_A-2m_\chi)\\ &+\sum_{q=u,d,s,c,t,b}\frac{3g_q^2 M_A}{12\pi}\left(1-\frac{4m_q^2}{M_A^2}\right)^{\frac{3}{2}}\Theta(M_A-2m_q)\,.\end{aligned}$$

Dependencies on the parameters introduced above can be seen: $m_\chi$, $M_A$, $g_q$ and $g_\chi$. Setting limits on a simplified model for a given mediator with multiple independent parameters is difficult to visualise and would be tedious to implement due to the large number of signal samples that would need to be generated. In practice values for the couplings are fixed and limits are set in the mass plane of the mediator and DM particle $M_A$-$m_\chi$. For the spin-1 benchmark model that

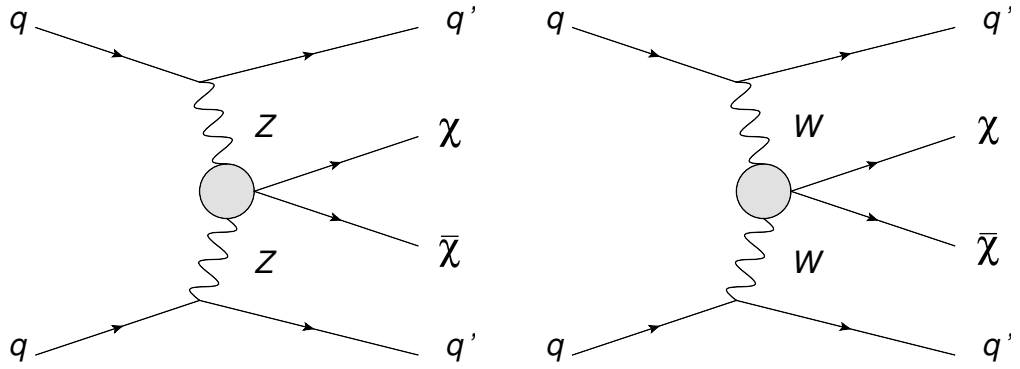


Figure 2.4.: Shown are two vector boson fusion diagrams for DM production through the operators D5 and D6 shown in Table 2.3. The right hand diagram additionally contributes to D7. More diagrams contribute overall depending on the operator [8].

is also considered later in this thesis, cf. sections 2.4 and 5, the couplings are chosen to be $g_q = 0.25$ and $g_\chi = 1$ following recommendations by the ATLAS CMS Dark Matter Forum.

### An Effective Field Theory of Weakly Interacting Dark Matter

In effective field theories (EFTs), boson exchange between particles is replaced by contact interactions. A prominent example of an EFT is Fermi's Theory [37]. It presents a first theoretical description of the beta-decay via a contact interaction of the particles involved without having knowledge of the existence of the W-boson. For the models in this thesis, EFTs assume contact interactions between DM and the SM. DM particles are assumed to be Dirac fermions and denoted $\chi$. Effective Lagrangians of dimension $> 4$ can then be constructed based on the idea that BSM physics has a higher energy scale than the SM showing minimal dependence on model assumptions. The general Lagrangian can be written as

$$\mathcal{L} = \mathcal{L}^{\mathrm{SM}} + \frac{f^{(5)}}{\Lambda} \sum \mathcal{O}^{(5)} + \frac{f^{(6)}}{\Lambda^2} \sum \mathcal{O}^{(6)} + \frac{f^{(7)}}{\Lambda^3} \sum \mathcal{O}^{(7)} + ...$$

Here, $\mathcal{L}^{\mathrm{SM}}$ is the Lagrangian of the SM with dimension four. The additional terms are extensions with higher dimensionality. The $f^{(i)}$ are Wilson coefficients for the operators of dimension $i$, $\mathcal{O}^i$. Wilson coefficients are ignored in the following, because operators are considered separately and shifts in cross-section can also be obtained by varying $\Lambda$ and the masses of $\chi$. $\Lambda$ is the suppression scale of the set of operators. EFT operators for electroweak interactions between SM and DM particles of such a set of different operators including the suppression scales are shown in Table 2.3 [8]. The analysis presented in Chapter 5 sets limits on two of these operators. The effective Lagrangians describe contact interactions between weak gauge bosons of the SM and DM particles. Example Feynman diagrams for the operators are shown in figure 2.4. The only other parameter is the effective suppression scale $\Lambda$. For the assumption of contact interactions to be valid the mass of the particle mediating the interaction has to be large with respect to $\sqrt{s}$. This needs to be assured by choosing proper values for $\Lambda$. Choosing one (or several) operators and fixing $\Lambda$ and the mass of $\chi$ allows for the prediction of cross-sections and event kinematics.

| Name | Operator |
|---|---|
| Dimension 5 | |
| D5a | $\frac{1}{\Lambda}\left[\bar{\chi}\chi\right]\left[\frac{Z_\mu Z^\mu}{2}+W^+_\mu W^{-\mu}\right]$ |
| D5b | $\frac{1}{\Lambda}\left[\bar{\chi}\gamma^5\chi\right]\left[\frac{Z_\mu Z^\mu}{2}+W^+_\mu W^{-\mu}\right]$ |
| D5c | $\frac{g}{\Lambda}\left[\bar{\chi}\sigma^{\mu\nu}\chi\right]\left[\frac{\partial_\mu Z_\nu-\partial_\nu Z_\mu}{\cos\Theta_W}-ig(W^+_\mu W^-_\nu-W^+_\nu W^-_\mu)\right]$ |
| D5d | $\frac{g}{\Lambda}\left[\bar{\chi}\sigma_{\mu\nu}\chi\right]\epsilon^{\mu\nu\sigma\rho}\left[\frac{\partial_\sigma Z_\rho-\partial_\rho Z_\sigma}{\cos\Theta_W}-ig(W^+_\sigma W^-_\rho-W^+_\rho W^-_\sigma)\right]$ |
| Dimension 6 | |
| D6a | $\frac{g}{\Lambda^2}\partial^\nu\left[\bar{\chi}\gamma^\mu\chi\right]\left[\frac{\partial_\mu Z_\nu-\partial_\nu Z_\mu}{\cos\Theta_W}-ig(W^+_\mu W^-_\nu-W^+_\nu W^-_\mu)\right]$ |
| D6b | $\frac{g}{\Lambda^2}\partial_\nu\left[\bar{\chi}\gamma^\mu\chi\right]\epsilon^{\mu\nu\sigma\rho}\left[\frac{\partial_\sigma Z_\rho-\partial_\rho Z_\sigma}{\cos\Theta_W}-ig(W^+_\sigma W^-_\rho-W^+_\rho W^-_\sigma)\right]$ |
| Dimension 7 | |
| D7a | $\frac{1}{\Lambda^3}\left[\bar{\chi}\chi\right]W^{i,\mu\nu}W^i_{\mu\nu}$ |
| D7b | $\frac{1}{\Lambda^3}\left[\bar{\chi}\gamma^5\chi\right]W^{i,\mu\nu}W^i_{\mu\nu}$ |
| D7c | $\frac{1}{\Lambda^3}\left[\bar{\chi}\chi\right]\epsilon^{\mu\nu\sigma\rho}W^i_{\mu\nu}W^i_{\mu\nu}$ |
| D7d | $\frac{1}{\Lambda^3}\left[\bar{\chi}\gamma^5\chi\right]\epsilon^{\mu\nu\sigma\rho}W^i_{\mu\nu}W^i_{\mu\nu}$ |

Table 2.3.: EFT Lagrangrians of various dimensions for Dark Matter produced via interactions with electroweak gauge bosons [8]. $g$ is the electroweak coupling constant.

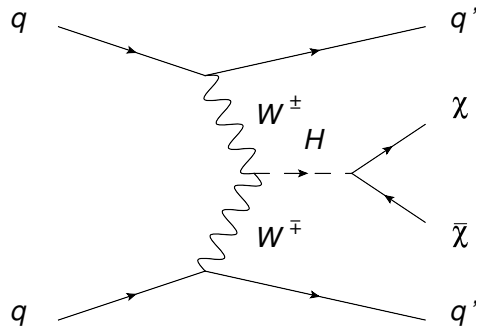


Figure 2.5.: Leading order Feynman diagram for the VBF production of a Higgs boson decaying into DM particles.

### Invisible Decays of the Higgs Boson

The SM predicts a small branching fraction of the Higgs boson into invisible particles via the process $H \to ZZ \to \nu\nu\nu\nu$. This branching fraction is 0.1% [38, 39], which too small for detection by contemporary LHC measurements [40]. However, various DM models predict this branching fraction to be larger due to the Higgs coupling either directly to massive DM particles or to a new mediating particle. Figure 2.5 shows a Feynman diagram for the first case with the production of a Higgs boson via vector boson fusion.

Taking DM as a scalar singlet as an example, a simple extension to the SM can be written out by including a bare mass term for the scalar and a coupling to the SM Higgs doublet [41],

$$\mathcal{L}_{\text{Higgs-DM}} = -\frac{1}{2}\mu_\chi^2\chi^2 - \frac{1}{2}\lambda_{h\chi}\chi^2 H^\dagger H.$$

In this model the mass of the DM particle $\chi$ after electroweak symmetry breaking is given by

$$m_\chi = \sqrt{\mu_\chi^2 + \frac{1}{2}\lambda_{h\chi}v_0^2},$$

with $v_0$ being the SM Higgs vacuum expectation value. If the decay of the Higgs boson into a pair of DM particles is kinematically allowed, i.e. for $2\,\mathrm{m}_\chi < \mathrm{m}_h$, the contribution to the invisible decay width of the Higgs from this process is given by

$$\Gamma_{\text{inv}} = \frac{\lambda_{h\chi}^2 v_0^2}{32\pi m_h}\left(1\text{–}4m_\chi^2/m_h^2\right)^{1/2}.$$

There exist also more complex extensions to the SM in the context of invisible Higgs decays such as Higgs portal models [42, 43]. There the Higgs and a new real scalar particle mix leading to an increased branching ratio of the Higgs into invisible particles by introducing DM as a fermionic singlet.

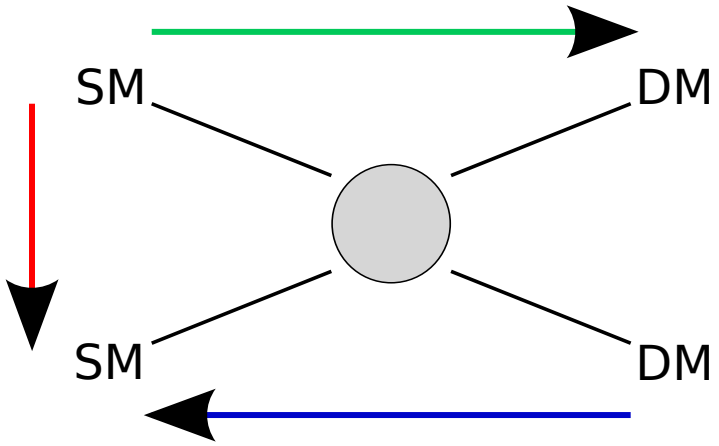


Figure 2.6.: The three detection modes for DM: direct detection (red), indirect detection (blue), and production and detection at a collider (green).

## 2.4. Detection Efforts

Assuming an interaction between SM and DM particles, there are three detection strategies, which are depicted in figure 2.6. DM particles can annihilate into SM particles (indirect detection, blue), DM can interact with SM particles via a momentum transfer (direct detection, red), or standard model particles can annihilate into DM particles (collider searches, green).

Indirect detection experiments search for an excess of SM particles in accordance with DM annihilation [44]. There are various experiments investigating different signatures. The AMS experiment for instance is located at the international space station and measures the cosmic ray spectrum [45]. The neutrino telescopes ANTARES [46] and Ice-Cube [47] are examples of earthbound experiments used for the indirect detection of DM.

Direct detection experiments search for atomic recoil caused by a stream of DM particles. Large tanks kept at low temperatures filled with active materials such as Argon or Xenon are often used. DM can either interact with the nuclei or the electrons of the active material. The experiments are usually sensitive to ionisation, scintillation, heat, or a combination of these signatures caused by collisions of DM particles and the active medium [48]. XENON, LUX, and PandaX are three examples of direct detection collaborations that ran experiments in recent years [49–51]. Figure 2.7 shows limits obtained by direct and indirect detection experiments. Limits are set on the spin-independent WIMP-nucleon cross-section in dependence of the WIMP mass and are from 2016. In 2017 the XENON collaboration published results [49] with a new detector, the XENON1T experiment, improving their limits and extending them slightly beyond the limits set by LUX shown in Figure 2.7.

In collider searches, produced DM particles escape the experiment without interacting with the detector. Hence they are designed around one of two approaches that do not require this interaction. One approach is to require other particles being produced in association with DM to allow for a recoil. In this case the signature is missing transverse momentum, $p_{\mathrm{T}}^{\mathrm{miss}}$[1]. The additional particles in the final state are for instance photons or jets from initial state radiation or vector bosons from associated production. In the other approach the final state

[1] In this section $E_{\mathrm{T}}^{\mathrm{miss}}$ will be used as the symbol instead, because it is the convention in Figure 2.8. Within ATLAS, $p_{\mathrm{T}}^{\mathrm{miss}}$ and $E_{\mathrm{T}}^{\mathrm{miss}}$ both describe missing transverse momentum and the symbols are usually interchangeable.

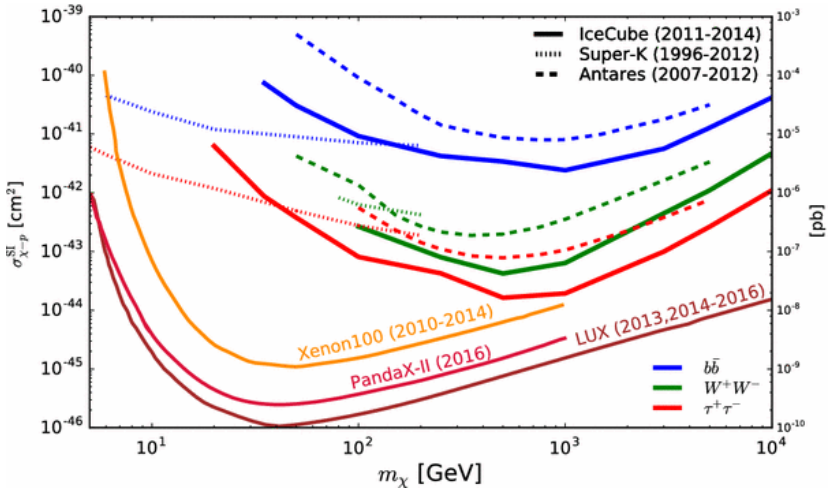


Figure 2.7.: Shown are limits on the spin-independent WIMP-nucleon cross-section in dependence of the WIMP mass by direct detection experiments (Xenon100, PandaX-II, and LUX) and indirect detection experiments (IceCube, Super-K, and Antares). For the latter limits are shown for different modes. Image taken from [52].

does not contain DM particles. In these dijet searches the final state consists of jets. They are used to search for new resonances in the dijet mass spectrum to infer mediating particles. Figure 2.8 shows exclusion limits obtained by various ATLAS searches in the plane of DM mass and mediator mass for Dirac fermion DM and an axial-vector mediator via s-channel exchange in a simplified model, cf. Section 2.3. Also shown are constraints from perturbative unitarity, production kinematics, and the relic density. The coupling strengths of the mediator to quarks, leptons, and DM particles are fixed. $E_{\mathrm{T}}^{\mathrm{miss}}$ + jet, $E_{\mathrm{T}}^{\mathrm{miss}}$ + Z, and $E_{\mathrm{T}}^{\mathrm{miss}}$ + $\gamma$ follow the first approach of analysis strategy. Here, the SM particles produced together with DM are jets, Z bosons, and photons, respectively. The $E_{\mathrm{T}}^{\mathrm{miss}}$ + jet search is introduced on more detail in Section 4.1. Limits from several variations of dijet searches are also shown that follow the second approach. Dijet + ISR [53] additionally requires a jet or a photon from initial state radiation in the final state. Dijet TLA [54] is the ATLAS trigger level analysis which avoids restrictions coming from bandwidth limitations of the trigger by using partially reconstructed events for the analysis. As the figure shows, limits from dijet searches only minimally depend on the DM mass, because DM particles do not need to be produced for the investigated final states. The limits from $E_{\mathrm{T}}^{\mathrm{miss}}$ + jet, $E_{\mathrm{T}}^{\mathrm{miss}}$ + Z, and $E_{\mathrm{T}}^{\mathrm{miss}}$ + $\gamma$ explicitly depend on the masses of the DM particles and the mediator. For each analysis the shape and extend of the limits varies with the models and couplings considered [55].

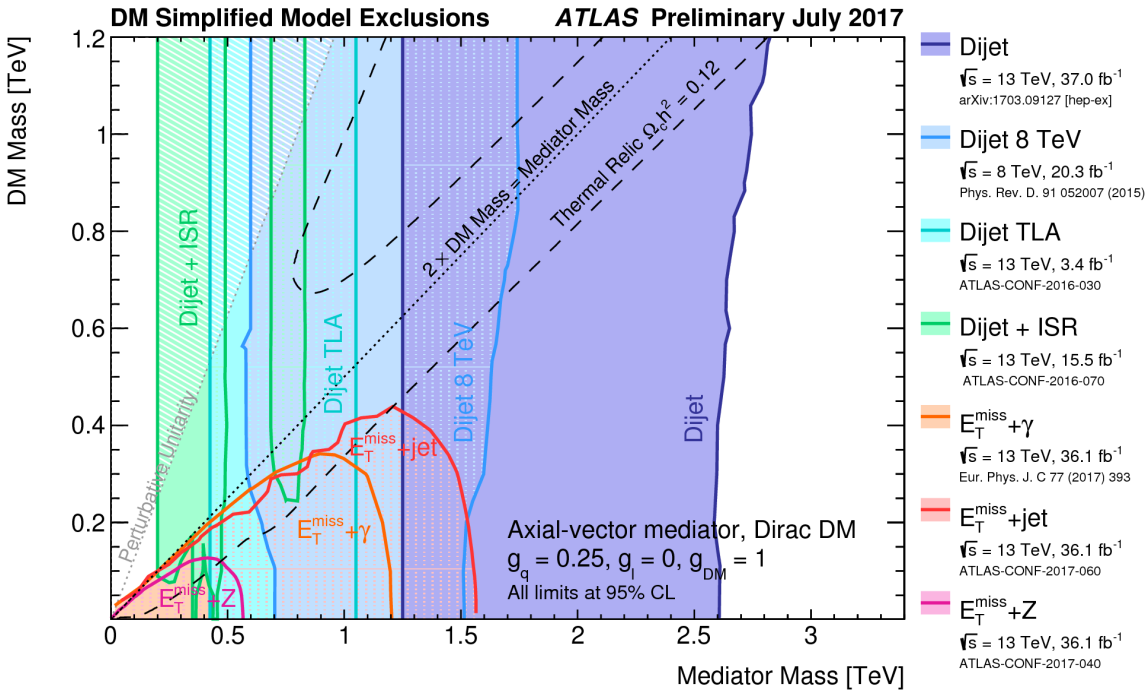


Figure 2.8.: The ATLAS summary plot for exclusion limits on a simplified model with an s-channel axial-vector mediator and Dirac fermion DM. Limits from various ATLAS analysis are shown [55].

# 3. Experimental Setup and Techniques

The analysis and studies described in this thesis were performed using data collected by the ATLAS experiment at the LHC at CERN near Geneva, Switzerland. In this chapter, these two machines are briefly described. More information on them can be found in [56] and [57][1]. Additionally, key experimental techniques are discussed, such as object reconstruction with ATLAS, physics at hadron colliders, and Monte Carlo Simulations. A focus it put on hadronic jets, since they are the central detectable objects in $p_{\mathrm{T}}^{\mathrm{miss}}$ + jets searches.

## 3.1. The Large Hadron Collider

The Large Hadron Collider (LHC) is currently the largest and most energetic man-made particle accelerator. It is a two-ring superconducting circular accelerator located at the tunnels of the former CERN experiment LEP, the Large Electron-Positron Collider. The circumference of the ring is 26.7 km and the tunnels are up to 175 m below the surface. The project LHC was approved in December 1994 while LEP was still in operation and the tunnels were upgraded according to the new design starting in 2000. The accelerator itself consists of eight straight and eight curved segments, the design collision energy and luminosity are $\sqrt(s) = 14\,\mathrm{TeV}$ and $10^{34}\,\mathrm{cm}^{-2}s^{-1}$, respectively. In addition to protons, heavy ions can be injected as well. The proton source is a bottle of hydrogen gas. An accelerator chain, including several former CERN main accelerators, is used to accelerate the ionised hydrogen atoms to 450 GeV before the beams are injected into the LHC: LINAC 2, the Proton Synchrotron Booster (PSB), the Proton Synchrotron (PS) and the Super Proton Synchrotron (SPS) form this chain.

The LHC hosts four large experiments, ATLAS[2], CMS[3] [58], LHCb[4] [59] and ALICE[5] [60]. ATLAS and CMS are multi-purpose detectors with a diverse physics program that includes standard model measurements and searches for new physics. LHCb and ALICE are specialised towards specific physics programs. LHCb focuses on precision measurements of hadron decays into c- and b-quarks and investigates CP violation. The ALICE experiment on the other hand focusses on collisions of heavy ions to better understand the early phase of the Universe and the formation of quark gluon plasma. A schematic with the different experiments located around the ring of the LHC can be found in Figure 3.1.

For the lattice high-end technology is used: superconducting NbTi magnets are used and kept at a temperature of 2 K. The beam bending dipole magnets are the limiting factor in beam energy. The design beam energy is 7 TeV, which requires the dipole magnets operating at above 8 T and a current of approximately 11 kA. In total, 1232 dipole magnets for beam bending,

[1] If not indicated otherwise, these are the sources for the presentations in sections 3.1 and 3.3.
[2] Formerly 'A Torodial LHC ApparatuS', now used as a proper name
[3] Compact Muon Solenoid
[4] LHC beauty
[5] A Large Ion Collider Experiment

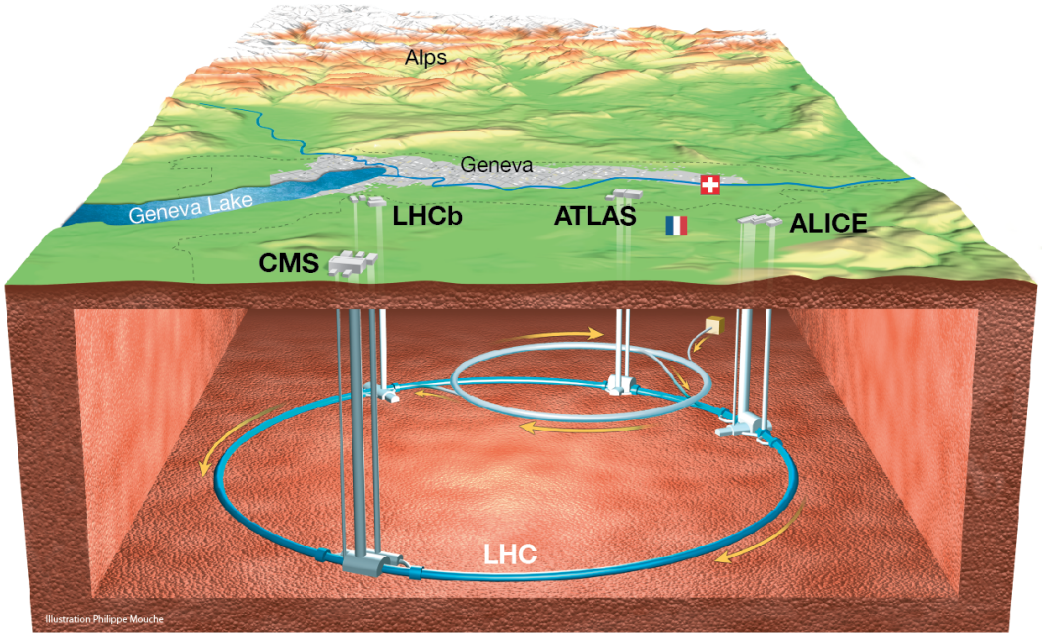


Figure 3.1.: A schematic view of the LHC ring with the four main experiments and the Geneva region [61].

382 quadrupole magnets for beam focussing and about 3700 additional dedicated magnets, e.g. kicker magnets for the beam dump, are installed.

A central quantity in LHC physics is the instantaneous luminosity $\mathcal{L}$. For the simplified case of two beams with Gaussian bunches of similar spread in a head-on collision it takes the form [19]

$$\mathcal{L} = \frac{N_1 N_2 f_{\mathrm{ref}} n_b}{4\pi\sigma_x\sigma_y} \,. \tag{3.1}$$

It is a measure of the *beam brightness*. The subscripts 1 and 2 refer to the two opposing beams, $n_\mathrm{b}$ is the number of bunches into which the beam is quantised, $N_\mathrm{i}$ is the number of protons per bunch, $f_\mathrm{ref}$ the revolution frequency, and $\sigma$ is the beam spread in the horizontal (x) and vertical (y) plane[1]. The instantaneous luminosity is proportional to the number of bunches in the machine, the number of protons each bunch carries on average, the revolution frequency of the beams in the LHC and antiproportional to the beam widths in x and y directions. Each beam is quantised into 3564 bunch slots, which can contain proton bunches. At full intensity 2808 bunch slots are occupied according to the initial design of the LHC. Other schemes are however possible and used as well [62]. The revolution frequency is dictated by the circumference of the LHC and the speed of light yielding 11.2 kHz. The average number of interactions per

[1] In the right-handed coordinate system of the LHC at a given interaction point, x points to the centre of the ring, y points upwards and z points along the counter clockwise circulating beam 2.

bunch crossing at the interaction point at the ATLAS detector was 13.7 for the dataset collected in 2015 and 24.9 in 2016.

The instantaneous luminosity is related to the integrated luminosity via

$$\mathcal{L}_{int} = \int \mathcal{L}\, dt. \tag{3.2}$$

Dataset sizes are usually quoted in terms of their integrated luminosity.

Physics operation of the LHC is structured into Runs which are separated by long shutdowns. Run-1 lasted from 2010 until 2012 and included periods with centre-of-mass energies of $\sqrt{s} = 7\,\text{TeV}$ and $\sqrt{s} = 8\,\text{TeV}$. For Run-2, which started in 2015 and will last until the end of 2018, the collision energy was increased to 13 TeV. The 2015 and 2016 datasets recorded by ATLAS encompass $3.9\,\text{fb}^{-1}$ and $35.6\,\text{fb}^{-1}$ respectively [63]. For the future it is foreseen to increase the energy to its design energy of $\sqrt{s} = 14\,\text{TeV}$ and to increase the luminosity even further in later upgrades.

## 3.2. Physics at Hadron Colliders

### 3.2.1. Parton Distribution Functions and Cross-Sections

Although proton-proton collisions at the LHC take place at $\sqrt{s} = 13\,\text{TeV}$ in Run-2, the partons, i.e. the constituents of the protons, collide at lower energies. This is because partons carry only a fraction of the total energy of the proton. This energy fraction is parametrised by *parton distribution functions* (PDFs). PDFs cannot be predicted by QCD because their energy regime is inaccessible via perturbation theory. They are usually extracted from measurements of structure functions in deep inelastic scattering experiments [19]. Although PDFs at a given energy scale are not predictable, their evolution, i.e. their change in shape going from one energy scale to another, is described theoretically by the DGLAP equations. They are named after Dokshitzer, Gribow, Lipatow, Altarelli, and Parisi, [64–67] and allow for extrapolations to the scale of the LHC.

PDFs are parametrised as $f_i(x, Q^2)$, which describes the probability for finding parton $i$, a gluon or quark of a particular flavour, with momentum fraction $x$ at the energy scale of the hard interaction $Q^2$ [68, 69]. A variety of PDF sets exist that are developed by different groups. As an example, Figure 3.2 shows the PDF set MSTW 2008 NLO PDFs for two different energy scales. The curves reflect the composition of protons containing two up quarks and a down quark. These valence quarks carry most of the protons momentum fraction. For the other quarks, referred to as sea quarks, the PDFs are identical for the respective quarks and anti-quarks because they must be produced via pair-production. The mass relations of the quarks can be read from the curves of the sea quarks with the heavier quarks having lower probabilities. The gluon PDF dominates at low momentum fractions and is scaled down by a factor of ten to fit the plot.

PDFs are an important ingredient for the calculation of cross-sections. The hadronic production cross-section of $X$ from proton-proton collisions can be written as

$$\sigma_{pp\to X} = \int dx_a f_a(x_a, Q^2) \int dx_b f_b(x_b, Q^2) \hat{\sigma}_{ab\to X}, \tag{3.3}$$

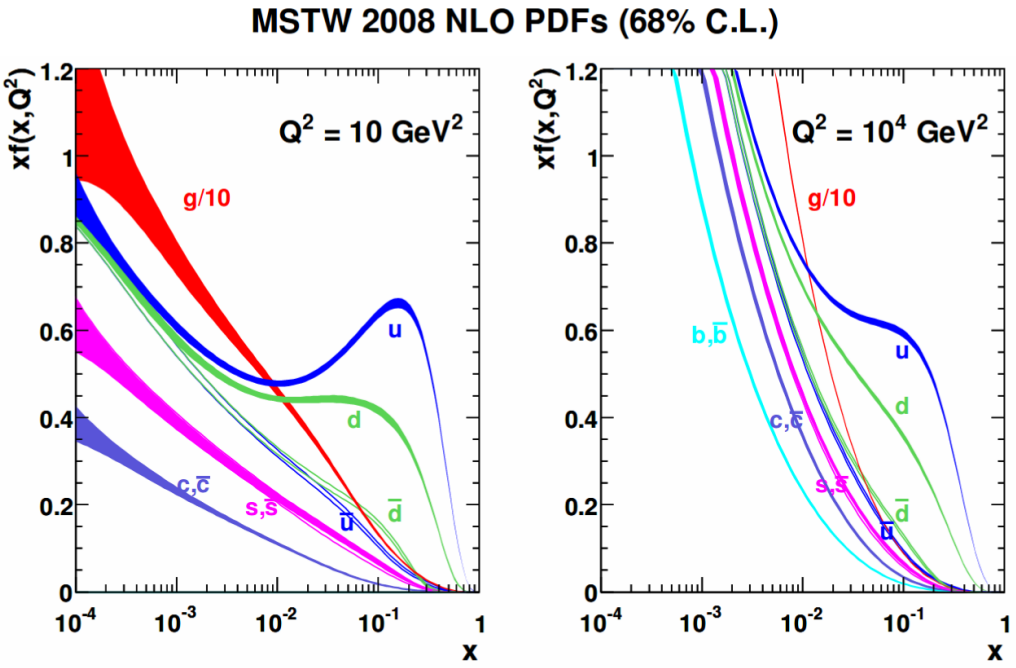


Figure 3.2.: The proton PDF set MSTW 2008 NLO is shown for two different energy scales. It can be seen that the valence quarks of the proton typically carry larger momentum fractions. The gluon PDF is shown at one tenth of its actual size. One sigma confidence level uncertainty bands are shown [69].

where $f_a$ and $f_b$ are the PDFs of the partons from the protons in the initial state and $\hat{\sigma}_{ab\to X}$ is the *partonic* cross section of the process. $\hat{\sigma}_{ab\to X}$ is often referred to as the hard scatter cross-section. Equations 3.2 and 3.3 are connected by the number of events $N$ with a specific final state $X$ that are produced in a dataset with a integrated luminosity $\mathcal{L}_{\text{int}}$ via

$$N = \sigma_{pp\to X} \cdot \mathcal{L}_{\text{int}}. \tag{3.4}$$

### 3.2.2. Pile-Up

*Pile-up* describes effects coming from overlapping events. The LHC operates at a high instantaneous luminosity, as defined in Equation 3.1, in order to provide the best discovery potential. Thus, the average number of colliding protons per bunch-crossing, $\mu$, is typically larger than one at the interaction point of ATLAS. For the 2015 dataset collected by the ATLAS experiment the average number of interactions per bunch crossing is 13.7 and for 2016 dataset it is 24.9 as is shown in Figure 3.3. Furthermore, a narrow *bunch spacing* is chosen. This refers to the temporal separation of bunches at the LHC, of nominally 50 ns during Run-1 and 25 ns for most of Run-2[1].

If the event overlap originates in events from the same bunch-crossing because of high $\mu$, it is referred to as *in-time* pile-up. If the event overlap comes from consecutive bunch-crossing such

[1]There was a brief period of 50 ns bunch spacing in the beginning of 2015 during the recommissioning after LS1.

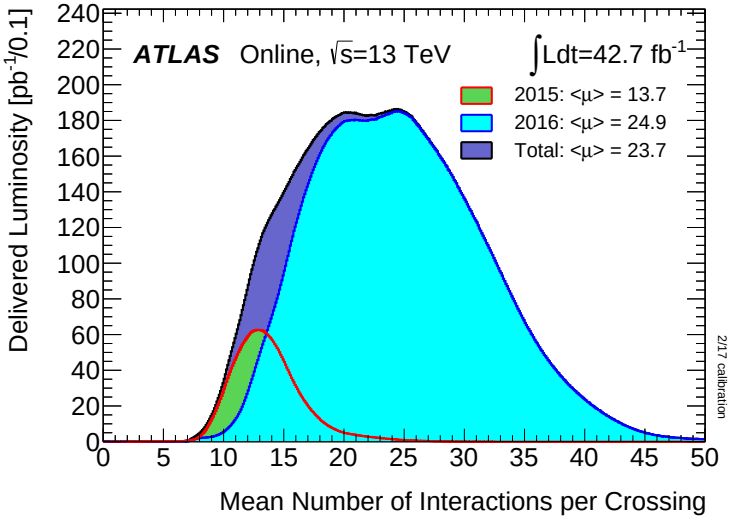


Figure 3.3.: The mean numbers of interactions per bunch crossing for the 2015 and 2016 datasets collected by the ATLAS experiment. All data delivered by the LHC to ATLAS with stable beams are shown [63].

that the signals stack over time, it is called *out-of-time* pile-up. Usually both are considered together and the combined pile-up poses experimental challenges. It affects trigger rates, cf. Section 3.3.4, by creating artificial transverse momentum imbalances for given events. This lead to the development of additional pile-up subtraction algorithms on hardware level that were realised during the first long shutdown of the LHC between Run-1 and Run-2 [70]. Additionally it can impact analyses by affecting object reconstruction and identification, cf. Section 3.4, for instance by assigning objects to the wrong interaction vertex or by distorting energy measurements in calorimeter cells [71]. Many of the design choices, reconstruction schemes, and calibrations introduced throughout this chapter were implemented to reduce the impact of pile-up.

## 3.3. The ATLAS Experiment

The ATLAS Experiment is a multi-purpose particle physics detector with a length of 44 m, a width of 25 m and a total mass of approximately 7000 t. It has cylindrical shape, covers almost $4\pi$ solid angle and is composed of three main subsystems in an onion-like design: closest to the interaction point (IP) is the inner detector containing the tracking system, which is fully surrounded by the calorimeter system. The outermost layer is the muon spectrometer. Figure 3.4 shows a schematic view of the ATLAS detector.

The tracking system allows for the reconstruction of trajectories of charged particles and plays a central role in particle identification. It enables the identification of primary and secondary vertices by extrapolating the flight paths and assists pile-up rejection. The calorimeter is divided into two parts: an inner electromagnetic (EM) calorimeter layer and an outer hadronic (HAD) calorimeter layer. It is central to the energy determination of most physics objects. Information on the shower shapes support particle identification. Muons are the only visible particles which are able to leave the ATLAS detector before decaying, because of their minimally ionising nature.

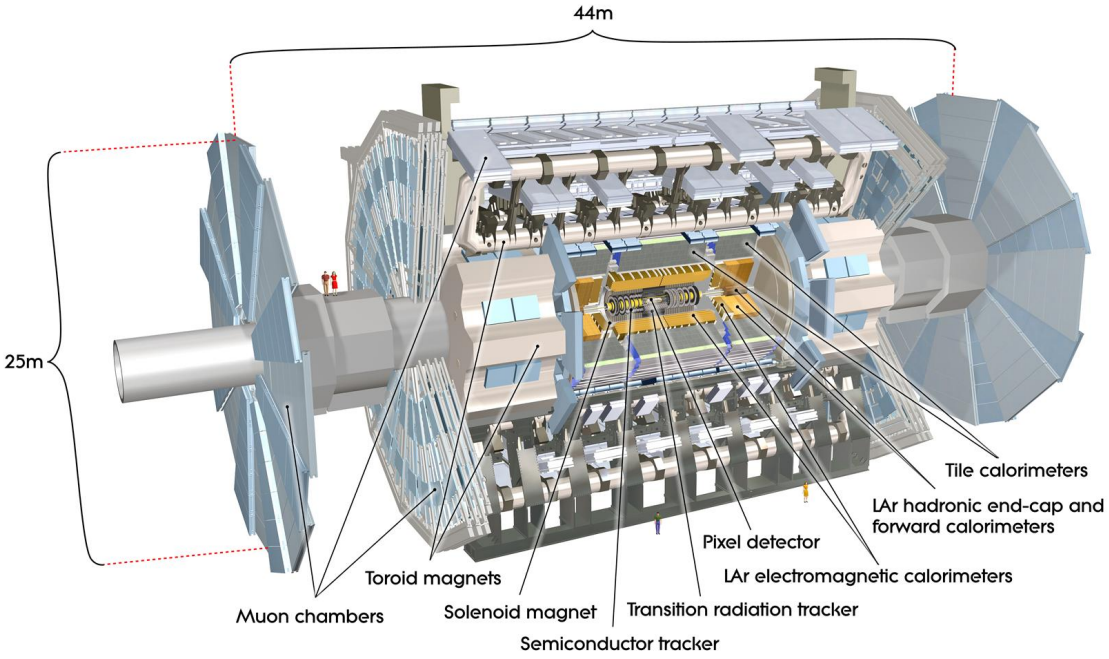


Figure 3.4.: A schematic illustration of the ATLAS detector [57].

Here, visible refers to particles interacting via the strong or electromagnetic force. The muon spectrometer (MS) reconstructs their flight paths and thus allows for their detection and the precise measurement of four-momenta. Whenever possible the tracks in the MS are combined with information from the tracking system to grant more precise trajectory reconstruction.

ATLAS hosts two large magnetic systems that bend the flight paths of charged particles. This enables the momentum determination of particle candidates from the bending radius. A solenoid magnet with a field strength of about 2 T is built around the inner detector and a system of three toroid magnets delivers a magnetic field of 0.5 – 1 T for the MS.

Three smaller systems form the ATLAS forward detectors: LUCID (LUminosity measurement using Cerenkov Integrating Detector), the ZDC (Zero-Degree Calorimeter), and ALFA (Absolute Luminosity for ATLAS). LUCID and ALFA provide luminosity measurements and the main purpose of the ZDC is the detection of forward neutrons in heavy-ion collisions.

An orthogonal, right-handed coordinate system with its origin at the interaction point is used, where x points to the centre of the ring, y points upwards and z points along beam 2 which circulates counter clockwise. Following the spatial symmetry of particle collisions, two angles are usually used to describe coordinates: the (pseudo-)rapidity y ($\eta$) and the azimuthal angle $\phi$. $\phi$ has its point of origin at the x-axis and lays in the transverse plane. The forward angle is $\eta$ = - ln tan($\theta$/2), where the polar angle $\theta$ is defined with respect to the positive x-axis. The pseudorapidity is the high energy limit[1] of the rapidity y = 1/2 ln [(E + $p_z$)/(E - $p_z$)] of a particle with momentum p and energy E. Using rapidity for the polar angle is useful, because differences in that angle $\Delta$y are invariant under Lorentz boosts.

[1]Equivalent to the limit of negligible mass.

In LHC physics the z boost of the colliding partons is unknown, cf. Section 3.2. As a consequence absolute values of energy and momentum are typically given as transverse values $E_T$ and $p_T$, e.g. $E_T = \sin(\theta) \cdot E$. This corresponds to a projections of the original value into the x-y plane. In this coordinate system the distance between two points are given by

$$\Delta R = \sqrt{\Delta\eta^2 + \Delta\phi^2}. \tag{3.5}$$

### 3.3.1. Inner Detector

The purpose of the inner detector [72] is to allow for the reconstruction of charged particle tracks and for the precise localisation of the primary and secondary vertices. It makes use of the energy loss by ionisation that relativistic particles experience when passing through a medium. The energy loss per unit length is described by the Bethe-Bloch equation,

$$\frac{dE}{dx} \approx -4\pi\hbar c^2\alpha^2 \frac{nZ}{m_e v^2} \cdot \left( ln\left[ \frac{2\beta^2\gamma^2 c^2 m_e^2}{I_e} \right] - \beta^2 \right). \tag{3.6}$$

Here, the particle's velocity is $v = \beta c$, Z and n are the atomic number and number density of the medium, $m_e$ is the electron mass, $\alpha$ the electromagnetic fine structure constant,$\gamma$ the Lorentz factor and $I_e$ the effective ionisation material averaged over all atomic electrons [19]. The products of ionisation, i.e. electrons for a gaseous medium and electron-hole pairs for semiconductor-based detectors, are then measured. Additional use is made of transition radiation.

The ATLAS inner detector has been designed to achieve a momentum resolution of

$$\frac{\sigma_{pT}}{p_T} = 0.05\% \cdot p_T \oplus 1\% \tag{3.7}$$

for charged particles within its volume defined by $|\eta| < 2.5$. It can reliably measure tracks with $p_T > 400\,\text{MeV}$. Three complementary sub-systems form the ID in an onion-like arrangement. These three are the pixel detector (PD) at a radial distance of about 3-15 cm from the beam, the semi-conductor tracker (SCT) at approximately 30-56 cm, and the transition radiation tracker (TRT) at around 56-107 cm. Figure 3.5 shows the ID with its sub-detectors. In total the ID is 6.2 m long and has a maximum radius of 2.1 m. This translates to a coverage of $|\eta| < 2.5$ for the PD and SCT and $|\eta| < 2.0$ for the TRT.

The PD is made of three concentric barrel layers and two end-cap modules of three disks each and has a high granularity. It consists of more than 80 million individual pixel sensors most of which have a size of $50 \cdot 400\,\mu$m distributed over 1744 sensor modules. By design a charged particle will leave on average three hits in the PD. The spatial resolution in each layer is $10\,\mu$m in the transverse plane and $115\,\mu$m along z (R) and in the barrel (end-cap). The PD has been upgraded during LS1 with the insertable b-layer (IBL). It is an additional layer closest to the new beam pipe in order to enhance performance with a resolution of $10\,\mu$m in R - $\phi$ and $66.5\,\mu$m in z [73]. Its inclusion improves flavour tagging and vertex identification.

Moving outwards, the SCT is the next sub-system. It consists of four barrel layers and eighteen end-cap discs. In total it contains 15912 individual silicon microstrip sensors. It is designed such that charged particles traverse four modules leading to an average of eight hits in the SCT.

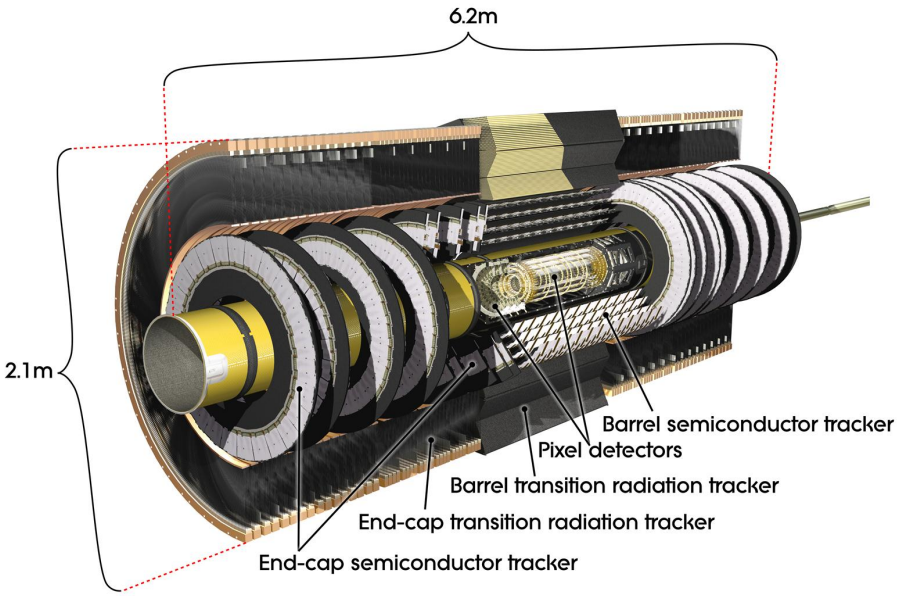


Figure 3.5.: The ATLAS inner detector with its sub-detectors in its initial design [57].

The spatial resolution per module is in the barrel 17 $\mu$m in the transverse plane and 580 $\mu$m along z. In the end-cap discs it is 580 $\mu$m along R.

The outermost layer is the TRT, which is a combined tracking and transition radiation detector and has approximately 351000 readout channels. It is the largest sub-detector of the ID and consists of polyamide straw tubes filled with a Xe-based gas mixture. According to its design a charged particle causes on average 36 hits in the TRT. The resolution is 130 $\mu$m in the transverse plane. $z$ is not measured, because the straws are aligned parallel to the beam. The measurement of transition radiation (TR) allows for the identification of electrons and the discrimination against other charged particles.

### 3.3.2. Calorimeters

Calorimeters are built to contain the showers of charged and neutral particles and to measure their energies. For photons and electrons, electromagnetic interactions with matter are described by the radiation length $X_0$, which obeys

$$X_0 \propto \frac{1}{nZ^2 \cdot \log(287/Z^{1/2})}. \tag{3.8}$$

$X_0$ yields the average distance an electron travels in a medium before its energy is reduced by a factor of $1/e$ via bremsstrahlung [19]. Charged hadrons mostly interact with the calorimeter via ionisation and strong interactions with the nuclei. Neutral hadrons deposit their energies purely via nuclear interactions. Because of this hadronic showers typically have a larger depth and a more complex structure [74].

The ATLAS calorimeters cover a total of $|\eta| < 4.9$ using different techniques that suit varying demands. Calorimeter cells are finer segmented in the central region, where the ID can be used

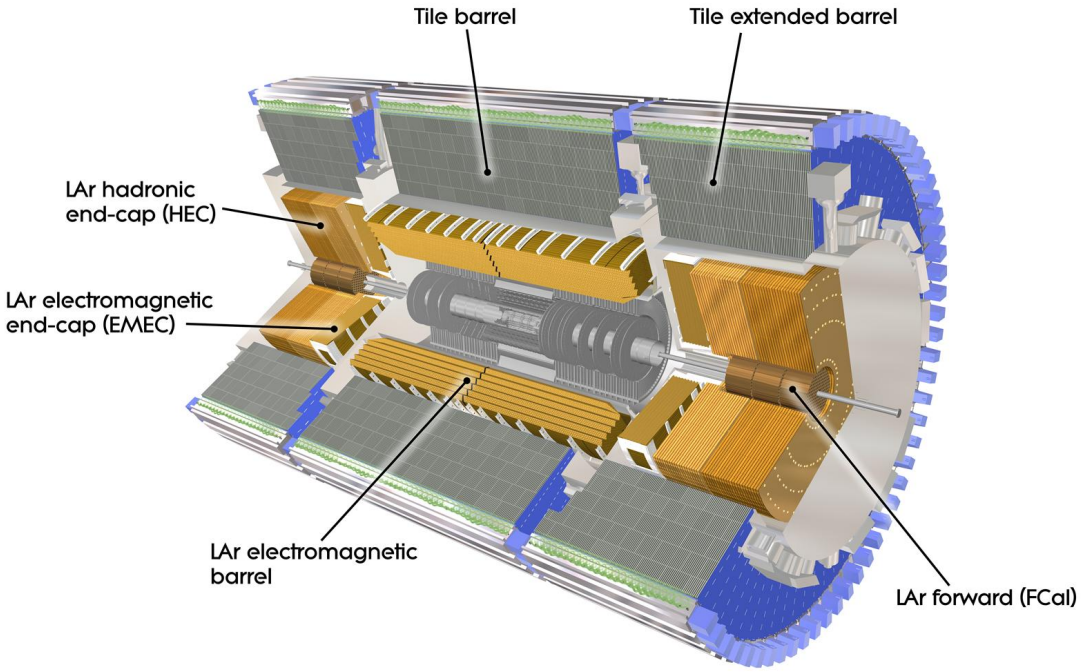


Figure 3.6.: Schematic illustration of the ATLAS calorimeters [57].

complementary, to provide precision measurements of electrons and photons. In the forward regions the segmentation is coarser, but still suited for accurate measurements of jets. They are built to contain electromagnetic and hadronic showers and to minimise punch-through into the muon spectrometer [57]. The calorimeter system is divided into electromagnetic (EM) and hadronic (HAD) parts: electrons and photons are likely to deposit all of their energy in the EM calorimeter, whereas hadronic showers often continue into the HAD calorimeter. Design choices were made accordingly and are discussed below. A schematic illustration of the calorimeter system can be seen in Figure 3.6.

### Electromagnetic Calorimeter

The EM calorimeter makes use of modern liquid argon (LAr) technology and consists of a barrel part, $|\eta < 1.475|$, parallel to beam axis, and the end-caps (EMEC), $1.375 < |\eta| < 3.2$, perpendicular to beams. The barrel itself is made of two identical parts, which are fit together at $|\eta| = 0$. Each end-cap is also made of two parts: an outer wheel ($1.375 < |\eta| < 2.5$) and an inner wheel ($2.5 < |\eta| < 3.2$), with the latter being closer to the beams than the former. In addition, one of the forward calorimeters, discussed below in the hadronic section, is actually optimised for EM showers and thus extends the total EM coverage to $|\eta| < 4.9$.

The LAr calorimeter is made of lead absorbers and copper-etched electrodes arranged in an accordion-shaped design. The gaps between the two are filled with liquid argon and a 2 kV potential between absorbers and electrodes is applied nominally. The accordion geometry provides fast signal extraction while naturally lending itself for full $\phi$ coverage. Within the central region of $|\eta| < 2.5$, there are 3 layers in depth. The first layer has a very fine granularity

providing high resolution enabling measurements of electron-photon conversion. Most of an EM objects energy however is deposited in the 2nd layer, and the 3rd layer typically collects the tails of an EM shower. As a consequence the granularity decreases outwards. The region beyond $|\eta| = 2.5$ has two EM layers, each of coarser granularity than the barrel. In the central-most part, the EM calorimeter is compensated by using presamplers that correct for energy losses of electrons and photons that occurred before they entered the calorimeter.

The thickness of the EM calorimeter is 22 $X_0$ in the barrel and 24 $X_0$ in the end-caps. Its design energy resolution is

$$\frac{\sigma_E}{E} = \frac{10\%}{\sqrt{E}} \cdot p_T \oplus 0.7\%. \tag{3.9}$$

#### Hadronic Calorimeter

The HAD calorimeter is split into three parts according to regions in $\eta$: from central to forward these are scintillating tile-based (TileCal), the Lar hadronic end-caps (HEC) and the Lar forward calorimeter (Fcal).

TileCal envelopes the EM barrel and end-caps and consists of three parts: one central ($|\eta| < 1.0$) and two extended barrels ($0.8 < |\eta| < 1.7$). Its active materials are scintillating tiles. Steel is used as the absorber. The inner (outer) radius is 2.28 m (4.25 m), segmented into three layers such that it provides coarse depth information. The read-out is performed via wavelength shifting fibres and photomultiplier tubes.

The HEC extends to $|\eta| < 3.2$ and has small overlaps in range with TileCal and the Fcal. Similar to the EMEC, the hadronic end-caps are perpendicular to the beam axis and capture showers that occurred more forward. Following the design from the EM calorimeter, LAr is the active material and the electrodes are made of copper. The HEC extents radially to 2.03 m.

Lastly, the FCal covers the forward region up to $|\eta| < 4.9$ and is placed in a distance of around 4.7 m from the IP. It is made of three segments. The first, closest to the IP, uses copper as the absorber in order to improve heat removal and is optimised for EM showers. Moving further outwards, the other two segments use mainly tungsten for absorption and are optimised for hadronic showers thus minimising lateral spread and providing containment [75].

The thickness of the HAD calorimeter is approximately 7.4 nuclear interaction lengths at $\eta = 0$ [76] and its design energy resolution for (1) barrel and end-cap and (2) the forward region are:

$$(1)\frac{\sigma_E}{E} = \frac{50\%}{\sqrt{E}} \cdot p_T \oplus 3\%, \qquad (2)\frac{\sigma_E}{E} = \frac{100\%}{\sqrt{E}} \cdot p_T \oplus 10\%. \tag{3.10}$$

### 3.3.3. Muon Spectrometer

Muon detection makes use of similar techniques as described in Section 3.3.1. However, muons barely emit transition radiation, because of their high mass.

The muon spectrometer (MS) is a sub-detector that allows for the reconstruction of tracks left by muons. It is also used for triggering and provides specialised chambers for that purpose. Muons

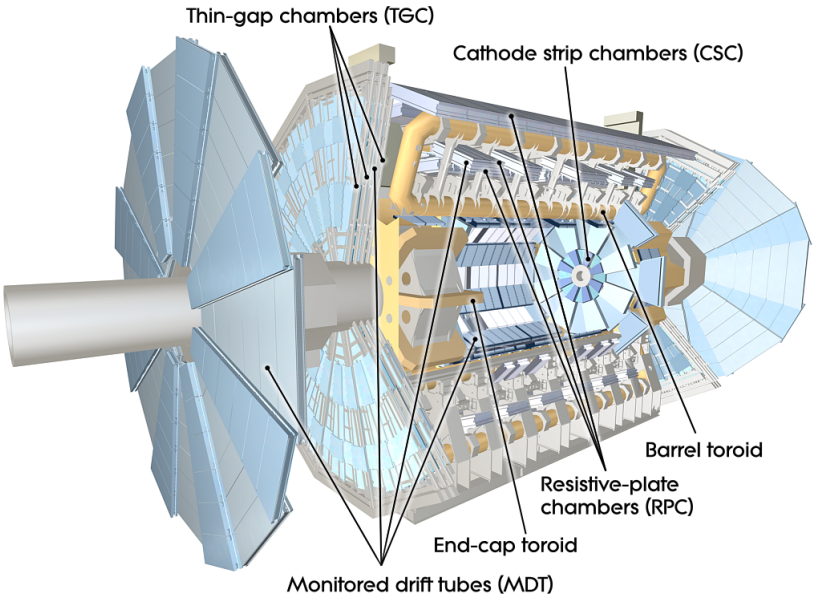


Figure 3.7.: Cut-away view of the muon spectrometer [57]. Also shown is the toroid magnet system.

tracks can be measured up to $|\eta| < 2.7$ and used for the trigger within $|\eta| < 2.4$. The barrel and end-cap toroid magnets bend the trajectories of muons, which allows for $p_T$ measurements in addition to spatial measurements. The MS was designed with a performance goal of its $p_T$ resolution of

$$\frac{\sigma_{p_T}}{p_T} = 10\% \tag{3.11}$$

for a 1 TeV muon. The MS is made of different layers. In the central (barrel) region, there are three stages in an onion-like arrangement parallel to the beam axis. They are placed at distances of approximately 5 m, 7.5 m, and 10 m from the beam pipe. The MS is composed of four different kinds of detection chambers: monitored drift tubes, cathode strip chambers, resistive plate chambers and thin gap chambers. The former two's purpose is precision tracking, whereas the latter two are used for triggering and providing complementary coordinate measurements of muon tracks. A schematic view of the MS can be found in Figure 3.7.

Monitored drift tubes (MDTs) cover a range of $|\eta| < 2.7$ with a total of 1150 chambers and approximately 350000 signal-transmitting channels. An individual drift tube has a diameter of roughly 3 cm and is filled with a 93/7-mixture of $Ar/CO_2$ gas kept at 3 bar pressure. While passing trough the tubes, muons produce ionisation electrons. They are collected with a tungsten-rhenium wire at centre, which serves as an anode. The operation voltage of the MDTs is 3080V. The arrangement of the tubes allows for 20 individual measurements per track in both barrel and end-cap and allows for a resolution in z-direction of 35 $\mu$m. A main advantage of using a large number of individual tubes is resilience: if one tube fails the operation of the whole system is barely impacted.

The cathode strip chambers provide precision tracking in the forward region, where the highest muon flux occurs. They cover $2.0 < |\eta| < 2.7$ with 32 chambers in 31000 channels and can provide

a higher safe counting rate (approximately 1000 Hz/cm$_2$) than the MDTs (150 Hz/cm$_2$). The ionised gas mixture is $Ar/CO_2$ (80/20) and the operation voltage is 1900 V. The segmentation of the gaseous cathode strips allows for measurements of two separate spatial coordinates at a time. By design four measurements per track are provided by each passing muons with a resolution of 40 $\mu$m in R, and 5 mm in $\phi$.

In addition to providing information for bunch crossing identification, the two types of trigger chambers measure additional coordinates for tracks to complement the MDTs. In the barrel region, resistive plate chambers (RPCs) cover a range of $|\eta| < 1.05$ using 606 chambers and approximately 375000 channels. Each module consists of two resistive plates of a phenolic-melaminic plastic laminate, which are parallel and spaced at 2 mm distance. The volume in-between is filled with gas: $C_2H_2F_4$/Iso-$C_4H_10/SF_6$ (94.7/5/0.3). This mixture allows for a relatively low operating voltage of 9.8 kV and operation in avalanche mode. By design the RPCs register six hits in the barrel as each of the three layered segments performs two independent measurements of z and $\phi$. For both spatial coordinates the resolution is 10 mm.

Lastly, the thin gap chambers (TGCs) are used for triggering and additional coordinate measurements in the forward region: $1.05 < \eta < 2.4$[1]. There are 3588 TGC chambers providing approximately 320000 channels. The chambers consist of Au-coated anode wires, graphite cathodes and are filled with a gas mixture of $CO_2$ n-$C_5H_12$ (55/45). They are operated at approximately 2900 V. According to its design a muon can leave up to nine hits in these end-cap layers. The resolution is 2-6 mm in R, and 3-7 mm in $\phi$.

### 3.3.4. Trigger

The trigger is a central component of ATLAS, because of the high bunch-crossing rate of 40 MHz of the LHC and limited read-out capabilities of the detector. It acts as a filter and lets only potentially interesting events be read out, thus omitting the vast majority of collisions.

ATLAS was upgraded for Run 2 leaving almost no system untouched, because of increases in both the centre-of-mass energy and the average instantaneous luminosity. The upgrade included improvements of the trigger system and took place during the long shutdown between Run 1 and Run 2 (LS1, 2013-2015). The initial Run-1 trigger setup is described in [57] and more details on the changes to the system for Run-2 and its performance in 2015 can be found in [70].

If the trigger accepts an event, the Data Acquisition System (DAQ) retrieves the data for that event from the detector and stores it for later analysis. For the 2015 and 2016 (Run-2) datasets that were investigated for this thesis, the ATLAS trigger was a implemented as a 2-stage system into the in the Trigger and Data Acquisition (TDAQ) system. Figure 3.8 gives an overview on the TDAQ system. L1Topo and the FTK were still in commissioning during 2015 and 2016, and will hence not be further described here. More information on this new topological processor and the fast tracker can be found in [77] and [78], respectively.

The first stage of the trigger is Level-1 (L1) and is a hardware-implemented event filter that consists of three main parts: the Level-1 calorimeter trigger (L1Calo), the Level-1 muon trigger (L1Muon) and the central trigger. The processor of the central trigger (CTP) takes the inputs from the former ones to make decisions on whether to decline or accept an event via the Level-1 accept signal. L1 reduces the data rate to approximately 100 kHz. Events that are accepted are

[1] For triggering. 2.7 for the additional coordinate measurement.

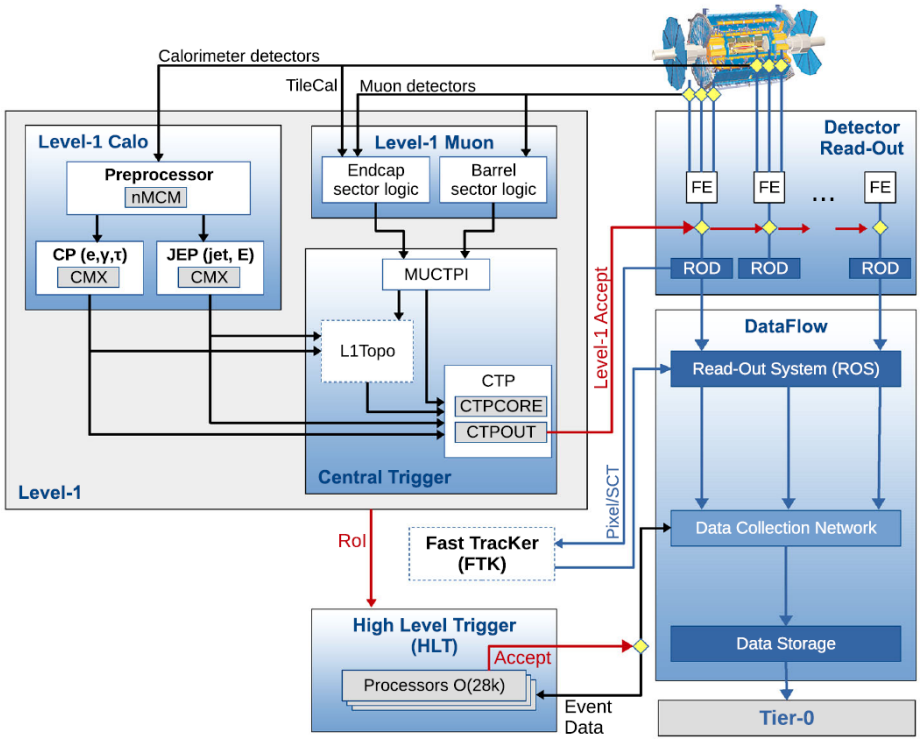


Figure 3.8.: The ATLAS trigger and data acquisition (TDAQ) system [70].

buffered in the Read-Out-System (ROS) while being processed by the 2nd stage of the trigger: the high level trigger (HLT). The L1 system sends regions-of-interest (RoIs) to the HLT, which can be used for partial reconstruction of events with finer granularities and a higher precision. The HLT applies another set of requirements to a given event and reduces to event rate by approximately another two orders of magnitude to roughly 1 kHz. The event requirements are defined in the trigger menu, a dedicated piece of software that allows for a selection of physics objects and thresholds. In the following an overview of the L1 and HLT systems will be provided.

### The Level-1 Trigger

The level-1 trigger consists of L1Calo, L1Muon and the central trigger which hosts the CTP. L1Calo itself is made of three processors. The preprocessor (PPr), the cluster processor (CP), and the Jet/Energy-sum processor (JEP).

The PPr system is the first block in the chain and receives analogue signals from the calorimeters. It digitises them, performs peak finding and bunch crossing identification algorithms and sends its results to the CP and JEP. The PPr received a large-scale upgrade during LS1 in which its main components, the multi-chip modules (MCMs), were replaced by more versatile and powerful successors, the new multi-chip modules (nMCMs). The new modules provide improved digitisation and come with FPGA[1] chips instead of ASICs[2] like their predecessors. This allows

[1]Field Programmable Gate Array
[2]Application-Specific Integrated Circuit

for improved algorithms and a dynamic pile-up subtraction, which is important for the higher luminosities and larger average number of interactions per event of Run-2.

The CP and JEP systems run in parallel and have separate purposes. The CP looks for signatures of electrons, photons, and $\tau$ leptons, counts those that reach certain energy thresholds and transmits these multiplicities to the CTP using the extended cluster merger modules (CMXs). The purpose of JEP is identifying jets and global event features, such as $E_{\mathrm{T}}^{\mathrm{miss}}$ and the total event energy. Again threshold multiplicities are counted and transmitted via the CMX to the CTP.

Likewise, L1Muon sends muon triggers to the CTP. For this it uses information from the RPCs and TGCs which provide spatial and temporal coincidence measurements as well as pre-defined $\mathrm{p}_T$ thresholds.

The CTP processes the various inputs it receives from the upstream systems. Based on the configurations in the trigger menu it accepts the event (L1A) or declines it. In the case of an L1A, RoIs are transmitted to the HLT.

#### The High Level Trigger

The HLT runs on a server farm using commercial hardware. It reconstructs events either fully or partly based on RoIs from L1. The HLT reconstruction provides a better resolution of $\mathrm{p}_T$ and spatial coordinates of the trigger objects than L1. An important difference to L1 is the access to tracking information from the ID. This allows for good performance of the HLT with respect to triggers that select charged particles. Reconstruction is also improved by access to the full calorimeter granularity such that HLT can perform discrimination based on detailed information of shower shapes. For muons as trigger items, the HLT can access information from all four different kinds of muon chambers to make decisions. The exact set of conditions that need to be fulfilled for an event to pass this trigger stage is dictated by the trigger menu.

After an event is accepted by the HLT it is stored in Tier0, CERNs data-centre for offline reconstruction and can be accessed by ATLAS scientists.

## 3.4. Object Reconstruction with the ATLAS Experiment

*Physics objects*, i.e. photons, electrons, muons, $\tau$ leptons, and hadronic jets, are identified using the various sub-detectors of ATLAS introduced above. Object selection in ATLAS is split into two parts. First, candidate objects are reconstructed and calibrated to the appropriate scale. The definition of candidate objects is usually very loose to yield a high efficiency. However, the candidates contain many misidentified objects, often called *fakes*. To reject the misidentified objects and to make the sample of selected objects sufficiently pure, the second step of identification is applied. The object identification algorithms process all reconstructed candidates and decide often based on complex discriminants, such as shower shape variables or outputs of multivariate analyses, whether or not an object passes selection. Usually, several working points are defined for the identification, which yield different selection efficiencies.

In the following the standard ATLAS object reconstruction and identification algorithms are briefly introduced. They are implemented in the ATLAS Athena framework, which has been

used in the releases 20 and 21 for this thesis [79, 80]. If not indicated otherwise, these algorithms were used for the analyses and studies presented in chapters 5 and 6. Before discussing photons, electrons, muons, $\tau$ leptons, and hadronic jets, track reconstruction and calorimeter clustering algorithms are explained.

**Tracks** are created by charged particles traversing the inner detector of the ATLAS experiment. They are built from hits in the sensors of the individual sub-systems that form the ID. There are two chains of tracking algorithms [81], which are used for different $p_T$ regimes. The inside-out algorithm is the primary tool to reconstruct tracks with a $p_T$ of more than 400 MeV. Below that $p_T$ threshold the algorithm becomes too inefficient and hence unreliable. It starts with three-hit seeds in the pixel and SCT detectors and then extends outwards to the TRT after resolving potential track ambiguities. This algorithm chain aims at identifying tracks from so-called primary particles, which are defined as final state particles with a mean lifetime greater than $t_{io} = 3 \cdot 10^{-11}$ s or as the remnants of decays of particles with a mean lifetime shorter than $t_{io}$ [82]. The other algorithm chain ("outside-in") uses an a *backtracking* technique. Here the algorithm starts from seed segments in the TRT and moves inwards. Its purpose is to reconstruct tracks of secondary particles that were produced by interactions of primary particles. Several track quality conditions exist. Typically, primary tracks need to fulfil *loose* quality criteria, which are formally defined as $p_T > 400$ MeV, $|\eta| < 2.5$, and at least seven hits in the SCT. Additionally, no more than two holes in the SCT and one hole in the pixel detectors are allowed. A hole is defined as an expected but missing hit in a track. Lastly, only one shared module is allowed, which is defined as a hit in the pixel detector that is shared by at least two tracks or as two shared hits in the same SCT layer [83]. Tracks are also central to vertex reconstruction, where primary vertex seeds are obtained by extrapolating tracks to the beamline and extracting their z-positions. Using the vertex seed and taking nearby tracks an iterative $\chi^2$ fit [84] is performed. The track quality requirement most often used is called *tight-primary* and requires an increased number of hits in the pixel detector: nine or more for $|\eta| \leq 1.65$ and eleven or more for $1.65 < |\eta| \leq 2.5$. Additionally, no pixel holes and one hit in either the IBL or the next-innermost pixel layer are required.

**Calorimeter clusters** are designed to contain the energy of particles showering into the calorimeters and are formed from cells in which the energy has been deposited. In ATLAS, two different algorithms are applied to construct clusters for different use cases: (1) clusters from sliding window algorithms are used for electron and photon reconstruction and (2) topological clusters are used for jet reconstruction [85]. Sliding window algorithms follow a simple concept: the calorimeter gets segmented in the $\eta - \phi$ plane into 200 x 256 calorimeter towers. Then a window of fixed size in clusters in $\eta$ and $\phi$ direction is slid on the entire plane and the energies of the calorimeter towers are summed up. If a local maximum is found that is above a certain energy threshold, the seed for a cluster is found. The window size and threshold are chosen to minimise the chance of noise being falsely identified as clusters and to maximise efficiency. The position of the seed is defined as the energy weighted barycenter of all contributing calorimeter towers. Around the seed the final cluster is formed by iterating over the calorimeter layers and including cells within layer-dependent windows. The algorithm for topological clusters lets clusters grow around seed-cells with a high signal-to-noise ratio. Neighbouring cells are added to the so-called proto-clusters if their signal-to-noise ratios is above certain thresholds. In the process of growing topological clusters, nearby proto-clusters can be merged into a single proto-cluster. The algorithms ends when either every cell has been added to a proto-cluster or

[1] Assuming locally homogeneous granularity.

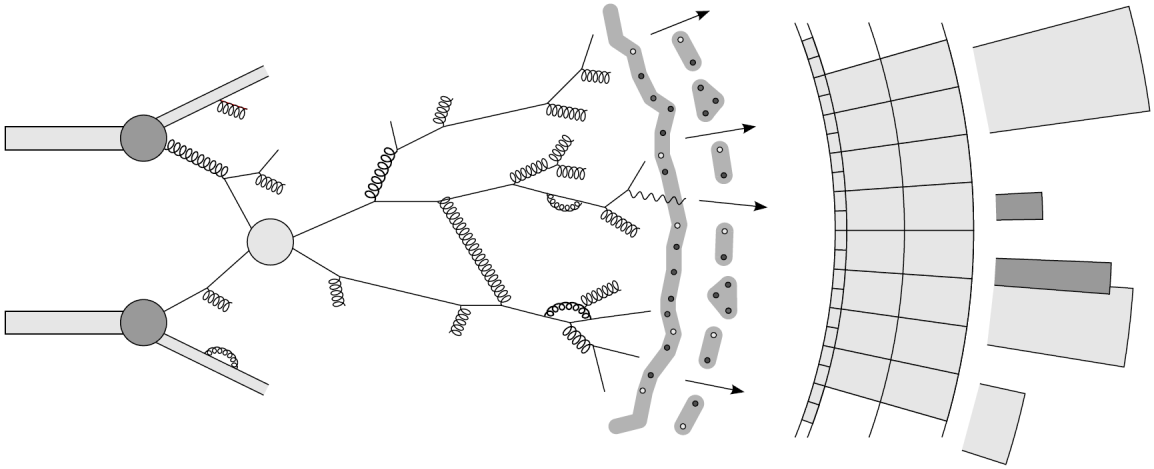

Figure 3.9.: Schematic illustration of jet production and its energy deposits in calorimeter cells. Taken from [86].

has been discarded because of an unfavourable signal-to-noise ratio. Neighbouring cells are the eight cells surrounding the central cell in the same calorimeter layer[1] and the cell(s) in adjacent layers with overlapping $\eta - \phi$ coordinates.

### 3.4.1. Hadronic Jets and Their Reconstruction

Due to the nature of quantum chromo dynamics, quarks and gluons cannot be observed by themselves. They fragment until low energy scales are reached where $\alpha_s$ becomes large, $\mathcal{O}(1\,\text{GeV})$, and the coloured partons hadronise into colorless hadrons due to confinement. These sprays of particles are called hadronic jets. The jets leave energy deposits in the calorimeters and tracks in the inner detector in the case of charged hadrons. Figure 3.9 illustrates this: the left hand side shows a hard interaction from partons in a proton-proton collision and the subsequent parton shower and hadronisation. The right hand side schematically depicts parts of a calorimeter and energy depositions in its cells. Jet algorithms can be defined to describe these objects. They take inputs and cluster them into higher-level objects following a combination sequence. These input can either be measured quantities, such as tracks or calorimeter clusters, or the final state particles of a hadronic jet when considering simulated events, cf. Section 3.5.

In ATLAS the standard jet algorithm is anti-k$_t$ [87], which is infrared safe and collinear. This means that both the emission of additional soft gluons and the collinear splitting of a particle do not change the jet significantly. Anti-k$_t$ is a *sequential combination algorithm* meaning that pairs of objects are combined until an exit condition is met. The combination of objects is performed by adding their four-vectors. The central metric for the anti-k$_t$ algorithm is the distance parameter d$_{ij}$ between two objects i and j defined as:

$$d_{ij} = \min(p_{T,i}^{-2}, p_{T,j}^{-2}) \frac{\Delta R_{ij}^2}{R^2}. \tag{3.12}$$

Here, $p_{T,i}$ and $p_{T,j}$ are the transverse momenta of objects i and j, $R$ is the distance parameter given as an input to the algorithm, and $\Delta R_{ij}$ follows the definition of Equation 3.5. The algorithm starts by finding the smallest distance $d_{ij}$ in an event by evaluating every possible pair of input objects, including the distance to the beam $d_{iB}$. The two objects that fulfil this criterion are then combined. If the smallest $d_{ij}$ is larger than $d_{iB} = p_{T,i}^{-2}$, the exit condition is met and object $i$ is declared a jet and taken out of the algorithm. The algorithm is complete when no objects are left.

The anti-$k_t$ algorithm tends to cluster objects with large transverse momenta that are in close vicinity. This leads to the jets being clustered around high-$p_T$ seeds. The final jets have regular and approximately circular shapes with radius R. This is an important reason why the anti-$k_t$ algorithm is often preferred over other sequential combination jet algorithms, such as $k_T$ or Cambridge/Aachen, whose irregular jet shapes can cause experimental difficulties.

For the analysis and the additional studies presented in this thesis the radius parameter is R = 0.4. The inputs to the algorithm are topological clusters built from calorimeter cells on *reconstruction level* and final state particles after showering on *particle level*[1].

By default the jets are calibrated at the electromagnetic (EM) scale rather than the hadronic scale and need to be corrected for a variety of experimental effects. These effects encompass leakage at the outer part and non-compensation of the calorimeter, defect hardware and pile-up. Additionally, jets can carry energy in the form of neutral hadrons and neutrinos, which the EM scale does not account for. For this a dedicated calibration chain in is place that consists of sequential corrections [88]. An overview of this calibration can be seen in Figure 3.10: the clustering algorithm provides a base jet at the EM scale[2]. The origin correction corrects the coordinates of the jet such that its origin is not the center of the detector but the primary vertex with the highest $\sum p_T^2$. This improves the $\eta$ resolution of jets. Then two corrections for pile-up are applied. The jet area based pile-up correction is parametrised as a function of the pile-up energy density $\rho$ in the $\eta \times \phi$ plane and the jet area. The residual pile-up correction is parametrised as a function of the number of primary vertices and the average number of interactions per bunch-crossing. It captures in-time and out-of-time pile-up and removes a small dependence of the jet $p_T$ on pile-up that remains after the jet area based correction. The next step in the calibration are jet energy scale (JES) corrections. These corrections are parametrised in $\eta$ and the uncorrected jet energy. They relate the energy of reconstructed jets to the energy of truth jets using Monte Carlo samples. A small bias in the $\eta$ distribution of the jets can be observed which is caused by some regions being better instrumented than others. To resolve this an additional correction parametrised in the angle of the jet is applied.

After the above calibrations a jet response difference of up to 8% between quark initiated jets and gluon initiated jets is still observed [89]. The jet response $\mathcal{R}$ is defined as $\mathcal{R} = p_T^{\text{reco}}/p_T^{\text{truth}}$, with $p_T^{\text{reco}}$ and $p_T^{\text{truth}}$ being the $p_T$ of a jet after reconstruction and on truth level respectively. To resolve this the global sequential correction is applied. It corrects the jet energy based on shower shape information using tracks, the calorimeters, and the muon spectrometer. These variables are sensitive to the particle that initiates a jet. The correction leaves the mean jet energy response unchanged, which is already properly calibrated by the earlier steps. Its application significantly reduces uncertainties with respect to the jets. After this MC based calibration, jets are finally corrected *in-situ* using data. For these corrections jets are required to recoil against

[1] For a brief discussion of reconstruction level and particle level cf. Section 3.5.

[2] Constituents of the jets can also be locally calibrated and weighted clusters (LCW). For the work presented in this thesis however, jet clusters start at the EM constituent scale.

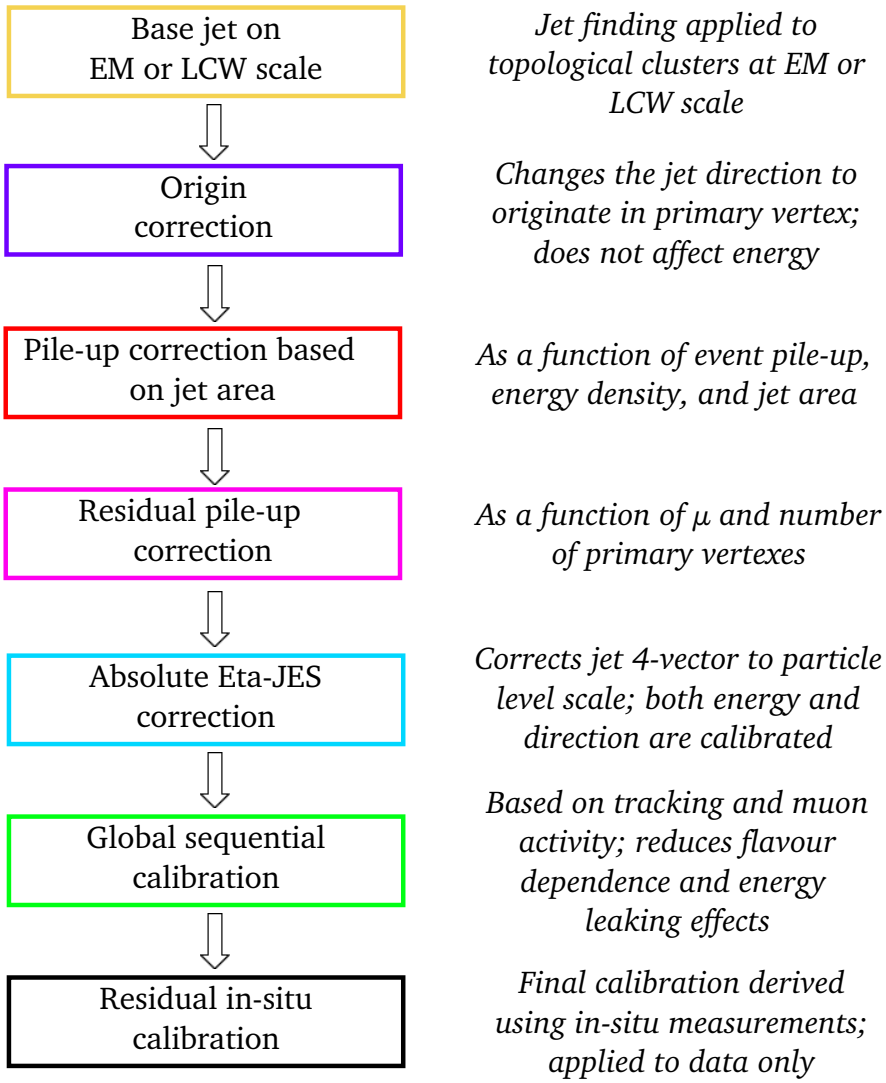


Figure 3.10.: A summary of the various steps of the ATLAS jet calibration [88].

objects that can be measured with higher accuracy, such as photons, leptonically decaying Z-bosons or, for forward jets, central jets. Using this *in-situ* technique corrections are derived for $\eta$, called the $\eta$-intercalibration or *relative in-situ* calibration, and for the jet energy, called the *absolute in-situ* calibration.

The complex nature of the JES leads to multiple sources of systematic uncertainty for jets. Figure 3.11 summarises the combined uncertainty in the JES for fully calibrated jets at $\eta = 0$. ATLAS considers a set of 80 terms for the total JES uncertainty, that originate in the *in-situ* technique, pile-up, jet flavour, punch-through, non-closure between data and MC, high $p_T$ jet uncertainties from single-particle responses and test-beam measurements. A full list with additional information can be found in [90].

Additional challenges with the assessment of jet quality are the identification and rejection of so-called "bad", or sometimes *fake*, jets and pile-up jets. "Bad" jet is a collective term for objects that do not originate in proton-proton collisions, but that look similar to hadronic jets from hard interactions. They can for instance be formed from showers of cosmic radiation. The term also

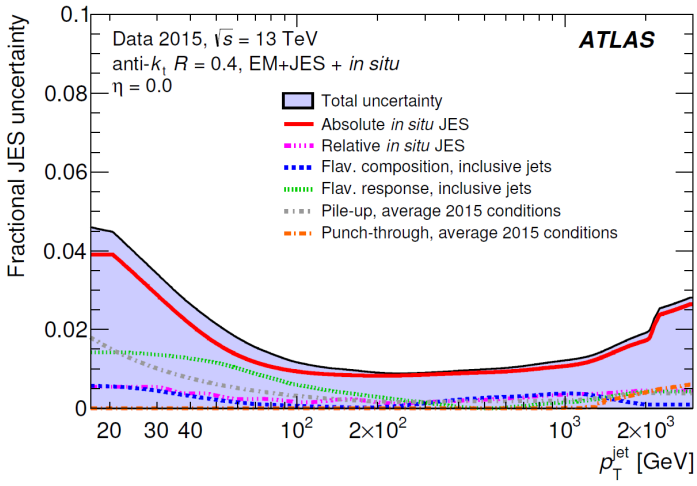


Figure 3.11.: The fractional uncertainties on the jet energy scale as a function of jet $p_{\mathrm{T}}$ for $\eta = 0$ [90].

incorporates beam induced backgrounds that originates in proton losses upstream of ATLAS and jets falsely built from clusters caused by calorimeter noise. Several jet quality variables are defined based on tracks, energy ratios and signal pulse shapes of the LAr calorimeter to reject these objects. Based on them two working points are defined: *LooseBad* and *TightBad*, which have 99.5% and 95% efficiencies for jets with $\mathrm{p}_T > 20$ GeV [91]. For the rejection of jets from pile-up, as introduced in Section 3.2.2, a variable called the jet vertex tagger (JVT) is introduced and cut on for each jet. JVT is a likelihood function that is sensitive to whether a jet originates in pile-up or the primary vertex using tracking and vertex information. The baseline cut is JVT $> 0.64$ for jets within $|\eta| < 2.4$ and 20 GeV $< \mathrm{p}_T <$ 50 GeV and yields an average efficiency of 92% [71, 92].

### 3.4.2. Electrons and Photons

#### Electrons

Electrons can be reconstructed within $|\eta| < 2.47$ allowing for tracks to be used. The first step of reconstruction is called seed-cluster reconstruction [93] and follows the calorimeter clustering algorithms explained above. Most of the energy of an electromagnetic shower is expected to be deposited in the 2nd layer of the EM calorimeter. The window size for seed-cluster reconstruction is chosen accordingly: 3 x 5 in units of 0.025 x 0.025 in $\eta - \phi$, which corresponds to the granularity of that calorimeter layer. The efficiency of seed-cluster reconstruction is about 95% (99%) for a particle with $\mathrm{E}_T = 7\,\mathrm{GeV}$ (15 GeV). Additionally, tracks are used for electron reconstruction. Reconstructed tracks are fit with an electron hypothesis and if the coordinates of an extrapolation to the 2nd EM layer agree with the position of the cluster, the two are matched. If several tracks are valid candidates the ambiguity is resolved by an algorithm taking into account variables such as track-cluster distance and the number of pixel hits. Lastly, the electron candidate is reclustered in units of in 3 x 7 (5 x 5) in the barrel (end-cap). The newly formed cluster yields the basis for the energy measurement and the track is used for the position of the electron candidate.

Following the reconstruction, an energy calibration for electromagnetic objects is performed [94]. For this a Monte Carlo simulation-based multivariate technique is applied that corrects for energy loss before the electron showers in the calorimeter and outside of the cluster. The former amounts to up to 20% for a 100 GeV electron and the latter to approximately 5%. To account for differences between data and Monte Carlo simulations, an additional in-situ energy scale calibration extracted from $Z \to e^+e^-$ events is performed.

This sample of electron candidates is contaminated by other objects. In order to discriminate proper electrons from for instance hadronic jets or converted photons, an identification (ID) algorithm is applied. The algorithm is based on a multivariate likelihood method (LH) that evaluates input variables and performs a discrimination. These inputs are related to shower shapes extracted from the calorimeter clusters, details of the tracks, track-cluster matching and variables sensitive to bremsstrahlung measurements. The full list can be found in [93]. Based on the LH output several working points are defined: *Loose*, *Medium* and *Tight*. These correspond to 92%, 87%, and 78% electron efficiencies respectively with increasing background rejection. In most analyses, selected electrons are required to be isolated. This is to discriminate prompt electron, e.g. in $Z \to e^+e^-$ events, from non-prompt electrons, e.g. from photon conversion or heavy flavour decays. Based on track- and calorimeter-isolation, seven working points are defined in ATLAS coming with varying efficiencies and that were designed for different use-cases [93].

### Photons

The reconstruction of prompt[1] photons [95] resembles the electron reconstruction. The formation of calibrated clusters is identical, but photons do not carry an electromagnetic charge and thus do not produce tracks in the ID. As a consequence, a calorimeter cluster without associated track becomes a candidate for an unconverted photon. However, approximately 40% of photon candidates are reconstructed as a convert electron-positron pair [96]: a cluster associated with two opposite-sign tracks becomes a candidate for a converted photon. At high $p_T$s the two tracks can merge due to the finite resolution of the tracking system and the huge conversion radius. In this case however the first layers of the ID typically do not register hits, which enables a classification as converted photon instead of an electron. The calibrations (MC-based and in-situ) follow the same lines as above.

Similar to electrons, there are many prompt photon candidates which have other origins, most notably hadronic jets or photons from hadron decays. Hence non-prompt photons are often correlated with hadronic activity in close vicinity, which allows for rejection. Hadronic showers usually extend into the hadronic calorimeter and are less narrow. This is the basis of photon identification algorithms, which are based on multivariate techniques. Two working points are defined: *loose* and *tight*. The *loose* ID only makes use of information from the hadronic and second electromagnetic sampling layer whereas the *tight* ID takes into account full calorimeter information. The latter provides a better background subtraction but also a lower signal efficiency. The ID algorithms are optimised for converted and unconverted photons separately. Electrons and photons share the same isolation working points.

[1] Here, prompt refers photons not originating from hadron decays.

### 3.4.3. Muons

The reconstruction of muons is performed with information from the ID and the MS. Only in rare cases the calorimeter is used in addition, because muons deposit only little energy in its cells. Tracks from the ID are reconstructed and used as described above. Information from the ID, MS, and calorimeters are then combined to form muon candidates.

The track reconstruction in the MS starts with fitted track segments formed from hit patterns in the individual chambers [97]. The chambers provide complementary coordinate information as described in Chapter 3.3.3. Muon track candidates are built from seed segments in the middle layer of the MS. Segments from the other layers are added to the candidate track by evaluating hit multiplicity, relative angles and positions, and fit quality. In the beginning an individual segment can belong to more than one candidate, but eventually an overlap removal is performed. In most of the acceptance region two segments are required to form a track candidate. The barrel-end-cap transition region poses an exception, where one high quality segment suffices. Hits are added and removed to track candidates based on a $\chi^2$ fit [84].

There are four different muon definitions for four different use-cases. Most commonly used are *combined muons* [97]. Here tracks from the ID and the MS are taken and combined using a global fit. During the fitting procedure individual hits from the MS can be added or removed to improve the fit quality. Usually, combined muons are reconstructed *outside-in* starting in the MS, extrapolating inwards and matching with an ID track. As a complementary approach they can also be constructed using an *inside-out* algorithm. If a muon crosses only one layer in the MS the *segmented-tagged* definition for muons becomes useful. This can occur due to low muon $p_T$ or because the trajectory traverses regions with reduced instrumentation. The segmented-tagged muon is constructed from an ID track that can be matched, once extrapolated, to at least one track segment in an MDT or CSC chamber. The very central region of the MS ($|\eta| < 0.1$) is only partly instrumented to allow for cabling and access to the calorimeters. For this part, *calorimeter-tagged muons* were defined because they recover lost acceptance. If an ID track can be matched to a calorimeter deposit compatible with a minimally-ionising particle, such a muon is constructed. The fourth muon definition compensates for the fact that the MS extends more forward ($|\eta| < 2.7$) than the ID ($|\eta| < 2.5$). For this small kinematic region in which the ID is inaccessible, *extrapolated muons* are defined. Such a muon is defined if a MS track can be reconstructed from three layers and is loosely compatible with having its origin at the IP. It can also be defined for the non-forward region in which case two contributing MS layers are sufficient. Ambiguities with ID tracks between the different types are resolved by giving priority to combined muons, then segmented-tagged ones, and lastly segmented-calorimeter muons. The overlap decision regarding extrapolated muons is made on a case-by-case basis by analysing the fit qualities and numbers of hits.

Muon transverse momenta can be measured to a high level of accuracy because of the precision measurements of ID and MS tracks. A calibration is applied to MC in order to describe the momentum resolution to the percent level and the momentum scale to the per-mille level. This is done using $Z \to \mu\mu$ and $J/\Psi \to \mu\mu$ resonance measurements and calculating correction factors accounting for differences between MC and data [97].

The muon identification algorithms aim at discriminating between prompt muons and muons from hadron decays. The former category encompasses for instance $Z \to \mu\mu$ or $W \to \mu\nu$ processes. Four working points are defined based on a set of quality variables. The working points are called *loose*, *medium*, *tight*, and *high-$p_T$*. The former three are defined inclusively, meaning

that every muon surviving the *tight* (*medium*) criteria also survives *medium* (*loose*) quality cuts. *high* $p_T$ is optimised for muons with $p_T > 100$ GeV for heavy Z' or W' resonance searches. The identification efficiencies for prompt muons (muons from hadron decays) with 20 GeV $< p_T < 100$ GeV are 98.1% (0.76%), 96.1% (0.17%), 91.8% (0.11%), and 80.4% (0.13%). The suppression of muons from hadron decays is so high, because they usually have distinct kinks in their trajectories, which worsen the fit qualities and are easily identifiable [97].

Muon isolation is defined similarly to electron isolation and they share the same seven working points. It can be an important tool for analyses to select muons from for instance Z decays, which are usually isolated, and reject semi-leptonic events, where muons are often surrounded by jets.

### 3.4.4. Taus

$\tau$ leptons are the heaviest known charged leptons and can decay into other charged leptons and hadrons. For this thesis, the interest in $\tau$ leptons comes from the desire to reject events in which they are present. In cases in which the $\tau$ decays into another charged lepton, the electron and muon vetoes[1] perform the rejections with high efficiencies. In 65% of the cases however, tau leptons decay hadronically. In 72% of the cases the hadronic decay produces one charged pion, called *one-prong decay*, and in 22% three charged pions, called *three-prong decay*. In the remaining decays kaons are often produced [98]. Additionally, there is an overall 78% chance for the associated production of a neutral pion.

To preserve lepton flavour the decays are accompanied by a $\nu_\tau$. This leads to missing transverse momentum and only a visible fraction of the total energy being deposited in the calorimeters. The hadronic visible decay products are referred to as $\tau_{\text{had-vis}}$.

The reconstruction of hadronically decaying $\tau$s, further on simply refered to as $\tau$s, uses tracks and calorimeter clusters [99]. The former limits the reconstruction of $\tau$ leptons to the acceptance of the ID, i.e. $|\eta| < 2.5$. The latter excludes the calorimeter transition region of $1.37 < |\eta| < 1.52$. So called $\tau_{\text{had-vis}}$ candidates are formed with the anti-$k_t$ clustering algorithm using a radius parameter of 0.4, cf. Section 3.4.1. The algorithm runs on topological clusters calibrated to a local hadronic scale. The barycenter of the cluster is determined and the $p_T$ of the $\tau_{\text{had-vis}}$ candidate is set to the total energy of clusters within $\Delta R < 0.2$ around it, because the shower is expected to be narrow. The primary vertex of an event is not necessarily identical to the $\tau$ vertex (TV) from which the hadronic shower originates. Tracks that are associated to the central part, $\Delta R < 0.2$, of the cluster are used to determine the TV and contribute later to the calculation of impact parameters.

In addition to the local hadronic calibration which corrects for energy deposited in dead material and calorimeter non-compensation, $\tau_{\text{had-vis}}$ candidates are corrected for two additional effects: pile-up and decay products being either too soft to create topological clusters or being outside of the $\Delta R < 0.2$ cone.

The reconstruction efficiency for hadronically decaying $\tau$ leptons is almost 100%. However, the sample of these objects is very impure, mostly contaminated by hadronic jets and, to a lesser extent, electrons. To reject the contaminating objects a dedicated $\tau$ ID algorithm is defined. The ID algorithm provides various techniques for discrimination against background.

[1] A *veto* is a cut aimed at rejecting events that contain certain objects.

$\tau_{\text{had-vis}}$ candidates can for instance be required to have either exactly one or three associated tracks corresponding to the two main $\tau$ decay modes. To provide further discrimination against hadronic jets, boosted decision trees (BDTs) are trained separately for the 1- and 3-prong cases using MC. As inputs both tracking and calorimeter information is used. The discrimination benefits from differences in shower shapes, the fractional distribution of $p_T$ in the decay products, and impact parameter information. Three BDT working points are defined: *Loose*, *Medium*, and *Tight*. These have $\tau$ identification efficiencies for the 1-prong (3-prong) candidates of 66% (50%), 0.55% (40%), and 0.45% (30%) and increasing background rejections, respectively. These values are low compared to electron and muon identification efficiencies, because the discrimination against hadronic jets is difficult. To improve discrimination between 1-prong decays and prompt electrons, a $\tau_{\text{had-vis}}$ candidate with one associated track is rejected if an electron with $p_T > 5$ GeV and a high electron ID likelihood score is within $\Delta R < 0.4$.

### 3.4.5. Missing Transverse Momentum

The central objects for this thesis are WIMP Dark Matter particles and neutrinos. They cannot be reconstructed and identified because they do not interact via the strong or electromagnetic force. However, they cause a momentum imbalance in the transverse plane of the detector, which can be seen as missing transverse momentum ($p_{\text{T}}^{\text{miss}}$). In ATLAS the terms $E_{\text{T}}^{\text{miss}}$ and $p_{\text{T}}^{\text{miss}}$ are usually[1] interchangeable and refer to the same concept.

For $p_{\text{T}}^{\text{miss}}$ all objects described above are considered. An additional soft term is defined that accounts for activity that is too soft to be reconstructed as objects. This term can be formed from calorimeter clusters or from tracks, that in both cases are not associated to reconstructed objects. Pile-up, cf. Section 3.2.2, impacts the soft term leading to a loss in resolution. Soft terms from calorimeter clusters are especially susceptible to this, because pile-up rejection is difficult. The soft terms from tracks (*track soft term*, TST) however provides pile-up discrimination by using only those tracks that are associated to the primary vertex of the event and that are not associated to reconstructed hard objects. A disadvantage is that is does not include soft neutral particles. Studies indicating good performance can be found in [100].

Missing momenta are constructed in the following way:

$$p_{\text{x(y)}}^{\text{miss}} = p_{\text{x(y)}}^{\text{miss, e}} + p_{\text{x(y)}}^{\text{miss},\gamma} + p_{\text{x(y)}}^{\text{miss},\tau} + p_{\text{x(y)}}^{\text{miss, jets}} + p_{\text{x(y)}}^{\text{miss},\mu} + p_{\text{x(y)}}^{\text{miss, TST}} \tag{3.13}$$

The individual terms correspond to the x(y) component of the negative vectorial sums of the selected and calibrated objects introduced above. The final $p_{\text{T}}^{\text{miss}}$ follows as:

$$p_{\text{T}}^{\text{miss}} = \sqrt{(p_{\text{x}}^{\text{miss}})^2 + (p_{\text{y}}^{\text{miss}})^2} \tag{3.14}$$

The vector $\mathbf{p}_{\text{T}}^{\text{miss}}$ is defined as the negative vector sum of the four-vectors of all objects mentioned above projected into the transverse plane. Consequently, $|\mathbf{p}_{\text{T}}^{\text{miss}}| = p_{\text{T}}^{\text{miss}}$ and it has a $\phi$-coordinate corresponding to the transverse direction of the missing momentum.

[1] In some ATLAS analyses $E_{\text{T}}^{\text{miss}}$ is used for the object described in this chapter but $p_{\text{T}}^{\text{miss}}$ refers to a similar quantity calculated purely from tracks.

Uncertainties on $p_{\mathrm{T}}^{\mathrm{miss}}$ include uncertainties from the reconstruction, calibration, and identification of all contributing objects.

## 3.5. Monte Carlo Simulations

### The Simulation Chain

*Monte Carlo* (MC) simulation refers to a complex chain of programs that provides simulated events of Standard Model and BSM scattering processes from high energy collisions [101]. Some parts in this chain are calculated from first principles, such as matrix elements. Others, such as hadronisation, are tuned to data using empirical models.

The first step is considering the hard scatter of the proton-proton collision. For this the matrix element (ME) calculation of the process of interest is performed up to a certain order. Contemporary event generators provide leading order (LO) or next-to-leading order (NLO) calculations, in some cases to higher orders. The cross section for a process in a proton-proton collision results from the convolution of the partonic cross-section and the PDF. In practice the PDF is typically provided by an external library as it cannot be determined purely from first principles, cf. Section 3.2.1. They are provided by several groups, the ones used extensively in the MC samples for the analysis presented in this theses are CT10, CT14, [102], NNPDF [103], and MMHT 2014 PDF [104]. Event generators also calculate the underlying event, which are the interactions of remnants of the proton involved in the hard scatter [105].

The second block is parton showering (PS). Some event generators, referred to as multi-purpose event generators, provide PS themselves whereas other generators need to be interfaced to dedicated PS programs. The purpose of PS is to add additional partonic radiation to an event and an effort is made to not double count radiation already provided by the ME. The radiation is evolved in time and can produce further emissions down to approximately 1 GeV. The string model [106] and the cluster model [107] are two hadronisation models that are widely used: the cluster model for instance in Sherpa [108] and the string model in Pythia [109, 110].

The last block is the detector simulation, where a detailed digital representation of the ATLAS experiment is built in software. It provides an accurate simulation of the different sub-detectors and materials and hence acceptances and efficiencies. With the transition from particle level to detector signal, hits of charged particles in the ID and MS, ionisation in the calorimeters, and much more is simulated. ATLAS uses Geant4 [111] for detector simulations.

A detailed description of the simulation setup used for this thesis can be found in Appendix A.

### Particle Level and Reconstruction Level

Before objects of an event interact with the detector, in simulation or in reality, the event and its objects are said to be on *truth* or *particle level* particle. After the interaction the event is on *detector* or *reconstruction level*. Distributions have been folded with detector responses leading to finite reconstruction and identification efficiencies, as described Section 3.4, altering event properties. The MC simulation chain allows to compare measured data, which is by definition on reconstruction level, to predictions from the SM or BSM models. Detector simulations are also used to *unfold* detector effects from measured events as will be discussed in Section 4.2.1.

# 4. Collider Searches Using $p_{\mathrm{T}}^{\mathrm{miss}}$ and Jets and How to Improve Them

In Chapters 1 and 2.4 various approaches for DM searches using collider experiments, such as ATLAS (cf. sectiom 3.3), were presented. Two search strategies were motivated: (1) investigating final states with $p_{\mathrm{T}}^{\mathrm{miss}}$ and the associated production of SM particles $X$, so called $p_{\mathrm{T}}^{\mathrm{miss}} + X$ searches and (2) investigating purely hadronic final states while searching for unknown resonances in mass spectra which reveal new mediator particles, the *dijet* searches.

This thesis introduces a novel approach to searches for Dark Matter using final states with $p_{\mathrm{T}}^{\mathrm{miss}}$ and jets. As a motivation, this chapter discusses the workflow of conventional $p_{\mathrm{T}}^{\mathrm{miss}}$ + jets searches by examining the latest ATLAS[1] paper featuring such a search called *Search for new phenomena in final states with an energetic jet and large missing transverse momentum in pp collisions at* $\sqrt{s} = 13$ *TeV using the ATLAS detector* [6]. In the following, an overview of the analysis strategy and selected results from this paper is given. Subsequently, potential improvements are discussed, the implementations of which lead this thesis and the paper *Measurement of detector-corrected observables sensitive to the anomalous production of events with jets and large missing transverse momentum in pp collisions at* $\sqrt{s} = 13$ *TeV using the ATLAS detector* [1].

## 4.1. The Conventional $p_{\mathrm{T}}^{\mathrm{miss}}$ + Jets Collider Search

The paper [6] was published in 2016 and the analysis investigated 3.2 $\mathrm{fb}^{-1}$ of integrated luminosity. It is the latest paper by ATLAS featuring a conventional DM search in hadronic topologies with large of amounts $E_{\mathrm{T}}^{\mathrm{miss}}$[2]. By counting event yields in signal regions and comparing them to expected values, exclusion limits are set on several DM models. In the following a short summary of the paper is given discussing key-aspects that are relevant for later chapters of the thesis.

Events are selected by an $E_{\mathrm{T}}^{\mathrm{miss}}$ trigger which is fully efficient at the cut value of 250 GeV. Further cuts ensure basic event quality, such as the detector not being in a faulty state, the presence of a primary vertex with associated tracks, and hadronic jets originating from energetic proton-proton collisions. Events containing reconstructed muons or electrons are rejected. The leading jet[3] is required to have $\mathrm{p}_T > 250\,\mathrm{GeV}$ to reflect the $E_{\mathrm{T}}^{\mathrm{miss}}$ cut and to be central such that its potential charged particles leave tracks in the ID. The inclusion of tracking information allows for tighter jet quality cuts. In addition to the leading jet, three central jets are allowed with $\mathrm{p}_T > 30\,\mathrm{GeV}$. The $\mathrm{p}_T$ cut makes the selection less vulnerable to jets originating from pile-up,

[1] As of November 2017.
[2] The analysis uses $E_{\mathrm{T}}^{\mathrm{miss}}$ instead $p_{\mathrm{T}}^{\mathrm{miss}}$ as notation for the scalar quantity. The negative vectorial sum, cf. Section 3.4.5, however is called $\mathbf{p}_{\mathrm{T}}^{\mathrm{miss}}$.
[3] In this thesis, *leading* always refers to $\mathrm{p}_T$.

| Selection Criteria | | | | | | | |
|---|---|---|---|---|---|---|---|
| Primary vertex | | | | | | | |
| $E_{\mathrm{T}}^{\mathrm{miss}} > 250\,\mathrm{GeV}$ | | | | | | | |
| Leading jet with $p_{\mathrm{T}} > 250\,\mathrm{GeV}$ and $\lvert\eta\rvert < 2.4$ | | | | | | | |
| At most four jets with with $p_{\mathrm{T}} > 30\,\mathrm{GeV}$ and $\lvert\eta\rvert < 2.8$ | | | | | | | |
| $\Delta\phi(\mathrm{jet}, \mathbf{p}_{\mathrm{T}}^{\mathrm{miss}})$ | | | | | | | |
| Jet quality requirements | | | | | | | |
| No identified muon with $p_{\mathrm{T}} > 10\,\mathrm{GeV}$ or electron with $p_{\mathrm{T}} > 20\,\mathrm{GeV}$ | | | | | | | |
| Inclusive signal region | IM1 | IM2 | IM3 | IM4 | IM5 | IM6 | IM7 |
| $E_{\mathrm{T}}^{\mathrm{miss}}$ (GeV) | $> 250$ | $> 300$ | $> 350$ | $> 400$ | $> 500$ | $> 600$ | $> 700$ |
| Exclusive signal region | EM1 | EM2 | EM3 | EM4 | EM5 | EM6 | |
| $E_{\mathrm{T}}^{\mathrm{miss}}$ (GeV) | [250 - 300] | [300 - 350] | [350 - 400] | [400 - 500] | [500 - 600] | [600 - 700] | |

Table 4.1.: This table summarises the cuts and signal regions of the conventional 2015 ATLAS $p_{\mathrm{T}}^{\mathrm{miss}}$ + jets search. Taken from [6].

cf. Chapter 3.2.2. Events with additional central jets are rejected to minimise contributions from $t\bar{t}$ processes, which typically have higher jet multiplicities. An event is also rejected if $\Delta\phi(\mathbf{p}_{\mathrm{T}}^{\mathrm{miss}}, \mathrm{jet}) < 0.4$, where $\Delta\phi$ is the difference in azimuthal angle of the four-vectors of the two objects and all potential four jets are considered. The cut reduces contributions from the multijet background in which one of the jets was mismeasured. Various signal regions (SRs) are defined based on additional $E_{\mathrm{T}}^{\mathrm{miss}}$ cuts. These SRs are either defined inclusively, meaning that all events that pass the cuts and that have $E_{\mathrm{T}}^{\mathrm{miss}}$ exceeding the requirement of the individual SR are included. Or they are defined exclusively, in which case the required $E_{\mathrm{T}}^{\mathrm{miss}}$ value for an event has to be within a certain range. A summary of all cuts and SRs can be found in Table 4.1.

This selection is sensitive to DM models with $E_{\mathrm{T}}^{\mathrm{miss}}$ and jets in the final state, which are considered signal in this analysis. Contributions from the SM are treated as background. The cutflow[1] selects hadronic events in association with large values of $E_{\mathrm{T}}^{\mathrm{miss}}$, which in the case of the SM (DM model) translates to neutrinos (DM particles) with large $p_{\mathrm{T}}$. The largest SM contributor to the SRs is the production of a Z-boson that decays into two neutrinos, $Z \to \nu\nu$ + jets. However, various other processes contribute to the SRs, especially W + jets events, in which the W decays leptonically. If the lepton is outside the detector acceptance, not reconstructed, or misidentified as a hadronic jet, the event can enter the signal selection. Among the W backgrounds, $\mathrm{W} \to \tau\nu$ + jets events have the largest contribution, because no selection for $\tau$ leptons that decay hadronically is applied. Hence these events cannot be rejected. Hadronic $\tau$ lepton decays form about 65% of all $\tau$ decays, cf. Chapter 3.4.4. Additional background originates in $Z \to l^+l^-$ + jets events, where $l^{\pm}$ denotes a charged lepton. The background contribution is significantly lower than for W + jets, because two instead of one charged leptons need to be out of acceptance or lost due to finite efficiencies. Also $t\bar{t}$, single top and dibosons production pose contributions via associated W-bosons, although they are much smaller. Lastly, small background contributions come from multijet events and non-collision backgrounds, such as cosmic rays. Depending on the size of the background and how well it is modelled in MC, the background estimate is performed either in a data-driven way with control samples in data or taken purely from MC. More details on the estimation procedures including global fits can be found in [6] and an overview is provided in Table 4.2.

Using the background estimates, event counts for the individual SRs can be predicted and be compared to the data. Table 4.3 shows observed and predicted event counts. Distributions of

[1] *Cutflow* describes the sequence of cuts on object and event variables that defines a SR.

| Background process | Method | Control sample |
|---|---|---|
| $Z(\rightarrow \nu\nu)$ + jets | MC and control samples in data | $W(\rightarrow \mu\nu)$ |
| $W(\rightarrow e\nu)$ + jets | MC and control samples in data | $W(\rightarrow e\nu)$ |
| $W(\rightarrow \tau\nu)$ + jets | MC and control samples in data | $W(\rightarrow e\nu)$ |
| $W(\rightarrow \mu\nu)$ + jets | MC and control samples in data | $W(\rightarrow \mu\nu)$ |
| $Z/\gamma^*(\rightarrow \mu^+\mu^-)$ + jets | MC and control samples in data | $Z/\gamma^*(\rightarrow \mu^+\mu^-)$ |
| $Z/\gamma^*(\rightarrow \tau^+\tau^-)$ + jets | MC and control samples in data | $W(\rightarrow e\nu)$ |
| $Z/\gamma^*(\rightarrow e^+e^-)$ + jets | MC only | - |
| $t\bar{t}$, single top | MC only | - |
| Diboson | MC only | - |
| Multijets | data driven | - |
| Noncollision | data driven | - |

Table 4.2.: Background processes and how they are estimated in the conventional 2015 ATLAS $p_{\mathrm{T}}^{\mathrm{miss}}$ + jets search. Taken from [6].

| Signal region | IM1 | IM2 | IM3 | IM4 | IM5 | IM6 | IM7 |
|---|---|---|---|---|---|---|---|
| Observed events (3.2 $\mathrm{fb}^{-1}$) | 21447 | 11975 | 6433 | 3494 | 1170 | 423 | 185 |
| SM prediction | 21730 ± 940 | 12340 ± 570 | 6570 ± 340 | 3390 ± 200 | 1125 ± 77 | 441 ± 39 | 167 ± 20 |
| Signal region | EM1 | EM2 | EM3 | EM4 | EM5 | EM6 | |
| Observed events (3.2 $\mathrm{fb}^{-1}$) | 9472 | 5542 | 2939 | 2324 | 747 | 238 | |
| SM prediction | 9400 ± 410 | 5770 ± 240 | 3210 ± 170 | 2260 ± 140 | 686 ± 50 | 271 ± 28 | |

Table 4.3.: Predicted and observed numbers of events in the various signal regions of the conventional 2015 ATLAS $p_{\mathrm{T}}^{\mathrm{miss}}$ + jets search. The numbers show a good agreement. Taken from [6].

$E_{\mathrm{T}}^{\mathrm{miss}}$ and the $p_T$ of the leading jet in the most inclusive SR are presented in Figure 4.1. They are compared to three BSM cases: SUSY (red), WIMP DM in a simplified model (blue), and an ADD model for large extra dimensions[1] (dark purple). In both distributions generally good agreement between the data and SM predictions is seen. Information on the indicated statistical and systematic uncertainties can be found in [6].

Exclusion limits are set in three BSM scenarios. The simplified model WIMP DM scenario will be revisited in Chapter 5 and is described in Chapter 2.3. The other scenarios will not be discussed further, because they are not relevant for the rest of this thesis. The WIMP model involves four parameters, two couplings ($g_q$: mediator-to-quarks; $g_\chi$: mediator-to-dark-matter) and two masses ($m_\chi$: DM particle mass; $m_A$: mediator mass). For the limit setting in the paper, the former two are fixed. In the plane of the masses, i.e. the $m_\chi$-$m_A$ plane, a multitude of points are chosen and signal Monte Carlo samples are produced with the parameters. One of these sampling points is shown in Figure 4.1 as the blue dashed line. Based on the agreement between the predictions of the BSM sample and the data, 95% expected and observed exclusion limits are set. Figure 4.2 shows these limits in the $m_\chi$-$m_A$-plane. Also shown are uncertainties and constraints from the relic density, the perturbation limit, and kinematically allowed decays. More details on each of these can be found in [6]. Values for the masses under the curve are excluded. The limit setting benefits from the exclusive signal regions, which act like a differential

[1] ADD stands for Arkani-Hamed, Dimopoulos, and Dvali. These models predict large extra spatial dimensions which are compactified [112].

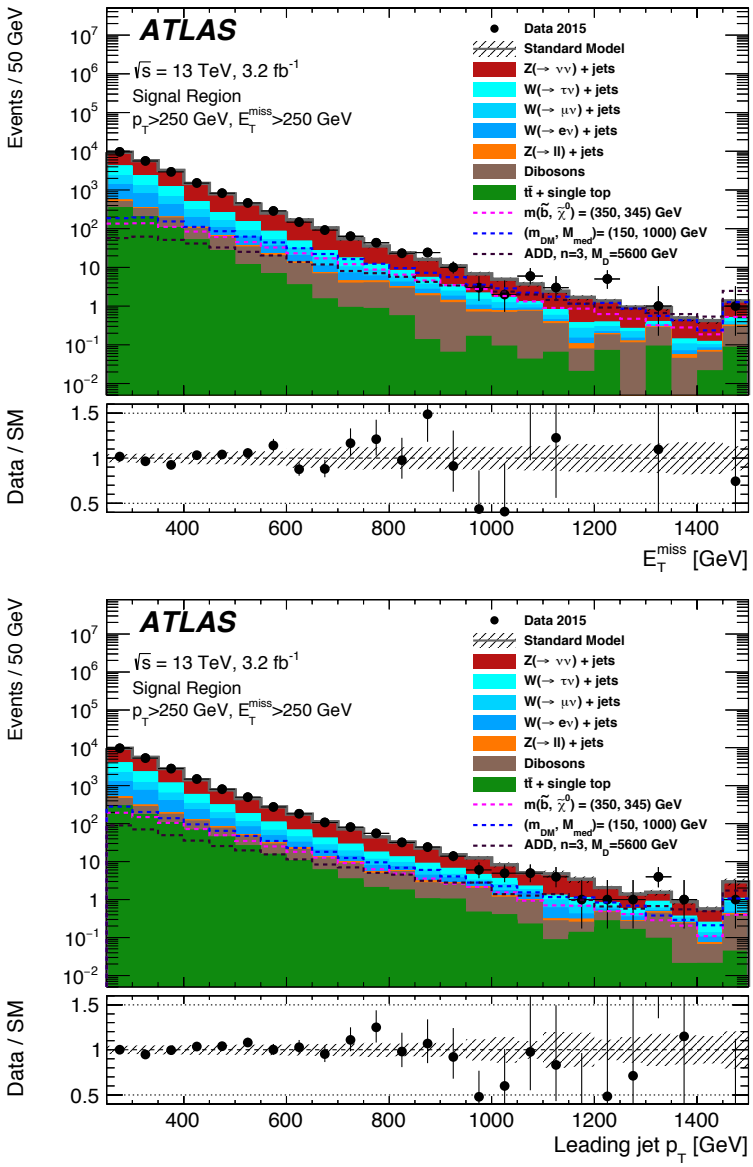


Figure 4.1.: $E_{\mathrm{T}}^{\mathrm{miss}}$ and leading jet $\mathrm{p}_T$ distributions of predicted and observed events in the conventional 2015 ATLAS $p_{\mathrm{T}}^{\mathrm{miss}}$ + jets search. For illustration purposes, a three BSM cases are also shown. Taken from [6], where details on the indicated uncertainties can be found.

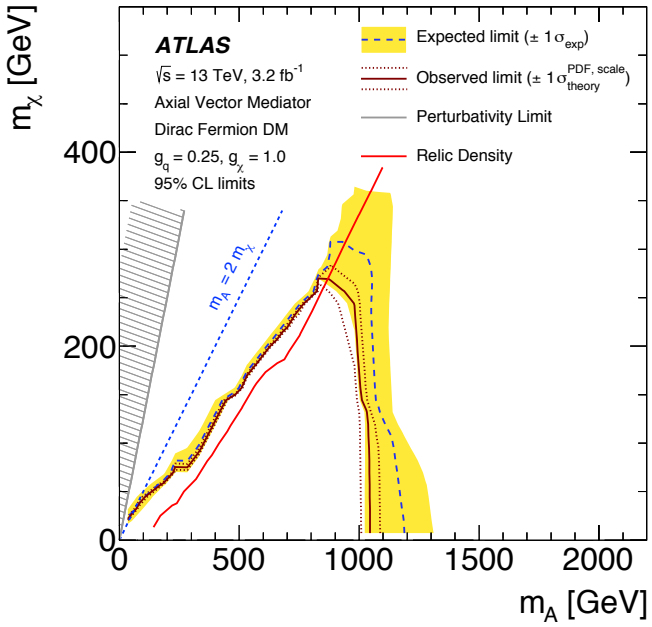


Figure 4.2.: 95% confidence exclusion limits with uncertainties for a simplified WIMP model[6]. The axes are $m_A$ as the mediator mass and $m_\chi$ as the DM particle mass. This plot is similar to Figure 2.8 and shows its $E_{\mathrm{T}}^{\mathrm{miss}}$ + jets contour in more detail.

distribution. This way shape information from $E_{\mathrm{T}}^{\mathrm{miss}}$ is thus used for constraining as well as normalisation.

To summarise, the analysis presented in this section uses an event selection sensitive to various Dark Matter models. The event selection vetoes on electrons and muons in the final state, but not on hadronically decaying $\tau$ leptons. A multitude of SRs are defined. However, these are identical kinematic regions with varying $E_{\mathrm{T}}^{\mathrm{miss}}$ cuts. The data are background subtracted and compared to three different pre-defined and pre-chosen BSM scenarios, and 95% exclusion limits are set. In the constraining process only event yields in the signal regions are used. Some of the SRs are exclusive in $E_{\mathrm{T}}^{\mathrm{miss}}$, which allows to make use of $E_{\mathrm{T}}^{\mathrm{miss}}$ shape information.

## 4.2. Improving $p_{\mathrm{T}}^{\mathrm{miss}}$ + Jets Collider Searches

In the following four techniques and tools are presented that can improve collider searches for Dark Matter. *Unfolding* and performing a *cross-section ratio measurement* are aimed at mitigating shortcomings of the conventional approach to $p_{\mathrm{T}}^{\mathrm{miss}}$ + jets searches. Adding *vector boson fusion topologies* and *boosted decision trees* aims at general performance improvements. The focus is put on the general concepts rather than implementations, which are detailed in Chapters 5 and 6.

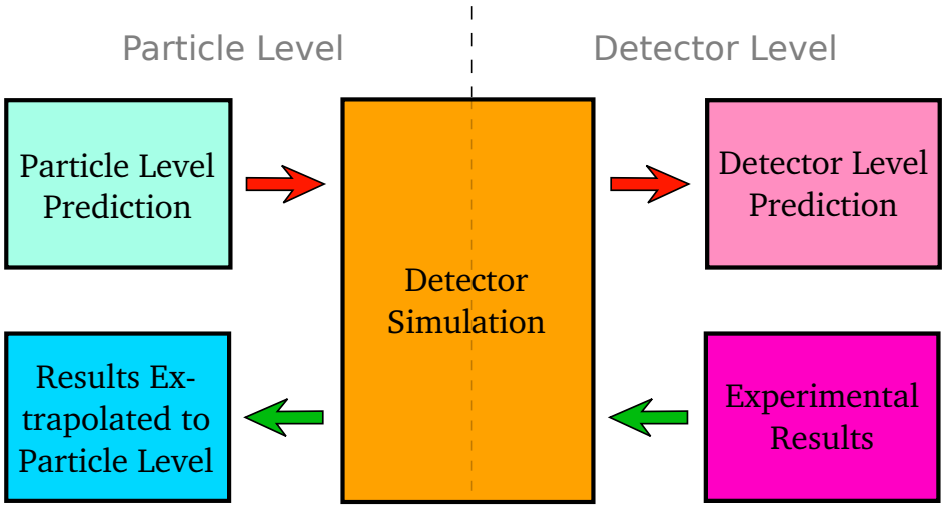


Figure 4.3.: Schematic illustration of simplified analysis workflows. Red arrows indicate the common method for the interpretation of results in the context of searches for BSM physics. Green arrows show the unfolding workflow which allows for comparisons between experimental results and BSM theories on particle level.

### 4.2.1. Unfolding

Unfolding is the process of removing detector effects, such as finite reconstruction and identification efficiencies, from a measurement result. A considerable limitation of many conventional searches for new physics is the inflexibility with respect to reinterpreting results. These searches set limits by measuring an event yield or a distribution and by comparing it to predictions of new physics models, cf. Section 4.1. This is done on *detector level* which means that the measured and predicted quantities suffer from resolution, efficiency and acceptance effects introduced by the detector. The output of a Monte Carlo simulation on *particle level* is taken and detector simulations are applied in order to have predictions of detector level. The detector simulations made by large experimental collaborations are accurate such that comparisons between measured and predicted quantities are valid. However, the detector simulations are not made public and thus unavailable to the theoretical community. As a consequence, the BSM physics interpretations of the results can only be accurately made by the experimental collaborations. The interpretations are limited to models that were popular and available at the time and that were considered when the research was published.

A way to open new physics interpretations of experimental results to theorists and to allow for easy comparisons to other experiments is to *unfolded* the measurement. Results can then be published on particle level. Figure 4.3 illustrates the conventional and the unfolding workflow schematically: most searches follow the red arrows. Particle level prediction are made for various BSM physics scenarios. They are subjected to a detector simulation to yield predictions on detector level, i.e. detector effects are folded onto the predictions. On detector level the predictions can now be compared to experimental results. The unfolding workflow follows the green arrows and is directed the opposite way. The starting point are the experimental results on detector level. Using knowledge of the experimental setup, e.g. with a detector simulation, detector effects are unfolded from the results to yield an extrapolation of the results to particle

level. The results can be directly compared to predictions from BSM physics models on particle level.

There are various approaches to unfolding [84]. The unfolding scheme used in the analysis presented in Chapter 5 is called bin-by-bin unfolding. Here, the bins in measured distributions are corrected for detector effects one-by-one and each correction factor is derived independently of the others. A disadvantage is that bin migration by resolution effects are ignored[1]. However, bin-by-bin unfolding was favoured, because the advantage of this method is its conceptual simplicity that makes it quick to implement and straight-forward to apply. The correction factors are derived from Monte Carlo simulations, because they yield access to both the particle level and detector level information. Bin-by-bin unfolding can be done by performing the analysis on MC on particle level and on detector level and by dividing the results. The ratio yields a correction factor from detector to particle level that can be applied to measured data. The unfolding scheme that is used for the unfolded DM search differs slightly and is explained, together with its advantages, in Section 5.6.

### 4.2.2. Cross-Section Ratio Measurements

Measuring ratios of cross-sections is a tool that is often used in precision measurements of the standard model, because it leads to the at least partial cancellation of correlated uncertainties.

The fiducial cross-section of a hard scattering process at a collider can be expressed as

$$\sigma^{\mathrm{fid}} = \frac{N}{\mathcal{L} \cdot C}\,, \tag{4.1}$$

with $N$ the number of observed and background-subtracted events and $\mathcal{L}$ the integrated luminositiy of the data used for the measurement. $C$ is a correction factor and corrects for finite detection efficiencies typically using Monte Carlo truth level information, cf. Section 4.2.1. In contrast to the total cross-section $\sigma^{\mathrm{tot}}$, the fiducial cross-section is defined for a specific detector volume, called the fiducial volume. To extrapolate to $\sigma^{\mathrm{tot}}$ an additional correction needs to be applied that accounts for kinematic and geometrical acceptance [114].

Equation 4.1 only yields the central value for the cross-section. All quantities involved suffer from uncertainties. In the simplified case of symmetric uncertainties, $\sigma^{\mathrm{fid}}$ has an uncertainty $\Delta\sigma^{\mathrm{fid}}$: $\sigma^{\mathrm{fid}} \pm \Delta\sigma^{\mathrm{fid}}$. Taking a ratio of cross-sections can lead to a smaller relative uncertainty on the ratio than on the individual components. For this uncertainties need to be strongly correlated. If uncorrelated, the relative uncertainty on the ratio is larger than the relative uncertainties of the numerator and denominator. Figure 4.4 shows the general case of two distributions f(A) and f(B) of the variables A and B. The black curves are the central values of the distributions and the dashed coloured curves correspond to their upper and lower $1\sigma$ uncertainties. If the uncertainties between A and B are uncorrelated, the ratio of A and B suffers from the combined uncertainties. This is depicted in (c). If the uncertainties are strongly correlated and the distributions of f(A) and f(B) are sufficiently similar, the uncertainties cancel at least partially leading to overall smaller uncertainties. This is, because in the correlated case the distributions are shifted simultaneously by the source of an uncertainty. Whereas in the uncorrelated case they need to be shifted separately according to their uncertainties.

[1] The detector resolution can lead to different values for a variable such as the $p_T$ of a jet on detector and particle level. It was however shown that this effect is negligible for the present analysis [113]

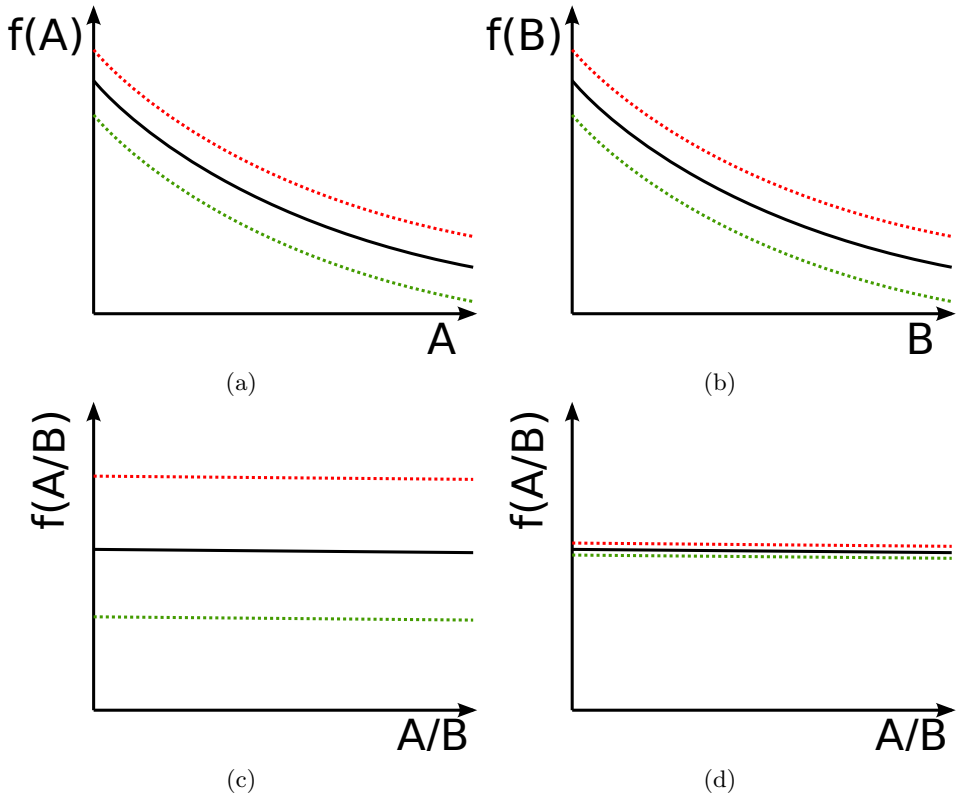


Figure 4.4.: Shown are two distributions (a) A and (b) B with central values in black, upper uncertainties in red and lower uncertainties in green. (c) shows a ratio of the distributions for the case that the uncertainties between A and B are uncorrelated and (d) for correlated uncertainties.

As an example, luminosity uncertainties $\Delta\mathcal{L}$ are fully correlated between two cross-section measurements that use identical datasets and cancel entirely in a ratio of the two.

ATLAS has published numerous standard model precision measurements that make use of cross-section ratios, a selection of which is given in [114–116]. In *Ratio of W and Z boson production cross-sections in association with jets* [115] the inclusive cross-sections for massive vector-bosons decaying to electrons and muons in association with jets were measured. At energies beyond the W and Z masses the kinematics of numerators (W + jets) and denominators (Z + jets) become more alike. The systematic uncertainties on the measurement can be split into various contributions, for instance jet uncertainties, determination of correction factors, background estimates from MC or using data-driven methods, and several others. The impact of the uncertainties was evaluated by simultaneously applying the systematic variations on both the numerators and denominators and repeating the entire analysis chain. It was found that in particular the jet uncertainties, i.e. jet energy resolution and jet energy scale, cf. Section 3.4.1, are strongly correlated between numerator and denominator and hence cancel in the ratio to a large extent. The same is true to various degrees for other sources of systematic uncertainties.

Another ATLAS measurement further illustrates the strength of this approach, *Measurement of $W^{\pm}$ and Z-boson production cross-sections in pp collisions at $\sqrt{s}$ = 13 TeV with the ATLAS detector* [114]. Here, fiducial and total cross-sections were measured and several ratios were taken. The analysis team quotes measured total cross-sections for W-production of $\sigma^{tot}_{W^+} = 11.83 \pm 0.02$

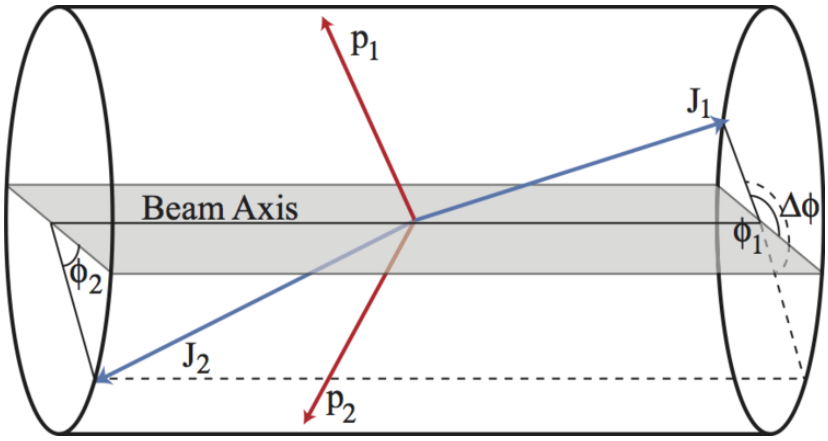


Figure 4.5.: An idealised VBF event in a detector volume. Because of the moderate momentum transfer the jets, shown in blue, are forward. Decay products of a mediator are shown in red. Taken from [120].

(stat) ± 0.32 (sys) ± 0.25 (lumi) and $\sigma^{tot}_{W^-} = 8.79 \pm 0.02$ (stat) ± 0.24 (sys) ± 0.18 (lumi). By measuring a ratio of cross-sections significant reductions in the systematic and luminosity uncertainties are found: $\sigma^{fid}_{W^+}/\sigma^{fid}_{W^-} = 1.295 \pm 0.003$ (stat) ± 0.010 (sys). Similar observations are made for the fiducial cross-section ratio measurement of $W^{\pm}$+jets/Z+jets.

The same method can be applied in searches for BSM physics, such as DM. It promises the reduction of uncertainties and hence more accurate results leading to better limits[1]. Additionally, this method supports unfolding, because the forming of a ratio also leads to the at least partial cancellation of detector-induced effects if numerator and denominator are sufficiently similar. As a consequence the unfolding correction factors do not need to account for as many effects as when not taking a ratio. For the analysis presented in this thesis, this explained in more detail in Section 5.6.

### 4.2.3. Vector Boson Fusion Topologies and Differential Distributions

Measurement channels involving vector boson fusion (VBF) or vector boson scattering (VBS) probe the electro-weak sector. They are of interest for investigations of the standard model [117, 118], Higgs physics [24, 25], and also bear potential for searches for Dark Matter [8].

In a VBF event two quarks from the colliding protons radiate virtual electro-weak gauge bosons ($W^{\pm}$, Z), which fuse, cf. for instance Figure 2.5. The two leading jets in a VBF event are typically forward at low scattering angles with moderate transverse momentum[2] as this arrangement has a large scattering amplitude [119]. Figure 4.5 illustrates a VBF event in which a boson is produced that subsequently decays into lighter particles, shown in red. The two forward jets are shown in blue.

The two leading jets in VBF events are favoured to be in opposite hemispheres of the detector. This provides a way to select VBF events by either requiring a significant angular separation (in $\eta$) between the two jets or a large invariant mass defined as

[1] At least in regions of the phase space where the denominator does not lead to statistical limitations.
[2] $\mathcal{O}(M_W)$

$$M_{jj} = 2 \cdot p_T^{\text{jet 1}} p_T^{\text{jet 2}} (\cosh(\eta^{\text{jet 1}} - \eta^{\text{jet 2}}) - \cos(\phi^{\text{jet 1}} - \phi^{\text{jet 2}})), \tag{4.2}$$

where the transverse momenta and geometrical coordinates correspond to those of the leading and subleading jets. An additional signature of VBF events comes from the characteristic color structure shown by the lack of a color connection between the two leading jets in the final state, cf. Figure 2.4. The color structure leads to a suppression of additional hadronic radiation in the rapidity gap between the two leading jets [121]. This contrasts the radiation patterns of production modes in which connecting color lines are present. As an example, using these selection criteria allowed for the measurement of the electro-weak production cross-section via VBF of $\mathrm{Z}(\rightarrow l^+l^-)$ + jets using the ATLAS experiment and Run-1 data [118].

As discussed earlier, the conventional $p_{\mathrm{T}}^{\mathrm{miss}}$ + jets search by ATLAS [6] examines one generic kinematic region that is sensitive to various models of DM. However, by adding a kinematic region especially sensitive to DM in VBF topologies, the sensitivity can be improved. It can be further extended by measuring various complementary differential distributions instead of event yields in different but similar signal regions. This provides shape information and different well-chosen distributions are sensitive to different attributes of DM candidates, such as mass or spin. Correlations between the two kinematic regions, generic and VBF-enhanced, need to be considered. These aspects will be discussed in Section 5.

Exploring VBF topologies also bears potential for improved triggering with respect to the conventional $p_{\mathrm{T}}^{\mathrm{miss}}$ + jets search approach. Here, a $p_{\mathrm{T}}^{\mathrm{miss}}$ trigger is usually used. A high threshold needs to be chosen to be able to use an unprescaled trigger[1], because of the bunch interaction rate and pile-up. The high threshold could be reduced by requiring additional VBF characteristics in an event, such as forward jets. This leads to a stronger sensitivity towards scenarios with low DM mass. However, for the work presented in this thesis such a VBF trigger was not implemented into the ATLAS trigger chain.

### 4.2.4. Boosted Decision Trees

The strength of multivariate techniques such as Boosted Decision Trees (BDTs) or Neural Networks is the combination of several weak discriminants into one powerful discriminant. ATLAS applies them in numerous use cases, when pattern recognition is important, such as for the $\tau$ lepton identification, cf. Section 3.4.4, identification ("tagging") of b-quarks [122], or as a part of the signal region definition [123].

The usecase for BDTs in this thesis, cf. Section 6.3, is the discrimination between one signal process and one background process. In the following the BDT algorithm for this kind of separation is briefly introduced, first by discussing decision trees and then boosting. A detailed discussion of BDTs can for instance be found in [84].

[1] Unprescaled triggers are experimentally favoured, because prescaled triggers lead to additional uncertainties in the turn-on region, where statistical uncertainties are large.

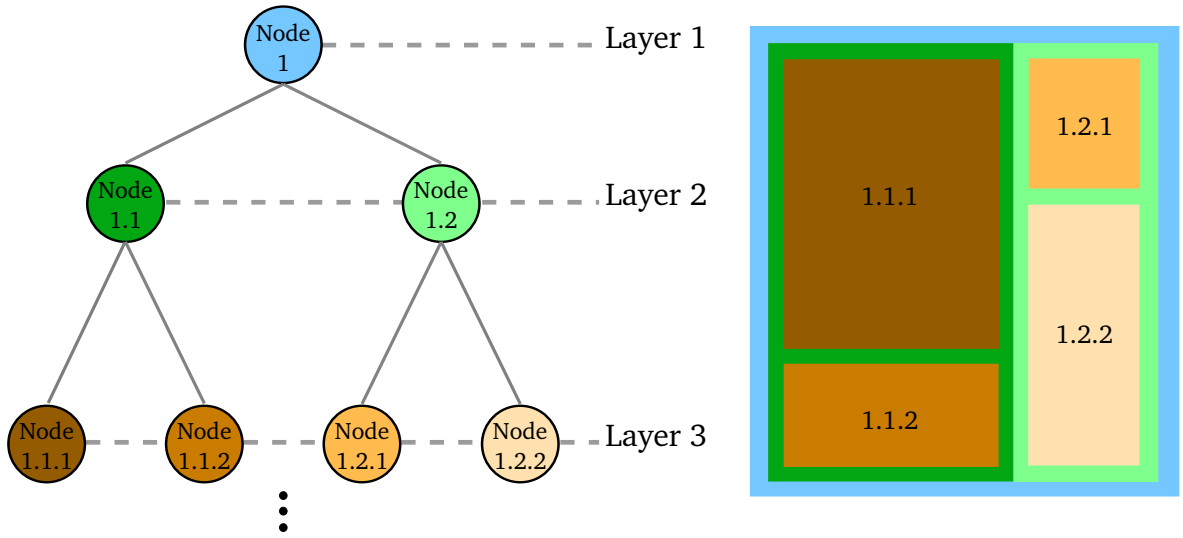


Figure 4.6.: Schematic illustration of a decision tree (left) and the rectangular regions it can create using two discriminants (right). The colours on the right hand side correspond to the data content of the nodes on the left hand side.

### Decision Trees

The dataset[1] on which the decision tree is constructed is separated into two parts. The optimisation algorithm is trained to the so-called *training sample* and the resulting BDT is then applied to the *test sample* to evaluate its performance. Usually the two samples are of equal size.

The algorithm for the construction of a decision tree starts by building a binary tree. Here, the training sample is grouped into rectangular regions according to previously defined discrimination variables. This is illustrated in Figure 4.6. The left hand side shows the first three layers of an example tree. In *Node 1* the full training sample is considered and a cut is placed on a discriminating variable. In the second layer, *Node 1.1* and *Node 1.2* contain complementary parts of the training sample defined by the cut in the first layer. In the nodes additional cuts are applied and the training dataset is split again leading to four complementary samples in the third layer. The right hand side depicts the rectangular regions that are created by the cuts in the three layers. The full sample (blue) encompasses the sub-samples in the second layer (shades of green) which encompass the sub-samples in the third layer (shades of brown). The example only contains two inputs in the form of discriminating variables represented by the two dimensions on the right hand side.

The cut in the first node is chosen to minimise the sum of gini-indexes $\sum g_i$ of the daughter nodes. The gini-index is defined as

$$g = P(1 - P)\,, \tag{4.3}$$

where P is the signal purity of the data in a given node,

[1] In the case of high energy physics it is typically based on Monte Carlo simulation.

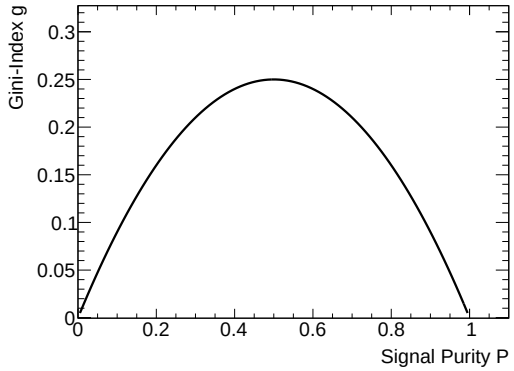


Figure 4.7.: The relationship between gini index $g$ and signal purity P.

$$P = \frac{N(\text{singal})}{N(\text{signal}) + N(\text{background})}\,, \tag{4.4}$$

with $N$ the event count of a given event category (signal or background) in the considered node. The gini index is plotted in Figure 4.7. It can be seen that the it is minimal for nodes that are pure in either signal or background and is large for mixed nodes.

Cuts on the other nodes are chosen to maximise the *separation gain*

$$G_S = N_{\text{node}} \cdot g_{\text{node}} - N_{\text{daughter 1}} \cdot g_{\text{daughter 1}} - N_{\text{daughter 2}} \cdot g_{\text{daughter 2}}\,, \tag{4.5}$$

where $N$ and $g$ refer to the numbers of events (or sum of weights in the case of MC) and the gini index of either the considered node or of one of the two daughter nodes.

This is repeated until an exit criterion is met. Typically two criteria are chosen: either a certain tree depth $\text{Depth}_{\text{tree}}$ is reached, i.e. a maximum number of layers is defined, or the event yield in a node falls below a pre-defined threshold $\text{N}_{\text{node}}$, for instance 5% of the total training sample dataset. Nodes in the last layer of the final tree are called leaves. Leaves with $\text{P} > 0.5$ are called signal leaves, the others background leaves. An event $x$ that ends up on a signal (background) leaf gets assigned the tree-output $C(x) = 1(-1)$. So far conventional decision trees have been described. BDTs are defined by an additional algorithm called *boosting*.

### Boosting

Although a single decision tree already combines multiple cuts on discriminants, they are rarely used on their owns in high energy physics. They are vulnerable to statistical fluctuations and often provide worse discrimination power than other techniques [84]. To enhance separation power and to yield more stability, additional trees are constructed and optimised on a reweighed training sample. The process of constructing more trees is called *growing a forest* and reweighing is performed according to a *boosting* algorithm.

Above, two important parameters of BDTs have been introduced: the maximal depth of individual trees and the minimum node size in terms of event yields. When growing a forest, a

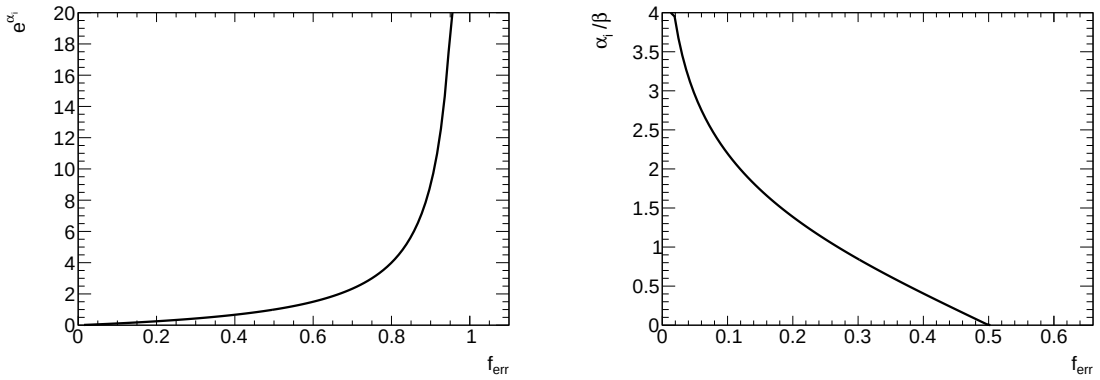


Figure 4.8.: The weight and the boosting exponent $\alpha_i$ in dependence of $f_{\mathrm{err}}$.

third parameter must be considered, the number of decision trees $\mathrm{N_{trees}}$ that constitute the forest. The algorithm for the construction of the consecutive trees, that are formed one-by-one, follows the same prescription as above. However, the training sample is reweighed each time according to the results of the previously constructed tree. This is done by reweighing misclassified events taking into account the error fraction of the previous tree

$$f_{\mathrm{err}} = \frac{N(\mathrm{misclassified})}{N(\mathrm{total})}\,, \tag{4.6}$$

where the $N$ corresponds to the weighted numbers of misclassified and total events. The sample is then renormalised to keep the sum of event weights constant among samples considered in different trees. The reweighing is called boosting. The boosting weight $w$ for a given misclassified event and for tree $i$ is defined as

$$w_i = w_{i-1} \cdot e^{-\alpha_i} \tag{4.7}$$

with

$$\alpha_i = \beta \cdot ln\frac{1 - f_{\mathrm{err}}}{f_{\mathrm{err}}}\,. \tag{4.8}$$

Here, $w_{i-1}$ is the weight of the event in the previously constructed tree. $\beta$ is a free parameter that is chosen beforehand. The weight $w_i$ and the boosting exponent $\alpha_i$ are shown in Figure 4.8 in dependence of $f_{\mathrm{err}}$.

The total BDT score for an event $x$ is then given by $y(x) = \sum_{i=1}^{N_{\mathrm{tree}}} \alpha_i \cdot C^i(\mathrm{x})$. In that formula $C^i(\mathrm{x})$ is the score of event $x$ from tree $i$. This output is usually a much stronger discriminant than the individual tree output and shows more resilience against statistical fluctuations in the training sample.

The studies involving BDTs in Section 6.3 use the ROOT TMVA package as the software framework [124].

# 5. The Unfolded Cross-Section Ratio Measurement

In Chapter 2 the cosmological evidence for Dark Matter was presented. It was also introduced why it is reasonable to assume that it is of particle nature and it was shown that the SM does not provide a viable candidate. Furthermore, the previous conventional $p_{\mathrm{T}}^{\mathrm{miss}}$ + jets collider search for DM and its shortcomings were summarised in Section 4.1 and it was discussed how to improve this class of searches.

This chapter presents a novel analysis that implements most of the discussed improvements. This includes a cross-section ratio measurement, unfolding and a dedicated kinematic region sensitive to processes involving vector boson fusion. These efforts have lead to the publication of the paper *"Measurement of detector-corrected observables sensitive to the anomalous production of events with jets and large missing transverse momentum in pp collisions at $\sqrt{s}$=13 TeV using the ATLAS detector"* [1]. It is a proof-of-concept analysis that establishes this novel way of using an unfolded measurement as a search for DM. It was performed on the 2015 dataset collected by the ATLAS experiment corresponding to 3.2 fb$^{-1}$ of integrated luminosity[1].

## 5.1. Analysis Strategy

This analysis features three major improvements with respect to conventional $p_{\mathrm{T}}^{\mathrm{miss}}$ + jets searches for DM:

- Measurement of a ratio of cross-sections in terms of differential distributions
- Corrections of the results for detector effects ("unfolding")
- Implementation of an additional kinematic region sensitive to vector boson fusion and setting limits on VBF DM models

Further improvements include various adaptations to the event and object selections allowing to investigate a larger kinematic region and a veto[2] on hadronically decaying $\tau$ leptons.

[1] Much of this chapter follows the discussions in the publication [1] and its ATLAS internal note [113], both of which the author has co-written. The entire analysis is presented and a focus is put on the author's contributions.

[2] *Vetoing* refers to the rejection of events that show a special characteristic such as the presence of a reconstructed charged lepton.

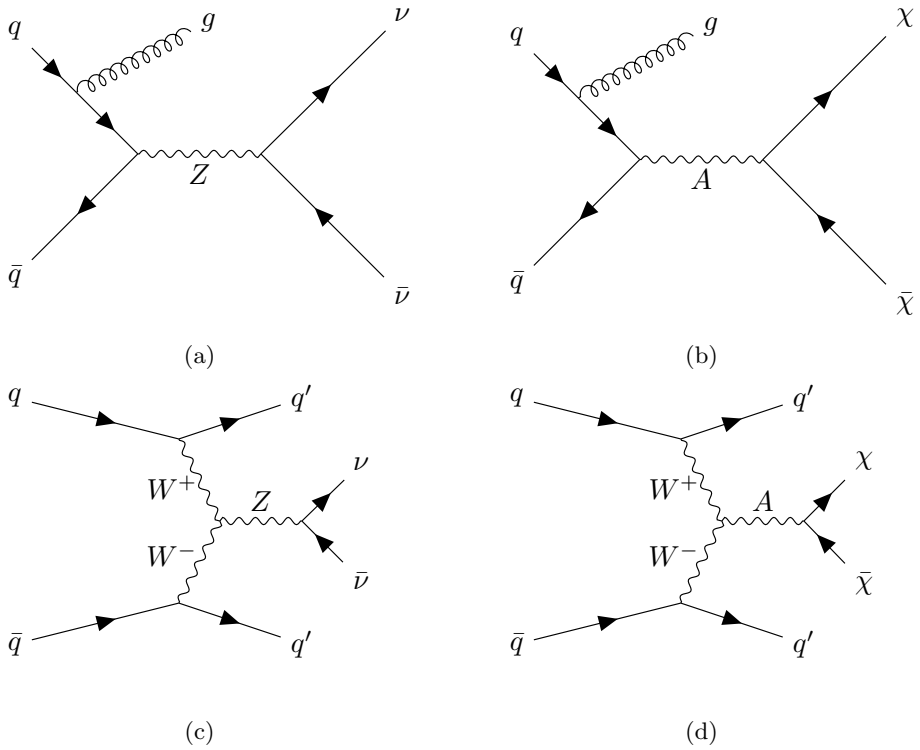


Figure 5.1.: Leading order Feynman diagrams of processes targeted by the numerator of this analysis. Shown is the SM process Z→ $\nu\nu$ + jet(s) produced (a) in association with a jet from initial state radiation and (c) via VBF. Also shown is the pair production of WIMP DM via a new mediator $A$ (b) with a jet from initial state radiation and (d) via VBF.

The cross-section ratio is defined as:

$$R_{\text{miss}} = \frac{\sigma^{\text{fid}}(p_{\text{T}}^{\text{miss}} + jets)}{\sigma^{\text{fid}}(Z \to l^{+}l^{-} + jets)} \,. \tag{5.1}$$

$l^{+}l^{-}$ in the denominator corresponds to a pair of same flavour, opposite sign charged leptons: $e^{+}e^{-}$ and $\mu^{+}\mu^{-}$. $\tau$ leptons are not selected for the denominator because of their challenging experimental signature. In the absence of BSM physics, the numerator is almost exclusively the SM cross-section $\sigma^{\text{fid}}$ ($\text{Z} \to \nu\nu$ + jets). Figure 5.1 (a) shows a leading order Feynman diagram for this process. In this case the kinematic properties of the numerator and denominator are very similar. As motivated in Section 4.2.2, systematic uncertainties and detector-induced effects cancel at least partially. This leads to smaller uncertainties and smaller corrections necessary by the subsequent unfolding procedure. Ignoring the fiducial volumes, experimental acceptances and a potential BSM signal, Equation 5.1 measures the ratio of branching fractions of the Z boson into neutrinos and a pair of charged leptons of opposite sign and a common specific flavour. The SM value is approximately six, because all three lepton flavours are considered in the numerator and the decay rate of the Z boson into neutrinos is about a factor of two larger than into charged leptons. This measurement is sensitive to the anomalous production of $p_{\text{T}}^{\text{miss}}$ in association with jets, for instance from DM. Figure 5.1 (b) shows an example for the production of DM in association with a jet from initial state radiation.

Providing unfolded distributions is one of the key features of this analysis. It alleviates the difficulty of reinterpreting the results after publication in the light of new developments and DM models. Here, the unfolding is performed via bin-by-bin unfolding, cf. sections 4.2.1 and 5.6. The final distributions and correlations among them are made public[1] and are easily usable for reinterpretation.

This analysis introduces an additional kinematic region dedicated to VBF. VBF topologies have not been considered in generic searches for DM in the past leading to uncharted territory in terms of set limits. Section 2.3 discussed a few models for which VBF topologies can lead to unprecedented sensitivity. The VBF kinematic region contains a different set of cuts with respect to the *inclusive* >= 1 jet kinematic region. The latter resembles the inclusive signal region of the conventional $p_{\text{T}}^{\text{miss}}$ + jets search but has looser cuts. The kinematic differences were briefly discussed in Section 4.2.3. Figure 5.1 shows leading order Feynman digrams for the VBF production of (c) a Z boson decaying into two neutrinos and (d) a DM mediator decaying into DM particles. Consequences for the event selection are discussed in the next section.

The four measured differential distributions are $p_{\text{T}}^{\text{miss}}$, $\text{m}_{jj}$ and $\Delta\phi_{jj}$. $p_{\text{T}}^{\text{miss}}$ is measured in both kinematic regions[2] while the others require two jets and are therefore only measured in the VBF region. $p_{\text{T}}^{\text{miss}}$ is defined in Section 3.4.5, $\text{m}_{jj}$ is the invariant mass of the two leading jets defined in Equation 4.2 and $\Delta\phi_{jj}$ is the difference in azimuthal angle between the two leading jets. These variables were chosen to yield good sensitivity towards various DM models. The differential distribution of $p_{\text{T}}^{\text{miss}}$ is interesting, because in many DM models large mediator masses and high interaction energy scales are predicted. These would lead to an overproduction of events with

[1] https://www.hepdata.net/record/78366

[2] For $p_{\text{T}}^{\text{miss}}$ the binning in the histograms is slightly different in the two kinematic regions. Since the overall event count is lower in the VBF region, the highest two bins are merged to allow for higher statistical precision. Otherwise the binning is motivated by the bin-by-bin unfolding applied eventually. It is chosen to be sufficiently coarse such that bin migration effects are negligible.

large values of $p_{\mathrm{T}}^{\mathrm{miss}}$. Events produced via vector boson fusion tend to have forward jets in opposite hemispheres and thus larger values of $\mathrm{m}_{jj}$. This makes the differential distribution of the invariant mass an interesting object of study for VBF models of DM, such as Higgs portal models as introduced in Section 2.3. In the case of seeing a signal, the $\Delta\phi_{jj}$ would be an interesting discriminant for various kinds of DM, since the shape of this distribution varies with different models. In the final distributions of his analysis, cf. Figure 5.21, it can be seen that the distributions provide complementary information with respect to different DM scenarios.

In the following sections the two fiducial cross-section measurements of Equation 5.1 will often be discussed separately and are simply referred to as the numerator and the denominator.

## 5.2. Object and Event Selection

In the following the event and object selections for the two kinematic regions are discussed at particle and detector level. Selections on both levels are necessary because of the bin-by-bin unfolding that is performed.

### Particle Level Event Selection

Final state particles are defined as all particles in an event that have a mean life-time longer than $10\,\mathrm{mm\,c^{-1}}$ with c the speed of light. A particle is referred to as *invisible*, if it does not interact via the strong or electromagnetic force. Hence it can escape the detector without leaving a trace. Otherwise it is referred to as *visible*. The selection cuts are summarised in Table 5.1 and detailed below.

Leptons are defined as dressed leptons. This means that four-momenta of radiated photons in a cone of $\Delta\mathrm{R} = 0.1$ around a lepton are absorbed into the four-momentum of the lepton. This technique accounts for QED final state radiation [125]. For the denominator the $l^+l^-$ ($= e^+e^-$, $\mu^+\mu^-$) are required to be a pair of prompt leptons, where prompt indicates that they do not originate from the decay of $\tau$ leptons or hadrons.

For $p_{\mathrm{T}}^{\mathrm{miss}}$ all objects in the event up to the edge of the calorimeter, which covers $|\eta| < 4.9$, are considered. $p_{\mathrm{T}}^{\mathrm{miss}}$ is a central variable for this analysis due to its sensitivity towards invisible particles. To make numerator and denominator as similar as possible, this variable is slightly changed for the denominator. The selected $l^+l^-$ pair is taken out of the negative vector sum in the calculation of $p_{\mathrm{T}}^{\mathrm{miss}}$, hence marking them *invisible*.

As described in Section 3.4.1, jets are built using the anti-$\mathrm{k}_t$ algorithm and with radius parameter of $\mathrm{R} = 0.4$. Muons and invisible particles are excluded in the jet definition due to their lack of calorimeter interaction. On truth level the clustering algorithm runs on (truth-)particles, which are decay products of the original final state partons.

The measured ratio $\mathrm{R}_{\mathrm{miss}}$ of Equation 5.1 is defined in terms of a *fiducial cross section*. The fiducial volume is motivated by the trigger, the acceptances of the ATLAS detector, background suppression, and the enhancement of VBF contributions in the case of the specialised kinematic region, which are detailed below. A summary of all cuts and selections can be found in Table 5.1.

| **Numerator & denominator** | $\geq 1$ jet | VBF |
|---|---|---|
| $p_{\mathrm{T}}^{\mathrm{miss}}$ | $> 200\,\mathrm{GeV}$ | |
| Lepton veto | No $e, \mu$ with $\mathrm{p}_T > 7\,\mathrm{GeV}$, $\lvert\eta\rvert < 2.5$ | |
| Jet $\lvert\eta\rvert$ | $< 4.4$ | |
| Jet $\mathrm{p}_T$ | $> 25\,\mathrm{GeV}$ | |
| $\Delta\phi$ ($\mathbf{p}_{\mathrm{T}}^{\mathrm{miss}}$, jet) | $> 0.4$, for the four leading jets with $\mathrm{p}_T > 30\,\mathrm{GeV}$ | |
| Leading jet $\mathrm{p}_T$ | $> 120\,\mathrm{GeV}$ | $> 80\,\mathrm{GeV}$ |
| Subleading jet $\mathrm{p}_T$ | - | $> 50\,\mathrm{GeV}$ |
| Leading jet $\lvert\eta\rvert$ | $< 2.4$ | - |
| $\mathrm{M}_{jj}$ | - | $> 200\,\mathrm{GeV}$ |
| Central jet veto | - | No jets with $\mathrm{p}_T > 25\,\mathrm{GeV}$ |
| **Denominator** | $\geq 1$ jet & VBF | |
| Leading lepton $\mathrm{p}_T$ | $> 80\,\mathrm{GeV}$ | |
| Subleading lepton $\mathrm{p}_T$ | $> 7\,\mathrm{GeV}$ | |
| Lepton $\lvert\eta\rvert$ | $< 2.5$ | |
| $\mathrm{M}_{ll}$ | 66 - 116 GeV | |
| $\Delta$R (jet, lepton) | $> 0.5$, otherwise jet is removed | |

Table 5.1.: Summary of the particle level event selection cuts for numerator and denominator and the two kinematic regions [1]. The detector level selection only deviates slightly and the differences are explained in Section 5.2.

Some of the cuts target the suppression of certain backgrounds. The veto on charged leptons, or additional charged leptons in the case of the denominator, leads to a considerable reduction of events containing leptonically decaying W-bosons. However, on particle level it is only applied to electrons and muons. Defining hadronically decaying $\tau$ leptons in terms of stable final state particles is challenging. The veto on events in which $\mathbf{p}_{\mathrm{T}}^{\mathrm{miss}}$ and the four-vectors of any of the first four leading jets are close to one-another in the transverse plane, i.e. $\Delta\phi$ ($\mathbf{p}_{\mathrm{T}}^{\mathrm{miss}}$, jet), reduces the contribution from multijet events by orders of magnitude. Details on the multijet background and its reduction are discussed in Section 5.3. For the denominator, the $m_{ll}$ requirement makes sure the origin of the lepton system is consistent with the decay of a Z-boson and reduces contributions from diagrams with a $\gamma$ mediator. Lastly, the asymmetric $\mathrm{p}_T$ cut on the pair of charged leptons was chosen, because it is consistent with a large Z-boson $\mathrm{p}_T$, which translates to large $p_{\mathrm{T}}^{\mathrm{miss}}$. Simultaneously it minimises $t\bar{t}$ contributions, in which leptons typically have lower values of $p_{\mathrm{T}}$.

The VBF enhancing cuts follow the line of arguments established in Chapter 4.2.3. Events with additional jets in the rapidity gap between the first two leading jets are rejected. The $\mathrm{m}_{jj}$ requirement favours the leading jets to be forward and in opposite hemispheres. Additionally, it reduces background events from di-boson production where one of the bosons decays hadronically, because here $\mathrm{m}_{jj}$ is not expected to be large.

### Detector Level Event Selection

Events for the numerator are selected using a trigger that requires a $p_{\mathrm{T}}^{\mathrm{miss}}$ of 70 GeV as calculated by the HLT, the second stage of the ATLAS trigger, cf. Section 3.3.4. Since muons are invisible to this trigger, it can also be used for the denominator when an opposite-sign pair of muons is

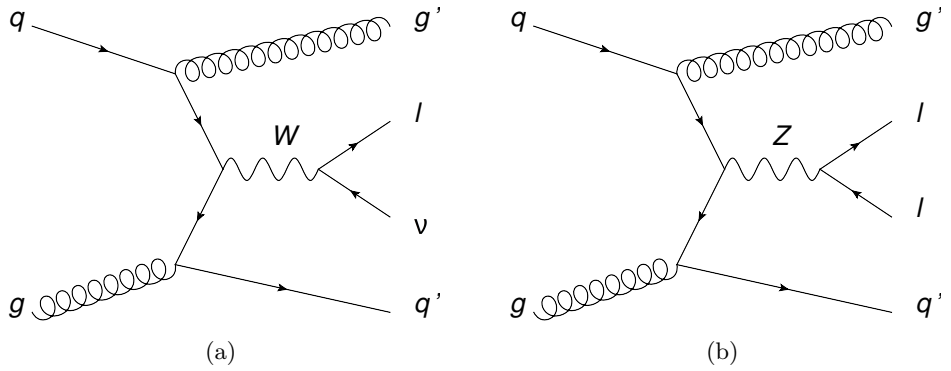


Figure 5.2.: Leading order Feynman diagrams of important processes: (a) $Z \to ll$ + jets and (b) $W \to l\nu$ + jets.

selected. When selecting electrons in the denominator, a combination of triggers requiring at least one electron is used.

Events have to fulfil a set of quality requirements. They must contain at least one reconstructed primary vertex with at least two associated tracks with transverse momenta of 400 MeV each[1]. Events in which parts of the detector were not running properly are excluded. In addition, events containing bad jets, i.e. jets not coming from proton-proton collisions (cf. Section 3.4.1), with $p_T > 20$ GeV are rejected.

The event selection cuts follow mostly the ones from particle level with a few exceptions and additions. Electrons are required to be outside of $1.37 < |\eta| < 1.52$ and $2.47 < |\eta| < 2.50$ for both the selection and vetoes. The first region corresponds to the barrel-endcap transition region, which is not fully instrumented. The second region is excluded because electrons are only identified within $|\eta| < 2.47$ owed to the reconstruction algorithm. They must fulfil *Loose* selection criteria as introduced in Section 3.4. Additionally, isolation criteria are applied for all electrons and muons used for the lepton veto following the *LooseTrackOnly* working point. Events containing identified hadronically decaying $\tau$ leptons are rejected if the visible decay remnants have $p_T > 20$ GeV. Leptonically decaying $\tau$s are vetoed on by the other two lepton vetoes if the kinematic and acceptance requirements are met. More information on the $\tau$ lepton veto can be found in Section 5.3. There is no dedicated selection for photons and they are treated as jets.

## 5.3. Backgrounds and their Reduction for the Numerator

### Background Overview

The largest background contribution to the numerator in both kinematic regions comes from events with genuine $p_{\mathrm{T}}^{\mathrm{miss}}$, one promt lepton and jets. In order to pass the event selection the lepton is either not properly reconstructed and identified or outside of the fiducial volume defined above[2]. This encompasses W + jets processes, events containing top quarks, i.e. single top and $t\bar{t}$ events, and some cases of diboson production. The first mode is dominant and depicted

[1] This corresponds to the minimum $p_T$ of reconstructed tracks in ATLAS [126].

[2] The former case is commonly referred to as *out-of-efficiency* and the latter one as *out-of-acceptance* background.

in Figure 5.2 (a). Here, events containing $\tau$ leptons pose the largest background component, because the average identification efficiency for hadronically decaying $\tau$ leptons is worse than for electrons and muons[1] while the fiducial volume for reconstruction is similar. All of the above can be summarised as events with a leptonically decaying W boson produced in association with jets. The estimation of this background is covered in Section 5.4.1 and is of about the same size as the standard model signal $Z \to \nu\bar{\nu}$.

Events containing Z-bosons that decay into two charged leptons, cf. Figure 5.2 (b), are another background for which lepton identification inefficiencies and acceptances play a major role. This background contributes significantly fewer events to the signal regions than the backgrounds described above. This is caused by the absence of prompt neutrinos, thus large quantities of $p_{\mathrm{T}}^{\mathrm{miss}}$, and due to the fact that two instead of only one charged lepton needs to be missed or misidentified for such an event to pass the selection cuts. These $Z \to l^+l^-$ events amounts to about 0.5% of the SM signal.

A final important background are multijet events. Multijet events are usually not associated with large amounts of missing transverse momenta due to the absence of energetic neutrinos. However, if the transverse momenta of jets in these events are mismeasured by significant margins, the $p_T$ sum over all objects in the event is no longer balanced and *fake* $p_{\mathrm{T}}^{\mathrm{miss}}$ arises. These events can mimic signal events and survive the cuts of the kinematic regions. A detailed discussion of the reduction of multijet events takes place in Section 5.3 and the background estimation technique is described in Section 5.4.2. The multijet background amounts to about 2% of the total background in the first $p_{\mathrm{T}}^{\mathrm{miss}}$ bin and rapidly decreases for larger values of $p_{\mathrm{T}}^{\mathrm{miss}}$.

The Monte Carlo prediction for the composition of the signal regions in terms of the SM signal and the background sources explained above in the four measured distributions is shown in Figure 5.3. The item called *Top* contains contributions from $t\bar{t}$ and single top processes. The multijet background is not shown due to large statistical uncertainties of the MC sample.

#### Reduction of events with hadronically decaying $\tau$ leptons

$\tau$ leptons decay hadronically in about 65% of the cases. 72% of the hadronic decays are into one charged pion and 22% into three charged pions. In order to optimally reject these events while keeping signal events, several $\tau$ identification strategies are compared. Apart from using the $\tau$ identification tool provided by ATLAS with different working points for the boosted decision tree (BDT) that discriminates against hadronic jets initiated by quarks or gluons, it is also tested to reject events based purely on the number of tracks of $\tau$ candidates. The BDT re-evaluates $\tau$ candidates and can identify whether the candidate is in fact a hadronic jet. The identification algorithm of the ATLAS tool is briefly described in Section 3.4.4.

Table 5.2 presents survival fractions of the hadronically decaying $\tau$ lepton veto when different methods for $\tau$ identification are used. The investigated MC samples are $Z \to \nu\nu$, $W \to \tau\nu$, and $Z \to \tau\tau$. All $\tau$ lepton decay modes are included in the samples. The $\tau$ identification methods are from top to bottom:

[1] The average identification efficiencies using the *Loose* criteria are above 90% for electrons and muons and only 66% for $\tau$ leptons, cf. Section 3.4.

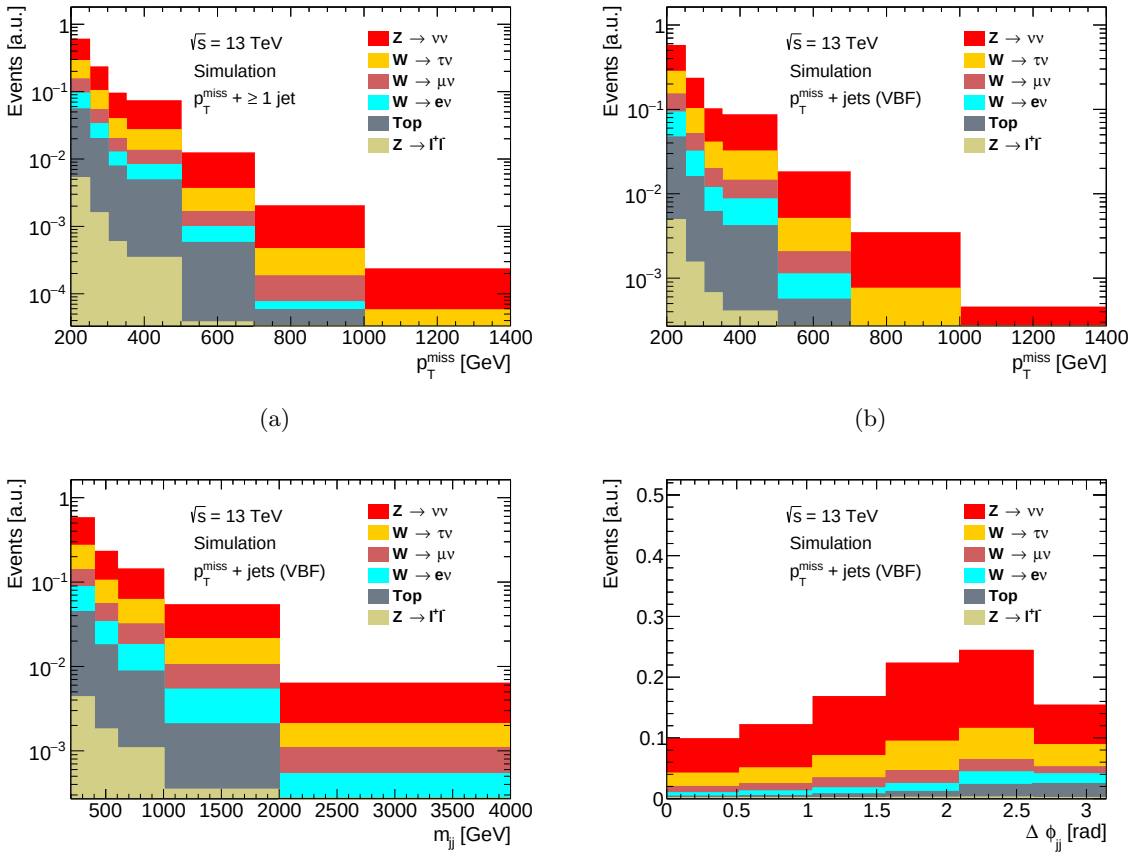


Figure 5.3.: Monte Carlo predictions for the compositions of the signal regions in terms of the four measured distributions in the two kinematic regions are shown. (a) and (b) are the $p_{\mathrm{T}}^{\mathrm{miss}}$ distributions in the $\geq 1$ jet and VBF kinematic regions, (c) is $\mathrm{m}_{jj}$ in the VBF region, and (d) $\Delta\phi_{jj}$ in the VBF region. MC estimates for the multijet background are not shown due to the low statistics of the simulated samples, which come with large statistical uncertainties. The samples are shown stacked and combined scaled to unity.

- None and thus not applying a veto.
- All reconstructed $\tau$ candidates with one or three tracks are considered identified $\tau$ leptons.
- The ATLAS tool is used and the BDT that discriminates between hadronically $\tau$ leptons and hadronic jets is disabled. In this case no $\tau$ candidates are removed from the pool although they are in fact hadronic jets.
- The ATLAS tool is used and the BDT is set to the *Loose* working point.
- The ATLAS tool is used and the BDT is set to the *Medium* working point, which is the default configuration.
- The ATLAS tool is used and the BDT is set to the *Tight* working point.

The tighter the working point, the less likely it is for a hadronic jet to be misidentified as a $\tau$ jet. Hence a tighter working points corresponds to a higher survival fraction of events, becuase events contain fewer reconstructed and identified $\tau$ leptons. If the jet BDT is used the signal efficiency of the $\tau$ veto is 100%, i.e. no $Z \to \nu\nu$ events are rejected. But the looser the working point the more events are rejected containing $\tau$ leptons. $Z \to \tau\tau$ is impacted more strongly than $W \to \tau\nu$, because it contains two prompt $\tau$ leptons instead of one. Applying no BDT and consequently not discriminating against hadronic jets leads to a decrease of the survival fraction for all three samples. $Z \to \nu\nu$ is impacted the least as it does not contain prompt $\tau$ leptons. However hadronic jets are more likely to become misidentified as the remnants of hadronically decaying $\tau$ leptons. Basing the $\tau$ identification purely on the number of tracks of the candidates further increases the number of objects falsely identified as $\tau$ leptons. Hence the survival fractions for the three samples are even lower.

For the analysis the "jet BDT: Loose" $\tau$ identification method was chosen, because it does not reduce the SM signal while best rejecting events containing prompt $\tau$ leptons.

#### Reduction of events from multijet background

Multijet production is the processes with the largest cross-section at the LHC. Jets can be mismeasured, because the jet energy resolution (JER) is finite. The mismeasurement can give rise to *fake* $p_{\mathrm{T}}^{\mathrm{miss}}$, because an in fact balanced event might no longer be reconstructed as balanced. By chance, such an event can be selected by the event cuts. Such extreme mismeasurements

| $\tau$ identidication method | $Z \to \nu\nu$ + jets | $W \to \tau\nu$ + jets | $Z \to \tau\tau$ + jets |
|---|---|---|---|
| No $\tau$ veto | 1 | 1 | 1 |
| Tracks = 1 or 3 | 0.24 | 0.15 | 0.10 |
| No Jet BDT | 0.74 | 0.55 | 0.40 |
| Jet BDT: Loose | 1 | 0.81 | 0.64 |
| Jet BDT: Medium | 1 | 0.84 | 0.68 |
| Jet BDT: Tight | 1 | 0.88 | 0.73 |

Table 5.2.: This table indicates survival fractions of events from different processes when a veto on hadronically decaying $\tau$ leptons is applied in the $\geq 1$ jet kinematic region. Numbers for the VBF kinematic region are comparable. The first column presents various methods for $\tau$ identification, cf. Section 3.4.4.

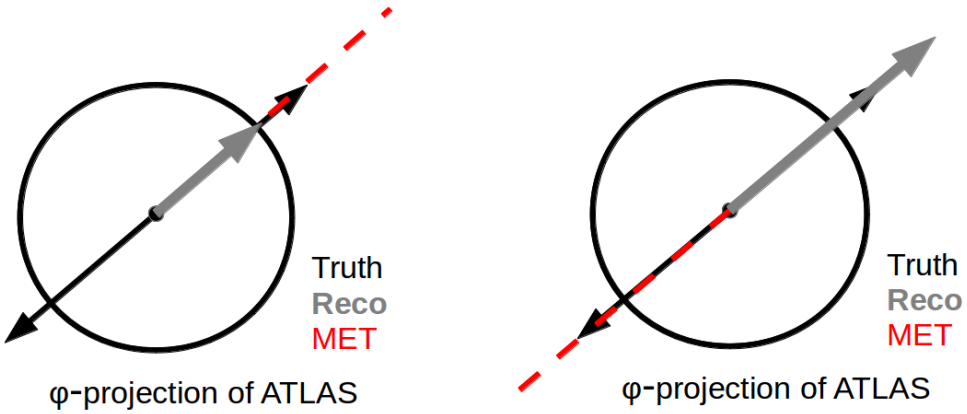


Figure 5.4.: The origin of fake $p_{\mathrm{T}}^{\mathrm{miss}}$ (MET, in red) in multijet events and its characteristic alignment in $\phi$. The black arrows indicate transverses components of the four-vectors of jets in a balanced di-jet event on truth level. The grey arrows show the mismeasured jets on reconstruction level.

are rare, but the cross-section of the multijet production is enormous [127], which is why this background has to be considered in this analysis.

Fake $\mathbf{p}_{\mathrm{T}}^{\mathrm{miss}}$ from mismeasured jets has a characteristic feature: if the $p_{\mathrm{T}}$ of a jet is underestimated, the $\mathbf{p}_{\mathrm{T}}^{\mathrm{miss}}$ algorithm identifies missing transverse momentum pointing along the mismeasured jet in $\phi$. If the $p_{\mathrm{T}}$ is overestimated, $\mathbf{p}_{\mathrm{T}}^{\mathrm{miss}}$ points in the opposite direction. For a balanced but mismeasured dijet event $\mathbf{p}_{\mathrm{T}}^{\mathrm{miss}}$ points along either of the jet as a consequence. Figure 5.4 illustrates these situations in a sketch. Black arrows correspond to transverse jet four-vectors on truth level, grey arrows to reconstruction level and the red dashed lines indicate the resulting *fake* $\mathbf{p}_{\mathrm{T}}^{\mathrm{miss}}$. The left hand side shows a dijet event in which one jet is mismeasured underestimating its $p_{\mathrm{T}}$ and the right hand side shows the opposite situation.

Distributions of the azimuthal angles between $\mathbf{p}_{\mathrm{T}}^{\mathrm{miss}}$ and jets can be used as discriminants for the multijet background. Figure 5.5 shows these $\Delta\phi$ distributions between the $\mathbf{p}_{\mathrm{T}}^{\mathrm{miss}}$ and the transverse projection of the first four leading jets for multijets and the SM signal $\mathrm{Z}\rightarrow\nu\nu$. As expected, the multijet events accumulate in certain region: there is a small accumulation at low values of $\Delta\phi$ ($\mathbf{p}_{\mathrm{T}}^{\mathrm{miss}}$, $\mathrm{jet}_1$), with $\mathrm{jet}_1$ as the leading jet, and a large peak for the back-to-back situation, $\Delta\phi$ ($\mathbf{p}_{\mathrm{T}}^{\mathrm{miss}}$, $\mathrm{jet}_1$) $> 2.0$. This distribution is not symmetrical, although this might by expected due to the almost symmetrical JER. However, if the $\mathrm{p}_T$ of the most energetic jet is strongly underestimated, it might no longer be the leading jet. The observed asymmetry of $\Delta\phi$ ($\mathbf{p}_{\mathrm{T}}^{\mathrm{miss}}$, $\mathrm{jet}_1$) is thus also reflected in $\Delta\phi$ ($\mathbf{p}_{\mathrm{T}}^{\mathrm{miss}}$, $\mathrm{jet}_2$). Figure 5.6 shows a correlation plot between the two distributions further showing this interdependence. Additional peaks of the multijet distribution can be seen for small values of $\Delta\phi$ ($\mathbf{p}_{\mathrm{T}}^{\mathrm{miss}}$, $\mathrm{jet}_2$) and $\Delta\phi$ ($\mathbf{p}_{\mathrm{T}}^{\mathrm{miss}}$, $\mathrm{jet}_3$) corresponding to the cases where energetic jets are mismeasured and become the second or third most leading jet on reconstruction level. Additionally, large statistical uncertainties on the multijet MC can be seen, which motivate the discussion in Section 5.4.2.

These distributions motivate the multijet rejection cut that is part of the SR definition: $\Delta\phi$ ($\mathbf{p}_{\mathrm{T}}^{\mathrm{miss}}$, $\mathrm{jet}_i$) $> 0.4$ for i = 1, 2, 3, 4. Taking also the forth jet into account cannot be motivated by Figure 5.5. However, once cutting on $\Delta\phi$ ($\mathbf{p}_{\mathrm{T}}^{\mathrm{miss}}$, $\mathrm{jet}_i$) $> 0.4$ for i = 1, 2, 3, the majority of

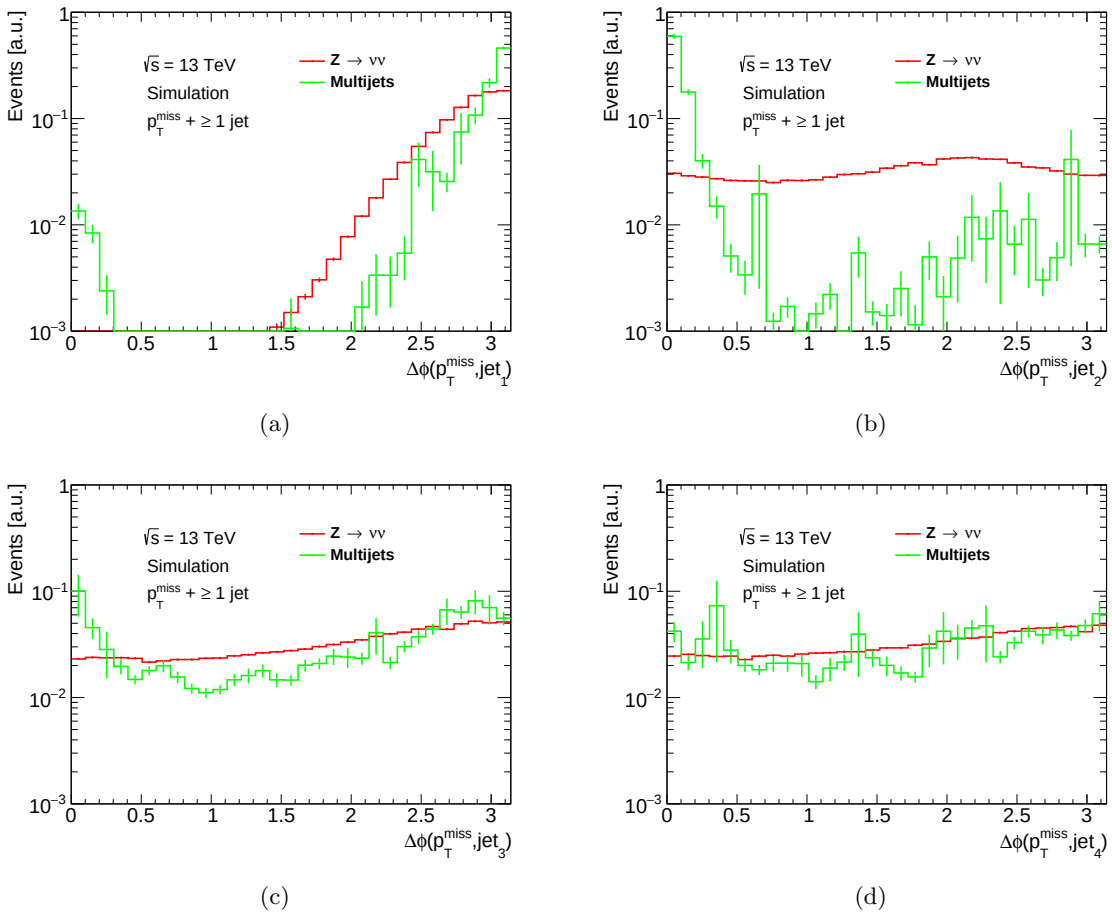


(a) (b)

(c) (d)

Figure 5.5.: The $\Delta\phi$ distributions between the four-vectors of $\mathbf{p}_{\mathrm{T}}^{\mathrm{miss}}$ and the first four leading jets. Shown are multijets and Z$\rightarrow \nu\nu$ in the $\geq 1$ jet kinematic region taken from MC before applying the multijet rejection cuts. Both samples are scaled to unity. Error bars indicate statistical uncertainties of the MC samples.

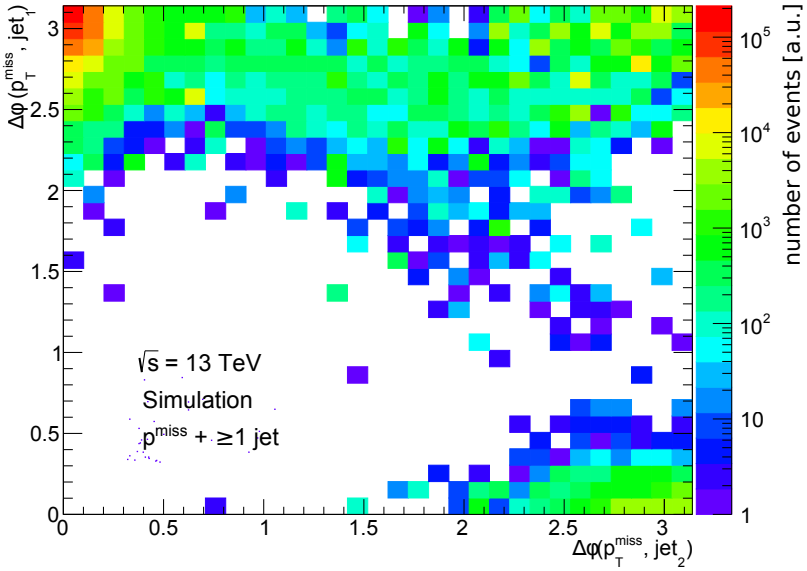


Figure 5.6.: Two dimensional plot of $\Delta\phi$ ($\mathbf{p}_{\mathrm{T}}^{\mathrm{miss}}$, $\mathrm{jet}_1$) versus $\Delta\phi$ ($\mathbf{p}_{\mathrm{T}}^{\mathrm{miss}}$, $\mathrm{jet}_2$) before applying the multijet rejection cut. It can be seen that events with large values of $\Delta\phi$ ($\mathbf{p}_{\mathrm{T}}^{\mathrm{miss}}$, $\mathrm{jet}_1$) usually have small values of $\Delta\phi$ ($\mathbf{p}_{\mathrm{T}}^{\mathrm{miss}}$, $\mathrm{jet}_2$) and vice-versa.

the multijet events accumulate at low values of $\Delta\phi$ ($\mathbf{p}_{\mathrm{T}}^{\mathrm{miss}}$, $\mathrm{jet}_4$), cf. Figure 5.7. Hence this cut yields additional background rejection.

A major advantage of these multijet rejection cuts is that they do not cut significantly into the expected SM signal. DM models are expected to behave more similar to $\mathrm{Z}\rightarrow \nu\bar{\nu}$ than to multijets, because they carry *real* $p_{\mathrm{T}}^{\mathrm{miss}}$. Hence these cuts are well applicable for this search.

Figure 5.8 shows $p_{\mathrm{T}}^{\mathrm{miss}}$ distributions before and after applying the $\Delta\phi$ cuts. The multijet background is reduced significantly while the signal remains fairly stable. The signal (multijet background) efficiency of the cut is $\epsilon_{\mathrm{eff}}^{\mathrm{sig}} = 0.87$ ($\epsilon_{\mathrm{eff}}^{\mathrm{bkg}} = 0.03$). $\epsilon_{\mathrm{eff}}$ is defined as the fraction of events that passes the cut.

## 5.4. Background Estimates for the Numerator

The previous section introduced the various backgrounds and their origins. This section describes the estimation methods for these background.

### 5.4.1. Events Containing Leptonically Decaying $W^{\pm}$ Bosons

For events containing leptonically decaying W-bosons, a data-driven background estimate is used. Background enriched control regions are defined and extrapolated to the signal region. The extrapolation is performed for two categories of backgrounds: (1) the lepton is outside the detector acceptance and (2) the lepton is inside the acceptance but not reconstructed or identified [128].

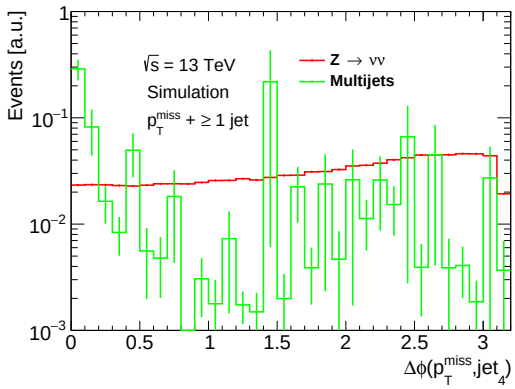


Figure 5.7.: Shown is $\Delta\phi$ ($\mathbf{p}_{\mathrm{T}}^{\mathrm{miss}}$, jet$_4$) after a applying the $\Delta\phi$ ($\mathbf{p}_{\mathrm{T}}^{\mathrm{miss}}$, jet$_i$) cuts on the first three jets. Error bars indicate statistical uncertainties of the MC samples.

In data, two control regions (CRs) per kinematic region are defined dedicated to W $\rightarrow \mu\nu$ and W $\rightarrow e\nu$ events. The cuts follow mostly the signal region definitions as listed for the numerator in Table 5.1, but there are differences due to lepton selection.

For the W $\rightarrow \mu\nu$ CR exactly one muon with $p_T > 25\,\mathrm{GeV}$ and $|\eta| < 2.5$ is required that is isolated from other particles. The higher $p_T$ cut with respect to the lepton veto in the signal region is motivated by an improved reconstruction efficiency [129]. Additional leptons are vetoed on. The muon is treated as invisible and hence not considered in the $p_{\mathrm{T}}^{\mathrm{miss}}$ calculation. This is done to make the CR more similar to the signal region: if an event containing a muon is not rejected in the SR, it was usually not reconstructed and identified. In this case it is not included in the $p_{\mathrm{T}}^{\mathrm{miss}}$ definition either. Events in this CR are selected by the same $p_{\mathrm{T}}^{\mathrm{miss}}$ trigger as described in Section 5.2.

For the W $\rightarrow e\nu$ CR exactly one electron is required with $p_T > 25\,\mathrm{GeV}$ and $|\eta| < 2.47$ excluding the barrel-endcap transition region. Here, the electron is included in the $p_{\mathrm{T}}^{\mathrm{miss}}$ calculation but calibrated at the hadronic scale, i.e. as a jet. This is also done to make this CR more similar to the SR: in the SR W $\rightarrow e\nu$ events survive the electron veto usually because the electron is misidentified as a hadronic jet. For this CR, the single-electron triggers mentioned in Section 5.2 is used.

W $\rightarrow \tau\nu$ events where the $\tau$ decays into either an electron or muon are also included in the two CRs defined above. However, there is no dedicated W $\rightarrow \tau\nu$ CR for hadronic $\tau$ decays, because of their experimentally challenging signature. Details on the estimate of this background contribution follow below.

The event yields in both CRs are corrected using lepton $p_T$ and $\eta$ dependent correction factors. The data are corrected for lepton reconstruction, identification, and isolation efficiencies. These efficiencies are taken from dedicated measurements in data [129, 130]. The electron CR is additionally corrected for inefficiencies of the trigger. The $p_{\mathrm{T}}^{\mathrm{miss}}$ trigger is fully efficient for the muon CR. The resulting corrected CRs are background subtracted using MC and used as the foundation for an extrapolation to the signal regions. A comparison between data and MC can be seen for the background subtracted control regions for two example distributions in Figure 5.9. Lepton efficiency corrections are included. In both CRs the corresponding W $\rightarrow l\nu$

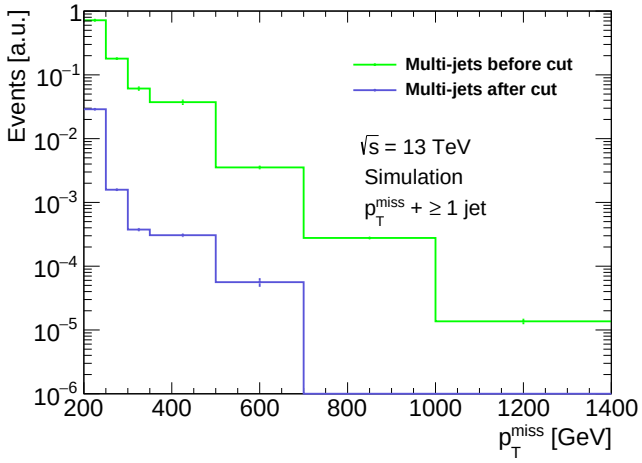


(a)

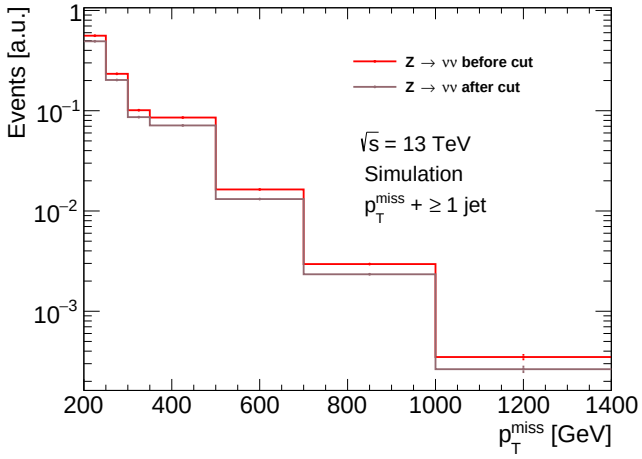


(b)

Figure 5.8.: $p_{\mathrm{T}}^{\mathrm{miss}}$ distributions taken from MC simulation in the $\geq 1$ jet signal region before and after applying the $\Delta\phi$ ($\mathbf{p}_{\mathrm{T}}^{\mathrm{miss}}$, jet$_i$) $> 0.4$ multijet rejection cuts. (a) shows the multijet background and (b) the SM signal Z$\rightarrow \nu\nu$. Samples are normalised to the event yields before the cut. It can be seen that the former gets suppressed by a significant margin: the multijet background efficiency $\epsilon_{\mathrm{eff}}^{\mathrm{bkg}} = 0.03$. The latter suffers much fewer losses, $\epsilon_{\mathrm{sig}}^{\mathrm{bkg}} = 0.87$. Error bars indicate statistical uncertainties of the MC samples.

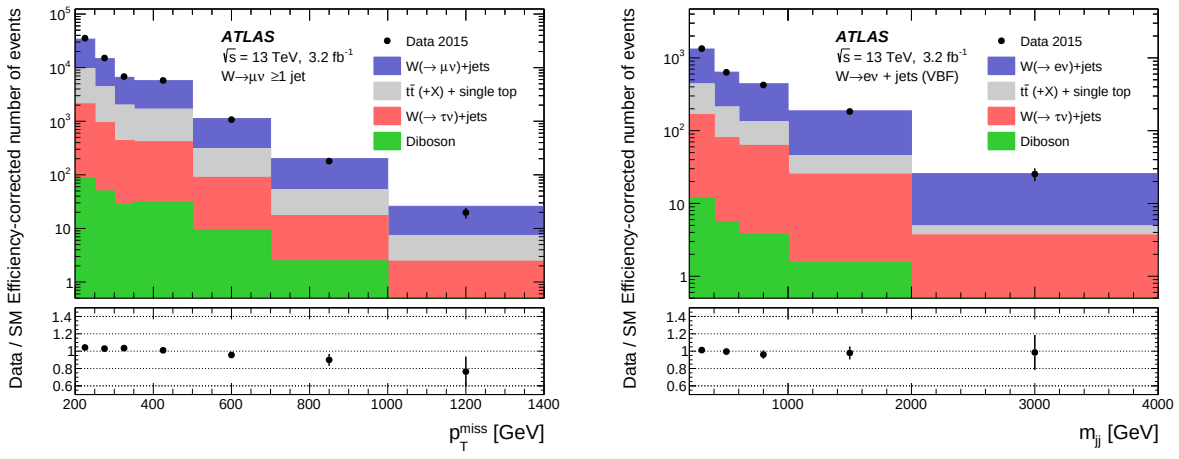


(a) (b)

Figure 5.9.: Comparisons between data and predictions for the SM: (a) the $p_{\mathrm{T}}^{\mathrm{miss}}$ distribution in the W$\rightarrow \mu\nu$ CR for the $\geq 1$ jet kinematic region and (b) the $M_{jj}$ distribution in the W$\rightarrow e\nu$ CR for the VBF kinematic region [1]. The distributions are background subtracted and lepton efficiency corrections are applied. Error bars indicate the statistical uncertainty on the data.

+ jets process is the dominant contribution. Smaller contributions come from $t\bar{t}$, single top, W $\rightarrow \tau\nu$ + jets and dibosons.

The extrapolation takes into account differences between SR and CRs is separately performed for cases in which a lepton is not reconstructed or identified, out-of-efficiency, or outside of detector acceptace, out-of-acceptance. The extrapolation takes the form

$$N_{\mathrm{eff}}^{\mathrm{bkg}} = \frac{N_{\mathrm{control}}}{\epsilon} \cdot \frac{a_7}{a_{25}} \cdot (1 - \epsilon) \tag{5.2}$$

and

$$N_{\mathrm{acc}}^{\mathrm{bkg}} = \frac{N_{\mathrm{control}}}{\epsilon} \cdot \frac{1}{a_{25}} \cdot (1 - a_7)\,. \tag{5.3}$$

Here, $N_{\mathrm{eff}}^{\mathrm{bkg}}$ is the total number of W background events from the out-of-efficiency contribution, $N_{\mathrm{acc}}^{\mathrm{bkg}}$ is for the out-of-acceptance contribution and $\mathrm{N_{control}}/\epsilon$ is the efficiency corrected yield in a CR as introduced above. $\mathrm{a_7}$ ($\mathrm{a_{25}}$) is the fraction of events with an in-acceptance lepton with $\mathrm{p}_T > 7\,\mathrm{GeV}$ (25 GeV) with respect to all events with in-acceptance leptons. In Equation 5.2, multiplying $\mathrm{N_{control}}/\epsilon$ with $\mathrm{a_7/a_{25}}$ corrects the former for the different $\mathrm{p}_T$ thresholds for leptons in the SR and CRs. By multiplying with (1 - $\epsilon$), the product is corrected for the leptons being out-of-efficiency, i.e. within detector acceptance but not identified, in the SR. In Equation 5.3, $1/\mathrm{a_{25}}$ corrects for the CR acceptance and the $(1 - \mathrm{a_7})$ factor extrapolates the yield to outside of the detector acceptance. The total W background follows from the sum of the two contributions.

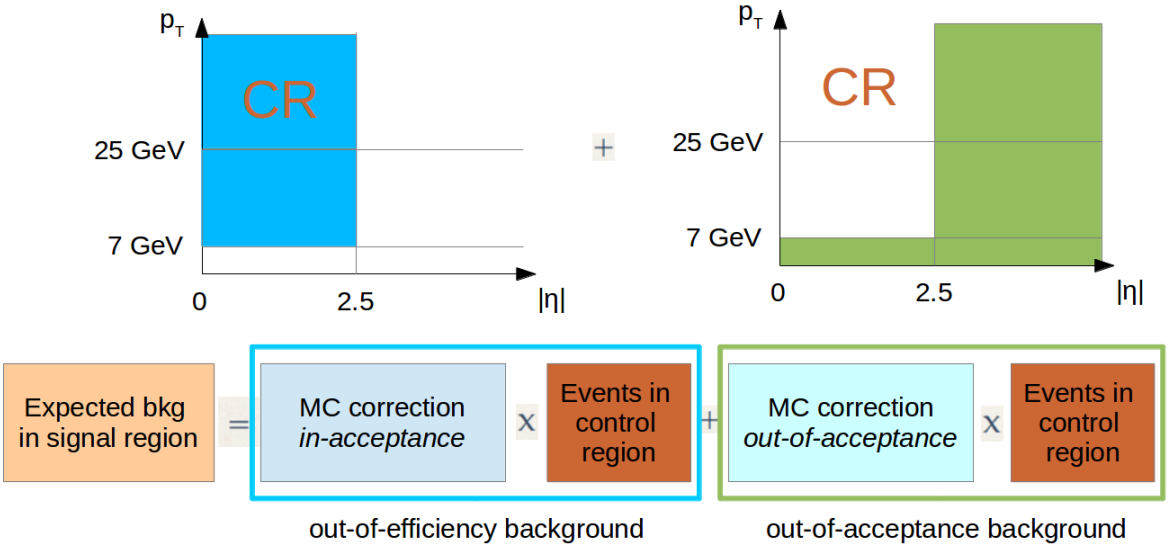


Figure 5.10.: This figure illustrates how the W-background technique extrapolates from the control regions into the signal regions by dividing the background contributions into two cases.

The equations are applied to each bin in all of the four measured distributions to provide the final background estimates.

This background estimation technique is sketched in Figure 5.10, where the left hand side depicts the out-of-efficiency background and the right hand side the out-of-acceptance background. For both background categories the starting point are the efficiency-corrected data in the CR, $N_{control}/\epsilon$. For out-of-efficiency background the MC correction *in-acceptance* is $a_7/a_{25}\cdot(1 - \epsilon)$ as explained above. Similarly, for the out-of-acceptance background the MC correction *out-of-acceptance* is $1/a_{25}\cdot(1 - a_7)$. The coloured parts in the sketched 2-dimensional plots show which region of the lepton $p_T - |\eta|$ space is covered by the two extrapolations. The total background is the sum of the two products.

A modification of the technique detailed above was used to obtain the background estimates for $W \to \tau\nu$, where the $\tau$ decays hadronically. Instead of having a dedicated $\tau$ CR, the CRs for electrons and muons are used. However, the $a_i$ are based on a $W \to \tau\nu$ Monte Carlo and it was taken into account that the hadronic $\tau$ veto has a higher threshold (20 GeV) than the other two lepton vetoes (7 GeV). The final prediction is taken as the midpoint between the individual predictions from the two CRs and the spread serves as an additional uncertainty. This is motivated by two arguments: on the one hand in the SR the hadronically decaying $\tau$ will often be misidentified as a hadronic jet and thus be taken into account for the $p_T^{miss}$ calculation. This is similar to the electron case. On the other hand, hadronic tau decays include additional neutrinos, which are not seen by the detector and are thus not part of the $p_T^{miss}$ calculation. This is closer to the muon case. Hence, the *real* value is expected to be in-between and is estimated by this procedure. Systematic uncertainties of this method are explained in Section 5.7.

### 5.4.2. Multijet Background

Applying the multijet rejection cuts, i.e. $\Delta\phi$ ($\mathbf{p}_{\mathrm{T}}^{\mathrm{miss}}$, jet$_i$) for i = 1,2,3,4 as explained in Section 5.3, reduces the multijet background to about 3% of its original size, cf. section. The remaining background ranges from about a few percent to smaller than a per-mill depending on the kinematic region and the $p_{\mathrm{T}}^{\mathrm{miss}}$ value. It needs to be estimated with a reliable method and reasonable uncertainties. In the following it will be motivated why this background needs special attention and the final background estimate will be explained.

Several ideas were explored before converging on the data-driven estimate using the smearing method that forms the main body of this section. Since the background contribution is so small, the estimate could be taken from Monte Carlo simulations. However, due to the way the multijet samples are generated this is unsuitable. It is generated in slices of leading jet $p_T$ where each slice contains approximately the same number of generated events. The chances for mismeasuring a jet so strongly that the event passes the SR cuts are small. Thus the count of generated events of the multijet MC in the SR is low leading to large statistical uncertainties and unreliable shapes of kinematic distributions, cf. for instance Figure 5.7. The generation of the multijet MC in slices of $p_{\mathrm{T}}^{\mathrm{miss}}$ on detector level would prevent this issue. This is however not practicable because of the structure of the event generation chain, because samples are first produced on particle level before being subjected to detector simulations. Consequently, further options needed to be explored.

A data-driven background estimate was chosen for multijet processes after testing several alternatives. Similar to Section 5.4.1, a CR in data is defined that is enriched in these events and an extrapolation to the SR is performed. For the extrapolation a transfer function is used that takes accounts for differences in SR and CR. The estimate is performed for each bin in each distribution according to

$$N_{\mathrm{SR}}^{\mathrm{bkg}} = R \cdot N_{\mathrm{CR}}^{\mathrm{bkg}}\,, \tag{5.4}$$

where $N_{\mathrm{SR}}^{\mathrm{bkg}}$ is the number of extrapolated multijet background events in the SR, $N_{\mathrm{CR}}^{\mathrm{bkg}}$ is the background subtracted number of events measured in the CR, and R is the transfer function which is discussed below.

The azimuthal angles between $\mathbf{p}_{\mathrm{T}}^{\mathrm{miss}}$ and the first four jets yield discrimination power between multijet production and the SM signal, cf. Figure 5.5. The multijet background accumulates significantly at low values in the four distributions. In these events the four-vector of $p_{\mathrm{T}}^{\mathrm{miss}}$ and the four-vector of the corresponding jet are close to each other in the transverse plane. Processes with *real* $p_{\mathrm{T}}^{\mathrm{miss}}$ do not show peaks in these regions of phase-space. Hence, the CR is defined similar to the SR, cf. Table 5.1, except for the multijet rejection cuts, which are replaced by

$$\Delta\phi(\mathbf{p}_{\mathrm{T}}^{\mathrm{miss}}, jet_i) < 0.1, \qquad i = 1,2,3,4. \tag{5.5}$$

The contamination of other processes to the control region is low as can be seen in Figure 5.13, which shows both data and background subtracted data in the CR. The difference between *Data in CR* and *Bkg Subtracted Data in CR* is the MC prediction for SM processes except for multijet production.

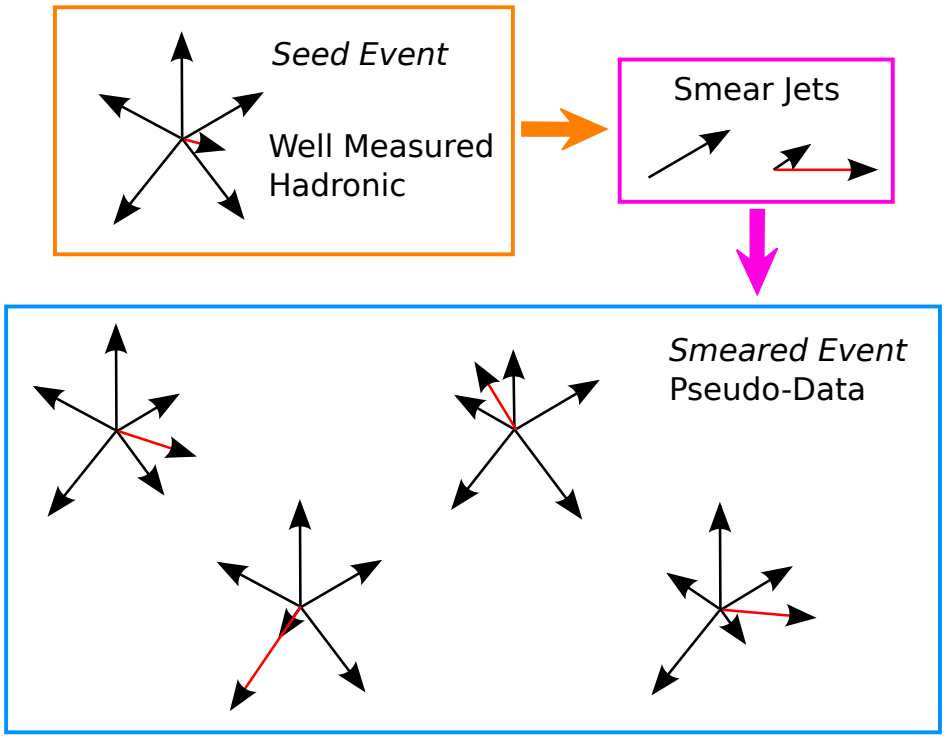


Figure 5.11.: This figure illustrates the jet smearing procedure. The detector level jets (black) of well-measured events in data are smeared numerous times to create a large pseudo-dataset showing fake-$p_{\mathrm{T}}^{\mathrm{miss}}$ (red), inspired by [131].

Two methods were tested to derive transfer functions R. It can be built from MC according to

$$R = \frac{N_{\mathrm{SR}}^{\mathrm{MC}}}{N_{\mathrm{CR}}^{\mathrm{MC}}}, \tag{5.6}$$

where $\mathrm{N}_{\mathrm{CR}}^{\mathrm{MC}}$ and $\mathrm{N}_{\mathrm{SR}}^{\mathrm{MC}}$ are the MC predictions for CR and SR, respectively. However, this technique suffers from the MC statistics problem explained above. To mitigate the large statistical uncertainties of the MC sample, it was tested whether the inclusion of an additional multijet MC sample solves the issue. In addition to the standard Pythia multijet MC that was used on its own before a Powheg-generated sample is used. The new transfer function is the statistical combination of the individual transfer functions weighted according to their uncertainties $\sigma$

$$R = \frac{\frac{R_{\mathrm{Pyth}}}{\sigma^2_{\mathrm{Pyth}}} + \frac{R_{\mathrm{PowPyth}}}{\sigma^2_{\mathrm{PowPyth}}}}{\frac{1}{\sigma^2_{\mathrm{Pyth}}} + \frac{1}{\sigma^2_{\mathrm{PowPyth}}}}. \tag{5.7}$$

The combination of the samples improves the performance, but it is still lacking in providing a physical, smooth shape of the distributions. This will be shown below in the validation study, cf. Figure 5.14.

The technique that is used for the final prediction deliberately *smears* the $p_{\mathrm{T}}$ jets in data [131, 132]. Well-measured multijet events in data ("seed events") are selected and their jets are smeared according to the known jet response. Thereby, jets are purposefully mismeasured. This can be done indefinitely for each seed event resulting in a set of *pseudo-data*. It does not suffer from the statistical uncertainties of the MC sample and it shows the characteristics of real mismeasured multijet events. The workflow of this technique is sketched in Figure 5.11, with jets as black arrows and the resulting fake $\mathbf{p}_{\mathrm{T}}^{\mathrm{miss}}$ as red arrows. The final transfer function is defined as

$$R = \frac{N_{\mathrm{SR}}^{\mathrm{Smr}}}{N_{\mathrm{CR}}^{\mathrm{Smr}}} \,. \tag{5.8}$$

The definition is similar to Equation 5.6, but smeared data events that pass SR (CR) cuts are used instead of MC events. The seed events are selected by a range of single-jet triggers with varying $\mathrm{p}_T$ thresholds. If the trigger selecting a specific event is prescaled [70], the event is weighted with the prescale factor. Additionally, the seed events are required to be hadronic, i.e. events containing charged leptons are vetoed, must contain at least one jet, and the standard event quality cuts are applied. Two cuts ensure that events are *well-measured*:

$$\frac{p_{\mathrm{T}}^{\mathrm{miss}} - M}{\sqrt{\sum E_T}} < 0.5 \tag{5.9}$$

$$\frac{p_{\mathrm{T}}^{\mathrm{miss}}}{p_{\mathrm{T,avg}}^{\mathrm{jet}}} < 0.2 \,. \tag{5.10}$$

The quantity defined in Equation 5.9 is called the $p_{\mathrm{T}}^{\mathrm{miss}}$ significance. M is a correction factor accounting residual biases introduced by the soft term of $p_{\mathrm{T}}^{\mathrm{miss}}$. It has been shown that a value of $\mathrm{M} = 8\,\mathrm{GeV}$ best alleviates the bias [131]. $\sum \mathrm{E}_T$ is the transverse energy sum over all reconstructed jets and $\mathrm{p}_{\mathrm{T,avg}}^{\mathrm{jet}}$ is the average $\mathrm{p}_T$ of all reconstructed jets in the events. Events being *well-measured* is important to reduce compounding effects when smearing the event later.

Jets in good seed events are simultaneously smeared 25000 times according to the jet response, shown in Figure 5.12. The response $\mathcal{R}$ is taken from MC, tuned to data [131] and binned in terms of $\mathrm{p}_T$. It is defined as $\mathcal{R} = \mathrm{p}_T^{\mathrm{reco}}/\mathrm{p}_T^{\mathrm{truth}}$, where $\mathrm{p}_T^{\mathrm{reco}}$ and $\mathrm{p}_T^{\mathrm{truth}}$ refer to the transverse momenta of a given jet at reconstruction level and truth level respectively. Requirements on jets to be smeared are centrality ($|\eta| < 2.5$) and $\mathrm{p}_T > 20\,\mathrm{GeV}$, because only for these jets a jet response is provided. The selection cuts for the SR and the CR are applied to the smeared data events, yielding $\mathrm{N}_{\mathrm{SR}}^{\mathrm{Smr}}$, $\mathrm{N}_{\mathrm{CR}}^{\mathrm{Smr}}$, and R.

Figure 5.13 shows the final estimate used in this analysis, as well as the background subtracted data in the CR and the transfer function derived using the smearing method. Appendix B shows the original distributions of the pseudo-dataset that form the basis for the transfer function which is the ratio of the original distributions in SR and CR. The systematic uncertainties for the multijet estimate are explained in Section 5.7.

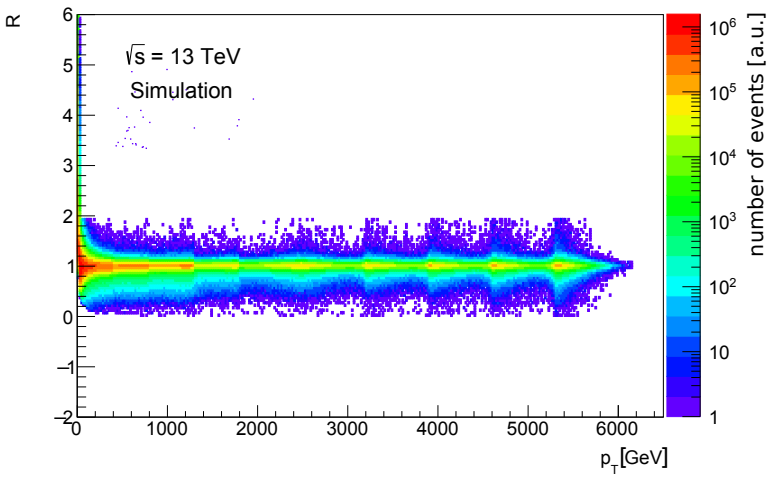


Figure 5.12.: The jet response $\mathcal{R}$ provided by the authors of the jet smearing tool [131, 132] which is used to smear the well-measured data events necessary for the multijet background estimate versus $p_T$. The pulse-like shape comes from the response being extracted from several Monte Carlo samples generated jet $p_T$ slices of similar dataset size.

### Validation Study

A validation study is performed to check the performance of the smearing method. The validation region is chosen to be similar to the SR, but enriched in multijet events. Therefore, the validation region (VR) definition follows the SR cuts, except for the multijet rejection cuts, which are replaced by the requirement

$$0.1 < \Delta\phi(\mathbf{p}_{\mathrm{T}}^{\mathrm{miss}}, jet_i) < 0.5\,, \tag{5.11}$$

for any of the first four leading jets i. Additionally the $p_{\mathrm{T}}^{\mathrm{miss}}$ and $m_{jj}$ are limited to maximum values of 500 GeV and 750 GeV[1], respectively. The CR for this study is the same as for the main analysis, but the extrapolation is now performed to the VR.

Results of the validation study can be found in Figure 5.14, where the background[2]-subtracted data in the VR is compared to predictions using the data-driven techniques. Taking the transfer function from MC using Equation 5.7 is plotted in red and taking it using the smearing method in blue. The smearing method outperforms the MC-based approach, which still suffers from large statistical uncertainties.

### 5.4.3. Other Backgrounds and Background Summary

Background events from the leptonic decays of $Z/\gamma^*$ are taken from MC as they form only a small and well modeled background. The final composition of the SRs including all the

[1] These were the blinding cuts of the analysis, which are also used in the validation study.
[2] Everything apart from multijets.

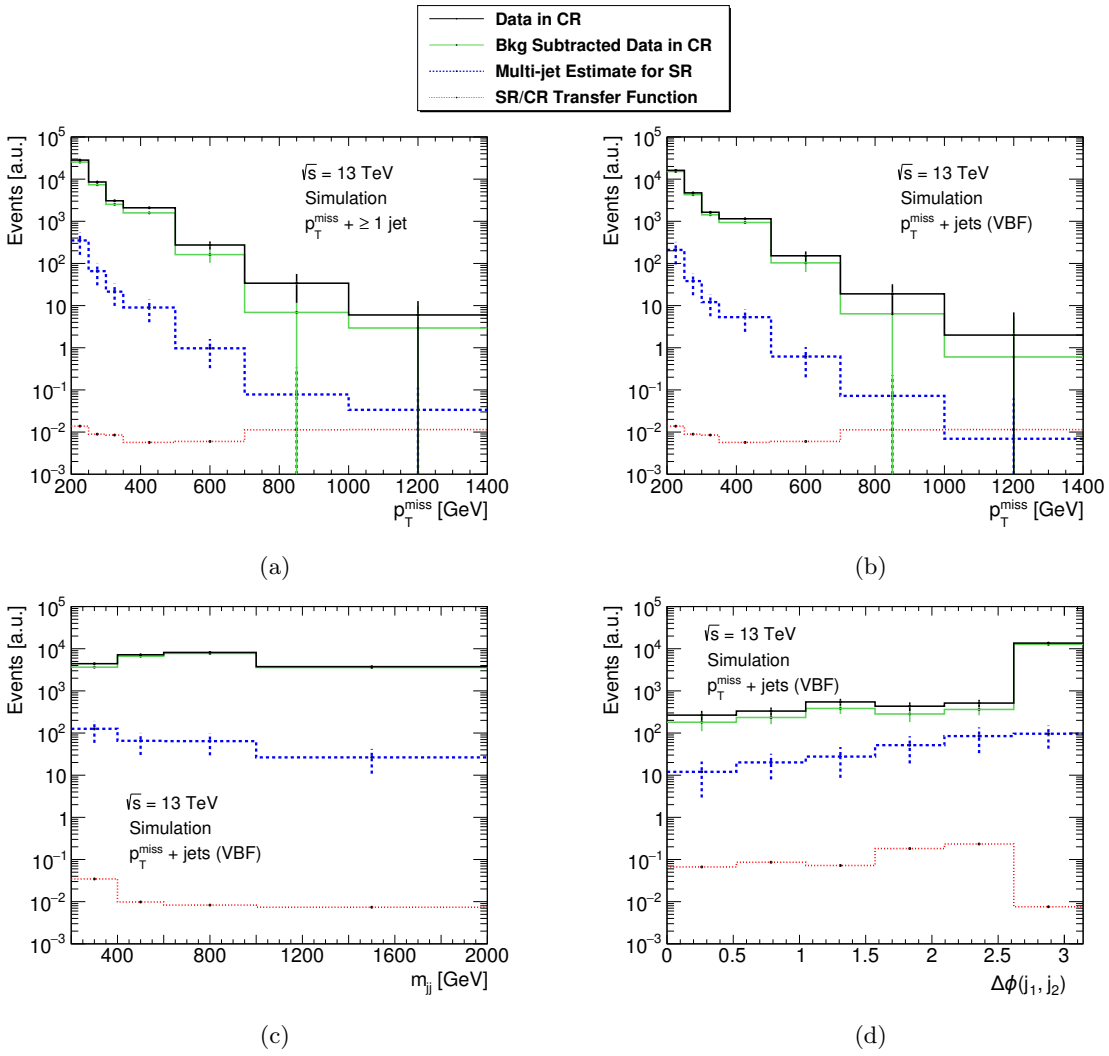


Figure 5.13.: The final multijet background estimate using the "smearing method" (blue) for the four measured distributions. Also shown are the data in the CR, both background subtracted (green) and not background subtracted (black) and the transfer function between SR and CR (red). The multijet background estimate follows from multiplying the background subtracted data with the transfer function. The error bars indicate statistical uncertainties except for the multijet estimate in the SR for which the uncertainties are explained in Section 5.7.

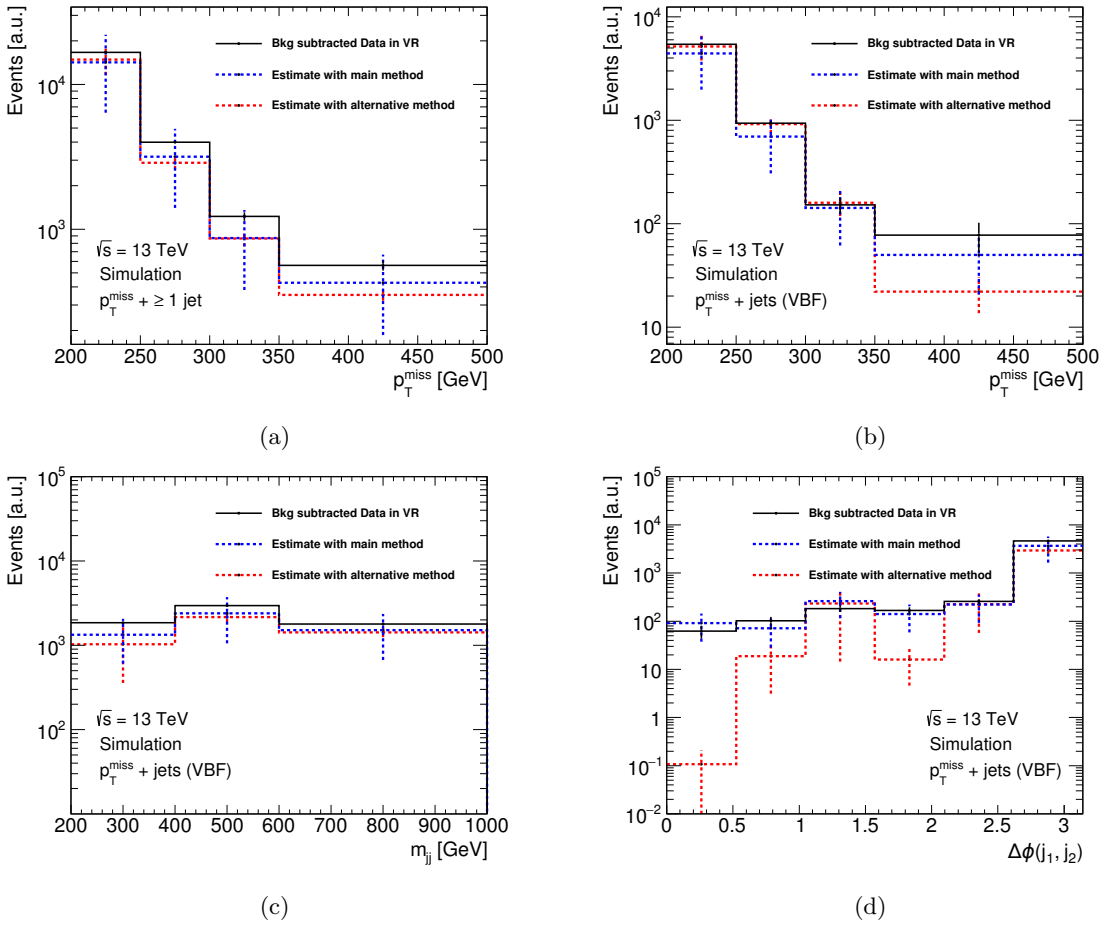


Figure 5.14.: Results of the validation study are shown. The data in the VR are corrected all processes except for multijet production. The data are compared to predictions using the data-driven techniques, both with taking the transfer function from MC using Equation 5.7 (red, alternative method) and with using the smearing method (blue, main method). The smearing method outperforms the alternative approach where issues of large statistical uncertainties of the MC sample can still be seen. The uncertainty on the alternative method is the combination of statistical uncertainties from data and the two MC samples. The uncertainty on the main method is described in Section 5.7.

background estimates detailed above can be found in Figure 5.15. An agreement between data and the predictions within uncertainties can be seen.

## 5.5. Background Estimates for the Denominator

The background estimates for the denominator follow a different scheme than the estimates for the numerator. The relevant background contributions are events from $t\bar{t}$ production, single-top, dibosons, W + jets and Z $\rightarrow \tau^+\tau^-$ + jets in order of descending contributions. Some of these processes can have the same final states as Z $\rightarrow e^+e^-$ and Z $\rightarrow \mu^+\mu^-$, such as $t\bar{t}$ and diboson production. For other backgrounds misidentifications must happen, such as for W + jets and Z $\rightarrow \tau^+\tau^-$ + jets in the case of hadronic dacays. The multijet background is found to be negligible.

All backgrounds are taken from Monte Carlo simulations and compared to data in a control region. The CR is defined similarly to the SR, but a pair of differently flavoured leptons ($e^{\pm}\mu^{\mp}$) is required. This CR is sensitive to most of the background processes, most notably the dominant $t\bar{t}$. Discrepancies of up to 50% depending on the bin and distribution considered are observed. The total background is reweighted by fitting a polynomial to the ratio of data and MC prediction. The same reweighting factors are also applied to the prediction for the SR yielding the final background estimate. The systematic uncertainties for this method are detailed in Section 5.7.

Figure 5.16 shows the data in the denominator comparing it to the prediction. An agreement within uncertainties can be seen for most bins.

## 5.6. Unfolding

The similarity between numerator and denominator is that in both cases Z + jets events are measured. The main difference is that there are no efficiency losses in the numerator, because energetic neutrinos always cause $p_{\mathrm{T}}^{\mathrm{miss}}$. In the denominator however, efficiencies are smaller than one for electron and muon reconstruction and identification. Hence, the main selection differences in numerator and denominator originate in the absence of charged leptons in the former and the requirement of a $e^{\pm}e^{\mp}$ or $\mu^{\pm}\mu^{\mp}$ pair in the latter. Associated uncertainties do not cancel in the ratio and are the main contributing effect to the detector correction that is applied. Additionally the resolution of the Z-p$_T$, hence $p_{\mathrm{T}}^{\mathrm{miss}}$, is slightly different, because it relies on jet measurements in the numerator and on lepton measurements in the denominator.

The method for detector correction in this analysis is bin-by-bin unfolding, cf. Section 4.2.1. Thus, this can be verified by considering the bin-by-bin correction factors for two scenarios: correcting for all possible differences or only taking into account differences in lepton selections. For the first case the correction is defined as the double ratio $\mathrm{R}_{\mathrm{miss}}^{\mathrm{particle}}/\mathrm{R}_{\mathrm{miss}}^{\mathrm{detector}}$ on MC, where the subscripts *"particle"* and *"detector"* correspond the measuring $\mathrm{R}_{\mathrm{miss}}$ in MC on particle or detector level. For the second case only the denominator is corrected for differences between particle and detector level. The event selections are performed separately using truth leptons and reconstructed leptons. The correction factor called $\mathrm{C}_Z$ follows from taking the ratio of event yield from the two selections in all bins of all distributions. Figure 5.17 shows a comparison for $p_{\mathrm{T}}^{\mathrm{miss}}$. Plotted are bin-by-bin correction factors obtained from the two different methods. Green

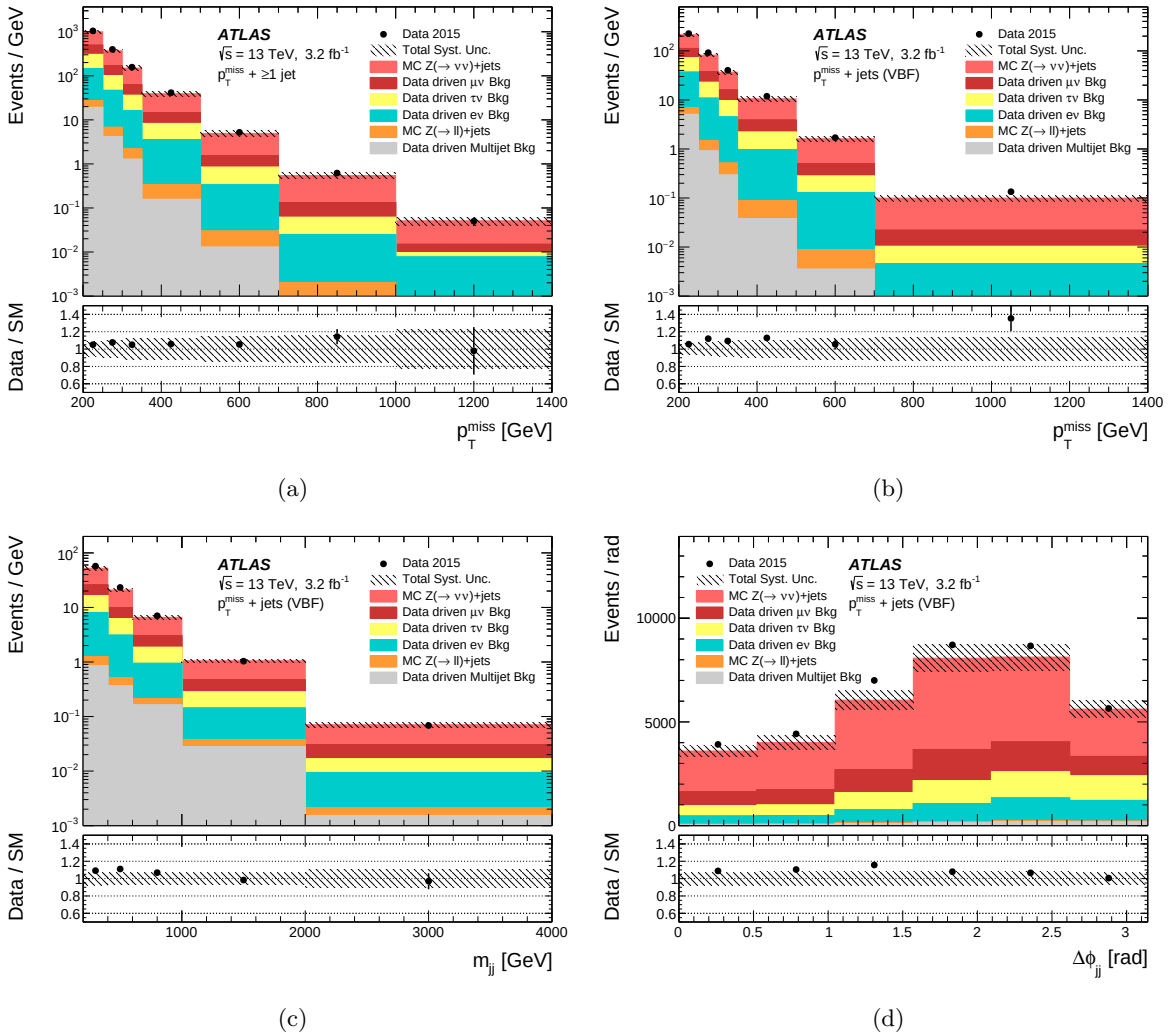


Figure 5.15.: Compositions of the SRs for the numerator with all final background estimates [1]. Data are compared to the predictions and the ratio panel shows the former divided by the latter. Error bars on data indicate statistical uncertainties and the origin of the uncertainties forming the bands are explained in Section 5.7.

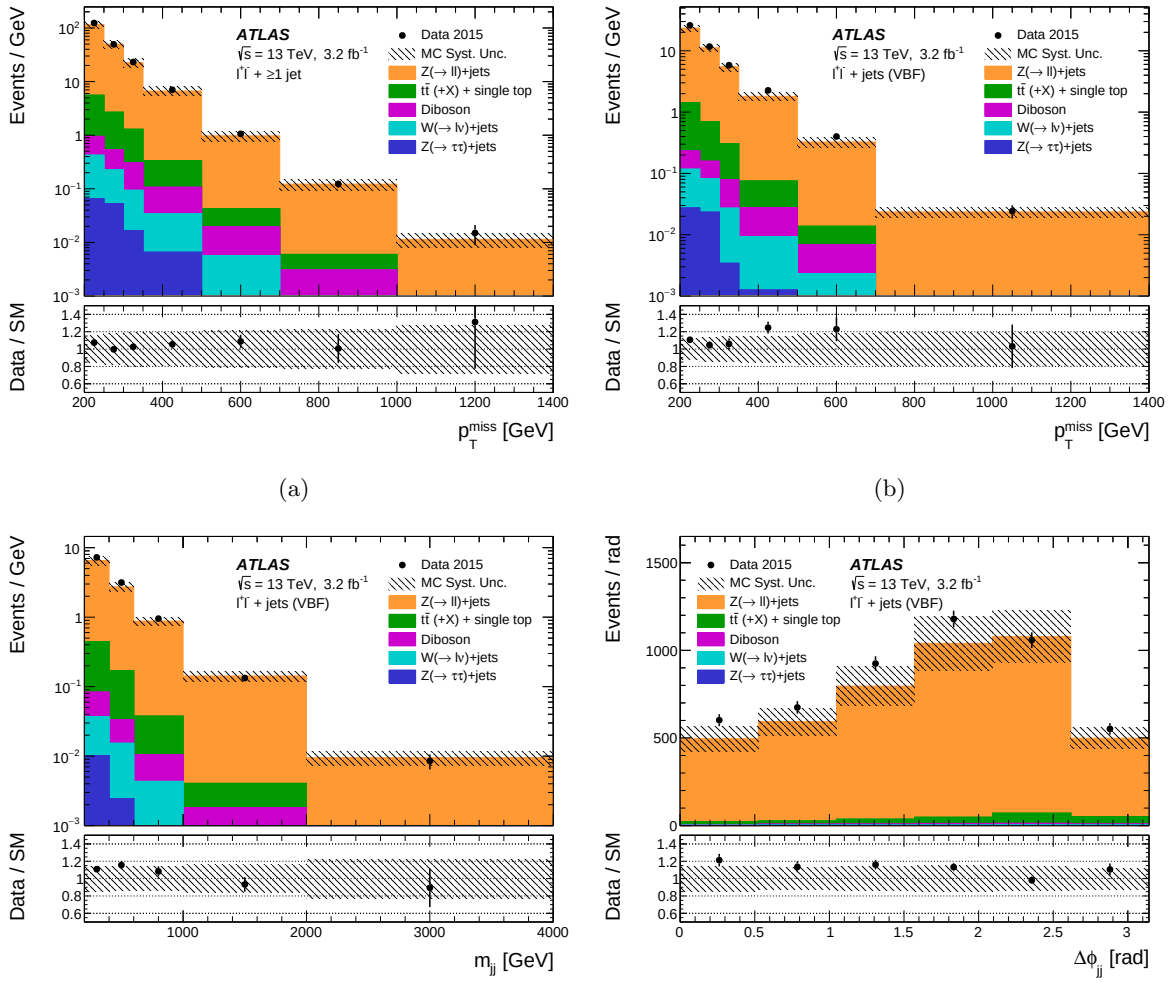


Figure 5.16.: Compositions of the SRs for the denominator (both channels combined) with all final background estimates [1]. Data are compared to the predictions and the ratio panel shows the former divided by the latter. Error bars indicate uncertainties and are explained in Section 5.7.

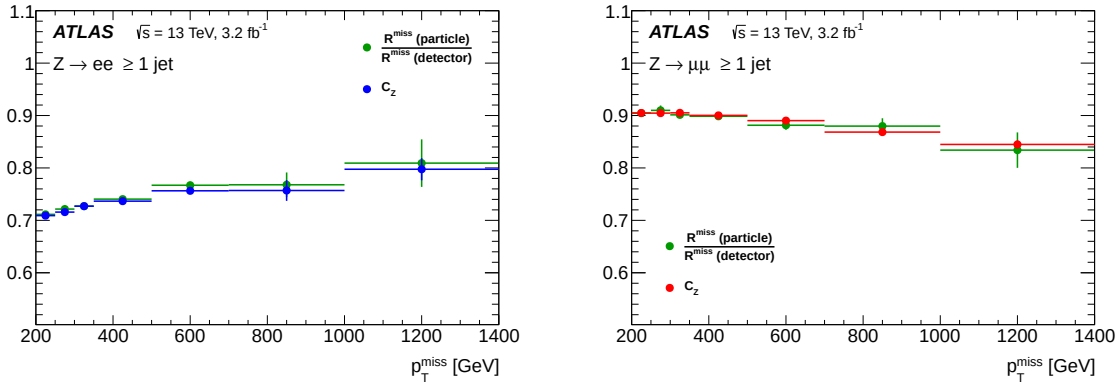


(a) (b)

Figure 5.17.: Considered correction factors in dependence of $p_{\mathrm{T}}^{\mathrm{miss}}$. The left (right) hand side shows the $\mathrm{Z} \to ee$ ($\mathrm{Z} \to \mu\mu$) denominator in the $\geq 1$ jet kinematic region. The double ratio and $\mathrm{C}_Z$ agree within statistical uncertainties [1], which are indicated by the error bars.

shows the double ratio of the ratio on truth particle level divided by the ratio on detector level. This correction factor accounts for all possible differences when moving from detector to particle level. $\mathrm{C}_Z$ correction factors using the second approach are shown in blue and red. They are based purely on lepton efficiency and resolution effects. The two kinds of correction factors are in good agreement with small differences explainable by statistical effects.

$\mathrm{C}_Z$ and the double ratio yield the same results. Thus, $\mathrm{C}_Z$ is chosen as the correction factor for this analysis. It allows for an easier treatment of systematic uncertainties, because only lepton-related uncertainties need to be considered. $\mathrm{C}_Z$ is a reflection of electron and muon reconstruction and identification efficiencies of the ATLAS detector for the selected analysis cuts. As a consequence, the values of $\mathrm{C}_Z$ for the muon channel are generally larger, because the muon efficiencies are larger for muons than for electrons.

Injecting a strong DM signal into the calculations of detector corrections has little impact on the final results. This can be seen in Figure 5.18. (a) shows the ratio on detector level, once with and once without an injected DM signal. The DM signal corresponds to the simplified model introduced in Section 2.3 with $g_q = 1.25$, $g_\chi = 1.25$, $m_\chi = 150\,\mathrm{GeV}$, and $m_A = 1\,\mathrm{TeV}$. A significant difference can be seen. (b) shows the correction factors that are obtained with and without the injection. Good agreement is observed indicating that the unfolding is independent on whether the SM or BSM physics is used to derive the corrections. The unfolding is performed for both channels of the denominator separately.

## 5.7. The Ratio and its Uncertainties

### Sources of Uncertainty

Various sources of systematic uncertainty are considered for this analysis. They are grouped as follows: lepton efficiency, jets, W$\to \tau\nu$ from the control region, multijet, statistical effects on the correction factor, W background statistical, W background theory, top quark cross-

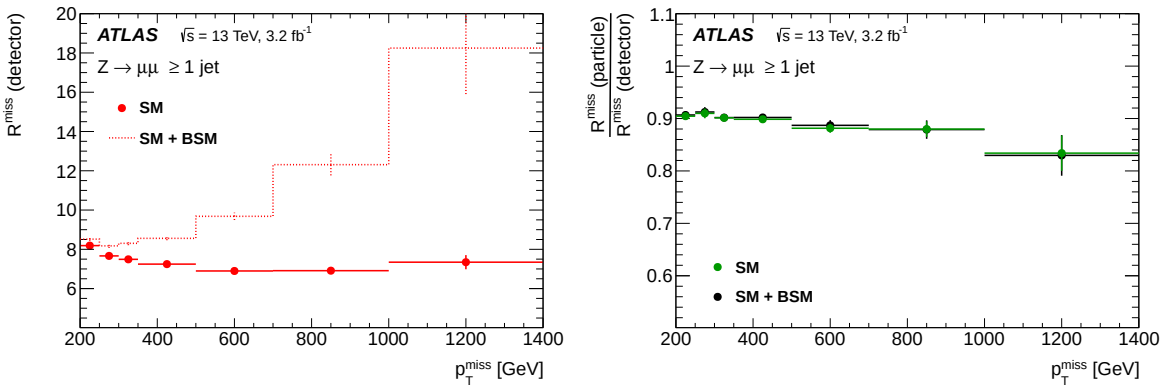


(a) (b)

Figure 5.18.: The left hand side shows $R_{miss}$ on detector level with and without injecting a DM signal into the numerator. A strong difference is observed. The right hand side shows detector corrections with and without the signal injected. No significant differences are observed. The DM signal model is a simplified axial-vector mediator model with couplings of $g_q = 1.25$, $g_\chi = 1.25$, a DM mass of $m_\chi = 150\,\text{GeV}$ and a mediator mass of $m_A = 1\,\text{TeV}$ [1]. Error bars indicate statistical uncertainties of the MC samples.

section, backgrounds to the denominator. For the final systematic uncertainties the individual contributions are added in quadrature.

**Lepton efficiency** uncertainties take into account effects from electron reconstruction and identification, isolation and the trigger efficiency. Since no muon trigger is used, it only encompasses reconstruction, identification, and isolation uncertainties for $\mu$. Less relevant but still considered are uncertainties related to the $\tau$ reconstruction, which affect the vetoes. The results are varied within the $\pm 1\sigma$ uncertainties of the individual contributors. The combined lepton efficiency uncertainties are the most important single source of systematic uncertainty for this analysis. They affect the detector corrections, the W-background estimates for the numerator, and all background estimates for the denominator.

**Jet** uncertainties result mainly from the jet energy scale and resolution effects. They affect the background predictions as well the correction factor due to small differences in event selection between numerator and denominator. An example is the overlap removal between leptons and jets in the denominator, which does not apply to the numerator. The results are varied within the $\pm 1\sigma$ uncertainties of the individual contributors.

The item called **$W \to \tau\nu$ from control region** originates in how the $W \to \tau\nu$ background is estimated, cf. Section 5.4.1. The central value for the estimate is the average of predictions using the muon and electron CRs. The spread between the two estimates is taken as the systematic uncertainty.

For the **multijet** estimate in the numerator, the $p_{\text{T}}^{\text{miss}}$ significance cut is varied by $\pm 0.1$ and the spread in the final results is taken as a systematic uncertainty. An additional 50% of the event count of the final predictions is added in quadrature in each bin. It was shown in the validation study, cf. Section 5.4.2, that this uncertainty covers differences between data and prediction and it is also recommended by the authors of the tool based on previous analyses [131, 133].

| **Systematic uncertainty source** | Low $p_{\mathrm{T}}^{\mathrm{miss}}$ [%] | High $p_{\mathrm{T}}^{\mathrm{miss}}$ [%] | Low $m_{\mathrm{jj}}$ [%] | High $m_{\mathrm{jj}}$ [%] |
|---|---|---|---|---|
| Lepton efficiency | +3.5, −3.5 | +7.6, −7.1 | +3.7, −3.6 | +4.6, −4.4 |
| Jets | +0.8, −0.7 | +2.2, −2.8 | +1.1, −1.0 | +9.0, −0.5 |
| $W \to \tau\nu$ from control region | +1.2, −1.2 | +4.6, −4.6 | +1.3, −1.3 | +3.9, −3.9 |
| Multijet | +1.8, −1.8 | +0.9, −0.9 | +1.4, −1.4 | +2.5, −2.5 |
| Correction factor statistical | +0.2, −0.2 | +2.0, −1.9 | +0.4, −0.4 | +3.8, −3.6 |
| $W$ statistical | +0.5, −0.5 | +24, −24 | +1.1, −1.1 | +6.8, −6.8 |
| $W$ theory | +2.4, −2.3 | +6.0, −2.3 | +3.1, −3.0 | +4.9, −5.1 |
| Top cross-section | +1.5, −1.8 | +1.3, −0.1 | +1.1, −1.2 | +0.5, −0.4 |
| $Z \to \ell\ell$ backgrounds | +0.9, −0.8 | +1.1, −1.1 | +1.0, −1.0 | +0.1, −0.1 |
| **Total systematic uncertainty** | +5.2, −5.2 | +27, −26 | +5.6, −5.5 | +14, −11 |
| **Statistical uncertainty** | +1.7, −1.7 | +83, −44 | +3.5, −3.4 | +35, −25 |
| **Total uncertainty** | +5.5, −5.4 | +87, −51 | +6.6, −6.5 | +38, −27 |

Figure 5.19.: The table shows the contributions of the different uncertainties detailed in the text for the lowest and highest $p_{\mathrm{T}}^{\mathrm{miss}}$ bin in the >= 1 jet kinematic region and for the lowest and highest $\mathrm{m}_{jj}$ bin in the VBF kinematic region [1].

**Correction factor statistical** and **W statistical** account for the finite MC sample size in the derivation of the unfolding factors $\mathrm{C}_Z$ and the W background estimates.

**W theory** encompasses a variety of theoretical uncertainties that affect the extrapolation from the W CR to the SR and hence the W background prediction. For this, factorisation, renormalisation, resummation, and CKKW scales are varied within their bands of uncertainty [134, 135]. The former three are varied by -50% and +100% and the latter from the nominal value of 20 GeV to 15 GeV and 30 GeV. This affects SR and CR in similar ways, hence these contributions are treated as fully correlated between the regions. PDF uncertainties were obtained from the default PDF set and two other sets[1], and applying the recommended uncertainty prescription on each. The envelope of the results obtained from this is taken as the total PDF uncertainty. An uncertainty on the strong coupling constant $\alpha_s$ is obtained by varying its value. The nominal value of 0.118 is varied to 0.117 and 0.119 and the spread in the results is the final uncertainty. Lastly parton shower modelling uncertainties are included by using two different versions of Sherpa MC[2] which generate parton showers differently. The difference in predictions is taken as an uncertainty.

**Top cross-section** uncertainties were added, because a disagreement of data and MC of up to 30% was observed in a top-enriched control region. The 30% are taken as a systematic uncertainty.

The way the backgrounds to the denominator are estimated lead to an additional uncertainty named $\mathbf{Z \to ll}$ **backgrounds**. As explained in Section 5.5, part of the background estimate is fitting a polynomial to the ratio of data and MC in the CR. The difference between this corrected estimate and the nominal MC prediction is taken as an uncertainty.

### Forming and Combining the Ratio

The $\mathrm{C}_Z$ unfolding factors are applied to all bins in all distributions of the two denominators measured in data separately after performing the background subtraction. The denominators

[1] default: NNPDF3.0nnlo [103]; variations: MMHT2014 [104] and CT14 [102]
[2] Versions v2.1 and v2.2.0

are combined statistically to yield an average for $Z \to l^+l^-$ for one lepton flavour. This is performed using the best linear unbiased estimate with the BLUE method [136], which allows for a treatment of correlations of uncertainties.

The combination is iterated once after replacing the statistical uncertainties on the data of the two channels with those coming from the first combination. This counteracts a potential bias in the combination arising from statistical fluctuations, which give one channel a weigh that is too large. A bootstrap method [137] accounts for bin-by-bin statistical fluctuations. Most sources of systematic uncertainty are treated as fully correlated due to being independent of whether electrons or muons are selected for the lepton pair. An exception is the background uncertainty coming from the fit method detailed in Chapter 5.5. It is taken as fully correlated between bins if the background fit increases the event yield in a bin with respect to the original MC estimate. It is taken as fully anti-correlated, the event yield decreases with the fit. Correlations between electron and muon efficiency uncertainties were treated on a case-by-case basis depending on the source.

Taking into account all distributions, the p-value for the compatibility is 74% between the two channels.

All background subtracted distributions of the numerator are divided by background subtracted distributions of the combined denominator, which yields the ratio. Systematic uncertainties between numerator and combined denominator are assumed to be fully correlated. The combination was cross-checked with a maximum likelihood method. The results are found to be consistent.

### Uncertainties on the Ratio

All sources of uncertainty are summarised in Figure 5.19 and given for four different regions of phase-space. "Low" and "High" $p_{\mathrm{T}}^{\mathrm{miss}}$ ($\mathrm{m}_{jj}$) refers to lowest and highest bin in $p_{\mathrm{T}}^{\mathrm{miss}}$ ($\mathrm{m}_{jj}$). The impact of the individual sources is shown in Figure 5.20 for the four measured distributions as a ratio to nominal.

Some observations about the uncertainties can be made:

- The jet uncertainties cancel to a large extend and mostly are subdominant, due to the fact that numerator and denominator are so similar [128]. An exception is the high $\mathrm{m}_{jj}$ bin.
- The uncertainties of lepton efficiencies are relevant in the whole phase space and do not cancel, because charged lepton selections are different in numerator and denominator.
- For large values of $p_{\mathrm{T}}^{\mathrm{miss}}$ and $\mathrm{m}_{jj}$ the analysis is statistically limited. This is caused by lower cross-section of the denominator.
- Although the uncertainties on the multijet estimate are large (more than 50% in each bin), their impacts on the final results are small because of the absolute size of this background.

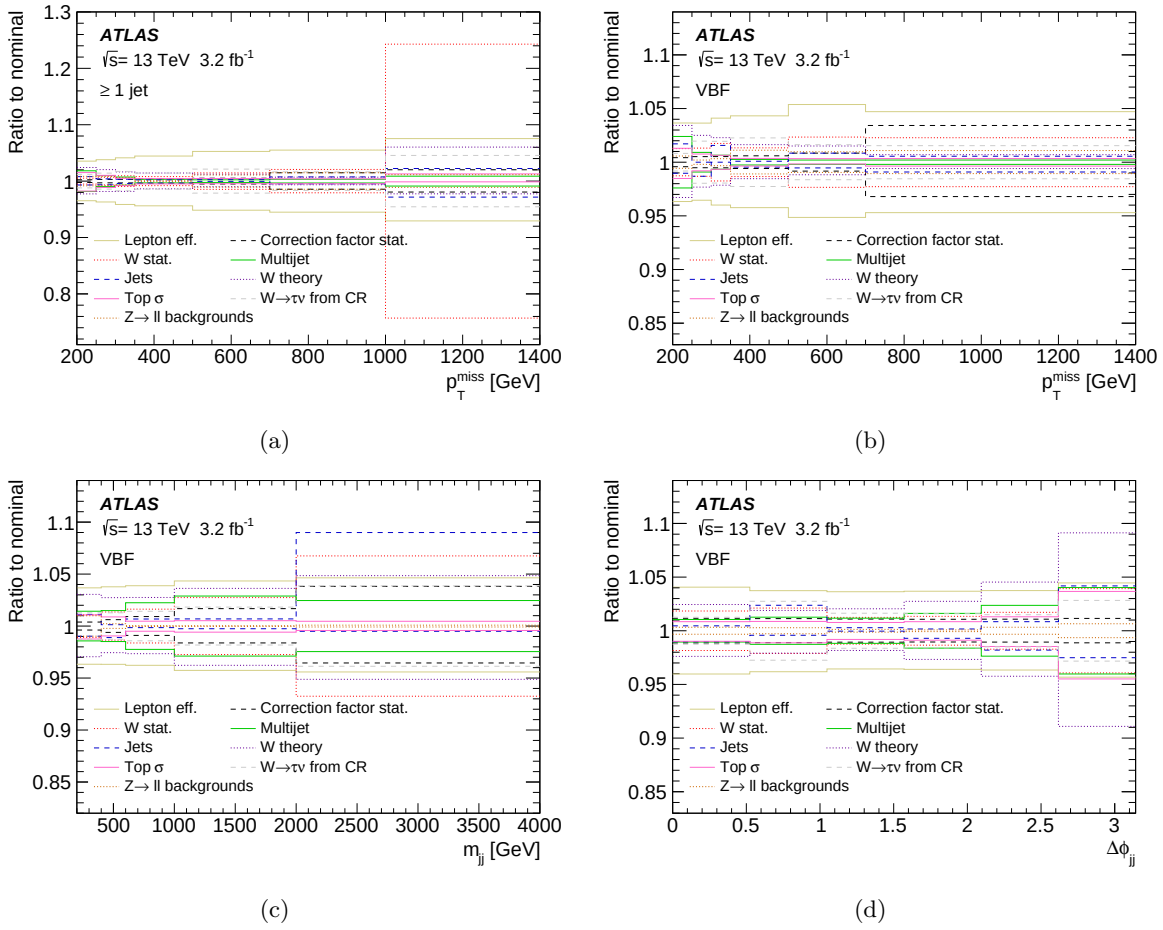


Figure 5.20.: Shown are the impacts of various sources of systematic uncertainty for the four measured differential distributions: $p_{\mathrm{T}}^{\mathrm{miss}}$ in the $\geq 1$ kinematic region, and $p_{\mathrm{T}}^{\mathrm{miss}}$, $\mathrm{m}_{jj}$, and $\Delta\phi_{jj}$ in the VBF kinematic region [1].

## 5.8. Results and Interpretation

After background subtraction, unfolding, combining, and ratio taking the final detector-corrected distributions with sensitivity to various DM models are obtained. They are the main and results of this analysis together with their correlation matrices. They have been uploaded to the online database HEP-Data and are at the disposal of other scientists to compare them to predictions from new physics models on particle level. They can also be used by other experimental groups for independent cross-checks.

The unfolded distributions of the four differentially measured variables can be seen in Figure 5.21. They are compared to various representative Dark Matter models, which were introduced in Section 2.3. More information on these models in the context of limit setting can be found in Section 5.8.1. Figure 5.22 shows the systematic and statistical correlations between all bins of all four distributions.

The SM prediction is taken from MC and shows a falling distribution in $p_{\mathrm{T}}^{\mathrm{miss}}$ for both kinematic regions approaching the value 5.9. This value is expected from a ratio of inclusive SM cross

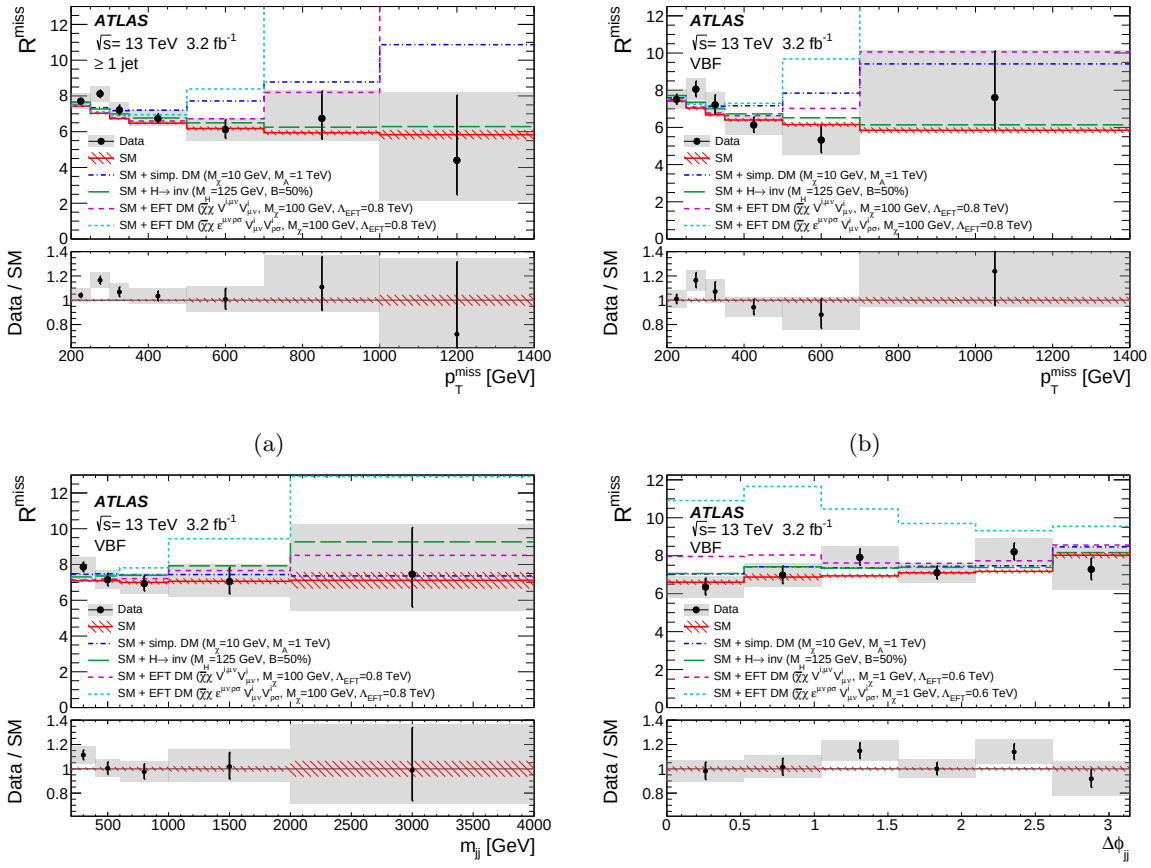


Figure 5.21.: The final unfolded results. $R_{miss}$ in the four measured distributions: $p_T^{miss}$ in the $\geq 1$ kinematic region, and $p_T^{miss}$, $m_{jj}$, and $\Delta\phi_{jj}$ in the VBF kinematic region [1]. Shown are the data and predictions from the SM and four BSM scenarios explained in Section 5.8.1. Error bars indicate statistical uncertainties of the data and error bands the systematic uncertainties introduced in Section 5.7.

sections. The falling shape can be explained by fiducial volume of the measurement, i.e. the lepton acceptances in the denominator. Charged leptons (e, $\mu$) are only reconstructed and identified in the central region of the detector ($\eta \lesssim 2.5$). Larger values of $p_T^{miss}$ correspond to a larger $p_T$ of the decaying Z boson and hence more central decay products. For lower values of $p_T^{miss}$ the denominator has on average smaller values, hence the leptons are more often out of the detector acceptance. Therefore the ratio has larger values.

The data are consistent with the SM prediction: the p-value [84] is 22% taking into account all distributions and all statistical and systematic correlations.

As was alluded to in Section 5.1, the four distributions have different constraining powers depending on the DM model. For instance, the simplified s-channel mediator WIMP model, in dark blue, can be constrained by the two $p_T^{miss}$ distributions, whereas the $m_{jj}$ distribution is insensitive to it. The opposite is true for the invisible Higgs decays, in the plot in green. Because of the VBF production mode of this model, $m_{jj}$ has the highest discrimination power and the $p_T^{miss}$ distributions are very close to the SM predictions. The two EFT models in magenta and

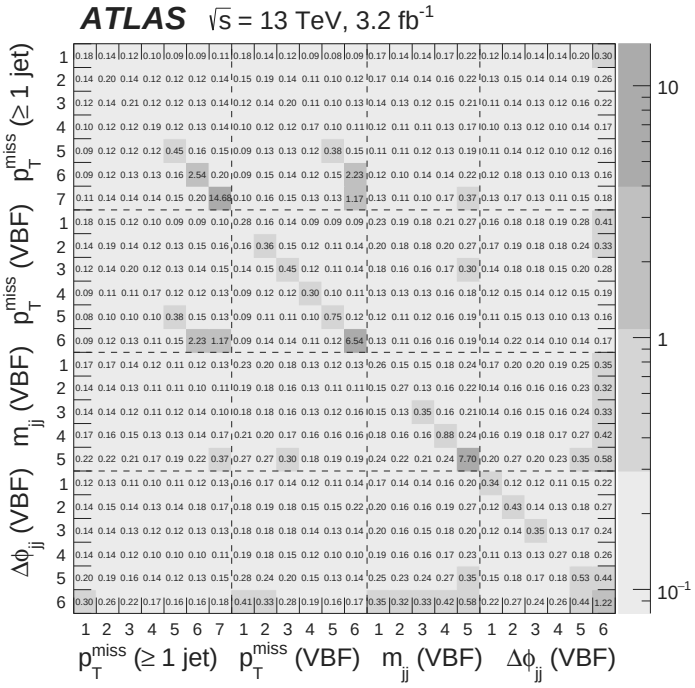


(a)

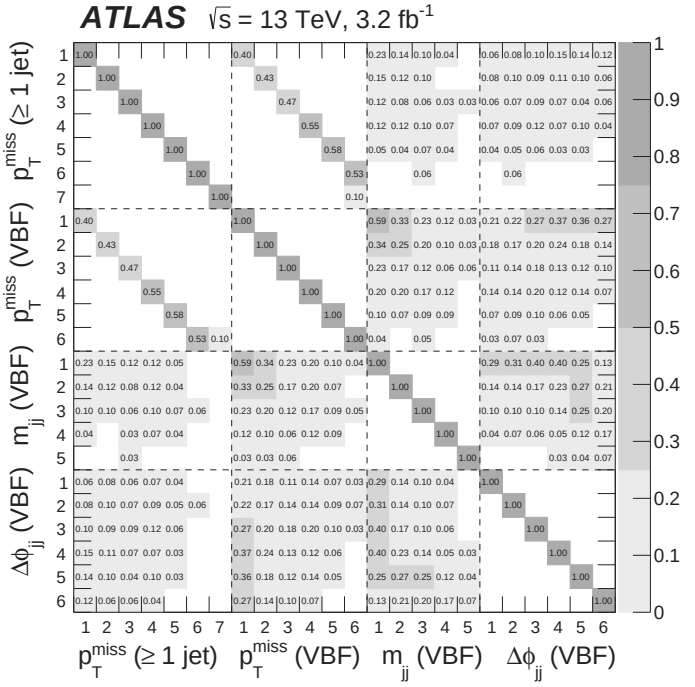


(b)

Figure 5.22.: This figure shows (a) the covariance matrix and (b) the statistical correlation matrix of the four measured distributions. Each entry corresponds to the degree of covariance (correlation) between the bins of the distributions indicated at the axes [1].

light blue differ in the charge-parity properties of the interaction and behave differently in the chosen distributions, especially in $\Delta\phi_{jj}$.

Limits are set on various DM models. Specific examples with fixed parameters are shown in Figure 5.21. For the limit-setting, a $\chi^2$ function [84] is constructed according to

$$\chi^2 = (\mathbf{y}_{\text{data}} - \mathbf{m}_{\text{pred}})^T C^{-1} (\mathbf{y}_{\text{data}} - \mathbf{m}_{\text{pred}}). \tag{5.12}$$

$\mathbf{y}_{\text{data}}$ is the vector of measured $\text{R}_{\text{miss}}$ values in all bins and all distributions, $\mathbf{m}_{\text{pred}}$ is the vector of predicted values of $\text{R}_{\text{miss}}$ coming from a specific model, either SM or BSM. $C$ is the total covariance matrix, which takes all statistical and systematic correlations into account, cf. Figure 5.22. For the derivation of upper limits, the $\text{CL}_s$ technique is used [138, 139]. Limits on three different classes of DM models are set: a simplified WIMP model with fixed couplings and varying s-channel axial-mediator and DM particle masses, two effective field theories in which the SM and DM interact only via weak bosons, and invisible Higgs-boson decays.

### 5.8.1. Limits on Beyond the Standard Model Theories

#### Simplified WIMP Axial S-Channel Mediator Model

For the simplified model fixed values for the couplings of the mediator to quarks ($\text{g}_q = 0.25$) and to the Dark Matter particles ($\text{g}\chi = 1$) are chosen as motivated in Section 2.3. Limits are set in the plane of mediator mass $\text{m}_A$ and Dark Matter particle mass $\text{m}_\chi$. These four parameters determine the production cross-section of DM. Several analyses have set limits previously on this model, cf. Figure 2.8. The limits from this analysis are compared to limits from the conventional ATLAS $p_{\text{T}}^{\text{miss}}$ + jets search, which studied the same dataset. Expected and observed limits are shown in Figure 5.23. For the former the $\pm\sigma$ bands of uncertainty are added. Three constrains are included: a line that shows points in agreement with measurements of the relic density by WMAP and Planck [140, 141], and a region in which $\text{m}_\chi > \sqrt{\pi/2} m_A$, where perturbative unitarity is violated. Lastly, a line indicates the phase space region in which $\text{m}_A = 2\text{m}_\chi$. Above this line DM particles are too heavy to allow for on-shell pair-production via the mediator decay.

Two features can be observed in comparison to the conventional $p_{\text{T}}^{\text{miss}}$ + jets search. Firstly, the expected and observed limits are stronger for the present analysis along $\text{m}_A = 2\text{m}_\chi$ in the exclusion plot. This is driven by the >= 1 jet kinematic region being more inclusive than the kinematic region considered by the conventional $p_{\text{T}}^{\text{miss}}$ + jets analysis[1]. Also, four differentially measured distributions and the correlations among them are used to constrain new physics. By contrast, the conventional $p_{\text{T}}^{\text{miss}}$ + jets search does not make use of various differentially measured distributions as was discussed in Section 4.1. The second key observation with regards to a comparison is that the expected limit for large mediator masses is weaker than the one from the $p_{\text{T}}^{\text{miss}}$ + jets analysis. This comes from the statistical limitation induced by the lower cross-section of the denominator.

[1] In particlar in terms of $p_{\text{T}}^{\text{miss}}$ and jet cuts. The >= 1 jet kinematic region has a $p_{\text{T}}^{\text{miss}}$ cut of 200 GeV, a leading jet $\text{p}_T$ cut of 120 GeV and no upper limit on the number of allowed jets per event. The 2015 $p_{\text{T}}^{\text{miss}}$ + jets analysis has in its most inclusive SRs a $p_{\text{T}}^{\text{miss}}$ cut of 250 GeV, a leading jet $\text{p}_T$ cut of 250 GeV and allows for at most four jets passing basic object selection requirements.

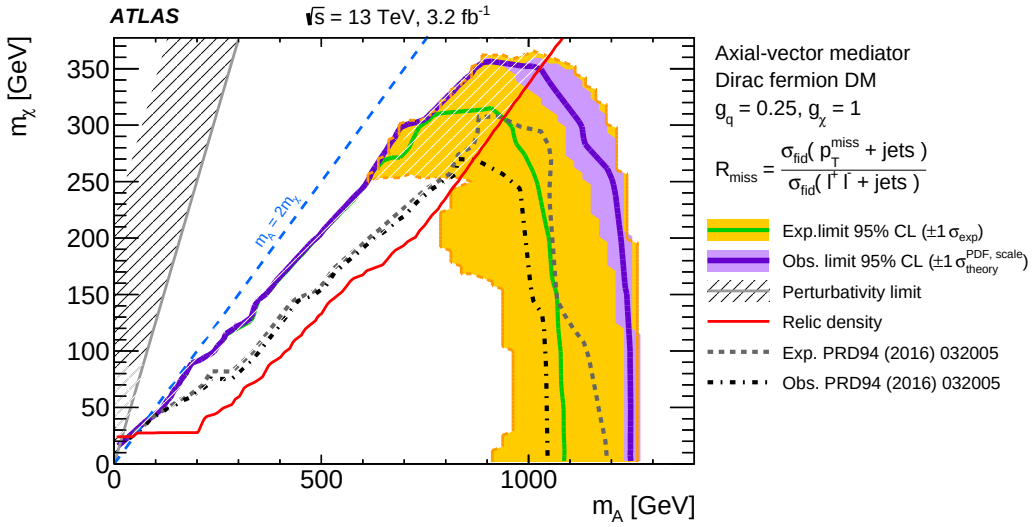


Figure 5.23.: Shown are limits on the simplified model with an axial s-channel mediator [1]. They are compared to limits previously obtained by the conventional $p_{\mathrm{T}}^{\mathrm{miss}}$ + jets search introduced in Section 4.1 and to constrains from other sources detailed in the text. Also shown are uncertainty bands originating in various sources.

It can be seen that the observed limits exclude a larger region at 95% confidence level than the expected limits in the presented analysis. This is especially visible for very large mediator masses and is caused by statistical fluctuations at large values of $p_{\mathrm{T}}^{\mathrm{miss}}$, cf. Figure 5.21. These events provide the most constraining power in this region of the mass-plane.

### Effective Field Theories for Weakly Interacting Dark Matter

Further exclusion limits are set at 95% confidence level on two effective field theory operators, in which DM in the form of Dirac fermions is produced via weak gauge bosons in contact interactions. The limits are set in the plane of Dark Matter mass $\mathrm{m}_\chi$ and the EFT scale $\Lambda$. These parameters determine the DM production cross-section. $\Lambda$ is proportional to the mediator mass in the UV-complete theory via $1/\Lambda^2 \sim g_{SM} g_\chi / M^2$. $g_{SM}$ and $g_\chi$ are the coupling constants of the mediator to the SM and the DM particles, respectively. The two considered operators are $\bar{\chi}\chi V^{\mu\nu} V_{\mu\nu}$ and $\bar{\chi}\chi \epsilon^{\mu\nu\rho\sigma} V_{\mu\nu} V_{\rho\sigma}$ with $V$ as W or Z bosons. The operators are of dimension seven and differ in charge-parity. $\bar{\chi}\chi V^{\mu\nu} V_{\mu\nu}$ is CP conserving and $\bar{\chi}\chi \epsilon^{\mu\nu\rho\sigma} V_{\mu\nu} V_{\rho\sigma}$ CP is violating.

Observed and expected limits are shown in Figure 5.24 and compared to limits set by indirect detection experiments [142–144], cf. Section 2.4. For the CP-conserving operator in (a), the expected 95% confidence level exclusion limits are between 600 GeV and 800 GeV on the EFT scale $\Lambda$ depending on the mass of the DM particles. The observed limits are about 100 GeV stronger. And for the CP-violating operator in (b), the expected limits on $\Lambda$ are between 800 GeV and 1000 GeV and again the observed limits are approximately 100 GeV stronger. For both operators the observed limits are within the uncertainties of the expected limits. The direct detection experiments exclude values of $\Lambda$ between 0 GeV and approximately 150 GeV depending on $\mathrm{m}_\chi$ for both operators.

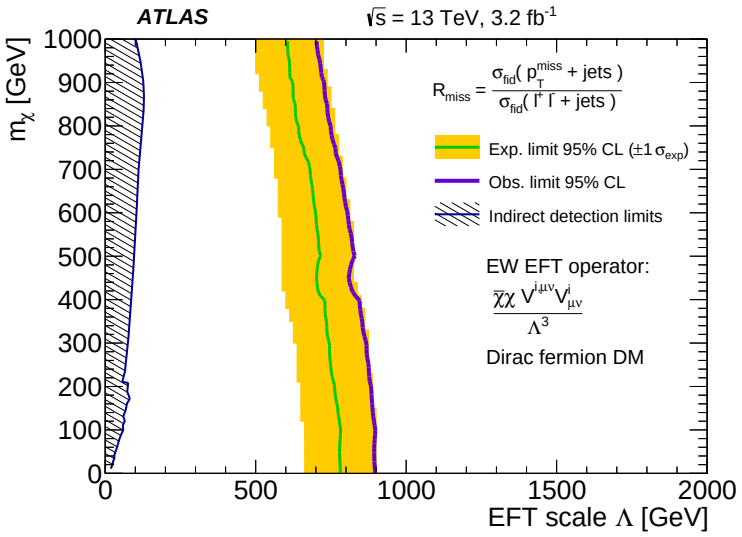


(a)

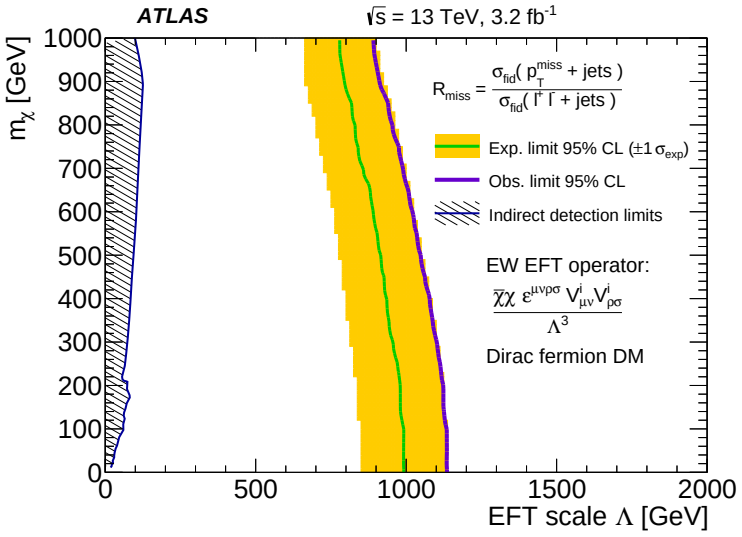


(b)

Figure 5.24.: Limits on two effective field theory operators treating DM as Dirac fermions explained in the text [1]. The contact interaction described by the operator in (a) conserves CP while the operator set limits on in (b) violates it. Limits are set in terms of the DM mass $m_\chi$ and the EFT scale $\Lambda$. They are compared to limits obtained by indirect detection experiments [142–144]. Also shown are uncertainty bands originating in various sources.

Figure 5.21 hints at the reason why the limits on the CP-violating operator are stronger. This operator leads to exotic shapes, which differ significantly from the SM prediction and the data. The predictions from the CP-conserving operator do not differ as much for the same set of parameters. For the limits presented here the operators are assumed to be independent.

### Invisible Decays of the Higgs Boson

95% confidence level exclusion limits are set on invisible decays of the Higgs boson using the four measured differential distributions and their correlations. It can be seen from Figure 5.21 that the $m_{jj}$ distribution on the VBF kinematic region yields the strongest discrimination power. $\Delta\Phi$ adds slightly to the constraint, but in contrast to the other considered models from above the impact of the $p_{\mathrm{T}}^{\mathrm{miss}}$ distributions are close to negligible. Exclusion limits are set as an upper limit on the Higgs boson branching fraction into invisible particles times Higgs boson cross-section normalised to the SM Higgs boson cross-section. The mass is taken as 125 GeV and the expected limit is $0.59^{+0.54}_{-0.12}$ with experimental uncertainties. The observed limit is 0.46. It is stronger because of the systematic uncertainty correlations in the measured distributions which were not considered for the expected limits.

Previously, limits have been set using 20 $\mathrm{fb}^{-1}$ of data collected by the ATLAS experiment at 8 TeV by a dedicated *Higgs-to-invisible* analysis [40]. The dataset size used by this analysis exceeds the one used here roughly by a factor of six, which allows for stronger constraints, 0.31 expected and 0.28 observed. As of now however, the presented analysis yields the best published 13 TeV limits on invisible Higgs decays using the ATLAS detector.

# 6. Studies for Future Improvements

The analysis detailed in Chapter 5[1] will be repeated and extended with a larger dataset and numerous changes to the analysis strategy.

The dataset for the new analysis will encompass the 2016 and 2017 periods of data taking with the ATLAS detector. They contain $35.6\,\text{fb}^{-1}$ (2016) and $46.9\,\text{fb}^{-1}$ (2017) of total recorded integrated luminosity. For the analysis strategy the general idea of an unfolded ratio measurement with sensitivity to new physics persists. There will however likely be more numerators and denominators with various lepton-multiplicities and additional selections. Figure 6.1 shows the five different signal regions, which are considered as future numerators and denominators. The unfolding the strategy will change to *topology unfolding* [145]. This means that instead of unfolding the cross-section related to specific processes, an inclusive event topology is unfolded. This method does not differentiate between signal and background and hence no background subtraction is performed[2]. The advantage is that no uncertainties from background estimates need to be considered and the theory uncertainties can be calculated *a-posteriori*. However, cases in which an object is misidentified as another object, for instance a jet as an electron, are usually baldy modelled in MC. And the unfolding will again rely on MC. Hence, backgrounds coming from these misidentifications, also referred to as *fakes*, will be estimated and subtracted from the results before the detector correction is applied. An example of such a fake background from the previous analysis is the multijet background, which originated in fake $p_{\text{T}}^{\text{miss}}$ from jet mismeasurements, cf. Section 5.3.

The studies presented in this chapter are aimed at enhancing the general performance of the kinematic region with $p_{\text{T}}^{\text{miss}}$ + jets in the final state and at easing the transition to multiple numerators and denominators. Therefore, the signal efficiency of the cutflow is revisited, a new variable that could replace the $p_{\text{T}}^{\text{miss}}$ selection cut is investigated, and boosted decision trees as an event selection tool are explored for improving the sensitivity to electroweak signatures.

## 6.1. Optimising the Multijets Rejection Cut

In the 2015 analysis, the background originating in multijet events was reduced by applying cuts on the azimuthal proximity of the four vector of $\mathbf{p}_{\text{T}}^{\text{miss}}$ and the first four leading jets: $\Delta\phi(\mathbf{p}_{\text{T}}^{\text{miss}}, \text{jet}) > 0.4$. This is also called the multijet rejection cut or the jet-$p_{\text{T}}^{\text{miss}}$ veto. The impact of this cut on multijet and $\text{Z}\rightarrow\nu\nu$ processes is shown in Figure 5.8 and the remaining background was estimated with the data-driven approach explained in Section 5.4.2.

Although the signal efficiency with respect to $\text{Z}\rightarrow\nu\nu$ of the jet-$p_{\text{T}}^{\text{miss}}$ veto is large, $\epsilon_{\text{eff}}^{\text{sig}} = 0.87$, signal events are still rejected. In order to recover signal efficiency, the $p_{\text{T}}^{\text{miss}}$ spectrum of the multijet background can be exploited, because it falls more steeply than in processes with real

[1] In the following referred to as *the 2015 analysis*.
[2] With the exception of backgrounds from *fakes* as detailed below.

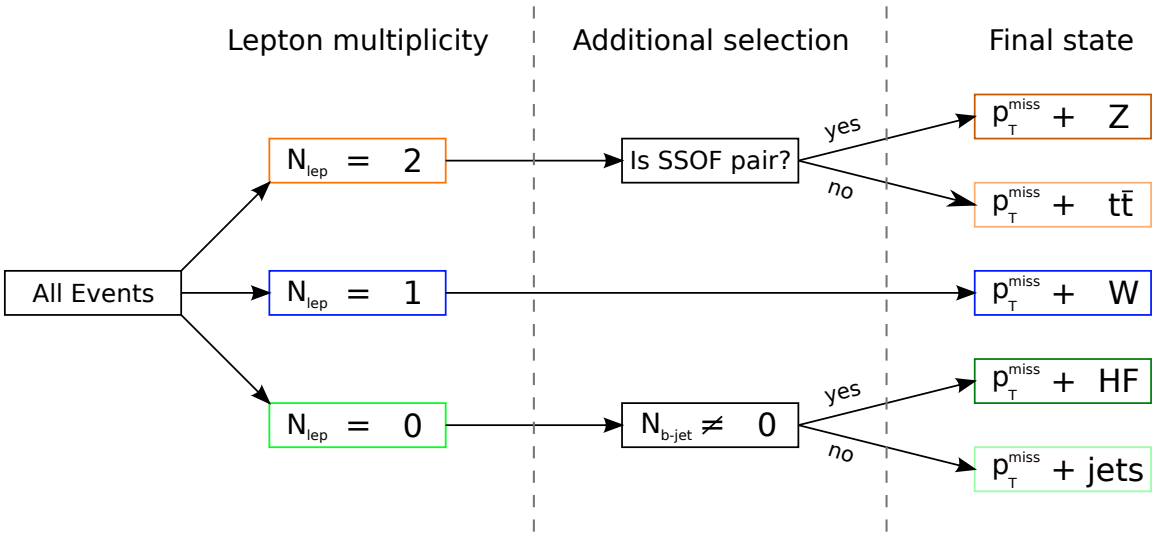


Figure 6.1.: Envisioned signal regions for a second analysis as of November 2017. SSOF stands for *same sign opposite lepton flavour* and HF for *heavy flavour*, which refers to 3rd generation quarks.

$p_{\mathrm{T}}^{\mathrm{miss}}$, cf. Figure 5.15. This is investigated by choosing an adaptive jet-$p_{\mathrm{T}}^{\mathrm{miss}}$ veto that depends on $p_{\mathrm{T}}^{\mathrm{miss}}$.

This study investigates an adaptive cut of the form

$$\Delta\phi(\mathbf{p}_{\mathrm{T}}^{\mathrm{miss}}, \mathrm{jet}_i) > \frac{\mathcal{C}}{p_{\mathrm{T}}^{\mathrm{miss}}}\,, \qquad i = 1, 2, 3, 4\,. \tag{6.1}$$

$\mathcal{C}$ is a constant that impacts the size of the $\Delta\phi$ slice that is used to reject events. Several values for $\mathcal{C}$ are tested. However, to avoid the multijet rejection cut from rejecting or letting pass too many events, the right hand side of Equation 6.1 is constrained to be between 0.1 and 0.4. This means if $\frac{\mathcal{C}}{p_{\mathrm{T}}^{\mathrm{miss}}} > 0.4$ ($< 0.1$) it is fixed to 0.4 (0.1). Cut efficiencies for $Z \to \nu\nu$ + jets and multijet MC using various values of $\mathcal{C}$ can be found in Table 6.1.

The efficiency of the cut in dependence of $\mathcal{C}$ behaves as expected: a low value of $\mathcal{C}$ decreases the impact of the cut leading to a higher survival fraction $\epsilon$ for both processes. A larger value leads to a stronger impact with a lower $\epsilon$. It can also be observed that $\mathcal{C} = 40\,\mathrm{GeV}$ leads to

| $\mathcal{C}$ [GeV] | $\epsilon(Z \to \nu\nu)$ | $\epsilon$(multijet) |
|---|---|---|
| 40 | 0.93 | 0.13 |
| 80 | 0.89 | 0.04 |
| 120 | 0.87 | 0.03 |
| Default (as in 2015 analysis) | 0.87 | 0.03 |

Table 6.1.: Efficiencies of the multijet rejection cut for $Z \to \nu\nu$ + jets and multijet MC for different values of $\mathcal{C}$. The entry at the bottom shows the efficiency of the cut using a fixed difference in azimuthal angle of 0.4 rad as it was used in the 2015 analysis, cf. Section 5.3.

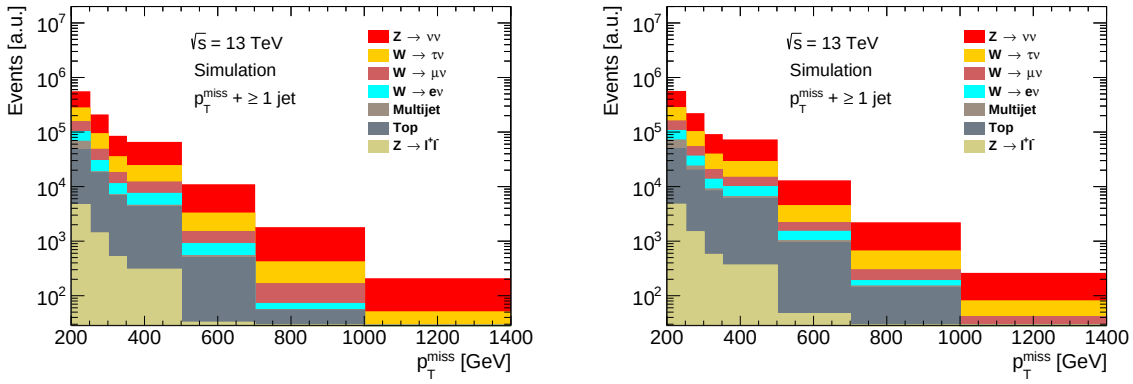


(a) (b)

Figure 6.2.: $p_{\mathrm{T}}^{\mathrm{miss}}$ distributions in the $\geq 1$ jet kinematic region for the relevant processes using MC. In (a) the jet-$p_{\mathrm{T}}^{\mathrm{miss}}$ veto of the 2015 analysis was applied as a part of the cutflow. In (b) the adaptive cut motivated in the text with $\mathcal{C} = 80\,\mathrm{GeV}$ was used. Differences in shape and normalisation are small but present.

a disproportional increase of $\epsilon(\text{multijet})$ with respect to $\epsilon(Z \to \nu\nu)$ when comparing to the default cut of the 2015 analysis. Thus $\mathcal{C} = 40\,\mathrm{GeV}$ is impracticable and was not studied further. $\mathcal{C} = 120\,\mathrm{GeV}$ has similar efficiencies as the default cut. Hence $\mathcal{C} = 80\,\mathrm{GeV}$ was considered in the following.

Figure 6.2 shows $p_{\mathrm{T}}^{\mathrm{miss}}$ distributions in the $\geq 1$ jet kinematic region after applying either (a) the default jet-$p_{\mathrm{T}}^{\mathrm{miss}}$ veto or (b) Equation 6.1 with $\mathcal{C} = 80\,\mathrm{GeV}$. A small difference in agreement with the expectation can be seen. Using the adaptive cut the total event yield is larger compared to the default. Since more events from both $Z \to \nu\nu$ + jets[1] and multijet processes pass the cuts, it is not obvious whether the analysis selection benefits from an adaptive multijet rejection cut. The multijet background is wanted to be small with respect to the other processes, because it will be subtracted from the results before unfolding. Hence bin-by-bin significances are investigated and shown in Table 6.2. The significance is defined as $\mathrm{sig} = \sqrt{2 \cdot ((s+b)\log(1+s/b) - s)}$ [146] with background $b$ (multijets) signal $s$ (everything else) for each bin comparing the two met-jet vetoes[2]. $b$ is estimated using the smearing method from Section 5.4.2 and $s$ is taken entirely from MC. The significance is always slightly larger for the selection using the adaptive multijet rejection cut.

In conclusion, an improved SM signal efficiency is observed for the adaptive met-jet veto using $\mathcal{C} = 80\,\mathrm{GeV}$. Additionally, the overall bin-counts are higher when using the adaptive veto, which is beneficial for the planned unfolding scheme: the higher the event yield in the signal region the smaller the statistical uncertainties that originate in the unfolding procedure. It was hence chosen to switch to the adaptive jet-$p_{\mathrm{T}}^{\mathrm{miss}}$ veto.

[1] All SM processes are observed to have more events passing the selection when the adaptive cut is applied.
[2] The significance is better known defined as $\mathrm{sig} = s/\sqrt{s+b}$, which is the limit for small signals.

| $p_{\mathrm{T}}^{\mathrm{miss}}$ range [GeV] | Bin significance with default cut | Bin significance with adaptive cut |
|---|---|---|
| 200 - 250 | $753 \pm^{54}_{88}$ | $766 \pm^{55}_{89}$ |
| 250 - 300 | $497 \pm^{33}_{55}$ | $522 \pm^{34}_{56}$ |
| 300 - 350 | $351 \pm^{21}_{34}$ | $378 \pm^{22}_{36}$ |
| 350 - 500 | $353 \pm^{18}_{29}$ | $389 \pm^{19}_{31}$ |
| 500 - 700 | $173 \pm^{8.1}_{13}$ | $197 \pm^{8.8}_{14}$ |
| 700 - 1000 | $77 \pm^{4.1}_{6.0}$ | $91 \pm^{4.4}_{6.5}$ |
| 1000 - 1400 | $30 \pm^{2.0}_{2.5}$ | $36 \pm^{2.1}_{2.7}$ |
| 1400 - 2000 | $11 \pm^{2.6}_{3.2}$ | $14 \pm^{2.8}_{3.3}$ |

Table 6.2.: Shown are significances for all of the $p_{\mathrm{T}}^{\mathrm{miss}}$ bins from Figure 6.2. The adaptive cut uses $\mathcal{C} = 80\,\mathrm{GeV}$. The multijet background is estimated using the smearing method, cf. Section 5.4.2. The uncertainty is a combination of the statistical uncertainty from the MC samples that were used and the systematic uncertainty on the multijet estimate as explained in Section 5.7.

## 6.2. Studies of $H_{\mathrm{T}}^{\mathrm{miss}}$

Including more signal regions with different lepton multiplicities to the analysis increases the amount of required storage space for data and Monte Carlo simulations of the relevant processes. One of the reasons is the treatment of systematic uncertainties, especially for $p_{\mathrm{T}}^{\mathrm{miss}}$. The cause for this is of technical nature and detailed in Appendix C.

The study in this chapter investigates whether a variable can be found that is sensitive to invisible objects with good resolution, while solving the size issue of systematic variations introduced by $p_{\mathrm{T}}^{\mathrm{miss}}$. A promising candidate is $H_{\mathrm{T}}^{\mathrm{miss}}$, which is defined via the the negative vector sum of the four-vectors of all selected objects in the event. *Selected* means that the objects pass the cut criteria, cf. Section 5.2. In the numerator of the 2015 analysis only jets are relevant. Thus the negative vector sum $\mathbf{H}_{\mathrm{T}}^{\mathrm{miss}}$ is defined as

$$\mathbf{H}_{\mathrm{T}}^{\mathrm{miss}} = -\sum_{sel.jets} \mathbf{p}_{T,jet} \tag{6.2}$$

and its value is $H_{\mathrm{T}}^{\mathrm{miss}} = |\mathbf{H}_{\mathrm{T}}^{\mathrm{miss}}|$. $\mathbf{p}_{T,jet}$ is the four vector of a selected jet projected onto the transverse plane. The advantage of this variable is that its systematic variations do not need to be stored separately in the dataset. Instead they can be calculated for each event individually from the already stored variations of the objects that contribute to $H_{\mathrm{T}}^{\mathrm{miss}}$, i.e. jets. A potential disadvantage is a decrease of resolution due to the disregard of soft terms with respect to $p_{\mathrm{T}}^{\mathrm{miss}}$.

The aim of this study is to investigate the correlation between $p_{\mathrm{T}}^{\mathrm{miss}}$ and $H_{\mathrm{T}}^{\mathrm{miss}}$ and to see whether a switch to $H_{\mathrm{T}}^{\mathrm{miss}}$ has a significant impact on the analysis. This was investigated for the numerator of the 2015 analysis.

Figure 6.3 shows $p_{\mathrm{T}}^{\mathrm{miss}}$-$H_{\mathrm{T}}^{\mathrm{miss}}$ correlations for Z$\rightarrow \nu\nu$ MC (a) before and (b) after selection cuts of the $\geq 1$ jet kinematic region are applied. A linear dependence can be seen. Furthermore, a comparison between (c) data collected by the ATLAS experiment in 2016 ($33.3\,\mathrm{fb}^{-1}$) and (d)

[1] $H_{\mathrm{T}}^{\mathrm{miss}}$ and $E_{\mathrm{T}}^{\mathrm{miss}}$ are limited to 500 GeV.

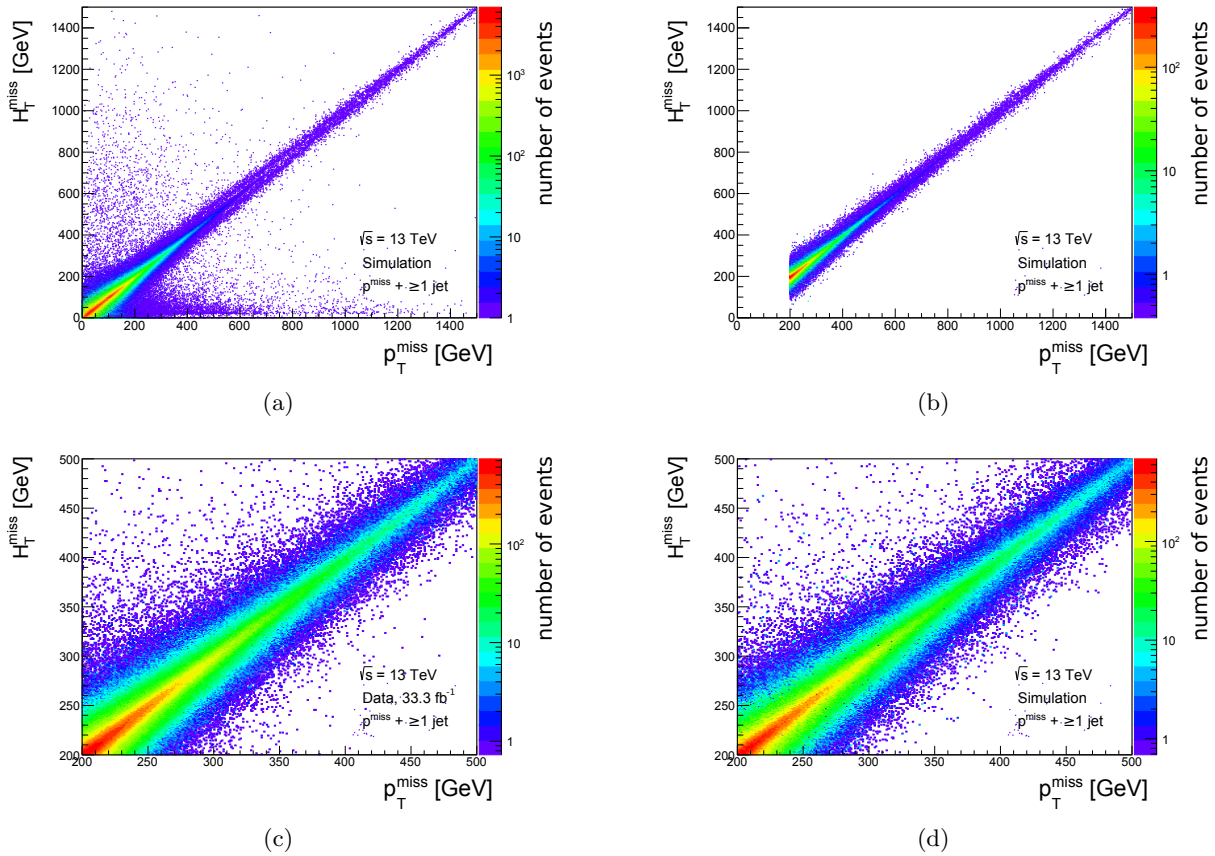


Figure 6.3.: Correlation between $H_{\mathrm{T}}^{\mathrm{miss}}$ and $p_{\mathrm{T}}^{\mathrm{miss}}$ for various scenarios. (a) shows it before and (b) after selection cuts of the $\geq 1$ jet kinematic region of the 2015 analysis using Z$\rightarrow \nu\nu$ + jets MC simulation. (c) shows data and (d) shows combined MC simulation (Z$\rightarrow \nu\nu$, Z$\rightarrow \tau\tau$, Z$\rightarrow \mu\mu$, Z$\rightarrow$, W$\rightarrow \tau\nu$, W$\rightarrow \mu\nu$, W$\rightarrow e\nu$) in the blinded SR, thus $p_{\mathrm{T}}^{\mathrm{miss}}$ is limited to 500 GeV.

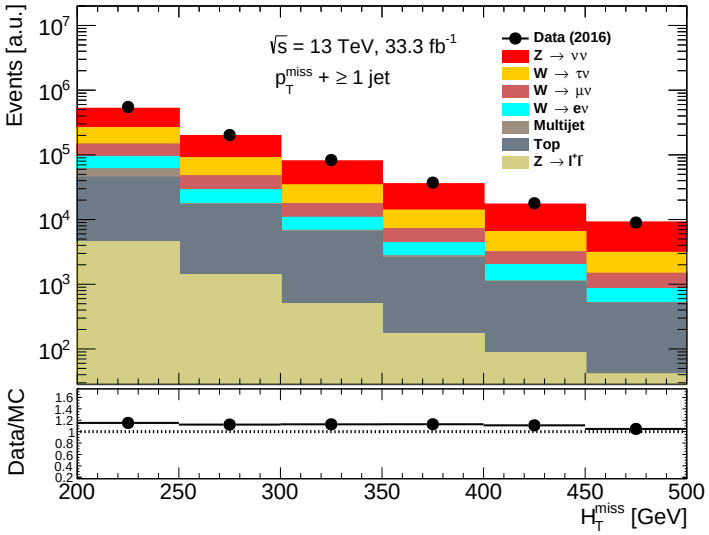


Figure 6.4.: The $H_{\mathrm{T}}^{\mathrm{miss}}$ distribution in the blinded $\geq 1$ jet kinematic region for data collected by the ATLAS experiment in 2016 (33.3 fb$^{-1}$) and MC. The ratio panel shows data/MC and the error bars. Statistical uncertainties on the data are too small to be visible in this plot.

MC is shown and similar behaviour can be seen. The signal region is still blinded[1], hence the limited reach of the plots.

Using $H_{\mathrm{T}}^{\mathrm{miss}}$ instead of $p_{\mathrm{T}}^{\mathrm{miss}}$ also has implications for the jet-$p_{\mathrm{T}}^{\mathrm{miss}}$ veto, which instead becomes a jet-$H_{\mathrm{T}}^{\mathrm{miss}}$ veto using the same cone-size as in the default case.

Figure 6.4 shows the $H_{\mathrm{T}}^{\mathrm{miss}}$ distribution for the 2016 data and MC in the blinded $\geq 1$ jet kinematic region. Here, the multijet rejection cuts have been modified to $\Delta\phi$ ($\mathbf{H}_{\mathrm{T}}^{\mathrm{miss}}$, jet) $> 0.4$ for the first four leading jets. The agreement between data and MC in $H_{\mathrm{T}}^{\mathrm{miss}}$ is comparable to the agreement in $p_{\mathrm{T}}^{\mathrm{miss}}$, cf. appendix D. The observed disagreement of approximately 15% is expected and can be improved by using data-driven techniques instead of MC.

The conclusion of this study is that $p_{\mathrm{T}}^{\mathrm{miss}}$ and $H_{\mathrm{T}}^{\mathrm{miss}}$ show a strong linear dependence and look similar in data and MC. Furthermore, the $H_{\mathrm{T}}^{\mathrm{miss}}$ distribution shows a similar agreement between data and MC as the $p_{\mathrm{T}}^{\mathrm{miss}}$ distribution. Hence, a switch to $H_{\mathrm{T}}^{\mathrm{miss}}$ in favour of smaller dataset sizes so far seems possible without decreasing performance. However, more potential challenges need to be investigated, such as the behaviour of $H_{\mathrm{T}}^{\mathrm{miss}}$ when also including leptons in its definition, comparisons between data and MC in more variables, and $p_{\mathrm{T}}^{\mathrm{miss}}$ trigger efficiencies in dependence of $H_{\mathrm{T}}^{\mathrm{miss}}$.

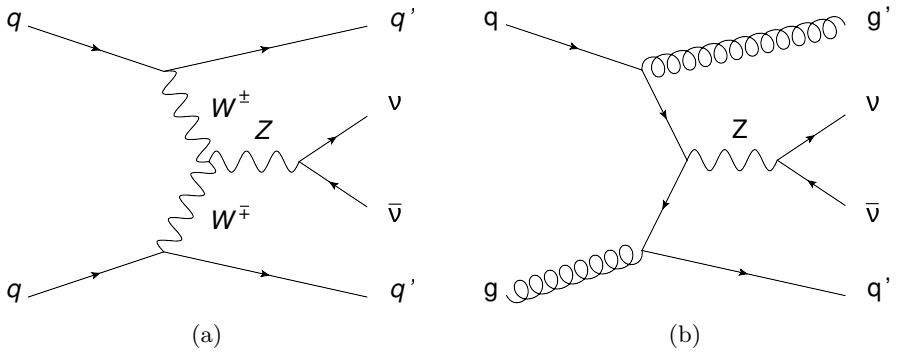


Figure 6.5.: Representative leading order Feynman diagrams for the process Z→ $\nu\nu$ + jets. (a) shows the EWK production via VBF and (b) the QCD production of the Z-boson.

## 6.3. Multivariate Optimisation and Quark-Gluon Tagging

Multivariate analysis (MVA) techniques such as boosted decision trees (BDTs) are useful tools for pattern recognition, cf. Section 4.2.4. MVA-assisted analyses have the potential to replace or complement purely cut-based analyses such as the 2015 analysis. This study[1] investigates whether the analysis can benefit from an MVA regarding to sensitivity towards electro-weak signatures. The VBF kinematic region is used as a baseline without applying the cut on $m_{jj}$ and the central jet veto, because this information might serve as inputs to the MVA.

BDTs are constructed and significance gains with respect to the default cut analysis are investigated. This is done both using *truth/particle* level and *recontruction* level information of the event. The former is used for estimating the optimal gain, when the MVA has access full information on the event before detector effects introduce inefficiencies. A Z $\rightarrow \nu\nu$ + jets MC sample, where the Z is produced purely electroweakly via VBF and semileptonic VV (V = W or Z) diagrams, is used as the signal sample, cf. Figure 6.5 (a). The background sample is composed of Z $\rightarrow \nu\nu$ + jets events in which the Z boson is produced in other, non-electroweak, topologies, cf. Figure 6.5 (b). In the following the former production mode will be referred to as the electroweak (EWK) production of a Z boson and the latter as the strong (QCD) production.

The tested input variables fall into three categories that correspond to ways to discriminate between the EWK and QCD productions of Z-bosons. Some of these aspects were discussed in Section 4.2.3.

- The jets in the final state of the VBF production diagram for Z→ $\nu\nu$ are not initiated by gluons at leading order, cf. Figure 6.5. However, in the QCD production, gluon initiated jets are allowed in the final state. Thus, one category of input variables is sensitive to whether a hadronic jet in the final state is initiated by a quark or a gluon. This is possible experimentally due to slightly different signatures associated with the quark/gluon

[1]Presented in this chapter is a representative selection of results of this study. Several more MVA types have been investigated, such as neural networks, Fisher discriminants, k-nearest neighbours, and others. Other boosting schemes apart from adaptive boost have also been tested. Additionally, more input variables than presented here were considered. For the sake of focus however, these results will not be presented as they do not change the study's conclusion.

| Rank | Variable Identifier | Separation |
|---|---|---|
| 1 | 2nd Jet Initiation via quark/gluon | $1.2 \cdot 10^{-1}$ |
| 2 | 1st Jet Initiation via quark/gluon | $8.7 \cdot 10^{-2}$ |
| 3 | 3rd Jet Initiation via quark/gluon | $3.2 \cdot 10^{-2}$ |
| 4 | 1st Jet y | $1.1 \cdot 10^{-2}$ |
| 5 | 3rd Jet y | $9.4 \cdot 10^{-3}$ |
| 6 | 2nd Jet y | $7.9 \cdot 10^{-3}$ |
| 7 | 3rd Jet $p_{\mathrm{T}}$ | $6.6 \cdot 10^{-3}$ |
| 8 | Truth Jets in Gap with $p_{\mathrm{T}} > 20$ GeV | $6.5 \cdot 10^{-3}$ |

Table 6.3.: Ranking in separation of the variables shown in Figure 6.6.

initiation of a hadronic jet. Jets initiated by gluons for instance tend to produce wider showers containing more particles compared to their quark counterparts [147].

- In contrast to the QCD diagrams there is no colour line connecting the two leading jets in the final state in the VBF case. The existence of a colour line correlates with additional hadronic activity in the rapidity gap between the two leading jets. Thus, the second category of investigated input variables is sensitive to this additional hadronic activity.

- There are kinematic differences between the VBF and QCD productions of Z-bosons, such as an on average larger gap in rapidity between the leading jets in the former case. Kinematic variables are the third category of input variables.

To estimate the potential of using a BDT in a best case scenario, a first set of input variables is selected that makes use of truth level information. Figure 6.6 shows the selected input variables with signal in blue and background in red. The first three variables, *i-th Jet initiation via quark/gluon*, show the quark/gluon initiation of the leading three reconstructed jets using truth information. A value of 0.5 (1.5) indicates jet initiation from a quark (gluon). Values of -0.5 for the third jet indicates the absence of a truth jet in an $\Delta R$ cone of 0.4 around the reconstructed jet. Hence no matching could be performed and the jet is likely to have originated from pile-up. The $\mathrm{p}_T$ of the third leading jet on reconstruction level, *3rd Jet* $p_{\mathrm{T}}$, is also used. Values of zero indicate its absence. The fifth input distribution is the number of truth jets with $\mathrm{p}_T > 20\,\mathrm{GeV}$ in the rapidity gap of the first two leading jets, called *Truth Jets in Gap* $p_{\mathrm{T}} > 20\,GeV$. This variable indicates hadronic activity. Lastly, the rapidity distributions of the first three leading jets, *i-th Jet y*, are used as inputs indicating differences in event kinematic. For *3rd Jet y*, the bin at zero contains events in which no third jet was present. Table 6.3 shows these variables ranked according the their *separation* $\langle S^2 \rangle$, which is defined as

$$\langle S^2 \rangle = \frac{1}{2} \int \frac{(\hat{y}_S(y) - \hat{y}_B(y))^2}{\hat{y}_S(y) + \hat{y}_B(y)} dy, \tag{6.3}$$

where $\hat{y}_S(y)$ and $\hat{y}_B(y)$ are the signal and background distributions of variable $y$ [124]. Larger values $\langle S^2 \rangle$ indicate a stronger difference in shape leading to a better discrimination potential. The largest separation comes from the truth information of the quark/gluon initiation of the jets followed by the rapidities of the jets, the $p_{\mathrm{T}}$ of the third leading jet and the number of truth jets in the rapidity gap.

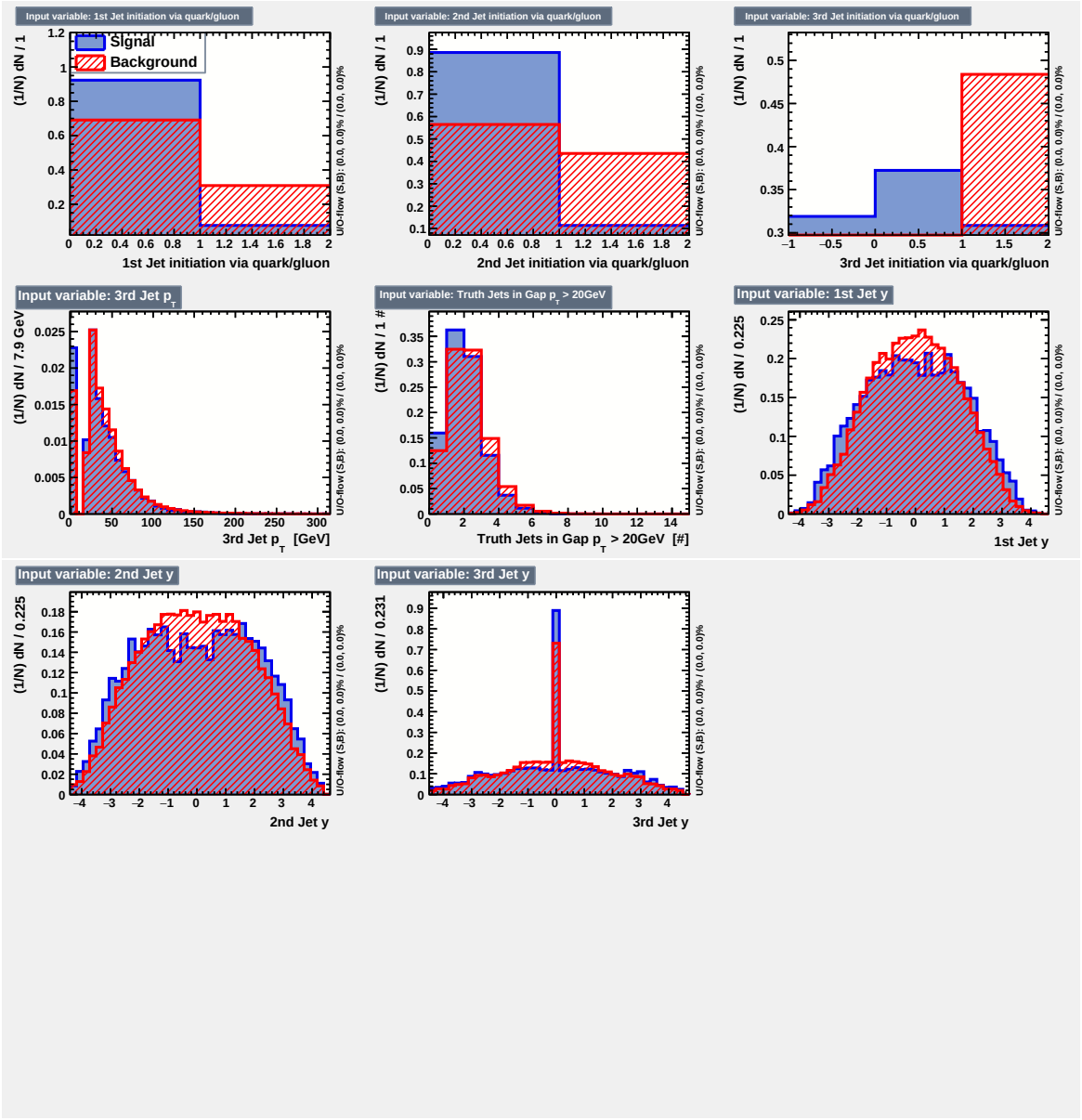


Figure 6.6.: Input variables for a first set of BDTs. Use of event truth information is made, such as the quark/gluon initiation of the first three leading jets and the number of truth jets with $p_{\mathrm{T}} > 20\,\mathrm{GeV}$ in the rapidity gap between the first two leading jets. Also used is the reconstructed $\mathrm{p}_T$ of the third leading jet and the rapidity distributions of the first three leading jets. Spikes at zero for 3rd Jet $p_{\mathrm{T}}$ and 3rd Jet y are due to the absence of a third jet.

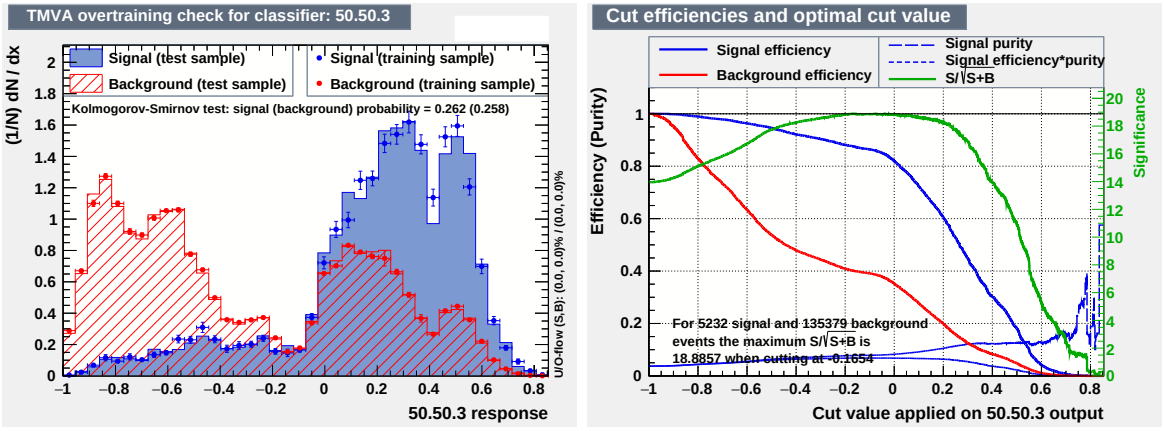


(a) (b)

Figure 6.7.: Shown are the output (a) and the performance (b) of the BDT using the input variables from Figure 6.6 and the parameters $N_{tree} = 50$, $N_{node} = 5\%$ and $Depth_{tree} = 3$.

The construction of BDTs is dependant on three parameters as introduced in Section 4.2.4: the tree depth, the minimum node size in terms of the total dataset size, and the number of trees used for boosting. For this study, multiple combinations of these parameters were systematically tested. A parameter set of 50 trees, 50 per mill minimum node size relative to the total dataset size, and a tree depth of three performs best. Deviating strongly from these values leads either to a decrease in performance or to an *overtraining* of the BDT [124]. A plot showing the convergence of the boost weight with respect to the tree number can be found in appendix E. Stability after 50 trees is observed. Figure 6.7 shows the output and performance of the BDT called 50.50.3 according to its parameters. (a) demonstrates that signal (blue) and background (red) have different response curves leading to a different population of output values. In (b) the signal and background efficiencies, signal purities and the significance can be seen in dependence of the cut value applied on the BDT response. Considering a value on the x-axis of the right hand plot corresponds to cutting at the same value on the left hand side and taking all events with a response larger than it. Consequently, -1 as the cut value applied to the output corresponds to accepting all events and thus to applying no BDT at all. It can be seen that the optimal cut value at approximately -0.17 leads to a significance gain of roughly 35% with respect to applying no BDT. This corresponds to a significance value of 18.9 instead of 14. This is an exemplary best-case estimation for the application of a simple boosted decision tree for this usecase.

For using a BDT in an analysis, the input variables need to be defined on reconstruction level. In a first attempt the inputs from Figure 6.6 were taken and the truth level information was replaced by reconstruction level counterparts. The quark/gluon initiation of the first three leading jets is replaced by the variable N90, which is the number of jet constituents, i.e. clusters, that contribute 90% of its energy. This variable, *i-th Jet N90*, is sensitive to the shower shape of the jet and hence to its initiation mode[1]. The number of truth jets with $p_T > 20\,\text{GeV}$ in the

[1] There is a *quark/gluon tagger* developed by ATLAS, which could be used instead. However, when this study was performed the tagger only made use of tracking information and its application is thus confined to the central region of the detector. Tracking-based variables provide good discrimination for high-$p_T$ jets. However, the interesting region in VBF events is the forward (high-$m_{jj}$) region, where no tracking information is available. Additionally, the events are dominated by low-$p_T$ jets, for which calorimeter based variables perform better [147]. Hence the ATLAS quark/gluon tagger was not used.

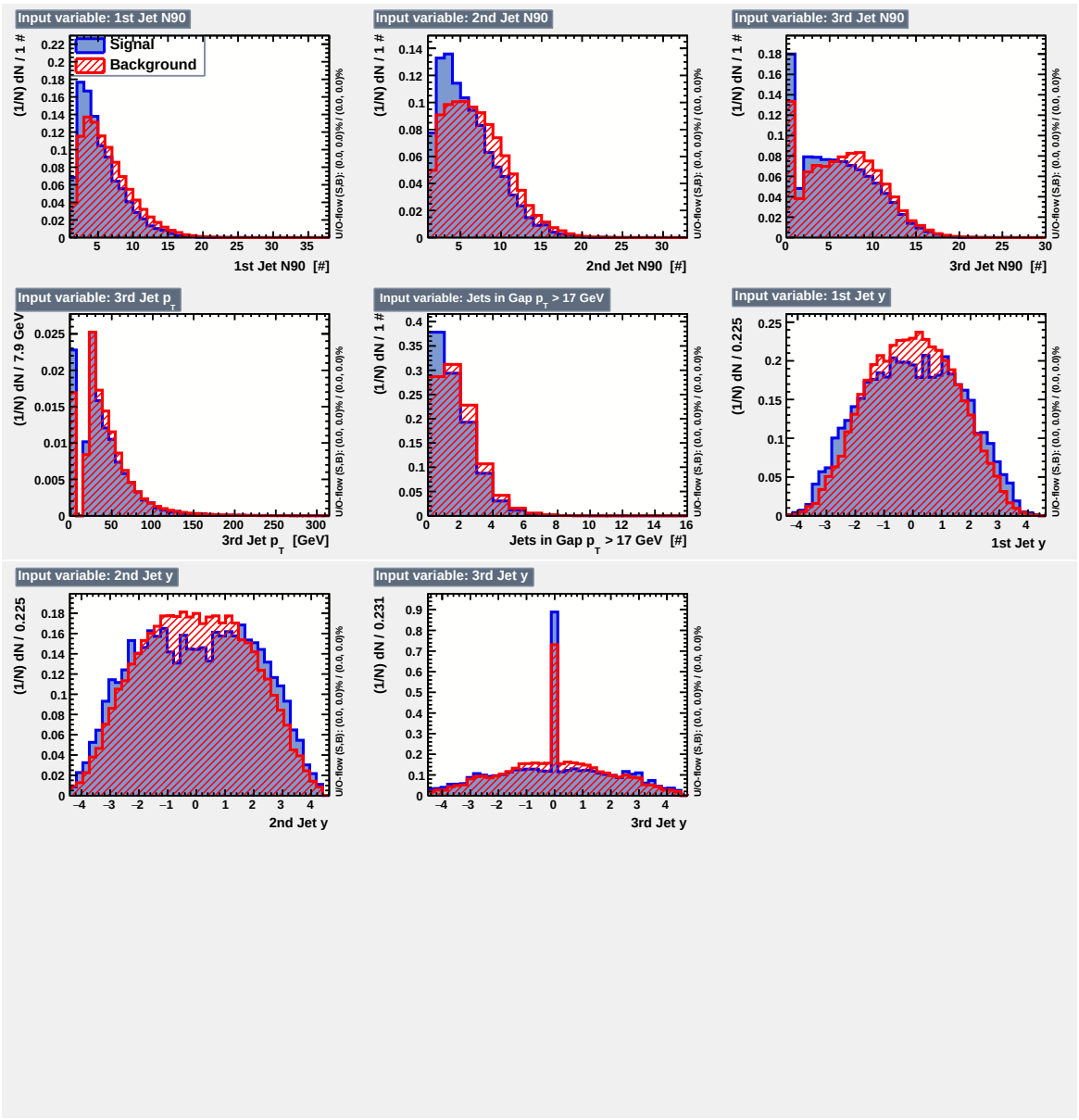


Figure 6.8.: Reconstruction level input variables for a BDT. They were chosen to be as similar as possible to the inputs presented in Figure 6.6 to allow for a comparison of results.

| Rank | Variable Identifier | Separation |
|---|---|---|
| 1 | 1st Jet N90 | $2.3 \cdot 10^{-2}$ |
| 2 | 2nd Jet N90 | $2.1 \cdot 10^{-2}$ |
| 3 | 1st Jet y | $1.1 \cdot 10^{-2}$ |
| 4 | Jets in Event with $p_{\mathrm{T}} > 25$ GeV | $1.1 \cdot 10^{-2}$ |
| 5 | 3rd Jet N90 | $9.6 \cdot 10^{-3}$ |
| 6 | 3rd Jet y | $9.4 \cdot 10^{-3}$ |
| 7 | 2nd Jet y | $7.9 \cdot 10^{-3}$ |
| 8 | 3rd Jet $p_{\mathrm{T}}$ | $6.6 \cdot 10^{-3}$ |

Table 6.4.: Ranking in separation of the variables shown in Figure 6.8.

rapidity gap was replaced by a reconstruction level counterpart. However, the $\mathrm{p}_T$ threshold is 17 GeV, which is the lowest possible value on reconstruction level, because below that jets are not calibrated in ATLAS and pile-up contributions become dominant.

A BDT parameter optimisation is performed similar to above and the same set of parameters is found to perform well. Figure 6.8 shows the input distributions for a BDT defined on reconstruction level input variables and Table 6.4 shows their ranking in separation. It can be seen that the separation power is lower and that N90 does not provide as strong shape differences as the truth information. Figure 6.9 shows BDT output and performance plots. A shape difference in BDT response between signal and background can still be seen. However, the difference is not as pronounced as above in Figure 6.7. The significance gain from applying the BDT is of the order of a few percent.

When using reconstruction level information only, the BDT performs worse. This is because the N90 constituents variable correlates only weakly with the quark/gluon initiation of a jet. In an attempt to mitigate this, more variables are taken as the input to another BDT on reconstruction level, several of which are additional jet shower shape variables. Table 6.5 lists them and shows their ranking in separation. *i-th Jet Width* is the calorimeter width of the jet defined as the energy-weighted distance of jet constituents to its centre. *i-th Jet Num Const* is the total number of constituents of the jet. *i-th Jet Num Tracks* is the number of tracks associated to a jet. $p_{\mathrm{T}}$ *Ratio i-th and j-th Jet* is the ratio of $\mathrm{p}_T$ of the $i$-th leading jet to the $j$-th leading jets. Distributions of all input variables can be found in appendix E. The third leading jet is always required to be in the rapidity gap of the fist two leading jets. Values of zero indicate the absence of a third jet in the rapidity gap in the relevant distributions.

The three BDT parameters are re-optimised and the same set as above shows to be on the performance plateau while not leading to overtraining. Figure 6.10 shows the BDT response (a) and the performance plots (b). The BDT response looks more different for signal and background than the response of the BDT using eight reconstruction level input variables. The significance gain is also larger: approximately 3.5% leading to a maximum significance of 14.6 for a cut value of -0.22. However, the significance gain is still much lower than for the BDT that uses of truth level information. This indicates that the combined shower shape variables lack at accurately predicting the quark/gluon initiation of a jet. Plots indicating the linear correlation coefficients of the 28 input variables for the signal and background samples can be found in appendix E. Clusters of strong correlation are visible suggesting that although more shower shape variables are used the combined benefit is not large. This statement can also be made about the variables indicating additional hadronic activity.

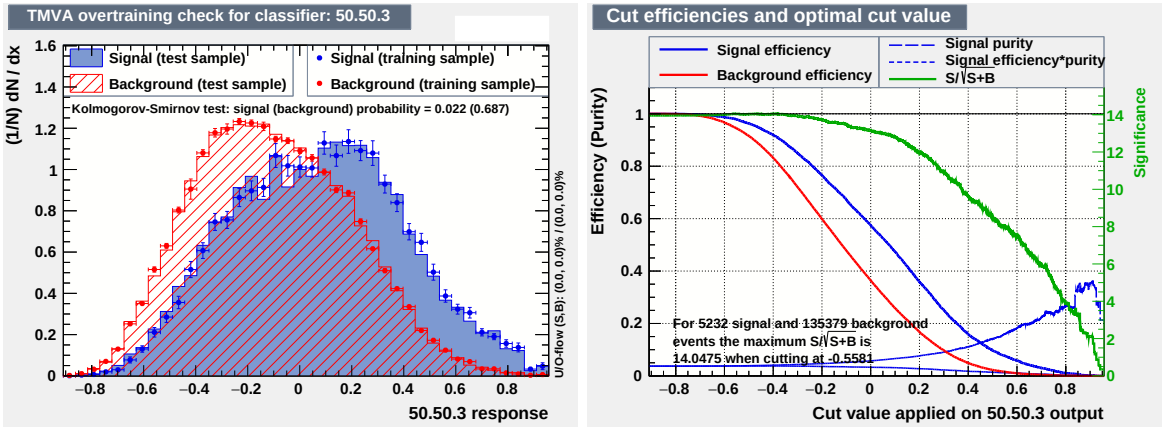


(a) (b)

Figure 6.9.: Shown are the output (a) and the performance (b) of the BDT using the input variables from Figure 6.8 and the parameters $N_{tree} = 50$, $N_{node} = 5\%$ and $Depth_{tree} = 3$.

In summary this study shows that by accessing truth level information about the quark/gluon initiation of hadronic jets the usage of a BDT can lead to an increase of approximately 35% in significance for the discrimination between EWK and QCD $Z \to \nu\nu$ events. However, this significance gain is not reproducible when using reconstruction level variables, which would be necessary for the implementation of a BDT into the analysis. Even the inclusion of a variety of shower shape variables and several kinematic variables, such as $m_{jj}$ and $p_T^{miss}$, is not able to improve the performance to the level of the first presented BDT. Although $m_{jj}$ and $p_T^{miss}$ ranks high in terms of separation by themselves. The best observed significance gain using reconstruction level variables is roughly 3.5%. This small gain does not justify integrating a signal region optimised by a BDT into the analysis.

| Rank | Variable Identifier | Separation |
|---|---|---|
| 1 | $m_{jj}$ | $6.3 \cdot 10^{-2}$ |
| 2 | 2nd Jet Width | $2.9 \cdot 10^{-2}$ |
| 3 | $\Delta\eta$ (1st Jet, 2nd Jet) | $2.8 \cdot 10^{-2}$ |
| 4 | $p_T$ Ratio 1st and 3rd Jet | $2.5 \cdot 10^{-2}$ |
| 5 | $p_T$ Ratio 2nd and 3rd Jet | $2.5 \cdot 10^{-2}$ |
| 6 | 1st Jet Width | $2.3 \cdot 10^{-2}$ |
| 7 | 1st Jet N90 | $2.3 \cdot 10^{-2}$ |
| 8 | 2nd Jet N90 | $2.1 \cdot 10^{-2}$ |
| 9 | $p_{\mathrm{T}}^{\mathrm{miss}}$ | $1.7 \cdot 10^{-2}$ |
| 10 | 1st Jet Num Tracks | $1.7 \cdot 10^{-2}$ |
| 11 | 1st Jet Num Const | $1.3 \cdot 10^{-2}$ |
| 12 | $\Delta\eta$ (2nd Jet, 3rd Jet) | $1.1 \cdot 10^{-2}$ |
| 13 | 3rd Jet Num Tracks | $1.1 \cdot 10^{-2}$ |
| 14 | 2nd Jet Num Const | $1.1 \cdot 10^{-2}$ |
| 15 | 1st Jet y | $1.1 \cdot 10^{-2}$ |
| 16 | Jets in Gap with $p_{\mathrm{T}} > 17$ GeV | $1.1 \cdot 10^{-2}$ |
| 17 | 2nd Jet Num Tracks | $1.0 \cdot 10^{-2}$ |
| 18 | $\Delta\eta$ (1st Jet, 3rd Jet) | $1.0 \cdot 10^{-2}$ |
| 19 | 3rd Jet N90 | $9.6 \cdot 10^{-3}$ |
| 20 | 3rd Jet y | $9.4 \cdot 10^{-3}$ |
| 21 | 1st Jet EM Fraction | $8.1 \cdot 10^{-3}$ |
| 22 | 2nd Jet y | $8.0 \cdot 10^{-3}$ |
| 23 | Jets in Event with $p_{\mathrm{T}} > 25$ GeV | $7.2 \cdot 10^{-3}$ |
| 24 | 3rd Jet $p_{\mathrm{T}}$ | $6.7 \cdot 10^{-3}$ |
| 25 | 2nd Jet EM Fraction | $6.4 \cdot 10^{-3}$ |
| 26 | $p_{\mathrm{T}}$ Ratio 1st and 2nd Jet | $1.4 \cdot 10^{-3}$ |

Table 6.5.: Ranking in separation of reconstruction level variables.

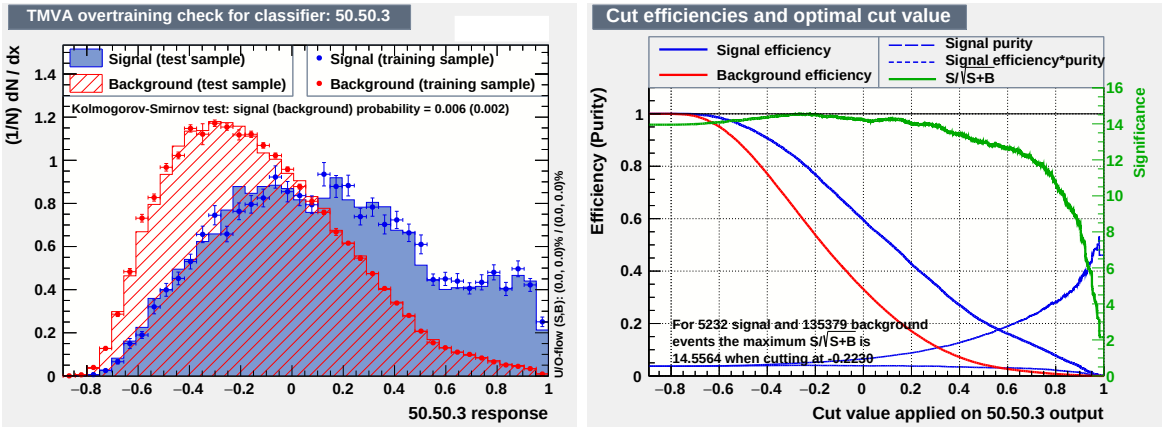


(a) (b)

Figure 6.10.: Shown are the output (a) and the performance (b) of the BDT using the 28 input variables from Table 6.5 and the parameters $N_{tree} = 50$, $N_{node} = 5\%$ and $Depth_{tree} = 3$.

# 7. Summary and Conclusions

This thesis presents the DM puzzle and a novel method for collider searches for DM using final states with $p_{\mathrm{T}}^{\mathrm{miss}}$ and hadronic jets. Shortcomings of the conventional $p_{\mathrm{T}}^{\mathrm{miss}}$ + jets searches are discussed, in particular the difficulty of reinterpreting the results in the context of new models once published. Several techniques are shown to improve $p_{\mathrm{T}}^{\mathrm{miss}}$ + jets collider searches both in terms of reinterpretation and general performance: measuring an unfolded cross-section ratio in terms differential distribution with an additional kinematic region dedicated to processes involving vector boson fusion. Boosted decision trees as an additional option to enhance sensitivity are discussed, too.

The analysis presented in Chapter 5 implements most of these techniques. A fiducial cross-section ratio is measured with $p_{\mathrm{T}}^{\mathrm{miss}}$ + jets in the numerator, which in the case of the SM corresponds to Z$\rightarrow \nu\nu$ + jets. The denominator is defined as $\sigma^{\mathrm{fid}}(Z \rightarrow l^{+}l^{-} + jets)$, which is measured in an electron channel and a muon channel and then combined. The similarity between numerator and denominator leads to the partial cancellation of many uncertainties, including detector effects. This simplifies the subsequent unfolding, which only needs to correct for the charged lepton reconstruction and identification efficiencies of the denominator. In total four different differential distributions in terms of the unfolded cross-section ratio are measured: $p_{\mathrm{T}}^{\mathrm{miss}}$ in a generic $\geq 1$ jet kinematic region and a dedicated VBF kinematic region and $m_{jj}$ and $\Delta\phi_{jj}$ in the VBF region. With these distributions limits can be set without the need for detector simulations. The limits shown here are set on a simplified s-channel axial-vector mediator WIMP model and an improvement in most regions of the $m_{\chi} - m_{A}$ plane with respect to the conventional ATLAS $p_{\mathrm{T}}^{\mathrm{miss}}$ + jets search is observed. For large mediator masses the limits from the cross-section ratio suffer from the low event count in the denominator. Additional limits have been set on invisible decays of the Higgs boson and two EFT operators.

In the future, the analysis will be improved and repeated using a larger data set. Chapter 6 shows three studies that are performed for this next iteration. It is shown that the multijet rejection cuts of the base analysis can be improved by introducing a dependence on the $p_{\mathrm{T}}^{\mathrm{miss}}$ of the event. This leads to significance improvements in all bins and to higher event yields, which is beneficial for the unfolding scheme. $H_{\mathrm{T}}^{\mathrm{miss}}$ as a potential replacement for $p_{\mathrm{T}}^{\mathrm{miss}}$ is studied in order to decrease to size of the datasets that need to be stored in hard disc drives. It is shown that $H_{\mathrm{T}}^{\mathrm{miss}}$ and $p_{\mathrm{T}}^{\mathrm{miss}}$ are strongly linearly correlated and yield similar differential distributions. Lastly, boosted decision trees are studied to potentially improve the performance of the analysis with respect to electroweak signatures, in particular VBF. Three categories of discriminants are identified: the quark/gluon initiation of the leading jets, additional hadronic activity in the central region, and kinematic variables. It is shown that especially the first category yields a strong separation potential. A BDT with access to truth information of the events yields a significance improvement of approximately 35%. However, this significance gain is not reproducible with reconstruction level information only. Even after more than tripling the number of input variables, the maximally found significance gain is roughly 3.5%. This small improvement shows that the analysis cuts were already well optimised.

# A. Samples Used for the Analysis Presented in This Thesis

This appendix[1] summarises the samples used for the analysis and the additional studies presented in this thesis.

For the simulation of events containing $W$ or $Z/\gamma^*$ bosons in association with jets the Sherpa v2.2.0 event generator was used. For up to two additional parton emissions MEs are calculated to NLO and for up to four additional emissions to LO. This was done with the Comix [148] and OpenLoops [149] ME generators merged with the Sherpa parton shower. The merging is performed using an improved CKKW matching procedure [134, 135] and an extension to NLO accuracy is achieved with the Meps@Nlo [150] technique. As the PDF NNPDF3.0nnlo [103] is used in conjunction with parton shower tuning performed by the Sherpa authors. For additional cross checks W/Z + jet events are also simulated using Mg5_aMC@Nlo v2.2.2 [151] interfaced to the Pythia [110] parton shower. NNPDF2.3lo is used together with the A14 tune. For the simulation of properties of bottom and charm hadron decays EvtGen v1.2.0 [152] is used. All W/Z + jet samples are normalised to NNLO cross section predictions.

For the simulation of processes with four electroweak couplings at tree level Sherpa v2.2.1 was used with the CT10nlo [153] PDF set. For fully leptonic diboson processes up to one additional emission emission is considered for $ZZ$ at NLO accuracy and 0 additional emissions for $WZ$, $WW$. At LO accuracy up to three additional emissions are allowed. Semileptonic diboson production and $Vjj$ (V = W,Z) production diagrams (including vector boson fusion) have been generated in combined samples at LO accuracy with one additional emission. These include interference and off-shell effects.

Matrix elements for the production of top-antitop pairs and interactions of single top-quarks in the $Wt$ and s-channels are generated using the Powheg-Box v2 [154] event generator and the CT10nlo PDF sets. Powheg-Box v1 is used for matrix element calculations at NLO for electroweak t-channel single top events using the four-falvour PDF set CT10f4 [153]. Pythia v6.428 and the CTEQ6L1 PDF set [155] with the Perugia 2012 tune [156] are used for PS, hadronisation, and the underlying event. EvtGen v1.2.0 [152] is again used for the simulation of properties of bottom and charm hadron decays. The top-pair and single-top samples are normalised to calculations at NNLO accuracy including soft-gluon resummation at next-to-next-to-leading logarithmic accuracy.

For multijet production via $2 \rightarrow 2$ partonic scattering Pythia v8 was used for the event generation and PS. NNPDF2.3lo and the A14 tune are used. Again EvtGen v1.2.0 [152] is used for the simulation of properties of bottom and charm hadron decays.

Samples for several BSM scenarios are generated. For the WIMP simplified model Powheg-Box v2 is used with an s-channel axial-vector mediator at NLO together with Pythia v8 for PS,

[1] Mostly taken from [1] and [113] and modified.

hadronisation and the underlying event. The NNPDF2.3lo PDF set is used together with the A14 tune. Couplings of the mediator to quarks and DM particles are set to 0.25 and 1 respectively, while a grid of different mediator masses (10 GeV - 2 TeV) and DM particle masses (1 GeV - 1 TeV) is generated. A similar setup but with Powheg-Box v1 and the CT10 PDF set is used for simulations of invisible decays of the Higgs boson via $H \to ZZ \to \nu\nu\nu\nu$. The EFT described in Section 2.3 is generated using MG5_aMC@NLO v2.2.3 [151] with the NNPDF2.3lo PDF set interfaced to PYTHIA v8.

GEANT 4 is used for the full detector simulation of ATLAS for all samples. Pile-up simulation is added to the samples. PYTHIA v8 with the MSTW2008lo PDF set [157] and the A2 parton shower tune [158] is used for these additional proton-proton collisions.

More details can be found in [1] and [113].

# B. Distributions of Smeared Pseudo-Data Set

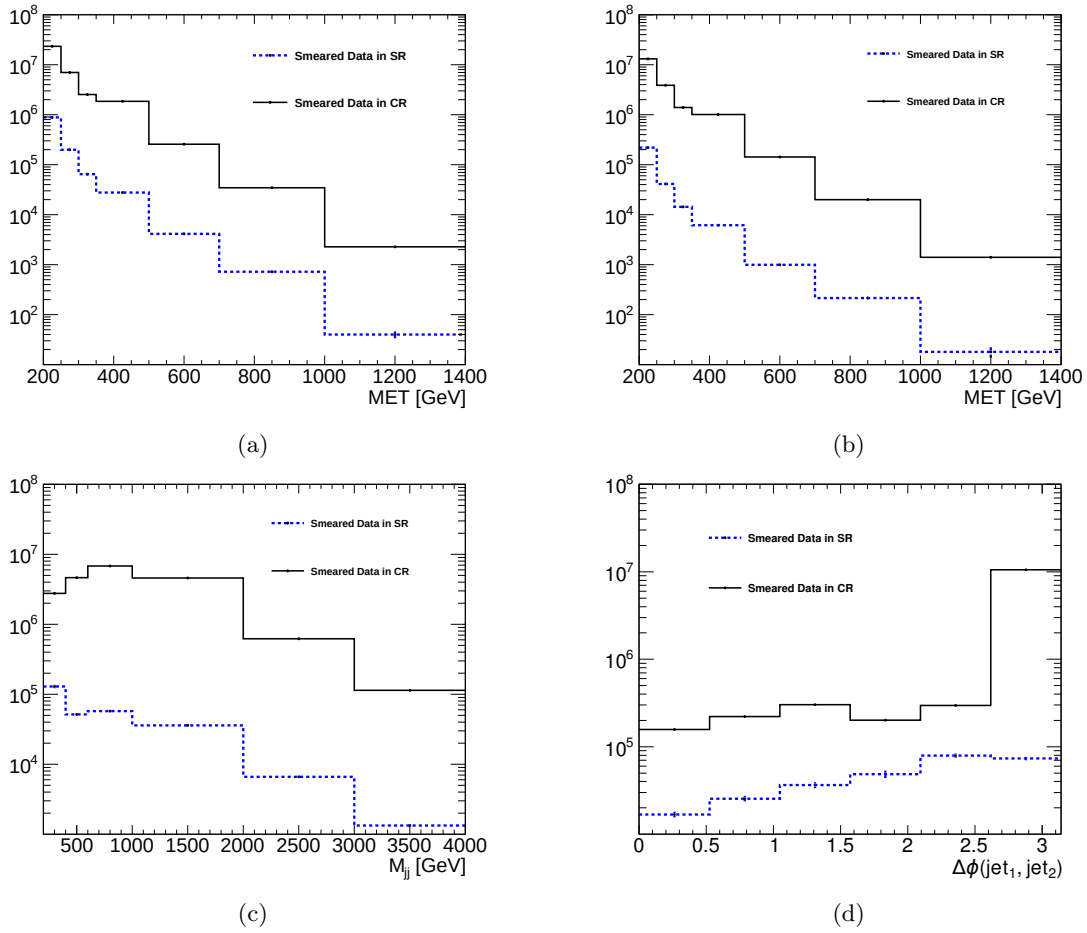


Figure B.1.: Distributions of the smeared pseudo-data set that was used to perform the multi-jet background estimate, cf. Section 5.4.2. Shown are signal region and control region for the four measured distributions. The ratio of the yields gives the transfer function.

# C. Details on Storing Data and Monte Carlo Simulations in the Context of Systematic Variations

In order to reduce the disk space needed for data sets[1], usually not full events are stored locally. Instead *skimmed and slimmed* data sets are used. This means that events are not stored if they do not fulfil basic pre-requirements, i.e. the data set is *skimmed*. And of stored events only those properties are saved that are relevant for the analysis, for instance physics objects above certain $p_T$ thresholds, i.e. events are *slimmed*. This process reduces the size of data sets considerably, approximately by two orders of magnitude. For the treatment of systematic uncertainties of objects, such as jets, properties of the object are varied according to shifts that correspond to the $\pm 1\sigma$ uncertainty with respect to a given source. The resulting systematic variation is then stored, too.

$p_{\mathrm{T}}^{\mathrm{miss}}$ is a special case, because its systematic uncertainty originates in the systematic variations of all objects it is constructed from, cf. Section 3.4.5. This means that for each variation of an underlying object, such as JES uncertainties of jets or momentum shifts of leptons, a separate copy the $p_{\mathrm{T}}^{\mathrm{miss}}$ object is made and stored. This leads to a huge size contribution of $p_{\mathrm{T}}^{\mathrm{miss}}$ to the overall data set[2]. It is also not practicable to perform the systematic variations of $p_{\mathrm{T}}^{\mathrm{miss}}$ on the pre-selected physics objects and to calculate it *in-situ*. The reason is the calculation of the soft term, which requires all reconstructed jets and not only selected jets. The jet object container however is one of the largest contributors to the total size of the stored data set, which makes storing it impracticable.

[1] Including both data collected by the ATLAS experiment and Monte Carlo simulations.
[2] For MC samples, all $p_{\mathrm{T}}^{\mathrm{miss}}$ objects combined are responsible for approximately 25-30% of the total size.

# D. Comparison Between Data and Monte Carlo Simulations using 2016 Data

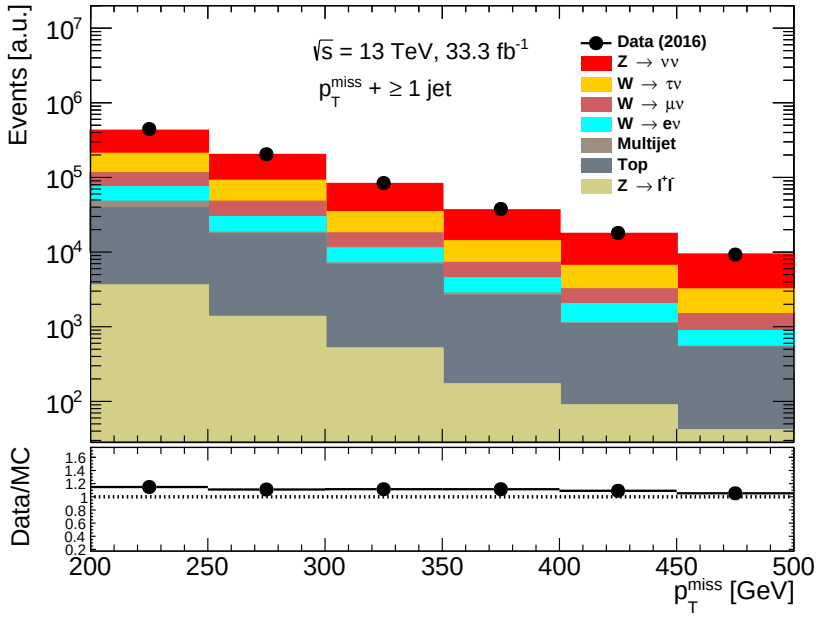


Figure D.1.: The plot shows the $p_{\mathrm{T}}^{\mathrm{miss}}$ distribution in the $\geq 1$ jet kinematic region. An agreement within approximately 15% can be observed.

# E. Additional Plots for the Multivariate Analysis Study in Section 6.3

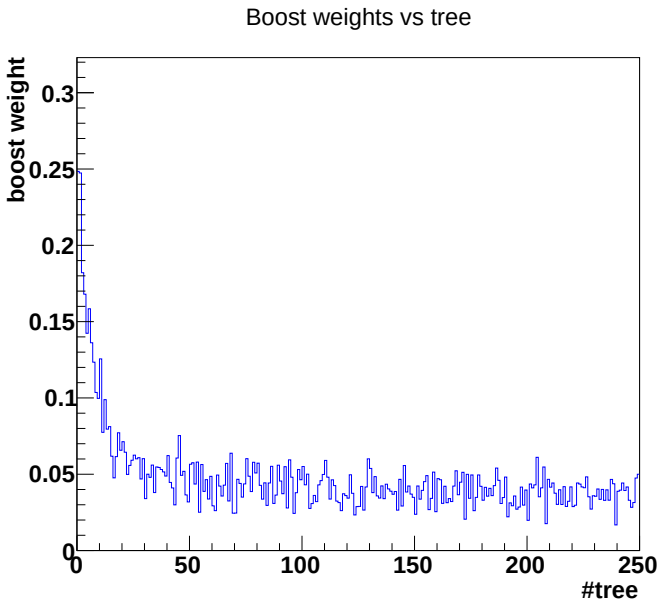


Figure E.1.: Boost weight versus the tree number when setting $N_{tree} = 250$ for the BDT including truth information. The boost weight has converged after approximately 50 trees, which eventually was chosen for $N_{tree}$.

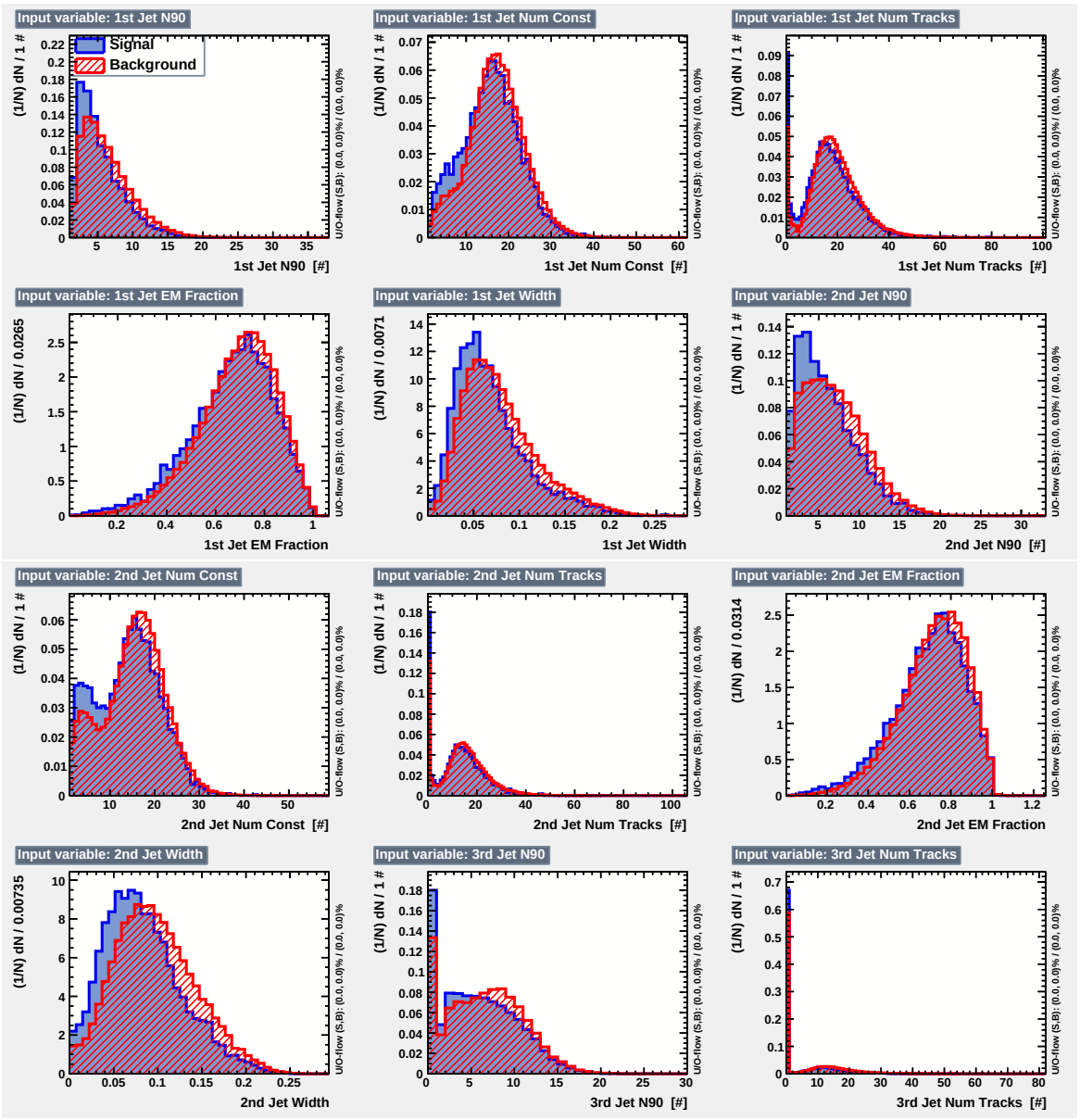


Figure E.2.: The first set of reconstruction level input variables for the BDT using a total of 28 input variables.

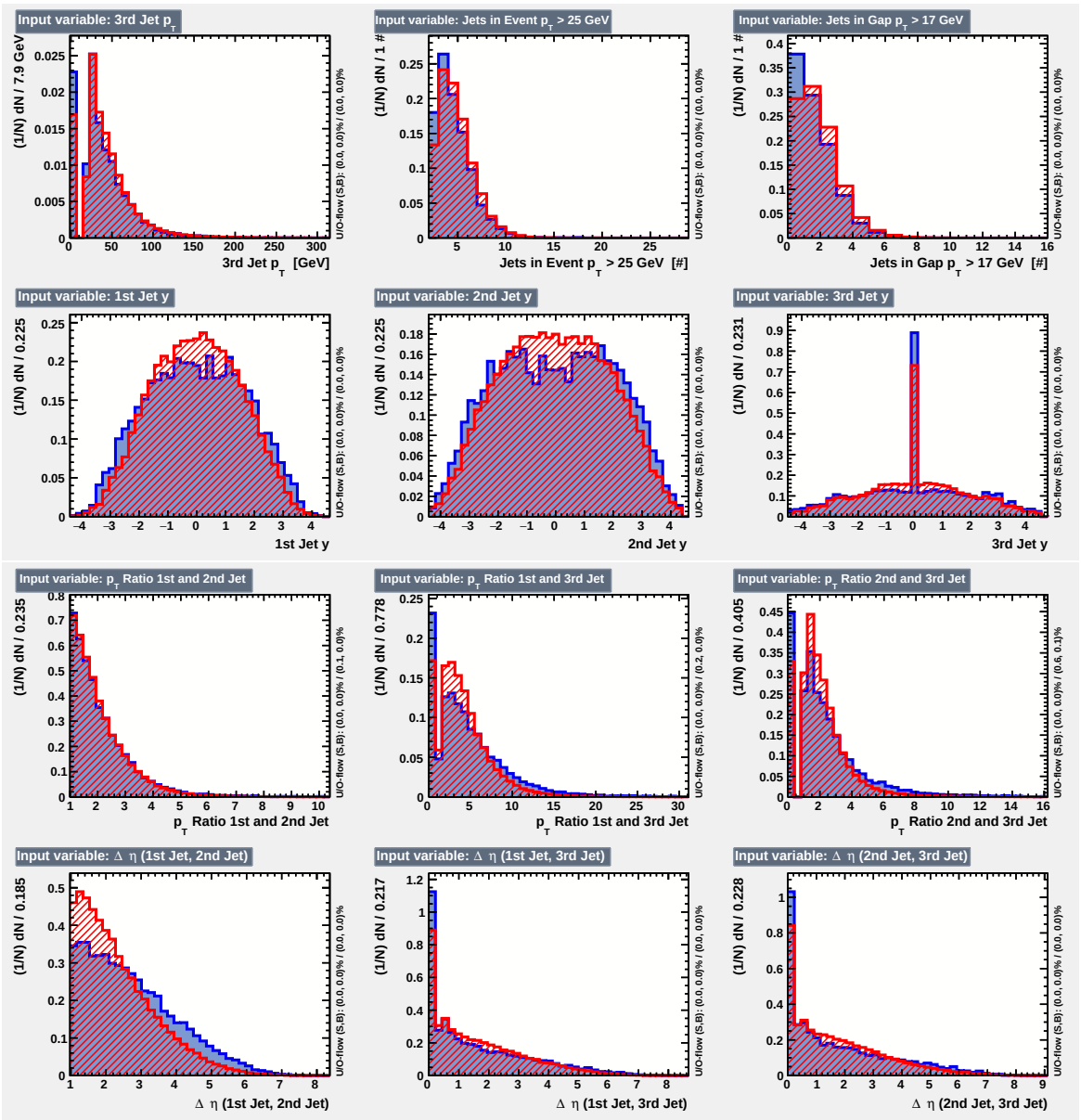


Figure E.3.: The second set of reconstruction level input variables for the BDT using a total of 28 input variables.

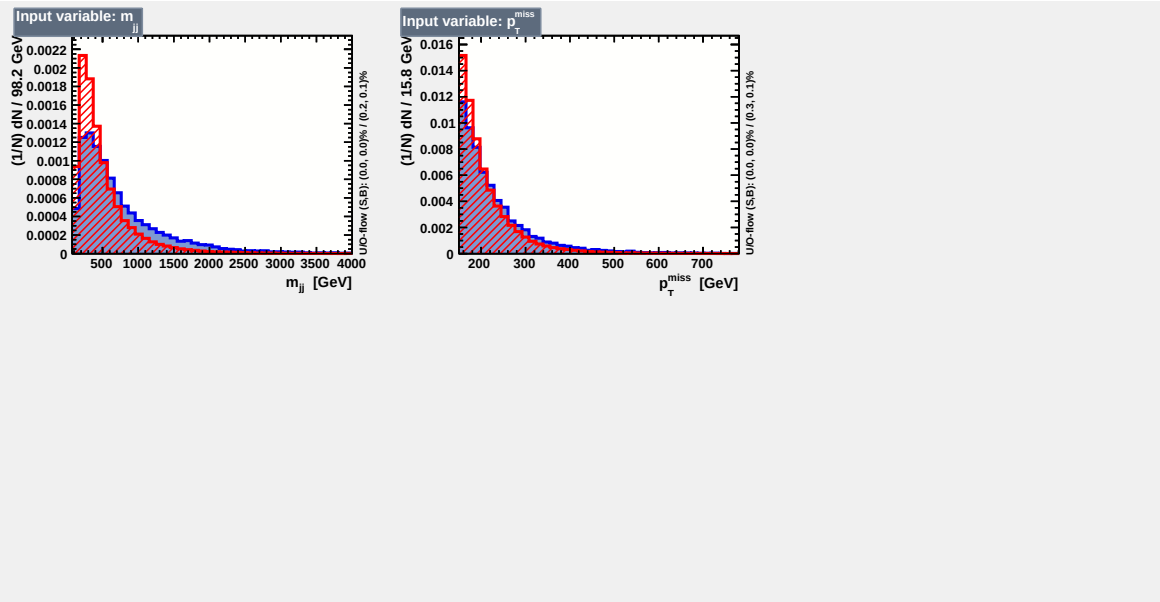


Figure E.4.: The third set of reconstruction level input variables for the BDT using 2 a total of 8 input variables.

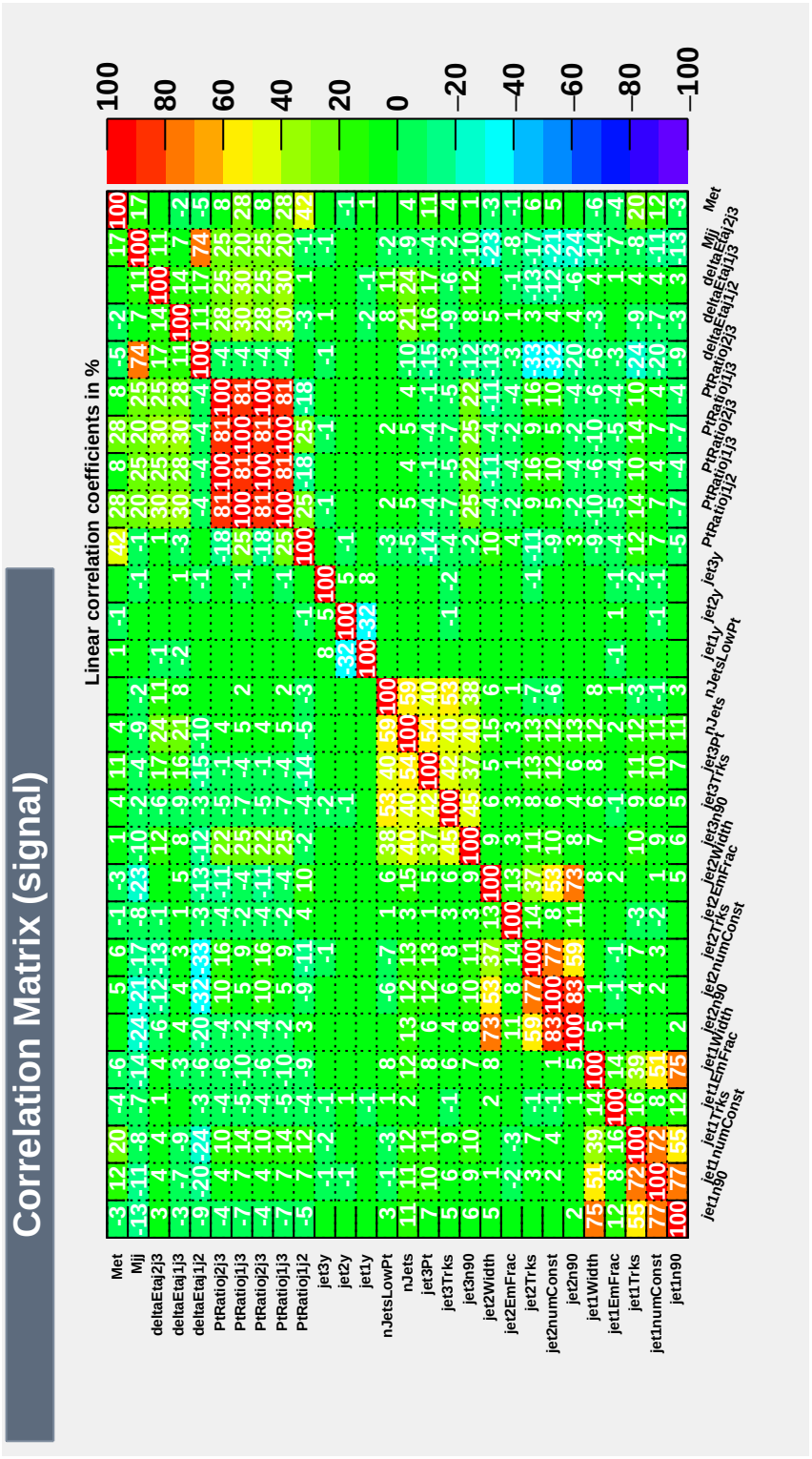


Figure E.5.: Shown are the linear correlation coefficients for the signal sample between the 28 input variables.

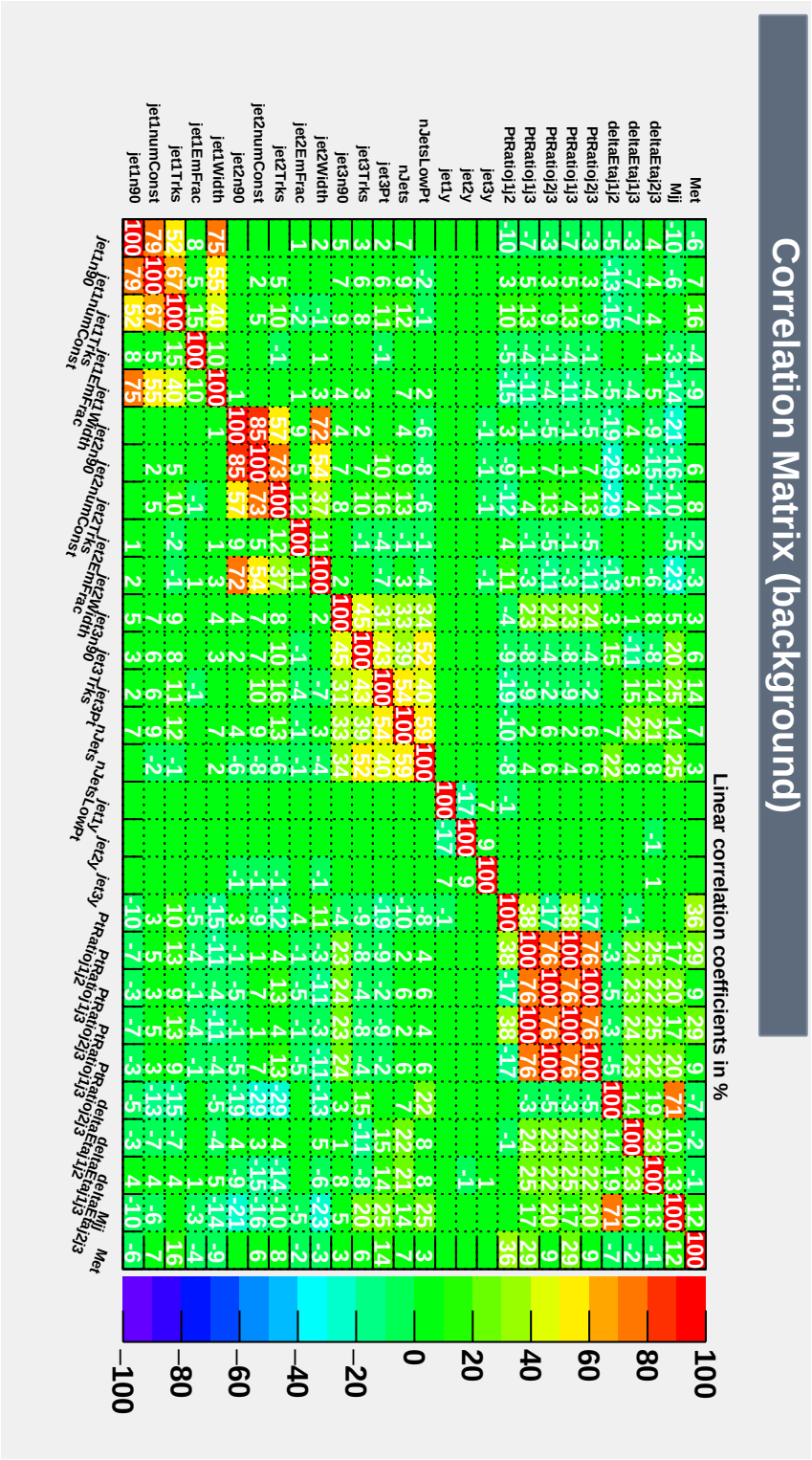


Figure E.6.: Shown are the linear correlation coefficients for the background sample between the 28 input variables.

# Bibliography


[1] ATLAS Collaboration, *Measurement of detector-corrected observables sensitive to the anomalous production of events with jets and large missing transverse momentum in pp collisions at $\sqrt{\mathbf{s}} = \mathbf{13}$ TeV using the ATLAS detector*, Eur. Phys. J. C77 (2017) p. 765, arXiv: 1707.03263 [hep-ex].

[2] Planck Collaboration, *Planck 2015 results. XIII. Cosmological parameters*, Astron. Astrophys. 594 (2016) A13, arXiv: 1502.01589 [astro-ph.CO].

[3] J. Oort, *The Force Exerted by the Stellar System in the Direction Perpendicular to the Galactic Plane and Some Related Problems*, Bull. Astron. Inst. Neth 6 (1932) p. 249.

[4] F. Zwicky, *Die Rotverschiebung von extragalaktischen Nebeln*, Helvetica Physica Acta 6 (1933) p. 110.

[5] G. Bertone and D. Hooper, *A History of Dark Matter*, Submitted to: Rev. Mod. Phys. (2016), arXiv: 1605.04909 [astro-ph.CO].

[6] ATLAS Collaboration, *Search for new phenomena in final states with an energetic jet and large missing transverse momentum in pp collisions at $\sqrt{s} = 13$ TeV using the ATLAS detector*, Phys. Rev. D 94 (3 2016) p. 032005.

[7] CMS Collaboration, *Search for dark matter produced with an energetic jet or a hadronically decaying W or Z boson at $\sqrt{s}$=13 TeV*, Journal of High Energy Physics 2017 (2017) p. 14, ISSN: 1029-8479.

[8] J. Brooke et al., *Vector boson fusion searches for dark matter at the LHC*, Phys. Rev. D 93 (11 2016) p. 113013.

[9] H. Davoudiasl, T. Han and H. E. Logan, *Discovering an invisibly decaying Higgs boson at hadron colliders*, Phys. Rev. D 71 (11 2005) p. 115007.

[10] B. Fuchs, *Dynamics of the Disks of Nearby Galaxies*, Astron. Nachr. 329 (2008) p. 916, arXiv: 0810.3503 [astro-ph].

[11] G Bertone, ed., *Particle dark matter*, Cambridge University Press, 2010, ISBN: 978-3-527-41058-3.

[12] M. Milgrom, *A Modification of the Newtonian dynamics as a possible alternative to the hidden mass hypothesis*, Astrophys. J. 270 (1983) p. 365.

[13] M. D. Seifert, *Stability of spherically symmetric solutions in modified theories of gravity*, Phys. Rev. D 76 (6 2007) p. 064002.

[14] M. Bartelmann and P. Schneider, *Weak gravitational lensing*, Physics Reports 340 (2001) p. 291 , ISSN: 0370-1573.

[15] T. Treu, *Strong Lensing by Galaxies*, Annual Review of Astronomy and Astrophysics 48 (2010) p. 87.

[16] D. Clowe et al., *A Direct Empirical Proof of the Existence of Dark Matter*, The Astrophysical Journal Letters 648 (2006) p. L109.

[17] M. White and E. F. Bunn, *The COBE Normalization of CMB Anisotropies*, 450 (1995) p. 477, arXiv: astro-ph/9503054.

[18] V. Springel et al., *Simulating the joint evolution of quasars, galaxies and their large-scale distribution*, Nature 435 (2005) p. 629, arXiv: astro-ph/0504097 [astro-ph].

[19] M. Thomson, *Modern Particle Physics*, Cambridge University Press, 2013, ISBN: 9781107034266.

[20] Wikipedia, *Standard Model — Wikipedia, The Free Encyclopedia*, Accessed 18.11.17, URL: https://en.wikipedia.org/wiki/Standard_Model.

[21] SNO Collaboration, *Measurement of the Rate of $\nu_e + d \rightarrow p + p + e^-$ Interactions Produced by $^8B$ Solar Neutrinos at the Sudbury Neutrino Observatory*, Phys. Rev. Lett. 87 (7 2001) p. 071301.

[22] SNO Collaboration, *Direct Evidence for Neutrino Flavor Transformation from Neutral-Current Interactions in the Sudbury Neutrino Observatory*, Phys. Rev. Lett. 89 (1 2002) p. 011301.

[23] Super-Kamiokande Collaboration, *Evidence for Oscillation of Atmospheric Neutrinos*, Phys. Rev. Lett. 81 (8 1998) p. 1562.

[24] ATLAS Collaboration, *Observation of a new particle in the search for the Standard Model Higgs boson with the ATLAS detector at the LHC*, Phys. Lett. B716 (2012) p. 1, arXiv: 1207.7214 [hep-ex].

[25] CMS Collaboration, *Observation of a new boson at a mass of 125 GeV with the CMS experiment at the LHC*, Phys. Lett. B716 (2012) p. 30, arXiv: 1207.7235 [hep-ex].

[26] G. Altarelli, *The Standard model of particle physics*, (2005), arXiv: hep-ph/0510281 [hep-ph].

[27] F. Englert and R. Brout, *Broken Symmetry and the Mass of Gauge Vector Mesons*, Phys. Rev. Lett. 13 (9 1964) p. 321.

[28] P. Higgs, *Broken symmetries, massless particles and gauge fields*, Phys. Lett. 12 (1964) p. 132 , ISSN: 0031-9163.

[29] G. S. Guralnik, C. R. Hagen and T. W. B. Kibble, *Global Conservation Laws and Massless Particles*, Phys. Rev. Lett. 13 (20 1964) p. 585.

[30] *Observation of $J/\psi p$ Resonances Consistent with Pentaquark States in $\Lambda_b^0 \rightarrow J/\psi K^- p$ Decays*, Phys. Rev. Lett. 115 (7 2015) p. 072001.

[31] D. Griffiths, *Introduction to Elementary Particles*, WILEY-VCH Verlag GmbH Co. KGaA, 2008, ISBN: 978-3-527-40601-2.

[32] Yu. A. Golfand and E. P. Likhtman, *Extension of the Algebra of Poincare Group Generators and Violation of p Invariance*, JETP Lett. 13 (1971) p. 323, [Pisma Zh. Eksp. Teor. Fiz.13,452(1971)].

[33] C. Munoz, *Models of Supersymmetry for Dark Matter*, (2017), [EPJ Web Conf.13,60100(2017)], arXiv: 1701.05259 [hep-ph].

[34] B. J. Carr et al., *New cosmological constraints on primordial black holes*, Phys. Rev. D 81 (10 2010) p. 104019.

[35] D. Abercrombie et al., *Dark Matter Benchmark Models for Early LHC Run-2 Searches: Report of the ATLAS/CMS Dark Matter Forum*, (2015), ed. by A. Boveia et al., arXiv: 1507.00966 [hep-ex].

[36] A. Albert et al., *Recommendations of the LHC Dark Matter Working Group: Comparing LHC searches for heavy mediators of dark matter production in visible and invisible decay channels*, (2017), arXiv: 1703.05703 [hep-ex].

[37] E. Fermi, *Versuch einer Theorie der β-Strahlen.*, Zeitschrift für Physik 88 (1934) p. 161, ISSN: 0044-3328.

[38] S. Dittmaier et al., *Handbook of LHC Higgs Cross Sections: 1. Inclusive Observables*, (2011), arXiv: 1101.0593 [hep-ph].

[39] S. Dittmaier et al., *Handbook of LHC Higgs Cross Sections: 2. Differential Distributions*, (2012), arXiv: 1201.3084 [hep-ph].

[40] ATLAS Collabortaion, *Search for invisible decays of a Higgs boson using vector-boson fusion in pp collisions at $$ \sqrt{s} = 8$$TeV with the ATLAS detector*, Journal of High Energy Physics 2016 (2016) p. 172, ISSN: 1029-8479.

[41] J. M. Cline et al., *Update on scalar singlet dark matter*, Phys. Rev. D88 (2013) p. 055025, [Erratum: Phys. Rev.D92,no.3,039906(2015)], arXiv: 1306.4710 [hep-ph].

[42] Y. G. Kim, K. Y. Lee and S. Shin, *Singlet fermionic dark matter*, JHEP 05 (2008) p. 100, arXiv: 0803.2932 [hep-ph].

[43] S. Baek, P. Ko and W.-I. Park, *Search for the Higgs portal to a singlet fermionic dark matter at the LHC*, JHEP 02 (2012) p. 047, arXiv: 1112.1847 [hep-ph].

[44] L. E. Strigari, *Galactic Searches for Dark Matter*, Phys. Rept. 531 (2013) p. 1, arXiv: 1211.7090 [astro-ph.CO].

[45] L. A. Cavasonza et al., *Constraints on leptophilic dark matter from the AMS-02 experiment*, Astrophys. J. 839 (2017) p. 36, arXiv: 1612.06634 [hep-ph].

[46] J. D. Zornoza and C. Toennis, *Results of dark matter searches with the ANTARES neutrino telescope*, J. Phys. Conf. Ser. 888 (2017) p. 012206, arXiv: 1611.02555 [astro-ph.HE].

[47] M. G. Aartsen et al., *Improved limits on dark matter annihilation in the Sun with the 79-string IceCube detector and implications for supersymmetry*, JCAP 1604 (2016) p. 022, arXiv: 1601.00653 [hep-ph].

[48] F. L. Rauch, *From Final Dark Matter Results and Background Shape Uncertainties in XENON100 to First Light in XENON1T*, PhD thesis, University of Heidelberg (2017).

[49] XENON Collaboration, *First Dark Matter Search Results from the XENON1T Experiment*, Phys. Rev. Lett. 119 (18 2017) p. 181301.

[50] D. S. Akerib et al., *First Searches for Axions and Axionlike Particles with the LUX Experiment*, Phys. Rev. Lett. 118 (2017) p. 261301, arXiv: 1704.02297 [astro-ph.CO].

[51] X. Cui et al., *Dark Matter Results From 54-Ton-Day Exposure of PandaX-II Experiment*, Phys. Rev. Lett. 119 (2017) p. 181302, arXiv: 1708.06917 [astro-ph.CO].

[52] IceCube Collaboration, *Search for annihilating dark matter in the Sun with*

*3 years of IceCube data*, The European Physical Journal C 77 (2017) p. 146, ISSN: 1434-6052.

[53] ATLAS Collaboration, 'Search for new light resonances decaying to jet pairs and produced in association with a photon or a jet in proton-proton collisions at $\sqrt{s} = 13$ TeV with the ATLAS detector', tech. rep. ATLAS-CONF-2016-070, CERN, 2016, URL: https://cds.cern.ch/record/2206221.

[54] ATLAS Collaboration, 'Search for light dijet resonances with the ATLAS detector using a Trigger-Level Analysis in LHC pp collisions at $\sqrt{s} = 13$ TeV', tech. rep. ATLAS-CONF-2016-030, CERN, 2016, URL: https://cds.cern.ch/record/2161135.

[55] ATLAS Collaboration, *ATLAS Dark Matter Limits Summary Plot*, (2017), URL: https://atlas.web.cern.ch/Atlas/GROUPS/PHYSICS/CombinedSummaryPlots/EXOTICS/index.html.

[56] L. Evans and P. Bryant, *LHC Machine*, JINST 3 (2008) S08001.

[57] ATLAS Collaboration, *The ATLAS Experiment at the CERN LHC*, JINST 3 (2008) S08003.

[58] CMS Collaboration, *The CMS Experiment at the CERN LHC*, JINST 3 (2008) S08004.

[59] LHCb Collaboration, *The LHCb Detector at the LHC*, JINST 3 (2008) S08005.

[60] Alice Collaboration, *The ALICE experiment at the CERN LHC*, JINST 3 (2008) S08002.

[61] P. Mouche, *Overall view of the LHC. View of the 4 LHC detectors: ALICE, ATLAS, CMS and LHCb*, (2014), URL: https://cds.cern.ch/record/1708847.

[62] Y. Papaphilippou et al., *Operational beams for the LHC*, (2014), arXiv: 1412.7857 [physics.acc-ph].

[63] ATLAS Collaboration, *ATLAS Public Luminosity Results of Run-2*, Accessed 07.11.17, URL: https://twiki.cern.ch/twiki/bin/view/AtlasPublic/LuminosityPublicResultsRun2.

[64] G. Altarelli and G. Parisi, *Asymptotic Freedom in Parton Language*, Nucl. Phys. B 126 (1977) p. 298.

[65] V. N. Gribov and L. N. Lipatov, *Deep inelastic e p scattering in perturbation theory*, Sov. J. Nucl. Phys. 15 (1972) p. 438, [Yad. Fiz.15,781(1972)].

[66] L. N. Lipatov, *The parton model and perturbation theory*, Sov. J. Nucl. Phys. 20 (1975) p. 94, [Yad. Fiz.20,181(1974)].

[67] Y. L. Dokshitzer, *Calculation of the Structure Functions for Deep Inelastic Scattering and e+ e- Annihilation by Perturbation Theory in Quantum Chromodynamics.*, Sov. Phys. JETP 46 (1977) p. 641, [Zh. Eksp. Teor. Fiz.73,1216(1977)].

[68] R. Placakyte, 'Parton Distribution Functions', *Proceedings, 31st International Conference on Physics in collisions (PIC 2011): Vancouver, Canada, August 28-September 1, 2011*, 2011, arXiv: 1111.5452 [hep-ph].

[69] A. D. Martin et al., *Parton distributions for the LHC*, The European Physical Journal C 63 (2009) p. 189, ISSN: 1434-6052.

[70] ATLAS Collaboration, *Performance of the ATLAS trigger system in 2015*, The European Physical Journal C 77 (2017) p. 317, ISSN: 1434-6052.

[71] ATLAS Collaboration, *Identification and rejection of pile-up jets at high pseudorapidity with the ATLAS detector*, Eur. Phys. J. C77 (2017) p. 580, [Eur. Phys. J.C77,no.10,712(2017)], arXiv: 1705.02211 [hep-ex].

[72] ATLAS Collaboration, *The ATLAS Inner Detector commissioning and calibration*, Eur. Phys. J. C 70 (2010) p. 787, arXiv: 1004.5293 [physics.ins-det].

[73] ATLAS Collaboration, 'IBL Efficiency and Single Point Resolution in Collision Events', tech. rep. ATL-INDET-PUB-2016-001, CERN, 2016, URL: https://cds.cern.ch/record/2203893.

[74] P.-G. R. C. Leroy, *Principles of Radiation Interaction in Matter and Detection*, World Scientific Publishing Co. Pte. Ltd., 2016, ISBN: 9789814603188.

[75] A. Artamonov et al., *The ATLAS forward calorimeters*, JINST 3 (2008) P02010.

[76] A. M. Henriques Correia, 'The ATLAS Tile Calorimeter', tech. rep. ATL-TILECAL-PROC-2015-002, CERN, 2015, URL: https://cds.cern.ch/record/2004868.

[77] E. Simioni, *The Topological Processor for the future ATLAS Level-1 Trigger: from design to commissioning*, (2014), arXiv: 1406.4316 [physics.ins-det].

[78] M Shochet et al., 'Fast TracKer (FTK) Technical Design Report', tech. rep. CERN-LHCC-2013-007. ATLAS-TDR-021, 2013, URL: https://cds.cern.ch/record/1552953.

[79] ATLAS Collaboration, *ATLAS Software Documentation of the ATHENA Framework*, Accessed 07.11.17, URL: https://atlassoftwaredocs.web.cern.ch.

[80] ATLAS Collaboration, 'ATLAS computing: Technical design report', tech. rep., 2005.

[81] T Cornelissen et al., 'Concepts, Design and Implementation of the ATLAS New Tracking (NEWT)', tech. rep. ATL-SOFT-PUB-2007-007. ATL-COM-SOFT-2007-002, CERN, 2007, URL: https://cds.cern.ch/record/1020106.

[82] ATLAS Collaboration, *Performance of the ATLAS Inner Detector Track and Vertex Reconstruction in High Pile-Up LHC Environment*, ATLAS-CONF-2012-042, 2012, URL: https://cds.cern.ch/record/1435196.

[83] ATLAS Collaboration, 'Track Reconstruction Performance of the ATLAS Inner Detector at $\sqrt{s} = 13$ TeV', tech. rep. ATL-PHYS-PUB-2015-018, CERN, 2015, URL: https://cds.cern.ch/record/2037683.

[84] O. Behnke et al., *Data Analysis in High Energy Physics*, WILEY-VCH Verlag GmbH Co. KGaA, 2013, ISBN: 978-3-527-41058-3.

[85] W Lampl et al., 'Calorimeter Clustering Algorithms: Description and Performance', tech. rep. ATL-LARG-PUB-2008-002. ATL-COM-LARG-2008-003, CERN, 2008, URL: https://cds.cern.ch/record/1099735.

[86] F. Müller, *Jet production measurement at the ATLAS experiment*, Heidelberg University, 2014, URL: https://www.kip.uni-heidelberg.de/Veroeffentlichungen/details.php?id=2966.

[87] M. Cacciari, G. P. Salam and G. Soyez, *The Anti-$k_t$ jet clustering algorithm*, JHEP 04 (2008) p. 063, arXiv: 0802.1189 [hep-ph].

[88] ATLAS Collaboration, 'Monte Carlo Calibration and Combination of In-situ Measurements of Jet Energy Scale, Jet Energy Resolution and Jet Mass in ATLAS', tech. rep. ATLAS-CONF-2015-037, CERN, 2015, URL: https://cds.cern.ch/record/2044941.

[89] ATLAS Collaboration, *Jet energy measurement and its systematic uncertainty in proton–proton collisions at $\sqrt{s} = 7$ TeV with the ATLAS detector*, Eur. Phys. J. C 75 (2015) p. 17, ISSN: 1434-6052.

[90] ATLAS Collaboration, *Jet energy scale measurements and their systematic uncertainties in proton-proton collisions at $\sqrt{s} = 13$ TeV with the ATLAS detector*, Phys. Rev. D96 (2017) p. 072002, arXiv: 1703.09665 [hep-ex].

[91] ATLAS Collaboration, 'Selection of jets produced in 13TeV proton-proton collisions with the ATLAS detector', tech. rep. ATLAS-CONF-2015-029, CERN, 2015, URL: https://cds.cern.ch/record/2037702.

[92] ATLAS Collaboration, *Performance of pile-up mitigation techniques for jets in pp collisions at $\sqrt{s} = 8$ TeV using the ATLAS detector*, Eur. Phys. J. C 76 (2016) p. 581, arXiv: 1510.03823 [hep-ex].

[93] ATLAS Collaboration, 'Electron efficiency measurements with the ATLAS detector using the 2015 LHC proton-proton collision data', tech. rep. ATLAS-CONF-2016-024, CERN, 2016, URL: https://cds.cern.ch/record/2157687.

[94] ATLAS Collaboration, 'Electron and photon energy calibration with the ATLAS detector using data collected in 2015 at $\sqrt{s} = 13$ TeV', tech. rep. ATL-PHYS-PUB-2016-015, CERN, 2016, URL: https://cds.cern.ch/record/2203514.

[95] ATLAS Collaboration, 'Photon identification in 2015 ATLAS data', tech. rep. ATL-PHYS-PUB-2016-014, CERN, 2016, URL: https://cds.cern.ch/record/2203125.

[96] ATLAS Collaboration, *ATLAS Public Electron Gamma Results*, Accessed 08.11.17, URL: https://twiki.cern.ch/twiki/bin/view/AtlasPublic/ElectronGammaPublicCollisionResults.

[97] ATLAS Collaboration, *Muon reconstruction performance of the ATLAS detector in proton–proton collision data at $\sqrt{s}$ =13 TeV*, Eur. Phys. J. C76 (2016) p. 292, arXiv: 1603.05598 [hep-ex].

[98] C. Patrignani et al., *Review of Particle Physics*, Chin. Phys. C40 (2016) p. 100001.

[99] ATLAS Collaboration, *Reconstruction of hadronic decay products of tau leptons with the ATLAS experiment*, Eur. Phys. J. C76 (2016) p. 295, arXiv: 1512.05955 [hep-ex].

[100] ATLAS Collaboration, 'Performance of missing transverse momentum reconstruction for the ATLAS detector in the first proton-proton collisions at at $\sqrt{s}$= 13 TeV', tech. rep. ATL-PHYS-PUB-2015-027, CERN, 2015, URL: https://cds.cern.ch/record/2037904.

[101] ATLAS Collaboration, *The ATLAS Simulation Infrastructure*, Eur. Phys. J. C 70 (2010) p. 823, arXiv: 1005.4568 [physics.ins-det].

[102] S. Dulat et al., *New parton distribution functions from a global analysis of quantum chromodynamics*, Phys. Rev. D 93 (3 2016) p. 033006.

[103] R. D. Ball et al., *Parton distributions for the LHC run II*, Journal of High Energy Physics 2015 (2015) p. 40, ISSN: 1029-8479.

[104] L. A. Harland-Lang et al., *Parton distributions in the LHC era: MMHT 2014 PDFs*, The European Physical Journal C 75 (2015) p. 204, ISSN: 1434-6052.

[105] Y. Kulchitsky, *Measurement of the underlying-event properties with the ATLAS detector*, (2016), arXiv: 1608.04954 [hep-ex].

[106] B. R. Webber, *A QCD Model for Jet Fragmentation Including Soft Gluon Interference*, Nucl. Phys. B238 (1984) p. 492.

[107] B. Webber, *A QCD model for jet fragmentation including soft gluon interference*, Nucl. Phys. B 238 (1984) p. 492 , ISSN: 0550-3213.

[108] T. Gleisberg et al., *Event generation with SHERPA 1.1*, JHEP 02 (2009) p. 007, arXiv: 0811.4622 [hep-ph].

[109] T. Sjöstrand, S. Mrenna and P. Z. Skands, *PYTHIA 6.4 Physics and Manual*, JHEP 05 (2006) p. 026, arXiv: 0603175.

[110] T. Sjöstrand, S. Mrenna and P. Z. Skands, *A Brief Introduction to PYTHIA 8.1*, Comput. Phys. Commun. 178 (2008) p. 852, arXiv: 0710.3820 [hep-ph].

[111] S. Agostinelli et al., *GEANT4: A simulation toolkit*, Nucl. Instrum. Meth. A 506 (2003) p. 250.

[112] N. Arkani-Hamed, S. Dimopoulos and G. R. Dvali, *The Hierarchy problem and new dimensions at a millimeter*, Phys. Lett. B429 (1998) p. 263, arXiv: hep-ph/9803315 [hep-ph].

[113] ATLAS Collaboration, *Search for the anomalous production of events containing jets and missing transverse momentum using a novel approach*, ATL-COM-PHYS-2016-719 (2016).

[114] ATLAS Collaboration, *Measurement of $W^{\pm}$ and Z-boson production cross sections in pp collisions at $\sqrt{s} = 13$ TeV with the ATLAS detector*, Phys. Lett. B759 (2016) p. 601, arXiv: 1603.09222 [hep-ex].

[115] ATLAS Collaboration, *A measurement of the ratio of the production cross sections for W and Z bosons in association with jets with the ATLAS detector*, The European Physical Journal C 74 (2014) p. 3168, ISSN: 1434-6052.

[116] ATLAS Collaboration, *Measurement of the inclusive $W^{\pm}$ and Z/gamma cross sections in the electron and muon decay channels in pp collisions at $\sqrt{s} = 7$ TeV with the ATLAS detector*, Phys. Rev. D85 (2012) p. 072004, arXiv: 1109.5141 [hep-ex].

[117] ATLAS Collaboration, *Measurements of electroweak $Wjj$ production and constraints on anomalous gauge couplings with the ATLAS detector*, Eur. Phys. J. C77 (2017) p. 474, arXiv: 1703.04362 [hep-ex].

[118] ATLAS Collaboration, *Measurement of the electroweak production of dijets in association with a Z-boson and distributions sensitive to vector boson fusion in proton-proton collisions at $\sqrt{s} = 8$ TeV using the ATLAS detector*, JHEP 04 (2014) p. 031, arXiv: 1401.7610 [hep-ex].

[119] M. Rauch, *Vector-Boson Fusion and Vector-Boson Scattering*, (2016), arXiv: 1610.08420 [hep-ph].

[120] M. R. Buckley and M. J. Ramsey-Musolf, *Diagnosing spin at the LHC*

*via vector boson fusion*, Journal of High Energy Physics 2011 (2011) p. 94, ISSN: 1029-8479.

[121] T. Plehn, *Lectures on LHC Physics*, Lect. Notes Phys. 844 (2012) p. 1, arXiv: 0910.4182 [hep-ph].

[122] ATLAS Collaboration, *Performance of b-Jet Identification in the ATLAS Experiment*, JINST 11 (2016) P04008, arXiv: 1512.01094 [hep-ex].

[123] ATLAS Collaboration, *Search for charged Higgs bosons in the $H^{\pm} \to tb$ decay channel in pp collisions at $\sqrt{s} = 8$ TeV using the ATLAS detector*, JHEP 03 (2016) p. 127, arXiv: 1512.03704 [hep-ex].

[124] A. Hocker et al., *TMVA - Toolkit for Multivariate Data Analysis*, PoS ACAT (2007) p. 040, arXiv: physics/0703039 [PHYSICS].

[125] 'Proposal for truth particle observable definitions in physics measurements', tech. rep. ATL-PHYS-PUB-2015-013, CERN, 2015, URL: https://cds.cern.ch/record/2022743.

[126] ATLAS Collaboration, *Performance of the ATLAS track reconstruction algorithms in dense environments in LHC Run 2*, The European Physical Journal C 77 (2017) p. 673, ISSN: 1434-6052.

[127] ATLAS Collaboration, 'Measurement of inclusive-jet cross-sections in proton-proton collisions at $\sqrt{s} = 13$ TeV centre-of-mass energy with the ATLAS detector', tech. rep. ATLAS-CONF-2016-092, CERN, 2016, URL: https://cds.cern.ch/record/2209210.

[128] V. Christodoulou, *Search for dark matter in events containing jets and missing transverse momentum using ratio measurements*, PhD thesis, University College London (2017).

[129] ATLAS Collaboration, *Muon reconstruction performance of the ATLAS detector in proton–proton collision data at $\sqrt{s} = 13$ TeV*, The European Physical Journal C 76 (2016) p. 292, ISSN: 1434-6052.

[130] ATLAS Collaboration, *Electron efficiency measurements with the ATLAS detector using 2012 LHC proton–proton collision data*, Eur. Phys. J. C 77 (2017) p. 195, ISSN: 1434-6052.

[131] C. M. Macdonald, *Searches for supersymmetry in final states containing b-tagged jets with the ATLAS detector*, PhD thesis, University of Sheffield (2017), URL: http://etheses.whiterose.ac.uk/17990/.

[132] S Owen, 'Data-driven estimation of the QCD multijet background to SUSY searches with jets and missing transverse momentum at ATLAS using jet smearing', tech. rep. ATL-PHYS-INT-2012-008, CERN, 2012, URL: https://cds.cern.ch/record/1423310.

[133] G. T. Fletcher, *Multijet Background Estimation For SUSY Searches And Particle Flow Offline Reconstruction Using the ATLAS Detector At The LHC.*, PhD thesis, University of Sheffield (2015), URL: http://etheses.whiterose.ac.uk/9629/.

[134] S. Catani et al., *QCD Matrix Elements + Parton Showers*, Journal of High Energy Physics 2001 (2001) p. 063.

[135] S. Höche et al., *QCD matrix elements and truncated showers*, Journal of High Energy Physics 2009 (2009) p. 053.

[136] R. Nisius, *On the combination of correlated estimates of a physics observable*, The European Physical Journal C 74 (2014) p. 3004.

[137] K. G. Hayes, M. L. Perl and B. Efron, *Application of the bootstrap statistical method to the tau-decay-mode problem*, Phys. Rev. D 39 (1 1989) p. 274.

[138] A. L. Read, *Presentation of search results: The CL(s) technique*, J. Phys. G28 (2002) p. 2693, [,11(2002)].

[139] T. Junk, *Confidence level computation for combining searches with small statistics*, Nuclear Instruments and Methods in Physics Research Section A: Accelerators, Spectrometers, Detectors and Associated Equipment 434 (1999) p. 435 , ISSN: 0168-9002.

[140] Planck Collaboration et al., *Planck 2015 results - I. Overview of products and scientific results*, AA 594 (2016) A1.

[141] G. Hinshaw et al., *Nine-year Wilkinson Microwave Anisotropy Probe (WMAP) Observations: Cosmological Parameter Results*, The Astrophysical Journal Supplement Series 208 (2013) p. 19.

[142] R. C. Cotta et al., *Bounds on dark matter interactions with electroweak gauge bosons*, Phys. Rev. D 88 (11 2013) p. 116009.

[143] M. Ackermann et al., *Constraining Dark Matter Models from a Combined Analysis of Milky Way Satellites with the Fermi Large Area Telescope*, Phys. Rev. Lett. 107 (24 2011) p. 241302.

[144] V. collaboration, *VERITAS deep observations of the dwarf spheroidal galaxy Segue 1*, Phys. Rev. D 85 (6 2012) p. 062001.

[145] B. Bernarding, *Towards Unfolding Topologies Proof of Concept within a Monojet Analysis*, MSc thesis, University of Heidelberg (2016), URL: http://www.kip.uni-heidelberg.de/Veroeffentlichungen/details.php?id=3475.

[146] G. Cowan et al., *Asymptotic formulae for likelihood-based tests of new physics*, Eur. Phys. J. C 71 (2011) p. 1554, [Erratum: Eur. Phys. J. C 73,2501(2013)], arXiv: 1007.1727 [physics.data-an].

[147] ATLAS Collaboration, *Light-quark and gluon jet discrimination in pp collisions at $\sqrt{s} = 7$ TeV with the ATLAS detector*, Eur. Phys. J. C74 (2014) p. 3023, arXiv: 1405.6583 [hep-ex].

[148] T. Gleisberg and S. Hoeche, *Comix, a new matrix element generator*, JHEP 12 (2008) p. 039, arXiv: 0808.3674 [hep-ph].

[149] F. Cascioli, P. Maierhofer and S. Pozzorini, *Scattering Amplitudes with Open Loops*, Phys. Rev. Lett. 108 (2012) p. 111601, arXiv: 1111.5206 [hep-ph].

[150] S. Hoeche et al., *QCD matrix elements + parton showers: The NLO case*, JHEP 04 (2013) p. 027, arXiv: 1207.5030 [hep-ph].

[151] J. Alwall et al., *The automated computation of tree-level and next-to-leading order differential cross sections, and their matching to parton shower simulations*, JHEP 07 (2014) p. 079, arXiv: 1405.0301 [hep-ph].

[152] D. J. Lange, *The EvtGen particle decay simulation package*, Nucl. Instrum. Meth. A462 (2001) p. 152.

[153] H.-L. Lai et al., *New parton distributions for collider physics*, Phys. Rev. D 82 (2010) p. 074024, arXiv: 1007.2241 [hep-ph].

[154] S. Frixione, P. Nason and C. Oleari, *Matching NLO QCD computations with Parton Shower simulations: the POWHEG method*, JHEP 11 (2007) p. 070, arXiv: 0709.2092 [hep-ph].

[155] J. Pumplin et al., *New generation of parton distributions with uncertainties from global QCD analysis*, JHEP 07 (2002) p. 012, arXiv: hep-ph/0201195 [hep-ph].

[156] P. Z. Skands, *Tuning Monte Carlo Generators: The Perugia Tunes*, Phys. Rev. D82 (2010) p. 074018, arXiv: 1005.3457 [hep-ph].

[157] A. D. Martin et al., *Parton distributions for the LHC*, Eur. Phys. J. C 63 (2009) p. 189, arXiv: 0901.0002 [hep-ph].

[158] ATLAS Collaboration, 'Further ATLAS tunes of PYTHIA6 and Pythia 8', tech. rep. ATL-PHYS-PUB-2011-014, CERN, 2011, URL: https://cds.cern.ch/record/1400677.

# Danksagung

Ich danke meinem Betreuer Prof. Dr. Hans-Christian Schultz-Coulon, der mir ermöglicht hat, als Seiteneinsteiger in die Teilchenphysik an spannenden Themen zu arbeiten. Er hat maßgeblich zum Erfolg meiner Promotion beigetragen und ein sicheres und qualitativ hochwertiges Arbeitsumfeld geschaffen.

Ich danke Prof. Dr. Andre Schöning dafür, dass er sich bereit erklärt hat, Zweitgutachter meiner Doktorarbeit zu sein.

Ich danke den hervorragenden Senior Post-Docs und Betreuern der ATLAS Arbeitsgruppe des Kirchhoff-Instituts für Physik: Dr. Monica Dunford, Dr. Martin Wessels, Dr. Rainer Stamen, Dr. Victor Andrei, Dr. Oleg Brandt und Dr. Pavel Starovoitov. Insbesondere Martins Unterstützung während der Service Task und Monicas Betreuung während der Analyse waren unermesslich hilfreich.

Ich danke meinen lieben Kollegen und Freunden aus den Gruppen F8 und F11. Die Bachelorstudenten, Masterstudenten, Promovierenden und noch nicht genannten Post-Docs standen nicht nur fachlich zur Seite, sondern boten auch die manchmal dringend benötigte Zerstreuung. Danke an Hanno, Jan, Daniel, Merve, Falk, Basti, Thomas, Sebastian, Aless, Julia, Konrad, David, Victor, Valerie, Stanislav, Claire, Nadia, Huangshan, Xiaoguang, Yonathan und all die anderen! Besonderer Dank gilt Petra für die stetige und immer gut gelaunte Unterstützung!

Ich danke meinen Kollegen bei L1Calo und meiner Analysegruppe für den herzlichen Empfang in ihrer Mitte und die super Zusammenarbeit: danke an Bruce, Murrough, Kate, Ivana, Eduard, Terry, Valentinos, Emily, Andy, Darren, Rebecca, Zara und alle anderen!

Ich danke den fleißigen Korrekturlesern: Sebastian, Thomas, Merve, Anke, Jan, Rainer, Monica und meinem großartigen Bruder Phil.

Ich danke meinen Freunden für die angenehme und vielfältige Zerstreuung, um auch mal abzuschalten. Ich danke Dome, Karo, Nils, Ferdi, Daniel, Hasi[1], Schnubbie[2], Katja, Andy, Jörn, Angi, Loth, Milan, Schulte, Jonathan, Kathy, Jan, Felix, Leo, Stef, Hilke, Tessi und all den anderen!

Ich danke meiner Familie, der ich ein priviligiertes, reiches und schönes Leben verdanke. Ihre anhaltende Unterstützung hat mir geholfen, meine Ziele zu erreichen und meine Träume zu verwirklichen.

Ich danke meiner hervorragenden Freundin und Lebensgefährtin Andrea, die mich trotz all der schlechten Witze und dummen Sprüche der vergangenen 7 1/2 Jahre irgendwie immer noch liebt.

[1] Ja, der wird wirklich so gerufen.
[2] Der auch.